2009

NCREE Research Programs and Accomplishments

National Center for Research on Earthquake Engineering

2009 NCREE Research Programs and Accomplishments

Foreword

The “2009 Report on Research Progress and Accomplishments” is the tenth issue of its kind. It highlights some important ongoing research projects conducted at the National Center for Research on Earthquake Engineering (NCREE), Taiwan. The selected 50 articles contained in this report cover a broad spectrum of research efforts made in the year 2009. It encompasses seven major categories as follows:

- Research on performance-based seismic design methods to enhance earthquake resilience of new structures;
- Research on seismic performance assessment and retrofit techniques for buildings with various experiments conducted on full-scale school buildings;
- Enhancement of Taiwan Earthquake Loss Estimation System with Web-GIS technology and facility module;
- Research on innovative seismic-resisting technologies to deliver smart and sustainable structural system;
- Development of advanced experimental technologies, numerical simulation software, and imagery measurement capability;
- Integration of seismology and earthquake engineering for enhancement of research on strong motion including the fracture mechanism of fault, the earthquake source parameters, and micro-tremor site characteristics study; and
- Research on geotechnical engineering such as seismic performance evaluation of pile foundation and shaking table tests.

It is our sincere hope that these vibrant research efforts at NCREE could be evaluated and recognized by the earthquake engineering community through the continuous publication of such progress report. Thus, we look forward that this information will create opportunities for exchange of research findings as well as make contributions to the national coordination and international collaboration in the field of earthquake engineering.

The full version of each research discussed in the progress report can be requested from the corresponding authors. The electronic version (in PDF format) of the report can be downloaded also from NCREE’s official web site (http://www.ncree.org).

Kuo-Chun Chang, Director

June 1, 2010

Catalog

Preliminary Improvement on the Performance-Based Seismic Design of Buildings in Taiwan (Ⅲ)

Tsung-Jen Teng, Juin-Fu Chai, Wen-I Liao, Wen-Yu Jean,

Yuan-Tao Weng, Shyh-Bin Chiou, Fan-Ru Lin, and Te-Kuang Chow

鄧崇任 [1]、柴駿甫 [2]、廖文義 [3]、簡文郁 [4]、翁元滔 [5]、邱世彬 [6]、林凡茹 [7]、周德光 [8]

Abstract

The objective of this study is to link efficiently the current classical force-based design code to a future version of performance-based design guideline. For this purpose, a transition design framework has been proposed to combine the concepts of seismic use group and seismic design category, which are both recommended by FEMA450 and IBC2006. Moreover, the provisions and the associated commentaries were developed, and it can be expected to serve as an intermediate version of the performance-based design code.

Keywords: intermediate version of performance-based design, performance objective, deformation requirement, performance evaluation, acceptance criteria

Introduction

In general, the seismic performance of a building depends on both its strength and deformation capacities. The main objective of the traditional seismic design code is only to achieve the strength requirement based on a predefined deformation capacity. In order to link smoothly the current classical force-based design code to a future version of performance-based design code, a design framework was proposed to incorporate the current sophisticated force-based design methodology with the concepts of seismic use group and seismic design category which are recommended by FEMA 450 and IBC 2006. Based on the design framework, the provisions and commentaries were developed, and it can be expected to serve as an intermediate version of performance-based design guideline.

The strategy in developing the intermediate version of performance-based design guideline is to arrange the performance related provisions in specific chapters: (1) the design performance objectives are specified in Chapter 1: General Provision, (2) the seismic demands are specified in Chapter 2: Ground Motions, (3) the deformation requirement (deflection and drift limits) is specified in Chapter 3: Structural Design Criteria, and (4) the procedures to determine the story drift is specified in Chapter 4: Structural Analysis.

Provisions and Commentary on Design Performance Objectives

In order to implement the performance matrix, the associated provision and commentary are specified as follows:

> 1.2.2 Design performance objectives.
>
> Buildings designed in compliance with the provisions for each Seismic Use Group (SUG) are intended, as a minimum, to be capable of providing the performance indicated in Table 1-1.

Each building or structure should be assigned to one of three Seismic Use Groups on the basis of their intended occupancy and use. Most commercial, residential and industrial structures are assigned to SUG I. Buildings occupied by large numbers of persons or by persons with limited mobility, or that house with large quantities of potentially hazardous materials are assigned to SUG II. Buildings that are essential to post-earthquake disaster response and recovery operations are assigned to SUG III. Buildings in each of SUGs II and III are intended to provide a better performance than buildings in SUG I.

Figure C1-1 is the original performance matrix as proposed in the transition design framework, which defines the design objective for SUGs I, II and III. For each SUG, the design objective consists of multiple design goals, and each goal shall consist of a target Building Performance Level (Operational, Immediate Occupancy, Life Safety or Collapse Prevention) and an Earthquake Hazard Level (EQ-I, EQ-II or EQ-III).

It can be found from Fig. C1-1 that the Earthquake Hazard Level EQ-I is defined by 50% probability of exceedance within 50 years (50%/50), and the expected building performance levels are Life Safety and Operational for SUGs I and III, respectively. Based on the current force-based design code, the designed building shall be kept elastic for a small earthquake with spectral acceleration demand of $S_{aD}/4.2$. Thus, instead of the deformation performance for earthquake hazard of 50%/50 yrs as shown in Table 1-1, the design goal for small earthquakes is defined as the same as that specified by the current seismic design code. It means that Earthquake Hazard Level EQ-I can be defined directly by $S_{aD}/4.2$, and all buildings shall be kept elastic for EQ-I. The result is that we do not have to define the seismic demand for earthquake hazard of 50%/50 yrs and the acceptance criteria for Operational performance level.

As shown in Fig. C1-1, the building performance levels for EQ-Ⅲ (2%/50) are Collapse Prevention and Life Safety for SUGs I and III, respectively. Based on the structural analysis of buildings that is designed in compliance with the detailing requirements as specified by the current force-based design code, it can be found that the resulted ductility will reach the dominant ductility capacity and allowable ductility capacity for SUGs I and III, respectively. Hence, the Collapse Prevention and Life Safety performance levels for SUGs I and III, respectively, can be satisfied automatically. Therefore, for all buildings (SUGs I, II and III) that follow the detailing requirements, the check of deformation capacity can be replaced by the check of maximum shear strength of each building level.

Therefore, excluding EQ-I and EQ-III as mentioned before, the expected performance will be checked only for EQ-II (10%/50). The Building Performance Levels shall be described quantitatively, and the limit values for Immediate Occupancy and Life Safety levels are dependent on the structural systems. For the newly developed intermediate version of performance-based design guideline, the performance index is defined by the story drift and the allowable story drift for SUGs I, II and III for EQ-II (10%/50) are defined as shown in Table 3-4.

In other words, based on the intermediate version of performance-based design guideline, the strategy in implementing the performance-based design is to achieve the preliminary design following the current force-based design code, and then check the drift demand for EQ-II (10%/50) by comparing with the allowable story drift. The key provisions for drift limit and story drift determination will be described in the following sections.

Provisions for Deflection and Drift Limit

The deformation requirement (deflection and drift limits) is specified in Chapter 3: Structural Design Criteria, and the key provision is specified as follows:

> 3.5.2 Deflection and drift limits.
>
> The design story drift, Δ, shall not exceed the allowable story drift, Δ_a, as obtained from Table 3-4 for any story. For structures with significant torsional deflections, the maximum drift shall include torsional effects. All portions of the structure shall be designed and constructed to act as an integral unit in resisting seismic forces unless separated structurally by a distance sufficient to avoid damaging contact under total deflection, , as determined in Sec. 4.2.9.2.
>
> Structures assigned to Seismic Design Categories C, the deflection in the plane of the diaphragm, as determined by engineering analysis, shall not exceed the permissible deflection of the attached elements. Permissible deflection shall be a deflection that permits the attached elements to maintain their structural integrity under the individual loading and to continue to support the prescribed loads.
>
> Structures assigned to Seismic Design Categories D shall comply with the same requirements as those of Seismic Design Categories C. In addition, every structural component not included as part of the seismic-force-resisting system in the direction under consideration shall be designed to be adequate for the effects of gravity loads in combination with the induced moments and shears resulting from the design story drift Δ.
>
> Exception: Beams, columns and their connections not designed as part of the seismic-force-resisting system but meet the detailing requirements for either intermediate moment frames or special moment frames are permitted to be designed to be adequate for the effects of gravity loads in combination with the induced moments and shears resulting from the deformation of the building under the application of the design seismic forces.
>
> To determine the moments and shears in components that are not included as part of the seismic-force-resisting system in the direction under consideration, the stiffening effects of adjoining rigid structural and nonstructural

elements shall be considered and a rational value of member and restraint stiffness shall be used.

Provisions for Story Drift Determination

The procedures to determine the story drift is specified in Chapter 4: Structural Analysis, and the key provision is specified as follows:

4.2.9.2 Story drift determination.

The design story drift, Δ, shall be computed as the difference of the deflections at the center of mass at the top and bottom of the story under consideration. For structures having plan irregularity Type 1a or 1b of Table 3-3, the design story drift shall be computed as the largest difference of the deflections along any of the edges of the structure at the top and bottom of the story under consideration.

The deflection of Level x, δ_x, shall be determined in accordance with following equation:

$$\delta_x = \frac{C_d \delta_{xd}}{I} \tag{4-15}$$

Where

C_d = the deflection amplification factor from Table 3-1.

δ_{xd} = the deflections determined by an elastic analysis. The elastic analysis of the seismic-force-resisting system shall be made using the prescribed seismic design forces of Sec.4.2.6, and

I = the occupancy importance factor determined in accordance with Sec.1.3.

To determine compliance with the story drift limits of Sec.3.5, it shall be permitted to determine the elastic drifts, δ_{xd}, using seismic design forces based on the computed fundamental period of the structure without the upper limit as specified in Sec.4.2.2.

Where nonlinear analysis is required by Sec. 4.2.11 and the nonlinear static procedure is used, the design story drift, Δ, shall be determined according to Sec.4.5.2.4.

Conclusions

In order to incorporate the proposed performance matrix into the current seismic design code, the design framework and the contents of the current seismic design code has been reorganized for the additional provisions on the analysis procedures to evaluate the maximum story drift and the acceptance criteria. The intermediate version has the merit of, for example, when a structural engineer designs a building in accordance with the requirements on the various Seismic Use Group, he can determine and make sure if the building can achieve the specified design objectives. This implies that he needs not to perform the performance evaluation procedure that may be much cumbersome. In this situation, it makes no difference with the classical one. Also, this intermediate version provides an option beyond the current seismic code, as it is designed for specific performance, rather than simply achieving code compliance, a performance evaluation shown in Fig. 1 may be performed. It is expected that the intermediate version as proposed in this study can link smoothly the current classical force-based design code to the future version of performance-based design guideline.

References

ASCE Standard (2006), ASCE/SEI 7-05, Minimum Design Loads for Buildings and Other Structures, American Society of Civil Engineers.

FEMA-356 (2000), Pre-standard and Commentary for the Seismic Rehabilitation of Buildings, Federal Emergency Management Agency, SAC Joint Venture, Sacramento, California.

FEMA-450 (2003), Building Seismic Safety Council. Recommended provisions for seismic regulations for new buildings and other structures Part1: Provisions, Washington DC, Building Seismic Safety Council, National Institute of Building Sciences.

IBC 2006 (2006), 2006 International Building Code, International Code council.

Teng, T.-J., J.-F. Chai, W.-I Liao, W.-Y. Jean, Y.-T. Weng, S.-B. Chiou, F.-R. Lin, and T.-K. Chow (2007), Research on Performance-Based Seismic Design Guideline for Buildings (III), NCREE Report, NCREE-07-010 (in Chinese).

Table1-1 Performance Objectives

Earthquake Hazard Level	Seismic Use Group		
	I	II	III
EQ-I (S_{aD}/4.2)	Retain elastic	Retain elastic	Retain elastic
EQ-Ⅱ (10%/50)[1]	Life Safety (LS)	0.5×（LS+IO）	Immediate Occupancy (IO)
EQ-Ⅲ (2%/50)[2]	Collapse Prevention (CP)	0.5×（CP+LS）	Life Safety (LS)

Note 1: The limit value for Immediate Occupancy (IO), Life Safety (LS) and Collapse Prevention (CP) Building Performance Levels are dependent on the structural systems, see Table 3-4.

Note 2: For EQ-Ⅲ (2%/50yrs), instead of the check of deformation capacity, the maximum shear strength of each building level for all SUGs shall be evaluated.

Table3-4 Allowable Story Drift, Δ_a [a,b]

Structure	Seismic Use Group		
	I	II	III
Structures, other than those using masonry seismic-force-resisting system, four stories or less in height with interior walls, partitions, ceilings, and exterior wall systems that have been designed to accommodate the story drifts	$0.025h_{sx}$[c]	$0.02\ h_{sx}$	$0.015\ h_{sx}$
Masonry cantilever shear wall structures[d]	$0.01\ h_{sx}$	$0.01\ h_{s}$	$0.01\ h_{sx}$
Other masonry shear wall structures	$0.007\ h_{sx}$	$0.007\ h_{sx}$	$0.007\ h_{sx}$
Special masonry moment frames	$0.013\ h_{sx}$	$0.013\ h_{sx}$	$0.01\ h_{sx}$
All other structures	$0.02\ h_{sx}$	$0.015\ h_{s}$	$0.01\ h_{sx}$

a. h_{sx} is the story height below Level x
b. For SDC D, the allowable story drift shall comply with the requirements of Sec. 3.5.
c. There shall be no drift limit for single-story structures with interior walls, partitions, ceilings, and exterior wall systems that have been designed to accommodate the story drifts.
d. Structures in which the basic structural system consists of masonry shear walls designed as vertical elements cantilevered from their base or foundation support which are so constructed that moment transfer between shear walls (coupling) is negligible.

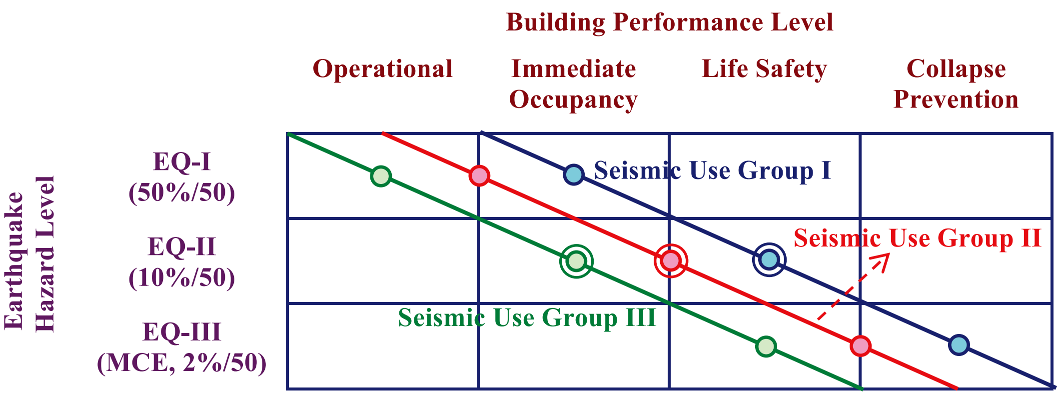

Fig. C1-1 Proposed performance matrix corresponding to the Seismic Use Group (The symbol ◎ indicates the deformation capacity should be checked during the performance-based design)

Development of a Ground Motion Scaling Method Considering Multi-mode Effects

Yuan-Tao Weng [1], Keh-Chyuan Tsai [2] and Ya-Ran Chan [3]

翁元滔 [1]、蔡克銓 [2]、詹雅嵐 [3]

Abstract

Non-linear dynamic time-history analyses conducted as part of a performance-based seismic design approach often require that the ground motion records are scaled to a specified level of seismic intensity. Recent research has demonstrated that certain ground motion scaling methods can introduce a large scatter in the estimated seismic demands. The resulting demand estimates may be biased, leading to designs with significant uncertainty and unknown margins of safety. This paper proposed a novel ground motion scaling method considering multi-mode effects for seismic evaluation of high-rise buildings. It is shown that the scaling method works well in reducing the scatter in estimated peak seismic demand for a wide range of structural characteristics.

Keywords: Multi-mode effects, performance-based seismic design, non-linear dynamic analysis, RSA, scaling of ground motions

Introduction

The amount of tall buildings located in seismic regions has increased rapidly in recent years. The seismic responses of tall buildings are much influenced by higher modes. The seismic demands of higher modes may be more critical than those of the first vibration mode for some specific responses. Although the elastic design response spectrum is enough for the elastic response spectrum analysis (RSA), the sets of scaled ground motion records, which are consistent with the design response spectrum, are still required for nonlinear response-history analysis (NLRHA). Ground motion records should be selected from actual earthquakes considering magnitude, distance, site condition, and other parameters that affect the characteristics of ground motions. Historical ground motion records can be scaled by either matching the peak ground acceleration or some specific spectral responses. According to the latest building codes (ICBO 2006), no less than seven two-component sets of ground motion time history should be used for each assessment of seismic performance. Thus, there should be 14 sets of ground motion time history available for the service and collapse prevention level assessments by using response-history analyses (RHA).

The advantage of historical ground motion scaling is that individual ground motion record retains its original characteristics including peaks and valleys of the response spectrum. However, to avoid the response being dominated by the peaks and valleys of any single one ground motion, it is recommended that there shall be no less than seven ground motion records to be used for NLRHA (ICBO, 2006).

Scaling of Historical Ground Motions

In order to gain insights into the nonlinear responses of multi-storey buildings under the excitation of historical ground accelerations, extensive NLRHA have been conducted. The techniques of ground motion scaling methods (Shome and Cornell, 1998; Kurama and Farrow, 2003) have also been studied in the research. Two of the most common ground motion scaling methods, for a building having T_1 as the fundamental vibration period in the considered direction, are described as follows:

[1] Associate Research Fellow, National Center for Research on Earthquake Engineering, chai@ncree.org.tw
[2] Professor, Dept. of Civil Engineering, Taiwan University, kctsai@ncree.org.tw
[3] Structural Engineer, Federal Engineering Consultants Inc., r95521215@ntu.edu.tw

1. Code method: This refers to the ground motion scaling procedure prescribed in IBC (ICBO, 2006). Given a suite of ground motion records, a scale factor is applied to each record to either increase or decrease its intensity. Each scale factor is determined such that the corresponding spectral accelerations between the period ranges from $0.2T_1$ to $1.5T_1$ satisfying that the average of response spectrum from the scaled motion does not fall below the target design response spectrum.
2. Sa (T_1) method (Shome and Cornell, 1998): In here, each ground motion is scaled so that its spectral acceleration value, Sa (T_1), at the linear-elastic fundamental period of the structure being analyzed matches the target design response spectrum.

The accuracy of any ground motion scaling procedure such as MMS in reducing the scatter in estimated peak seismic demands for buildings must be evaluated for a wide range of systems and ground motions, with the goal of establishing its range of applications and limitations. Therefore, one of the key tasks in this study is to evaluate comprehensively the multi-mode ground motion scaling (MMS) procedure and compare its results with those obtained from other commonly used methods. Seismic demands computed from the smoothed design spectrum and scaled spectrum obtained from the natural earthquake accelerations using three methods for the SAC buildings (Gupta and Krawinkler, 1999) will be presented first. The selected SAC buildings represent three building heights, 3-storey, 9-storey and 20-storey buildings in Los Angeles, USA.

Multi-Mode Ground Motion Scaling (Mms) Procedure

The principal idea of MMS is to minimize the first few modal participating difference between the spectral accelerations or displacements of a scaled ground motion and that of the smoothed target design response spectrum. For discussion purposes, the SRSS rule was used to illustrate the computation of the scaling factor proposed in the MMS method. Thus, given the acceleration response spectra, the base shears (V_d and V_{EQ}) and roof displacements ($u_{roof,d}$ and $u_{roof,EQ}$) can be expressed as:

$$V_D = \sqrt{\sum_{n=1}^{N}\left(\Gamma_i L_i S_{ai,des}\right)^2}\,,\quad V_{EQ} = \sqrt{\sum_{n=1}^{N}\left(\Gamma_i L_i S_{ai,EQ}\right)^2} \qquad (1)$$

and

$$u_{roof,d} = \sqrt{\sum_{n=1}^{N}\left(\Gamma_i S_{ai,des}/\omega_i^2\right)^2}\,,\quad u_{roof,EQ} = \sqrt{\sum_{n=1}^{N}\left(\Gamma_i S_{ai,EQ}/\omega_i^2\right)^2} \qquad (2)$$

where V_d (or $u_{roof,d}$) and V_{EQ} (or $u_{roof,EQ}$) are calculated from the smoothed design spectrum and the spectrum obtained from the natural earthquake accelerations, respectively. On the other hand, Γ_i and L_i are the modal participation factor and modal excitation factor of the i^{th} mode, respectively. Finally, $S_{ai,des}$ and $S_{ai,EQ}$ are the spectral accelerations in the smoothed design spectrum and the spectrum obtained from the natural earthquake accelerations, respectively.

Computation of the scaling factors from the MMS method

The least square error fitting method can be used to reduce the modal participating difference between the spectral accelerations or displacements of a scaled ground motion of the first few modes and that of the smoothed design response spectra. The square error of the smoothed spectral set and the original un-scaled spectral set of accelerations can be expressed as:

$$(error)^2 = \sum_{i=1}^{N} W_i\left[S_{ai,des} - SF\cdot S_{ai,EQ}\right]^2,\ (i = 1 \sim N) \qquad (3)$$

where SF is the scaling factor whereas W_i is the i^{th} modal weighting factor. The minimum error can then be achieved when the partial derivative of $error^2$ with respect to the scaling factor SF becomes zero:

$$\frac{\partial\left(error^2\right)}{\partial(SF)} = 0 \qquad (4)$$

Thus, SF can be expressed as:

$$SF = \sum_{i=1}^{N} W_i\cdot S_{ai,des}\cdot S_{ai,EQ} \Big/ \sum_{i=1}^{N} W_i\cdot\left(S_{ai,EQ}\right)^2,\quad (i = 1 \sim N) \qquad (5)$$

Since the elastic peak base shear, V_i is expressed in terms of $\Gamma_i L_i S_{ai}$ (see Eq. 1), it is proposed that the weighting factors, W_i for each mode be expressed as shown in Eq. (6) for the computation of scaling factors. For the interest of computing base shear:

$$W_i = \Gamma_i^2 L_i^2 \Big/ \sum_{i=1}^{N}\Gamma_i^2 L_i^2\,,\ (i = 1 \sim N) \qquad (6a)$$

Whereas, for computation of roof the displacement:

$$W_i = \left(\Gamma_i/\omega_i^2\right)^2 \Big/ \sum\left(\Gamma_i/\omega_i^2\right)^2,\ (i = 1 \sim N) \qquad (6b)$$

Thus, weighting factor given in Eq. (6a) can be applied in Eq. (5) for the computation of scaling factors when base shear is considered as the key design parameter. Eq. (6b) has been found satisfactory in reducing the scatter of peak roof displacement estimates but not for other response parameters in the seismic performance evaluation of a 34-storey steel building (Weng et al., 2008). Thus in this paper, only the weighting factors given in Eq. (6a) proposed for computing the scaling factor were applied. The effectiveness of applying Eqs. (6a) and (5) in computing the seismic demand for the SAC buildings in Los Angeles is presented in this paper. The effects of the number of modes included which were not studied previously are also discussed for the performance evaluation of the 34-storey steel building. When the RSA method is applied, it has been suggested that the number of modes be determined to include at least 90% of the total building effective mass (ICBO, 2006).

Comparisons of the MMS Methods versus Current Ground Motion Scaling Methods

Description of the example structures

The proposed procedure was investigated using three steel moment frame (MF) model buildings under various ground motion scenarios. The example buildings were the three 'post-Northridge' designs of 3-, 9-, and 20-storey model buildings for the city of Los Angeles (developed in the SAC Steel Project (Gupta and Krawinkler, 1999)). It is referred to as the SAC buildings in this paper. These structures meet the seismic code requirements as per UBC-94 (ICBO, 1994) and represent typical low-, medium-, and high-rise buildings designed for Los Angeles at that time. Details regarding frame dimensions, material properties, and loads can be found in the reference (Gupta and Krawinkler, 1999). For each building, a 3-dimensional model was constructed. For the discussion purposes, the responses of the North-South frames of each building are presented in this paper. The bilinear elastic-perfect-plastic beam-column element without strain hardening has been used for modeling all beams and columns. Effects of gravity loads and the P-Delta effects were considered. Damping ratios of 5% were assumed for the first two modes. For the purpose of illustrating the effectiveness of the MMS method, only two modes (constitute more than 90% of the total building effective mass) were incorporated into the computation of the scaling factors. Table 1 shows the first two fundamental periods, modal participation factors Γ_i, modal excitation factors L_i, and each weight factor for the first two modes in the North-South direction of the three SAC buildings.

Table 1. Modal properties and weighting factors of Los Angeles-SAC Buildings.

Modal Characteristics	Los Angeles		
	3-story	9-story	20-story
T_1	1.07	2.33	4.00
T_2	0.31	0.88	1.38
Γ_1	1.27	1.37	1.35
Γ_2	-0.34	-0.54	-0.55
L_1	1990	5338	6576
L_2	-1387	-1899	-2100
W_1	0.97	0.98	0.98
W_2	0.03	0.02	0.02

SAC Ground Motions

In the SAC project, two sets of 20 ground motion records representing exceedance probabilities of 50% and 2% in 50 years, denoted as 50%in50yr and 2%in50yr, respectively, have been assembled for the Los Angeles City. These two sets of ground motions were adopted in evaluating the MMS procedure for different earthquake hazard levels. In order to match the seismic demand of the smoothed 5% damped elastic acceleration response spectra for Los Angeles, two sets of corresponding synthetic ground accelerations were constructed incorporating the phase angles (Chai et al., 2002) in the two sets of 20 natural ground motions stated above for the 50%in50yr and 2%in50yr hazard levels. In order to evaluate the scatter of the peak seismic demands computed from both the RSA and RHA methods, a coefficient of variance (COV) factor was defined as

$$COV = \sqrt{\sum_{i=1}^{n}\left(X_i - \hat{X}\right)^2 / (n-1)} \Big/ \hat{X} \tag{4.1}$$

where n is the number of earthquake records, X_i is the peak response value determined from the RSA or RHA procedure associated with the i^{th} scaled natural earthquake acceleration record. The $\hat{X}$ is the mean value of the peak responses calculated by the RSA procedure (using the smoothed design spectrum) or the RHA procedure (using the aforementioned synthetic earthquakes compatible with the smoothed design spectrum). The COV parameter provides comparison for all the earthquakes considered for each SAC building.

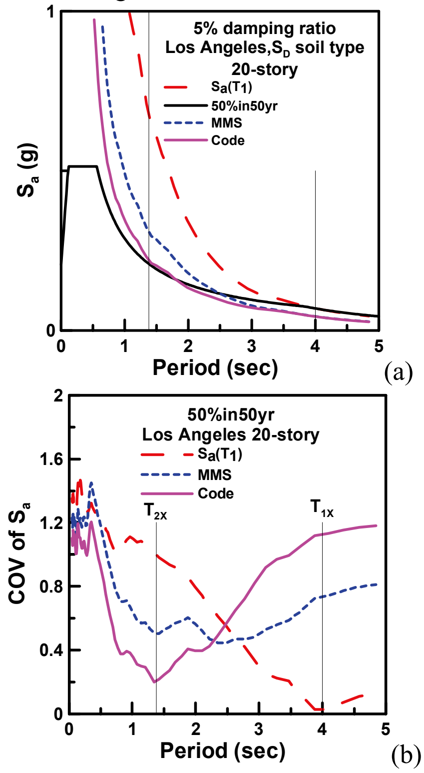

Fig. 1 (a) The mean elastic 5%-damped spectral acceleration; (b) the corresponding COV spectrum after the 50%in50yr LA ground motion set scaled by three scaling methods for the 20-story SAC building

Figure 1a shows the smoothed 5% damped elastic acceleration response spectrum for the LA 50%in50yr earthquake. In the same figure, three other response spectra, constructed from the averaged responses of the 50/50 set of LA ground motions scaled according to three different methods, are also compared. Figure 1b shows the COVs of the response spectra, with respect to the LA smoothed 50%in50yr response spectrum, computed from the ground motions using three scaling methods. It can be found in Figures 1a that the average of the twenty spectra computed using MMS method is closer to the smoothed design spectrum in the overall range from periods of T_1 to T_2, particularly near the first mode period T_1. Further studies described later will allow us to compare the effectiveness of the MMS with that of the Code or $S_a(T_1)$ method in reducing the scatter of the peak seismic demands computed from both the RSA and RHA procedures.

Conclusions

Based on the conducted analyses, conclusions were drawn as follows:

- Among the three scaling methods considered in this study, including the MMS, the Code and the $S_a(T_1)$ methods, it appears that the MMS method results in more consistent seismic demands with those obtained using the smoothed design response spectra. This improved consistency is particularly significant for high-rise buildings.
- The MMS method can provide a better agreement between the V_{EQ} and V_D. In other words, it can match better the peak base forces induced from applying a series of scaled historical ground motion records to those computed using RSA procedures on a smoothed design spectrum.
- The $S_a(T_1)$ method often failed to reduce the scatter of the estimated peak story shear, overturning moment and peak inter-story drifts of all the investigated buildings.
- Compared to the other two scaling methods, the MMS method can reduce effectively the scatter of the spectral acceleration differences with respect to the smoothed design response spectrum.
- The MMS method can be applied conveniently for elastic RSA or NLRHA of low-to-high rise buildings. It appears to be particularly effective in reducing the scatter of the seismic demand estimates on the peak story shear, overturning moment and peak inter-story drift for tall buildings.

References

Chai, J. F., Loh, C. H. and Sato, H. (2002). "Modeling of phase spectrum to simulate design ground motions." *Journal of the Chinese Institute of Engineers*, Vol. 25, No. 4, pp. 447-459.

Chopra, A. K. (2003). "*Dynamic of structures: Theory and applications to earthquake engineering*." Prentice Hall, 2nd ed., Englewood, Cliffs, N J.

Gupta, A. and Krawinkler, H. (1999). "Seismic demands for performance evaluation of steel moment resisting frame structures (SAC task 5.4.3)." *Report No. 132*, John A. Blume Earthquake Engineering Center, Department of Civil and Environmental Engineering, Stanford University, Stanford, CA, U.S.A.

International Conference of Building Officials (ICBO). (1994). "*Uniform building code*." ICBO: Whittier, CA, U.S.A.

International Conference of Building Officials (ICBO). (2006). "*International building code*." ICBO: Whittier, CA, U.S.A.

Kurama, Y. C. and Farrow, K. T. (2003). "Ground motion scaling methods for different site conditions and structure characteristics." *Earthquake Engineering and Structural Dynamics*, Vol. 32: 2425-2450.

Lam, N., Wilson, J., Hutchinson, G. (1998). "The ductility reduction factor in the seismic design of buildings." *Earthquake Engineering and Structural Dynamics*, 27:749 –769.

Malhotra, P. K. (2003). "Strong-motion records for site-specific analysis." *Earthquake Spectra*, 19(3): 557-578.

Shome, N. and Cornell, C.A. (1998). "Normalization and scaling accelerograms for nonlinear structural analysis." *Sixth U.S. National Conference on Earthquake Engineering* (CD-ROM), Seattle, WA.

Tsai, K. C. and Lin, B. Z. "Development of an object-oriented nonlinear static and dynamic 3D structural analysis program." Center for Earthquake Engineering Research, National Taiwan University, *Report No. CEER/R92-04*, 2003. (in Chinese)

Weng, Y. T., Tsai, K. C., Chen, P. C., Chou, C. C., Chan, Y. R., Jhuang, S. J. and Wang, Y.Y. (2008). "Seismic performance evaluation of a 34-story steel building retrofitted with response modification elements." *Earthquake Engineering and Structural Dynamics*. (in Review)

Seismic Analysis of Asymmetric-Plan Structures with Soil-Structure Interaction

Jui-Liang Lin [1] and Keh-Chyuan Tsai [2]

林瑞良 [1]、蔡克銓 [2]

Abstract

An efficient approximate method that uses the multi-degrees-of-freedom (MDOF) modal equations of motion for the seismic response history analysis of asymmetric elastic buildings with soil-structure interaction (SSI) is presented. The systems considered are two-way asymmetric shear buildings resting on the surface of an elastic half-space, which are excited by two-directional seismic ground motions. The SSI forces were simulated using frequency-independent soil springs and dashpots. First, the MDOF modal equations of motion for the SSI systems were derived. The modal response histories were obtained by solving the MDOF modal equations of motion using the step-by-step integration method. Subsequently, the seismic response histories of the whole SSI system were determined from the arithmetic summation of the modal response histories. The MDOF modal equations of motion retain the property of non-proportional damping of the original SSI system. The proposed method has the advantages of the conventional modal response history analysis, which requires only first few vibration modes to obtain accurate analytical results. Finally, the efficiency of the proposed method was validated using numerical examples of a two-way asymmetric four-story building with small and large SSI effects.

Keywords: modal analysis, soil-structure interaction, asymmetry, seismic analysis, approximation methods.

Introduction

The seismic responses of linear symmetric buildings with soil-structure interaction (SSI) have been well-investigated in the past decades (Wolf 1988). The complexity of the SSI effect arises from two aspects: the frequency-dependent interaction forces, and the non-proportional damping of the soil-structure system. In order to deal with the frequency-dependent interaction forces, the SSI problem was processed in the frequency domain using either Fourier transformation or Laplace transformation. However, frequency domain analysis is only capable of dealing with linear responses and is not popular among practicing structural engineers (Wolf 1988). To facilitate the analysis of the stated problem in the time domain, the soil springs and dashpots were approximated by frequency-independent expressions (Richart *et al.* 1970). While such approximations may perform satisfactorily for the analysis of typical multistory buildings, they may not be adequate for other types of structures, such as concrete gravity dams. To deal with the non-proportional damping of SSI systems, equivalent modal damping was calculated to facilitate the conventional modal response history analysis. The equivalent modal damping was estimated either by quantifying the dissipated energy in the soil (Roesset *et al.* 1973; Novak and Hifnawy 1983) or by matching the approximate normal mode solution with the rigorous solution for a certain structural location (Balendra *et al.* 1982).

Conventional modal response history analysis, which neglects the off-diagonal terms of the transformed damping matrix for a non-proportionally damped one-way asymmetric building resting on a rigid base, is one of the common approximation

[1] Associate Researcher, National Center for Research on Earthquake Engineering, jllin@ncree.org.tw

[2] Professor, Department of Civil Engineering, National Taiwan University, kctsai@ncree.org.tw

approaches. However, this approximation approach may result in unacceptable errors under certain conditions.

The issue on seismic analysis of asymmetric-plan structures with soil-structure interaction subjected to bi-directional ground motions has been investigated by many researchers (Balendra *et al.* 1982). However, practicing engineers are usually not familiar with the complex-valued seismic analysis procedures in the frequency domain. Moreover, the equivalent modal damping estimated either by quantifying the dissipated energy in the soil, or by matching the approximate normal mode response with the rigorous solution is not readily available using a general purpose structural response analysis computer program. Thus, it is desirable to develop a simple and real-valued modal response history analysis procedure for engineering applications without the need of calculating the complicated equivalent modal damping. In this study, such a response history analysis procedure has been proposed using the multi-degree-of-freedom (MDOF) modal equations of motion. The proposed method can be applied conveniently using any general purpose computer program with the capability of solving equation of motion.

Equation of Motion of the SSI System

The mass of the building was assumed to be concentrated at the levels with rigid floor decks which were supported by massless, axially inextensible columns and walls. The center of mass (CM) and the center of stiffness (CR) of each floor were assumed to lie on two vertical lines. The system has $3N$+5 degrees of freedom, consisting of $3N$ degrees of freedom of the superstructure and 5 degrees of freedom due to interaction with the foundation. These 5 degrees of freedom include two horizontal translations, two rocking, and one twist (Fig. 1). The equation of motion for the whole SSI system is:

$$\mathbf{M}^*\ddot{\mathbf{W}} + \mathbf{C}^*\dot{\mathbf{W}} + \mathbf{K}^*\mathbf{W} = -\mathbf{P}^* \tag{1}$$

in which

$$\mathbf{W} = \begin{Bmatrix} \mathbf{U}'_{jc} \\ \mathbf{V}'_{jc} \\ \boldsymbol{\theta}^t_j \\ U_0 \\ V_0 \\ \theta_0 \\ \psi_0 \\ \phi_0 \end{Bmatrix}_{(3N+5)\times 1}, \quad \mathbf{P}^* = \begin{Bmatrix} \mathbf{m1}\ddot{u}_{gx} \\ \mathbf{m1}\ddot{u}_{gy} \\ \mathbf{0} \\ m_0\ddot{u}_{gx} \\ m_0\ddot{u}_{gy} \\ 0 \\ 0 \\ 0 \end{Bmatrix}_{(3N+5)\times 1} \tag{2a}$$

$$\mathbf{M}^* = \begin{bmatrix} \mathbf{m} &&&&&&& \\ & \mathbf{m} &&&&&& \\ && r^2\mathbf{m} &&&&& \\ &&& m_0 &&&& \\ &&&& m_0 &&& \\ &&&&& r^2 m_0 && \\ &&&&&& \sum_{j=0}^{N} I_{xj} & \\ &&&&&&& \sum_{j=0}^{N} I_{yj} \end{bmatrix} \tag{2b}$$

$$\mathbf{C}^* = \begin{bmatrix} \mathbf{C}_x & \mathbf{0}_{N\times N} & f\mathbf{C}_x & -\mathbf{C}_x\mathbf{1} & \mathbf{0} & -\mathbf{C}_x\mathbf{f} & \mathbf{0} & -\mathbf{C}_x\mathbf{h} \\ & \mathbf{C}_y & -e\mathbf{C}_y & \mathbf{0} & -\mathbf{C}_y\mathbf{1} & \mathbf{C}_y\mathbf{e} & -\mathbf{C}_y\mathbf{h} & \mathbf{0} \\ && \mathbf{C}_\theta & -\mathbf{C}_x\mathbf{f} & \mathbf{C}_y\mathbf{e} & -\mathbf{C}_\theta\mathbf{1} & e\mathbf{C}_y\mathbf{h} & -f\mathbf{C}_x\mathbf{h} \\ &&& C_T + \mathbf{1}^T\mathbf{C}_x\mathbf{1} & 0 & \mathbf{f}^T\mathbf{C}_x\mathbf{1} & 0 & \mathbf{1}^T\mathbf{C}_x\mathbf{h} \\ &&&& C_T + \mathbf{1}^T\mathbf{C}_y\mathbf{1} & -\mathbf{e}^T\mathbf{C}_y\mathbf{1} & \mathbf{1}^T\mathbf{C}_y\mathbf{h} & 0 \\ &&&&& C_Z + \mathbf{1}^T\mathbf{C}_\theta\mathbf{1} & -\mathbf{e}^T\mathbf{C}_y\mathbf{h} & \mathbf{f}^T\mathbf{C}_x\mathbf{h} \\ & symm. &&&&& C_r + \mathbf{h}^T\mathbf{C}_y\mathbf{h} & 0 \\ &&&&&&& C_r + \mathbf{h}^T\mathbf{C}_x\mathbf{h} \end{bmatrix} \tag{2c}$$

$$\mathbf{K}^* = \begin{bmatrix} \mathbf{K}_x & \mathbf{0}_{N\times N} & f\mathbf{K}_x & -\mathbf{K}_x\mathbf{1} & \mathbf{0} & -\mathbf{K}_x\mathbf{f} & \mathbf{0} & -\mathbf{K}_x\mathbf{h} \\ & \mathbf{K}_y & -e\mathbf{K}_y & \mathbf{0} & -\mathbf{K}_y\mathbf{1} & \mathbf{K}_y\mathbf{e} & -\mathbf{K}_y\mathbf{h} & \mathbf{0} \\ && \mathbf{K}_\theta & -\mathbf{K}_x\mathbf{f} & \mathbf{K}_y\mathbf{e} & -\mathbf{K}_\theta\mathbf{1} & e\mathbf{K}_y\mathbf{h} & -f\mathbf{K}_x\mathbf{h} \\ &&& K_T + \mathbf{1}^T\mathbf{K}_x\mathbf{1} & 0 & \mathbf{f}^T\mathbf{K}_x\mathbf{1} & 0 & \mathbf{1}^T\mathbf{K}_x\mathbf{h} \\ &&&& K_T + \mathbf{1}^T\mathbf{K}_y\mathbf{1} & -\mathbf{e}^T\mathbf{K}_y\mathbf{1} & \mathbf{1}^T\mathbf{K}_y\mathbf{h} & 0 \\ &&&&& K_Z + \mathbf{1}^T\mathbf{K}_\theta\mathbf{1} & -\mathbf{e}^T\mathbf{K}_y\mathbf{h} & \mathbf{f}^T\mathbf{K}_x\mathbf{h} \\ & symm. &&&&& K_r + \mathbf{h}^T\mathbf{K}_y\mathbf{h} & 0 \\ &&&&&&& K_r + \mathbf{h}^T\mathbf{K}_x\mathbf{h} \end{bmatrix} \tag{2d}$$

The **0** and **1** shown in the above equations are the column vectors whose all elements are equal to zero and one, respectively. On the other hand, **h** is the column vector composed of the story heights measured from the ground level to each floor. In these equations, e and f are the eccentricities measured from CR to CM along the X-axis and the Y-axis respectively, m_0 is the mass of foundation, r is the radius of gyration of any floor deck about CM, I_{xj} and I_{yj} are the moments of inertia of the jth floor about the axes through the CM and parallel to the X- and Y-axes respectively, $\ddot{u}_{gx}$ and $\ddot{u}_{gy}$ are the ground acceleration records along the X- and Y-axes respectively, and finally, U_0, V_0, θ_0, ψ_0, ϕ_0 are the degrees of freedom at the foundation associated with translations, twist and rocking, as defined in Fig. 1. $\mathbf{U}'_{jc}$, $\mathbf{V}'_{jc}$ and $\boldsymbol{\theta}^t_j$ are the degrees of freedom of the superstructure defined as:

$$\mathbf{U}'_{jc} = U_0\mathbf{1} + \phi_0\mathbf{h} + \mathbf{U}_{jc} \tag{3a}$$

$$\mathbf{V}'_{jc} = V_0\mathbf{1} + \psi_0\mathbf{h} + \mathbf{V}_{jc} \tag{3b}$$

$$\boldsymbol{\theta}^t_j = \theta_0\mathbf{1} + \boldsymbol{\theta}_{jc} \tag{3c}$$

In Eqs. (3a) to (3c), $\mathbf{U}_{jc}$, $\mathbf{V}_{jc}$ and $\boldsymbol{\theta}_{jc}$ are the degrees of freedom of the superstructure about the CM. The physical meaning behind these equations is depicted in Fig. 1. The $3N\times3N$ sub-matrices on the left upper corner of $\mathbf{M}^*$, $\mathbf{C}^*$, $\mathbf{K}^*$, are the mass, damping and stiffness matrices of the superstructure resting on a rigid base. Moreover,

$$\mathbf{K}_\theta = \mathbf{K}_{\theta R} + e^2\mathbf{K}_y + f^2\mathbf{K}_x \tag{4}$$

$\mathbf{K}_x$, $\mathbf{K}_y$ and $\mathbf{K}_{\theta R}$ are defined about the CR. The $\mathbf{m}$ shown in the previous equation is an $N\times N$ diagonal matrix composed of each floor mass. The interaction forces $P_x(t)$, $Q_x(t)$, $P_y(t)$, $Q_y(t)$ and $T(t)$ shown in Fig. 1 are expressed by frequency-independent soil springs and dashpots, which can be found in Richart, F.E. *et al.* (1970).

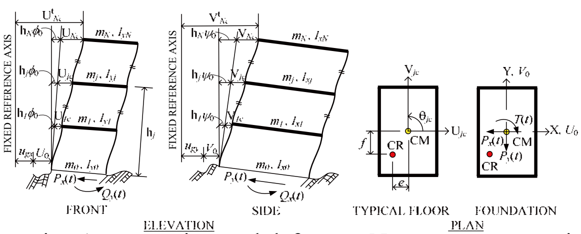

Fig. 1 Dynamic model for an N-story asymmetric shear building.

MDOF Modal Equations of Motion

The right-hand side of Eq. (1) can be represented as follows:

$$\begin{aligned}\mathbf{P}^* &= \sum_{n=1}^{3N+5}\mathbf{s}_n\left(\Gamma_{xn}\ddot{u}_{gx} + \Gamma_{yn}\ddot{u}_{gy}\right)\\ &= \sum_{n=1}^{3N+5}\mathbf{M}^*\boldsymbol{\varphi}_n\left(\Gamma_{xn}\ddot{u}_{gx} + \Gamma_{yn}\ddot{u}_{gy}\right)\end{aligned} \tag{5}$$

where $\mathbf{s}_n$ is the nth modal inertial force distribution equivalent to $\mathbf{M}^*\boldsymbol{\varphi}_n$. $\boldsymbol{\varphi}_n$ is the nth undamped mode shape obtained from $\mathbf{K}^*$ and $\mathbf{M}^*$. It was assumed that only the nth undamped modal displacement response, $\mathbf{W}_n$, of the whole system will be excited under the load, $\mathbf{s}_n(\Gamma_{xn}\ddot{u}_{gx}(t)+ \Gamma_{yn}\ddot{u}_{gy}(t))$. Thus, Eq. (1) can be written as:

$$\begin{aligned}&\mathbf{M}^*\ddot{\mathbf{W}}_n + \mathbf{C}^*\dot{\mathbf{W}}_n + \mathbf{K}^*\mathbf{W}_n\\ &= -\mathbf{s}_n\left(\Gamma_{xn}\ddot{u}_{gx}(t) + \Gamma_{yn}\ddot{u}_{gy}(t)\right),\end{aligned} \quad n = 1\sim 3N+5 \tag{6}$$

where

$$\begin{aligned}\mathbf{W}_n &= \boldsymbol{\varphi}_n D_n\\ &= \begin{bmatrix}\boldsymbol{\varphi}^T_{un} & \boldsymbol{\varphi}^T_{vn} & \boldsymbol{\varphi}^T_{\theta n} & \phi_{u_0 n} & \phi_{v_0 n} & \phi_{\theta_0 n} & \phi_{\psi_0 n} & \phi_{\phi_0 n}\end{bmatrix}^T D_n\end{aligned} \tag{7}$$

In Eq. (7), D_n is the nth generalized modal coordinate. The nth undamped modal displacement response, $\mathbf{W}_n$, was redefined as:

$$\begin{aligned}\mathbf{W}_n &= \begin{bmatrix}\boldsymbol{\varphi}_{un} & \mathbf{0} & \mathbf{0} & 0 & 0 & 0 & 0 & 0\\ & \boldsymbol{\varphi}_{vn} & \mathbf{0} & 0 & 0 & 0 & 0 & 0\\ & & \boldsymbol{\varphi}_{\theta n} & 0 & 0 & 0 & 0 & 0\\ & & & \varphi_{u_0 n} & 0 & 0 & 0 & 0\\ & & & & \varphi_{v_0 n} & 0 & 0 & 0\\ & symm. & & & & \varphi_{\theta_0 n} & 0 & 0\\ & & & & & & \varphi_{\psi_0 n} & 0\\ & & & & & & & \varphi_{\phi_0 n}\end{bmatrix}\begin{bmatrix}D_{un}\\ D_{vn}\\ D_{\theta n}\\ D_{u_0 n}\\ D_{v_0 n}\\ D_{\theta_0 n}\\ D_{\psi_0 n}\\ D_{\phi_0 n}\end{bmatrix}\\ &= \mathbf{T}_n\mathbf{D}_n\end{aligned} \tag{8}$$

For proportionally damped elastic systems, the elements of $\mathbf{D}_n$ are the same, i.e.:

$$D_{un} = D_{vn} = D_{\theta n} = D_{u_0 n} = D_{v_0 n} = D_{\theta_0 n} = D_{\psi_0 n} = D_{\phi_0 n} \tag{9}$$

Hence, Eq. (8) is identical to Eq. (7) for proportionally damped elastic systems. Substituting Eq. (8) into Eq. (6) and pre-multiplying both sides of Eq. (6) by $\mathbf{T}^T_n$, this results in:

$$\begin{aligned}&\mathbf{M}_n\ddot{\mathbf{D}}_n + \mathbf{C}_n\dot{\mathbf{D}}_n + \mathbf{K}_n\mathbf{D}_n\\ &= -\mathbf{M}_n\boldsymbol{\iota}\left(\Gamma_{xn}\ddot{u}_{gx} + \Gamma_{yn}\ddot{u}_{gy}\right),\end{aligned} \quad n = 1\sim 3N+5 \tag{10}$$

in which

$$\mathbf{M}_n = \mathbf{T}^T_n\mathbf{M}^*\mathbf{T}_n, \quad \mathbf{C}_n = \mathbf{T}^T_n\mathbf{C}^*\mathbf{T}_n, \quad \mathbf{K}_n = \mathbf{T}^T_n\mathbf{K}^*\mathbf{T}_n \tag{11}$$

where $\boldsymbol{\iota}$ is an 8×1 column vector with all elements equal to one, $\mathbf{M}_n$, $\mathbf{C}_n$, $\mathbf{K}_n$, are 8×8 matrices. Eq. (10) is the nth multi-degrees-of-freedom modal equation of motion. It was noted that if the original SSI system was proportionally damped, $\mathbf{C}_n$ can be represented as:

$$\mathbf{C}_n = \mathbf{T}^T_n\mathbf{C}^*\mathbf{T}^T_n = \mathbf{T}^T_n\left(\alpha\mathbf{M}^* + \beta\mathbf{K}^*\right)\mathbf{T}^T_n = \alpha\mathbf{M}_n + \beta\mathbf{K}_n \tag{12}$$

where α and β are constants. Since the original SSI system was non-proportionally damped, i.e. $\mathbf{C}^* \neq \alpha\mathbf{M}^* + \beta\mathbf{K}^*$, Eq. (12) becomes $\mathbf{C}_n \neq \alpha\mathbf{M}_n + \beta\mathbf{K}_n$. This implies that the MDOF modal equations of motion shown in Eq. (10) preserve the characteristics of the non-proportional damping of the original SSI system. The modal response histories, $\mathbf{D}_n(t)$, were obtained using the direct integration method in solving Eq. (10). Thus, the total response histories of the original SSI system were obtained as:

$$\mathbf{W}(t) = \sum_{n=1}^{3N+5} \mathbf{W}_n(t) \approx \sum_{n=1}^{3N+5} \mathbf{T}_n \mathbf{D}_n(t) \qquad (13)$$

Same as the conventional modal response history analysis, only the first few modal responses need to be included in the above summation to obtain satisfactory analytical results. This will be shown in the following numerical examples.

Numerical Examples

The SSI system selected is a four-story asymmetric-plan building resting on an elastic half-space, which is a modification of the examples adopted by Balendra *et al.* (1982). The details of the SSI system can be found in Lin et al. (2009).

In order to investigate the effectiveness of the proposed method, two soil types with shear wave velocities, V_s, of 65m/s (soft soil) and 300 m/s (hard soil) have been specifically chosen for this study. The SSI system resting on the soft (V_s =65m/s) and hard (V_s =300m/s) soils was denoted as System I and System II, respectively. The two systems represent structures with large and small SSI effects, respectively. Therefore, these two extreme cases should cover most SSI problems of interest in earthquake engineering practice. Both systems were subjected to the 1940 El Centro earthquake. The N-S and E-W components of the 1940 El Centro earthquake were applied along the X- and Y-axes, respectively. Another four-story asymmetric building with an identical superstructure but resting on a rigid base was denoted as the reference building. It will be regarded as the benchmark to indicate how the SSI affects the dynamic properties of the building.

The proposed approximation method that conducts modal response history analyses using MDOF modal equations of motion shown in Eq. (10) was denoted as App. On the other hand, the rigorous method, which uses the direct integration method to solve the equation of motion for the whole SSI system shown in Eq. (1), was denoted as Rig.

The estimated total response histories of System I and System II compared with the rigorous solutions (Lin et al. 2009) confirmed that the proposed method is applicable to a wide range of SSI effects generally considered in earthquake engineering practice. It is important to note that the approximate solutions were obtained by only considering the first three vibration modes. Not only the peaks but also the phases of the roof and foundation response histories determined via the proposed method were in good agreement with those obtained via the rigorous method.

Conclusions

The proposed approximate method transfers the frequency-independent equation of motion for the SSI system into a set of MDOF modal equations of motion. There are four advantages of this method at the expense of increasing degrees of freedom for each vibration mode. The first two advantages are similar to those of conventional modal response history analysis, whereby there is a significant decrease of the degrees of freedom required in the analytical work and the use of only the first few vibration modes to achieve satisfactory analytical results. On the other hand, another advantage is the preservation of the characteristics of non-proportional damping in the MDOF modal equations of motion. This would appeal to practicing engineers instead of performing calculations of the complicated equivalent modal damping. The final advantage is the transformation of the soil springs and dashpots into modal level. Thus, the impedance functions and their influences for each vibration mode can be explicitly quantified.

References

Balendra, T, Tat, C.W. and Lee S.L. (1982). “Modal damping for torsionally coupled buildings on elastic foundation.” *Earthquake Engineering and Structural Dynamics*, 10(5), 735-756.

Lin, J.L., Tsai, K.C. and Miranda, E. (2009). “Seismic history analysis of asymmetric buildings with soil-structure interaction.” *Journal of Structural Engineering*, 135(2), 101-112.

Novak, M. and Hifnawy, L.EL. (1983). “Effect of soil-structure interaction on damping of structures.” *Earthquake Engineering and Structural Dynamics*, 11(5), 595-621.

Richart, F.E., Hall, J.R. and Woods, R.D. (1970). *Vibrations of soils and foundations*, Prentice Hall, Englewood Cliffs, New Jersey.

Roesset, J.M., Whitman, R.V. and Dobry, R. (1973). “Modal analysis for structures with foundation interaction.” *Journal of Structural Division*, Proceedings of ASCE, ST3, 399-416.

Wolf, J.P. (1988). *Soil-structure-interaction analysis in time domain*, Prentice Hall, Englewood Cliffs, New Jersey.

Experimental Study on RC Building Frame Containing Walls Subjected to Bi-directional Cyclic Loading

Chien-Chuang Tseng[1], Shyh-Jiann Hwang[2] and Yeong-Kae Yeh[3]

曾建創[1]、黃世建[2]、葉勇凱[3]

Abstract

Tests on a two-story reinforced concrete building subjected to bi-directional reversed cyclic loadings were performed at the National Center for Research on Earthquake Engineering (NCREE) in Taiwan to examine the torsional effect caused by the eccentricity of the building plan layout. The tests were undertaken as part of an international collaboration project between the NCREE and the University of Houston, Houston, Texas (UH). In order to evaluate the torsional effect, two low-rise shear walls on the east side of the building and one mid-rise shear wall on the north side were designed to make the building structurally asymmetrical. This research focused on the development and progression of nonlinear combined actions in the experimental technology. Finally, results obtained from this experiment were used to correlate analytical tools and new design methodologies.

Keywords: reinforced concrete building frame, bi-directional cyclic loading, stiffness irregularity, torsional moment, eccentricity

Introduction

The objective of this integrated experiment is proposed to address the complex behavior of reinforced concrete buildings subjected to multi-directional earthquake loading and the subsequent interactions resulting from the nonlinear response of individual components that compound further the multi-directional effect of the ground motion. Emphasis was placed on using simulation response histories to provide the actuation forces that were applied to the reinforced concrete buildings to model reverse cyclic loading. The results reported herein will be used to develop analytical tools and new design methodologies.

Design of the RC Specimen

As shown in Fig. 1, the full scale test specimen was two stories tall, by one bay wide in the short direction and two bays wide in the long direction. The clear column height on the 1st floor was 2000 mm and the 2nd floor column height was 1500 mm. Additionally, the cross-sectional dimension of each column was 400 by 400 mm. All frame beam cross-sections measured 300 wide by 400 mm in height.

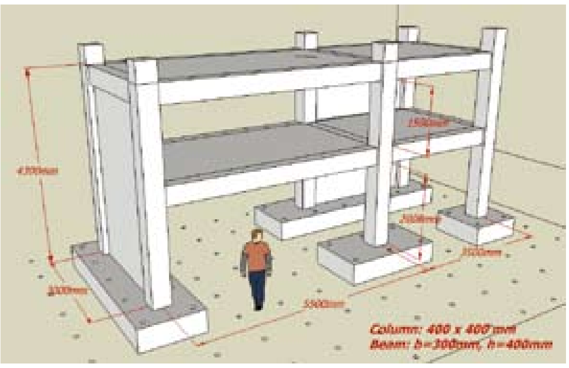

Fig.1 Drawing of RC building frame

Experiment Procedure and Allocation

In order to test the torsional effect, the walls of the building were designed to be asymmetrical. Two low-rise walls were located on the east side of the structure and one mid-rise wall was located on the

[1] Associate Research Fellow, National Center for Research on Earthquake Engineering, cctseng@ncree.org.tw
[2] Professor, Department of Civil Engineering, National Taiwan University
[3] Research Fellow, National Center for Research on Earthquake Engineering

north side, as shown in Fig. 2. The short spans on the east side (in the long axis direction of the structure) had a height to width ratio of 0.64 (Wall A) and a height to width ratio of 0.48 (Wall B) while the north side of the structure (the short axis) had a height to width ratio of 1.5 (Wall C). Walls A and B were shear critical while Wall C was both shear and flexure critical. Hence, the characteristic response of the various types of walls can be identified. Column C1-2F (column 1 on the 2nd floor) was designed as a short (shear critical) element and column C1-1F (column 1 on the 1st floor) was designed as a normal (flexure critical) element. Both columns were subjected to biaxial loading and axial compression loading (0.2 $f'c$). Column C2-2F (column 2 on the 2nd floor) was designed as a short (shear critical) element and C2-1F (column 2 on the 1st floor) was designed as a normal (flexure critical)element. These columns were both subjected to biaxial loading only. The structural behavior of the columns under various other conditions can also be examined with the test arrangement.

Fig.2 Overview photo of the test structure (showing the allocation of beans and columns.)

For the purpose of this investigation, the loading history must satisfy two conditions. First, to control the mass center displacement on the 2nd floor, the displacement ratio of the long to short direction must be 1:2. Second, the ratio of horizontal force must be 1.83, equivalent to the ratio of the story height. Fig. 3 shows the loading history consisting of the following drift cycles: 0.25%, 0.375%, 0.5%, 0.75%, 1.0%, 1.5%, 2.0%, 3.0%, with each loading having three cycles.

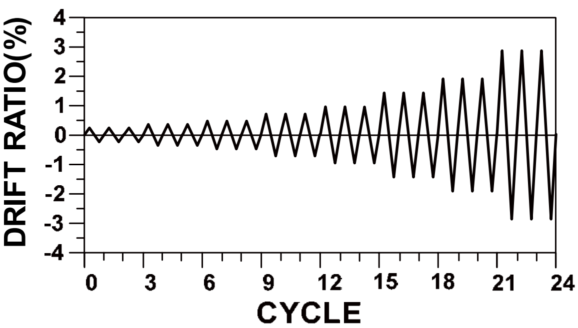

Fig.3 Loading history at various drift cycles.

Results and Analysis of Experiments

Figure 4 shows the relationship between base shear and roof displacement. The red curves are base shear versus roof displacement hysteresis loops. When drift ratio was -3.0 %, the specimen undergone shear critical to cause base shear decay on the 2nd floor. The blue curve on Fig.4 means a component of base shear and roof displacement at NS (North-South) direction, and the green curve means a component of base shear and roof displacement at EW (East-West) direction. When drift ratio reached 3.0 %, there are soft appearances on stiffness of the 1st floor. It can be seem form Figs.5 and 6 that the positive displacement is larger than the negative displacement, thus it means that the 1st floor experienced soft stiffness. Also, the column on the 2nd floor experienced shear failure to cause soft behavior as shown by the red curve on Fig. 5. The results of this experiment focused on developing new constitutive models for RC under combined axial/bending/shear/torsional loading in conjunction with available inelastic beam-column and shell elements.

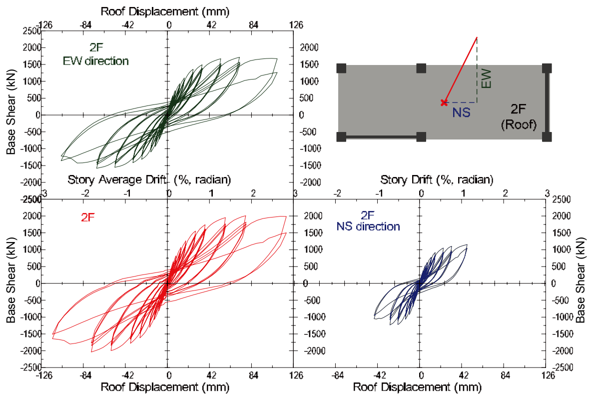

Fig.4 Base shear v.s. roof displacement hysteresis loops.

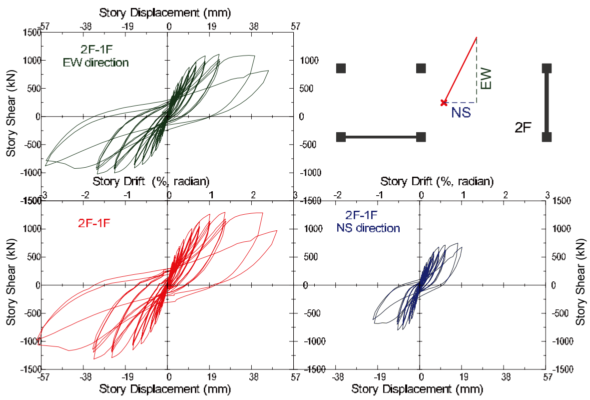

Fig.5 2nd floor story shear v.s. 2nd floor story displacement hysteresis loops.

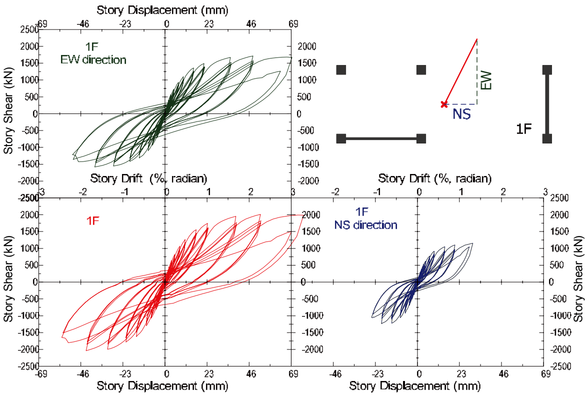

Fig.6 1st floor story shear v.s. 1st floor story displacement hysteresis loops.

Under the circumstances that the test specimen has no constrain, the results of loading and displacement hysteretic loops of mass center on the 2nd floor in the short (East-West) direction are shown in Fig. 7. And the test result of torque and twist hysteretic loops in the short direction can be observed in Fig. 8. The following results can be derived from Fig. 7: The stiffness of whole specimen in the short direction is 159.8 kN/mm. Each of them is 257.9 kN/mm on the 1st floor and 264.9 kN/mm on the 2nd floor. Figure 8 indicates the torsional stiffness of the whole specimen is 1,292.2 kN-mm/rad. And the torsional stiffness on the 1st floor is 2,085.8 kN-mm/rad, and 2,142.5 kN-mm /rad on the 2nd floor.

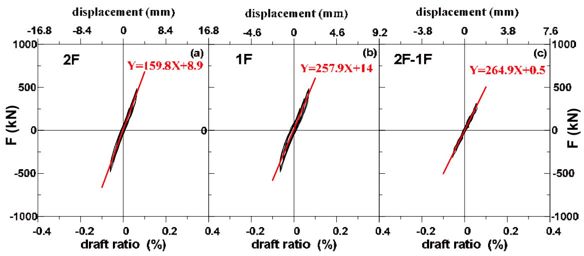

Fig. 7 Loading and displacement hysteretic loops in the short (EW) direction

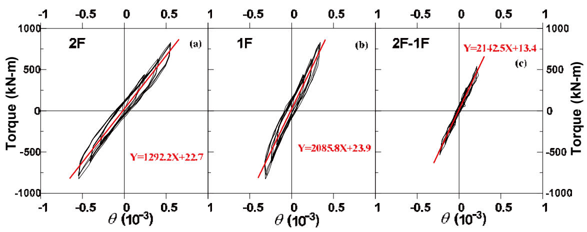

Fig. 8 Torque and twist hysteretic loops in the short (EW) direction

Under the circumstances that the test specimen has no constrain, the results of loading and displacement hysteretic loops of mass center on the 2nd floor in the long (North-South) direction are depicted in Fig. 9. And the test result of torque and twist hysteretic loops in the long direction is in Fig. 10. The following results can be obtained from Fig. 9: The stiffness of whole specimen in the long direction is 170.3 kN/mm. Each of them is 271.7 kN/mm on the 1st floor and 283.7 kN/mm on the 2nd floor. Figure 10 indicates that the torsional stiffness of the whole specimen is 1,940.1 kN-mm/rad. And the torsional stiffness on the 1st floor is 3,128.5 kN-mm/rad, and 3,079.4 kN-mm /rad on the 2nd floor.

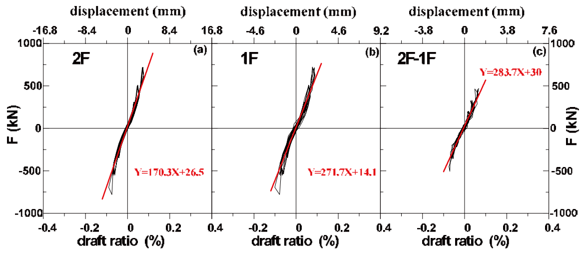

Fig. 9 Loading and displacement hysteretic loops in the long (NS) direction

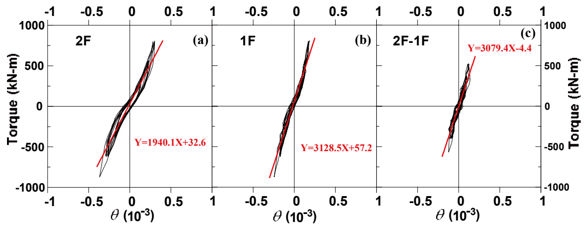

Fig. 10 Torque and twist hysteretic loops in the long (NS) direction

In order to record clearly all columns' loading history, cable-extension position transducers were placed on each beam-column joints to measure bi-directional reversed cyclic loading track. As shown in Fig. 11, due to the asymmetric design of walls, it caused obvious torsional effect and caused the biggest displacement on column C1 and the smallest displacement on column C4. Figure 12 indicates bi-directional reversed cyclic loadings track on 2nd floor, and Fig. 13 shows bi-directional reversed cyclic loadings track on the 1st floor.

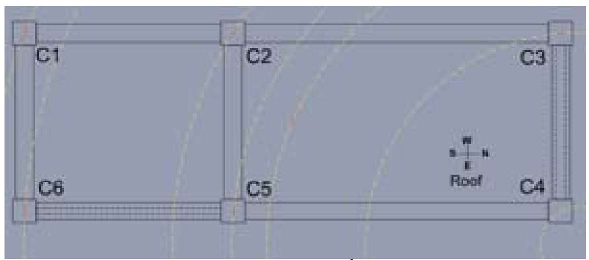

Fig. 11 Each column on the 2nd floor under bi-directional reversed cyclic loading track

Fig. 12 Each column on the 2nd floor under bi-directional reversed cyclic loading track

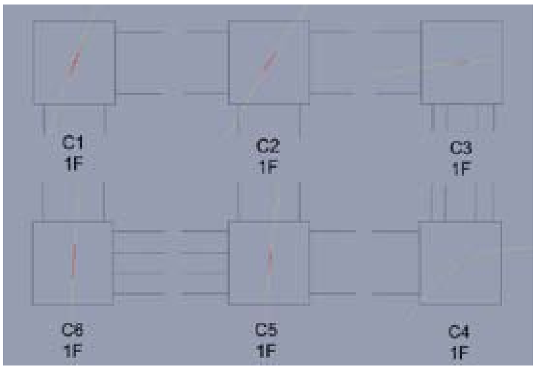

Fig. 13 Each column on the 1st floor under bi-directional reversed cyclic loading track

Figure 14 shows the failure sequences during the experiment. When the story drift was -2 % at the 3rd cycle, buckling occurred at the column C6-1F reinforcement. When the story drift was +3 % at the 1st cycle, buckling occurred at the column C1-1F reinforcement. On the other hand, when the story drift was +3 % at the 1st cycle, shear failure occurred at column C2-2F. Lastly, when the story drift was -3 % at the 2nd cycle, the column C1-2F reinforcement experienced collapse.

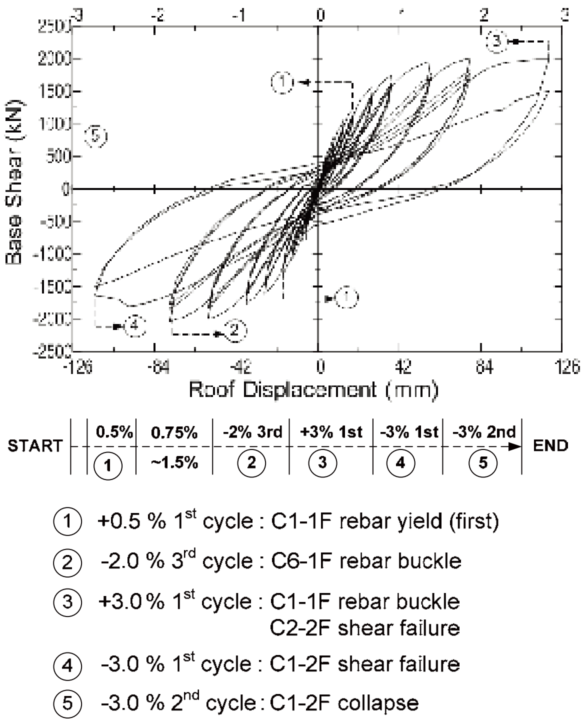

Fig. 14. Failure Sequences

Conclusions

We have tested a two-storey RC building frame subjected to bi-directional cyclic loading experiment in NCREE. The results of this experiment will be used on some related analytical tools and new design methodologies. The brief conclusions of this paper are as follows:

1. The magnitude of the cracks observed on the bottom of columns C1-1F and C2-1F are much more significant than those on the top of the columns. Thus, it can be observed that the inflection point is higher than the center of the column. The reason could be that the stiffness of the floor was smaller than the stiffness of the foundation.
2. Based on the experimental results, it has been observed that Wall C had significant torsional cracks when the story drift was 1.5%. This indicates that the walls, in fact, had suffered from the torsional moment induced in an asymmetric structure. When the structure experienced non-linear behavior, the stiffness center shifted to the wall and this shift exacerbated the torsional moment on the walls.
3. When the center of stiffness and the center of mass do not coincide at each story, torsional moment is induced in the building and torsional vibration occurs. The torsional moment may increase the shear stress of the structural components (i.e. columns and walls). Hence, torsional moment needs to be considered in the simulation of the interaction of the axial, flexural, and shear forces.

References

1. Experiments and Simulation of Reinforced Concrete Buildings Subjected to Reversed Cyclic Loading and Shake Table Excitation, 4ICEE, Taipei, Taiwan, Oct. 12-13, 2006, Paper No.175.
2. Wen-Hsiung Lin, Student Member, ASCE, Anil K. Chopra, and Juan Carlos De la Llera, Members, ASCE "Accidental Torsion in Building ：Analysis Versus Earthquake Motions" Journal of Structural Engineering May 2001 pp.475~481.
3. Tso, W.K. and Zhu, T.J. (1992). "Design of torsionally unbalanced structural systems based on code provisions I: ductility demand," Earthquake Engineering and Structural Dynamics, Vol. 21, pp. 609-627.
4. Kunnath, S.K. and Reinhorn, A.M. (1989). "Inelastic three dimensional response analysis of reinforced concrete building structures (IDARC-3D) Part –I Modeling," NCEER report no. 89-0011, State University of New York at Buffalo, New York.

Seismic Retrofit of Rectangular RC Beams Using CFRP Wrapping and CFRP Anchors

Min-Lang Lin[1] Pei-Ching Chen[2] Yuan-Sen Yang[3]
Chih-Tsung Lin[4] Keh-Chyuan Tsai[5] Jhih-Hao Huang[6]

林敏郎[1]、陳沛清[2]、楊元森[3]、林至聰[4]、蔡克銓[5]、黃志豪[6]

Abstract

Carbon fiber reinforced polymer (CFRP) wrapping is a general method used to enhance shear and moment capacity of reinforced concrete (RC) girders and beams for industrial applications. Among the experimental results in the past, bond failure has been observed at the interface between RC beams and CFRP sheets before the expected tensile strength of CFRP sheets has developed. In this study, CFRP anchors were utilized to provide the required bond strength at the interface without changing the appearance of RC beams. A total of six full-scale specimens were constructed and tested. Experimental results indicated that bond failure occurred at the shear region of the specimen retrofitted using CFRP wrapping during small deformation. Similar result was also observed on the specimen retrofitted using CFRP wrapping anchored by adhesive bolts. On the other hand, the application of CFRP anchors increased the bond strength such that the failure mode has been switched from brittle failure to flexural failure. The shear strength and the ductility were enhanced significantly as well. The advanced image-based measurement was introduced to acquire the global strain field of the external CFRP sheets. Moreover, the proposed novel retrofit method effectively provides sufficient anchoring force to prohibit the interface of CFRP sheets and RC surface from bond failure

Keywords: Seismic retrofit, CFRP wrapping, CFRP anchor, image-based measurement

Introduction

A large number of reinforced concrete structures were not adequately designed; therefore, retrofit has become an important research issue in the recent years. Carbon fiber reinforced polymer (CFRP) wrapping is widely used to retrofit the existing buildings due to its high strength, light weight and convenient application. Several experimental results indicated that the behavior of specimens with CFRP wrapping has been improved; however, bond failure occurred at the interface between CFRP sheets and RC surfaces before the expected tensile strength of CFRP has developed. In this study, “CFRP wrapping conjugate with CFRP anchors” retrofit method was proposed to enhance bond strength at the interface via additional anchorage force provided by CFRP anchors.

Specimen Design and Test Setup

A total of six full-scale specimens were constructed and tested. One as-built benchmark specimen without retrofitting was designed to have shear failure in purpose. The other five specimens retrofitted by different U-shaped CFRP wrapping schemes can be divided into three major groups: Group 1: one specimen, retrofitted by using only CFRP wrapping,

[1] Associate Research Fellow, National Center for Research on Earthquake Engineering, mllin@ncree.org
[2] Assistant Research Fellow, National Center for Research on Earthquake Engineering, pcchen@ncree.org
[3] Associate Professor, Department of Civil Engineering, National Taipei University of Science and Technology
[4] Associate Professor, Department of Civil Engineering, National Taipei University of Science and Technology
[5] Professor, Department of Civil Engineering, National Taiwan University
[6] Graduate Student, Department of Civil Engineering, National Taipei University of Science and Technology

Group 2: one specimen, retrofitted by using CFRP wrapping and adhesive anchors, and Group 3: three specimens, retrofitted by using CFRP wrapping with different designed numbers of CFRP anchors. Figure 1 shows the design details of the un-retrofitted specimens: the width and thickness of the concrete slab were 1,000mm and 120mm, respectively; the width and depth of the beam were 350mm and 530mm, respectively; and the length of each specimen was 4,300mm. There were six reinforcing bars at the bottom and two at the top with diameter of 22mm. The application of CFRP anchors, for example, is illustrated in Fig. 2. Different amounts of CFRP anchors were applied on Specimen R09RF4 and R09RF5. The tensile test results of reinforcements are shown in Table 1 and the compression test results of concrete cylinders are shown in Table 2. The instructions of each specimen are shown in Table 3.

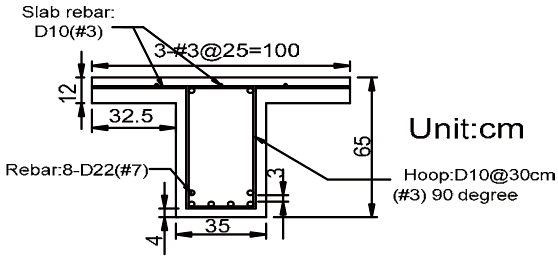

Fig. 1 Specimen design details

Table 1 Tensile test results of reinforcements

Bar Size	Nominal Strength (MPa)	Yield Strength (MPa)	Average Yield Strength (MPa)	Ultimate Strength (MPa)	Average Ultimate Strength (MPa)
#3	280	392	368	499	490
		349		495	
		363		477	
#7	420	475	478	696	695
		484		694	
		475		695	

Table 2 Compression test results of cylinders

Specimen	Nominal Strength (MPa)	28 Day Compression Strength (MPa)	Test Date Compression Strength (MPa)
R09BM	21	24.8	26.1
R09RF2			28.5
R09RF4			36.5
R09RF5			36.3
R09RF1		22.7	30.9
R09RF3			35.8

The test setup is shown in Fig. 3. Two vertical actuators were monotonically controlled with a velocity of 0.05mm/sec, providing shear force on the specimen through a transverse steel beam. Strain gauges, tilt meters, and displacement transducers were also installed on each specimen to acquire the needed test data. Furthermore, image-based measurement technique was introduced to realize the strain field on each specimen in this study.

Table 3 Instruction of tested specimens

Specimen		Retrofit Details
R09BM		bench mark
Group 1	R09RF1	Two layers, U-shaped of CFRP wrapping
Group 2	R09RF2	Two layers, U-shaped of CFRP wrapping with adhesive bolts anchored at the bottom of the concrete slab
Group 3	R09RF3	Two layers, U-shaped of CFRP wrapping with CFRP anchors applied at two sides along the direction of RC beams
	R09RF4	
	R09RF5	

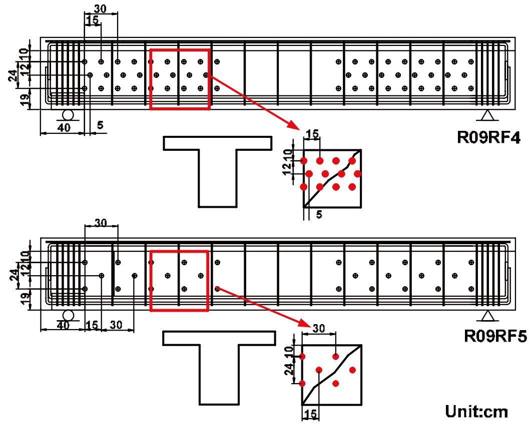

Fig. 2 Illustration of applied CFRP anchors on Specimen R09RF4 and R09RF5

Fig. 3 Test setup

Experimental Results

The displacement-versus-shear force relationships of the specimens are shown in Fig. 4. Shear failure occurred on Specimen R09BM when the deformation at mid-span reached 14mm. Figure 5 demonstrates the shear cracks on Specimen R09BM. The shear capacity of Specimen R09BM was 453.9kN which is 1.8 times of that calculated following the design code. Details of results for each specimen are further discussed below.

Specimen R09RF: Bond failure occurred at the interface between CFRP sheets and RC surface. The maximum shear strength was 421.1kN, indicating that the retrofit scheme was unable to increase the shear capacity as expected. Besides, the peak strain on the CFRP sheet was only 0.003, which is smaller than the design strain of CFRP, i.e. 0.004. Obviously, the design strain of CFRP, 0.004, is not conservative in this case.

Specimen R09RF2: The maximum shear capacity was increased to 476.4kN; however, bond failure still occurred at the interface, indicating that the adhesive bolts did not provide enough anchoring force. Using CFRP wrapping with adhesive bolts may not be effective on improving the ductility of the retrofitted components.

Specimen R09RF3: A total of 40 CFRP anchors with 15mm diameter were applied on two sides of the specimen. The amount of CFRP anchors is only half of the design requirement. The maximum shear force was 525.6kN when the deformation at mid-span reached 28mm. Bond failure was also observed on the specimen, yet the timing was delayed due to the usage of CFRP anchors. The failure mode was considered as flexural-shear failure.

Specimen R09RF4: A total of 104 CFRP anchors with 20mm diameter were applied on two sides of the specimen. The amount of CFRP anchors is 1.75 times the design requirement. Flexural cracks occurred when the mid-span deformation reached 97mm. The failure modes were considered as flexural and ductile failures. This specimen demonstrated the best performance among the six specimens.

Specimen R09RF5: A total of 56 CFRP anchors with 20mm diameter were applied on two sides of the specimen. The amount of CFRP anchors fairly satisfied the requirement. The longitudinal reinforcements yielded first and the strength increased slowly until the mid-span deformation reached 74mm. After the peak shear force was observed, the shear strength decreased smoothly until the CFRP sheets had broke. The ductility of Specimen R09RF5 was 7 times larger than that of Specimen R09RF1, showing that the application of CFRP anchors did enhance the bond strength at the interface and prevent the interface from bond failure in the early stage. The tensile strength of CFRP sheets were successfully developed during large deformation.

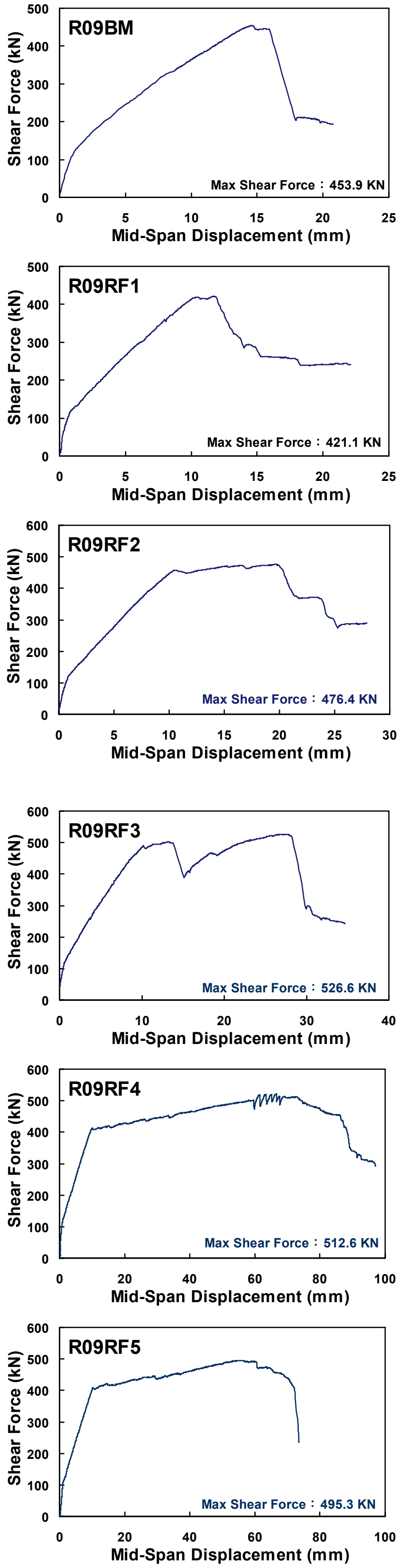

Fig. 4 The mid-span displacement versus shear force relationships of each specimen

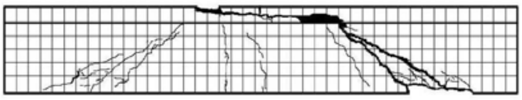

(a) North side

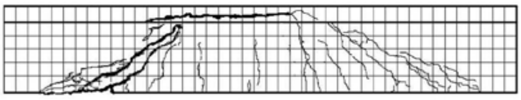

(b) South side

Fig. 5 Crack pattern of Specimen R09BM

The ultimate displacement (u_{max}) of each specimen is defined when the shear strength decreased to 80% of the peak strength. Figure 6 illustrates u_{max} values of each tested specimen. It is obvious that Specimens R09RF4 and R09RF5 behaved well compared with other specimens. The ultimate displacements of these specimens were 90mm and 70mm at mid-span, respectively. In contrary, the ultimate displacement of Specimen R09RF1 was only 12mm at mid-span, indicating that bond failure occurred in the early stage.

The dissipated energy is defined as the area surrounded below the displacement-versus-force curve until the displacement equals to u_{max}. Figure 7 shows the dissipated energy of each specimen, indicating that Specimen R09RF4 and R09RF5 dissipated more energy than the other three retrofitted specimens.

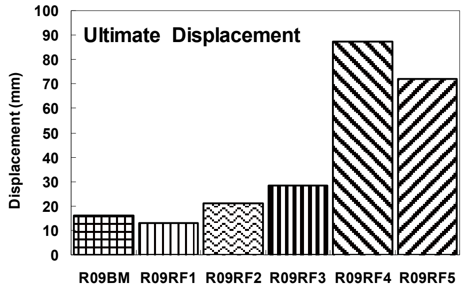

Fig. 6 Ultimate displacement of each specimen

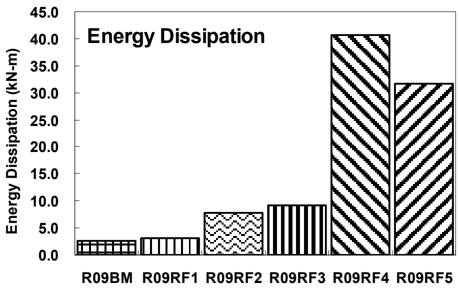

Fig. 7 Dissipated energy of each specimen

The strain field on the CFRP sheets that could not be seen by the eyes was recorded by the image-based measurement during each test. The software was developed by using two-dimensional plane analysis; therefore, the measurement was meaningless if bond failure occurred and CFRP sheets were bulging out. However, significant strain variation was observed at the location where bond failure occurred. The strain measured by this technology was quite close to that obtained by strain gauges. The difference was within ±0.001. Figure 7 shows the strain field on Specimen R09BM when the mid-span deformation was 19mm.

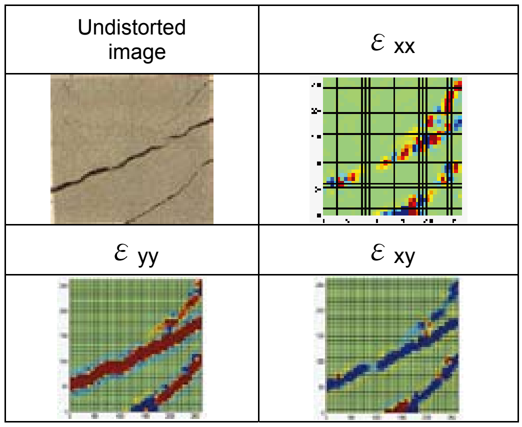

Fig. 7 Strain filed obtained by the image-based measurement

Conclusions and Future Works

1. Bond failure occurred in early stage on test of Specimen R09RF1 and R09RF2, thus the desired tensile strength of CFRP sheets has not been developed fully. More CFRP layers would have not been effective if the bond strength is not increased.
2. CFRP anchors evidently provide sufficient anchoring force at the interface between CFRP sheets and RC surface if the number of CFRP anchors is well designed.
3. Further researches on RC components retrofitted using CFRP wrapping and CFRP anchors will be continued to develop the mechanical theorem and modify design criteria of CFRP anchors.

References

Lin, M. L., Chen, P. C., Tsai, K. C., and Wu, Y. H., “Retrofit Tests on RC Columns Subjected to High Axial Force and Reverse-Curvature Moment,” National Center for Research on Earthquake Engineering, Report No. NCREE-08-025 (2008).

Lin, M. L., Lin, C. T., Chen, P. C., Tsai, K. C., and Wu, Y. H., “Seismic Retrofit of Rectangular RC Columns using CFRP Wrapping and CFRP Anchors,” National Center for Research on Earthquake Engineering, Report No. NCREE-09-014 (2009).

Yang, Y. S., Wu, C. L., Loh, C.H., Yang, C. M., Tu, W. H., Shih, M. H., Tung, S. H., and Capéran, Philippe, “Preliminary Study on Image-based Measurement,” National Center for Research on Earthquake Engineering, Report No. NCREE-08-013 (2008).

Experimental Study on Dynamic Behavior of Reinforced Concrete Frames with Non-seismic Detailing

Shyh-Jiann Hwang[1], Kenneth J. Elwood[2], Jack P. Moehle[3], Chiun-lin Wu[4], Pei-Yang Lin[4], Chin-Hsiung Loh[1], Cheng-Piao Cheng[4], Yuan-Sen Yang[5], Soheil Yavari[2], Shih-Han Lin[1], Pu-Wen Weng[4], Beyhan Bayhan[3]

黃世建[1], K.J. Elwood[2], J.P. Moehle[3], 吳俊霖[4], 林沛暘[4], 羅俊雄[1], 鄭橙標[4], 楊元森[5], S. Yavari[2], 林士涵[1], 翁樸文[4], B. Bayhan[3]

Abstract

In order to observe the interaction of structural elements at the onset of collapse, five frame specimens were tested at the National Center for Research on Earthquake Engineering of Taiwan in spring 2009. Each specimen consisted of a 1/2.25 scale model of a two-bay two-story reinforced concrete frame. The specimens were tested under high and low gravity loads to investigate the influence of axial loads on the collapse vulnerability of the structures. The test results will be employed to study the interaction of beams, columns and joints as collapse is initiated. Such studies will lead to a better understanding of the behavior of existing reinforced concrete structures, and more cost-effective retrofit strategies.

Keywords: collapse, shaking table tests, non-ductile concrete frames, concrete columns, concrete beam-column joints, shear and axial failure

Introduction

Observation of damage after several earthquakes world-wide shows that strong earthquakes can result in a wide range of damage to older concrete buildings, ranging from minor cracking to collapse. Current guidelines for the seismic assessment of existing concrete buildings are not sufficiently refined to enable engineers to distinguish between buildings which are expected to collapse and those that may only sustain minor damage. This lack of refinement, and the inherent conservatism in the guidelines, has resulted in nearly all older concrete buildings being considered collapse hazards during earthquakes. However, this result is not tenable considering the extensive building infrastructure constructed prior to the introduction of seismic provisions in modern building codes in the mid 1970's and the limited funds available for seismic retrofit. A modest investment in earthquake engineering research can result in a significant improvement in the assessment of existing buildings by providing the tools to understand the complex nonlinear behavior of structural systems during seismic events. In particular, given an understanding of the mechanisms leading to the progressive collapse of older concrete buildings, appropriate public policy measures can be initiated to mitigate the risk of multiple building collapses during a major earthquake and to provide the maximum possible earthquake resilience in communities using the limited resources available for infrastructure renewal.

The following describes a research project that directly addresses the significant life-safety risk faced by millions of people living and working in existing concrete buildings in Taiwan and worldwide. The research has been conducted in collaboration with researchers from Canada and the United States, hence leveraging knowledge gained through international research programs.

Significance of the Project

The project was part of a large research project entitled *Seismic Upgrading of Existing Concrete*

1 Department of Civil Engineering, National Taiwan University, Taipei, Taiwan
2 Department of Civil Engineering, University of British, Columbia, Vancouver, Canada
3 Pacific Earthquake Engineering Research Center, University of California, Berkeley, USA
4 National Center for Research on Earthquake Engineering, Taipei, Taiwan, clwu@ncree.org.tw
5 Department of Civil Engineering, National Taipei University of Technology, Taipei, Taiwan

Buildings being undertaken at the National Center for Research on Earthquake Engineering (NCREE) in Taiwan. The focus of the work was a series of shaking table tests to investigate the complex mechanisms that lead to collapse of concrete frame buildings during severe earthquakes. Shaking table studies provide the most accurate means of assessing the performance of structures when subjected to earthquakes.

Other participants in the NCREE project included the Canadian Seismic Research Network (CSRN) and the Network for Earthquake Engineering Simulation (NEES) in the United States. Currently, NEES has a project which includes large-scale testing of existing concrete building components, soil-structure interaction studies, collapse modeling, and regional simulations, all geared toward identifying seismically hazardous older concrete building construction and promoting effective mitigation strategies (NRC, 2004). The NEES project, however, does not include shaking table tests, but instead relies upon international collaboration with CSRN and NCREE to provide the critical data. The overall objective of the NCREE-CSRN-NEES collaboration was to provide engineers, building owners, and policy makers with tools to effectively mitigate the significant life-safety risk posed by collapse of concrete buildings during future earthquakes. The expected outcome of the research proposed herein is to provide benchmark data for the development and refinement of numerical models used in the assessment of existing concrete buildings. The benchmark data from the proposed shaking table tests will be provided to all participants in the NCREE-CSRN-NEES collaborative project. Refinement of the numerical models will allow for more accurate predictions of collapse potential for concrete buildings and enable engineers to identify the truly dangerous structures in need of immediate rehabilitation.

Project Background and Description

Collapse of a reinforced concrete frame during an earthquake can be caused by failure of beams, columns, or beam-column joints. Older gravity-based design methods result in a mechanism with weak columns and strong beams, and therefore, most building frames designed using such methods are expected to experience failure of columns or joints. To date, there have been relatively few tests on lightly confined reinforced concrete frame systems in the literature and rarely conducted dynamically to collapse. None of those tests investigated the effects of high axial load on the failure of non-ductile columns. In an attempt to fill the gaps in knowledge, this study involved dynamic testing to collapse of five two-dimensional, two-bay, two-story, and 1/2.25-scale reinforced concrete frames. Each frame contained non-seismically detailed columns whose proportions and reinforcement details allow them to yield in flexure prior to shear strength degradation and ultimately reach axial collapse (these columns are commonly referred to as flexure-shear-critical columns). The influence of non-confined joints on collapse behavior of the frame will also be investigated.

The NCREE shaking table tests completed in 2008-2009 will provide critical data to validate and improve numerical models for the assessment of the collapse vulnerability of concrete frame buildings, and, in turn, will allow for the refinement of guidelines used for seismic assessment. These tests focused on two previously unexplored issues: (1) the interaction of multiple vulnerable concrete components (i.e. beams, columns, and joints) within a building frame as collapse is initiated, and (2) the influence of high gravity loads on the collapse vulnerability of structure. Past shaking table collapse tests have focused on the performance of one specific component (i.e. columns) and only considered low to moderate gravity loads; however this simplifies the building response to such an extent that the results from these tests may not be representative of the true collapse behavior of real concrete frame buildings.

Figure 1 describes four shaking table specimens tested at NCREE in April and May 2009. Comparison of the results from MCFS and HCFS will reveal the influence of axial load on shear and axial behavior of flexure-shear-critical columns, while observations from MUF and MUFS will demonstrate the effects of unconfined joints on the overall behavior of the frame near the point of collapse and sequence of failure in the elements. Details of the specimens are described in the following section. In addition to the four specimens shown in Figure 1, one frame with specifications of specimen MCFS, but with moderate axial load only on the middle column was tested in the spring of 2009. This shaking table test was used to monitor the performance of many innovative elements employed in the tests, including the hydraulic jacks for the pre-stressing axial load system, top inertial mass system, instrumentation of the frame elements, connection of inertial mass system to the specimen, etc. Comparison of the results from this experiment with the MCFS test data also provides the opportunity to observe the effects of distribution of axial load on behavior of the frame.

Specimen MCFS: **M**oderate Axial Load **C**onfined Joints **F**lexure-**S**hear Columns	**Specimen HCFS:** **H**igh Axial Load **C**onfined Joints **F**lexure-**S**hear Columns
Specimen MUFS: **M**oderate Axial Load **U**nconfined Joints **F**lexure-**S**hear Columns	**Specimen MUF:** **M**oderate Axial Load **U**nconfined Joints **F**lexure Columns

Fig. 1 Description of shaking table specimens

Specimens and Test Setup

Figure 2 shows the dimensions of the two-dimensional concrete frames tested at NCREE. The geometries and details were selected to be representative of elements used in a seven-story hospital building. Final dimensions and reinforcement details of the frames were influenced by the following considerations: laboratory and shaking table limitations, replication of column details used in existing buildings, desired failure mode, and cost. The target failure mode was intended to be damage leading to collapse that would enable examination of gravity load redistribution during the test. The column details and loading were chosen to be typical of 1960s and 1970s building construction, with widely spaced ties formed with 90° hooks. The ratio of beam-to-column stiffness was considered to be similar to the prototype existing building. Since the overall width of the frame, and consequently the beam length, was limited by the dimensions of the shaking table; the beam depth was adjusted to achieve the target beam-to-column stiffness ratio. Beam transverse reinforcement with closed stirrups and 135° hooks provided sufficient shear strength to develop full flexural strength, while longitudinal reinforcement was chosen to create a weak-column-strong-beam mechanism typical of the older concrete construction. Neither beams nor columns had lap splices to eliminate the splicing effects from the scope of this study. Slabs were cast with the beams to include the effect of slabs on the beam stiffness and the joint demands.

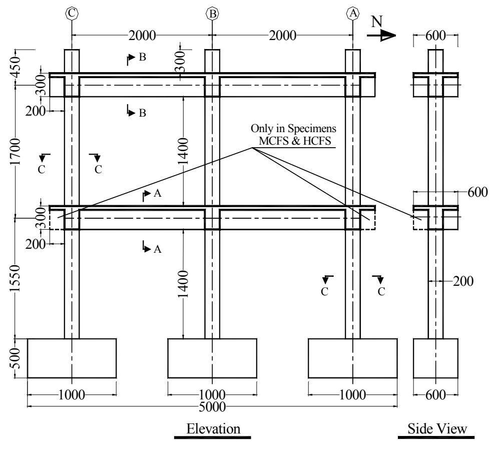

Fig. 2 Shaking table test specimen

As shown in Figure 3, to account for the upper stories of a seven-story building, post-tensioning (marked by a red rectangle) was used to achieve high axial load on the columns, and a lumped mass (marked by a red circle) was placed on rollers on the shaking table and connected to the top of the specimen, This innovative approach enabled the demands from upper stories to be captured while ensuring the structure can be tested safely up to the collapse limit state.

A stiff steel frame, bolted to the table, was used to brace the specimens in the out-of-plane direction by means of frictionless rollers at each beam level which allowed free in-plane motion (both horizontal and vertical) of the frame. Rigid transverse steel beams were connected to the supporting frame to catch the specimen after collapse and prevent any damage to the shaking table.

Specimen instrumentation consisted of: 1) force transducers (load cells) that measured shear, axial load, and bending moments at the base of the frame footings; 2) strain gages on longitudinal and transverse reinforcements of columns, beams, and joints; 3) accelerometers for horizontal and vertical accelerations; and 4) displacement transducers to measure both local column and global frame deformations. Figure 4 shows the instrumentation used for the measurement of the exterior joint deformations.

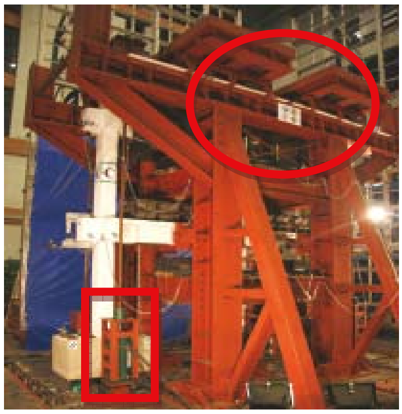

Fig. 3 Steel lateral supporting frame and inertial mass system

Fig. 4 Instruments for measuring the exterior joint deformations

Experimental Program

Each specimen was first subjected to a white noise to obtain the natural period and damping ratio of the structure, followed by two sequential scaled table motions (Test1 and Test2) selected from the Chi-Chi earthquake records. The natural periods of the frames were obtained in a range of 0.28 to 0.29 sec, while the damping ratio was determined to be 2-3%. The specimens performed differently during Test1 and Test2. The test frames did not collapse during Test1, but all of them were damaged to some extent. As expected, columns of frames MCFS and HCFS experienced shear and flexural cracks, while damage was mostly concentrated at the exterior first-story joints of specimens MUF and MUFS. The specimens did not perform similarly during Test2 and the failure mode was different for each frame. Specimen MUF did not collapse during Test2, while the other three frames experienced complete collapse. Figure 5 summarizes the failure modes for the four specimens. Frame MCFS collapsed due to shear and axial failure of the first-story columns. This was not observed for the other cases, where combination of plastic hinge development and damage to the structural elements caused the failure of the frame.

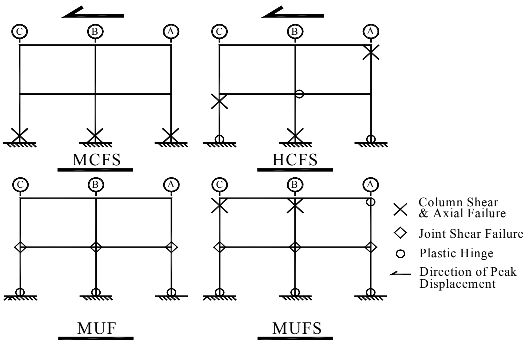

Fig. 5 Failure mode for each specimen

Figure 6 compares the base shear hysteretic response of the four frames for Test1. It is observed that the columns in specimens MUF and MUFS did not reach their shear capacity (V_p), while their first-story drift ratio was larger than MCFS and HCFS. This was expected for specimen MUF with ductile columns, however, similar performance by specimen MUFS, with flexure-shear-critical columns, suggests that the unconfined joints in these two specimens worked as a fuse and did not allow shear to be fully transferred to the first-story columns and accommodated much of the deformation demands.

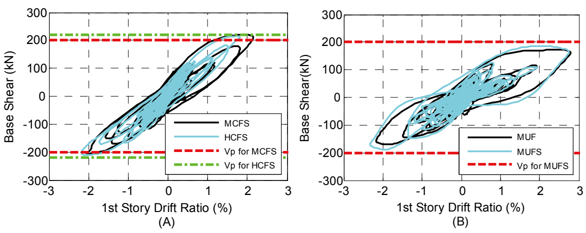

Fig. 6 Comparison of base shear hysteretic response of the frames during Test1

In specimen MCFS, shear failure of column B1 was initiated at approximately 1.9% drift ratio and a shear of 79.5kN (Test2). Column C1, taking higher shear forces due to overturning compression demands, experienced shear failure at 2.2% drift ratio and shear of 87.2kN. Finally, column A1 at a drift ratio of 2.8% and shear of 65.7kN commenced to fail. It was observed that the onset of shear failure happened at a larger drift ratio for specimen HCFS, where column B1 experienced shear failure at 2.3% drift ratio and a shear of 86.8kN and shear failure of column C1 commenced at 2.9% drift ratio and a shear of 81.6kN.

The beam-column joints from both frames MUF and MUFS underwent large shear deformations, although the exterior joints from specimen MUFS showed a stiffer behavior in Test1. Shear failure of the first-story joints released the moments at the top of the first-story columns and as a result, these columns did not experience significant damage. The same release of moments did not appear to occur at the base of the second-story columns possibly due to the restrain of the slab. Furthermore, the beam-column joints of the second story were well-confined and imposed fixed-end boundary condition, so that the second story columns experienced larger demands than those in the first story. This would explain the shear and axial failures which occurred at the top of columns B2 and C2 of specimen MUFS. The behavior of frame MUFS implies that the rotation at the ends of a non-ductile column plays a significant role in shear and axial failure of this type of columns.

Conclusions

Five frames with non-seismic details were tested at the National Center for Research on Earthquake Engineering under moderate and high axial loads in spring 2009. Details of the specimens and setup of the tests were described in this paper. Observation of interaction of failure in columns and joints during the tests suggests that frame geometry and layout of critical elements are crucial in determining failure sequence and ultimately collapse mechanisms.

Comparison of results from specimens MCFS and HCFS indicates that changes in axial loads can significantly impact the failure mode of the frame, and that larger axial load appears to increase the likelihood of failure in higher stories.

Test results of frames MUF and MUFS suggest that unconfined beam-column joints are playing a major role in the behavior of non-ductile frames. In both cases, large deformations at the joints enhanced the performance of the frames by reducing the rotation at the top of the first floor column.

Behavior of specimen MUFS indicates that inter-story drifts may not correlate well with shear failure of flexure-shear-critical columns, where shear failure initiation appears to be more related to column end rotations than column drifts.

References

National Research Council, (2004) “Preventing Earthquake Disasters: The Grand Challenge in Earthquake Engineering – A Research Agenda for the Network for Earthquake Engineering Simulation (NEES),” Committee to Develop a Long-Term Research Agenda for the Network of Earthquake Engineering Simulation (NEES), The National Academy of Science Press, Washington, D.C., http://www.nap.edu/catalog/10799.html.

Application and Improvement of the Coefficient Method of Displacement

Yuan-Tao Weng [1], Shyh-Jiann Hwang [2]

翁元滔 [1]、黃世建 [2]

Abstract

The understanding on the inelastic displacement ratio, i.e. the ratio of the maximum inelastic to the maximum elastic displacement of an SDOF system, allows the computation of its maximum inelastic displacement directly from the corresponding elastic one. This study presents a simple and effective method for the inelastic displacement ratio estimation of a structure under cyclic earthquakes. Extensive parametric studies were conducted to obtain expressions for the said ratio, in terms of the period of vibration, the viscous damping ratio, the strain-hardening ratio, the force reduction factor, and the soil class. It has been found that the post-stiffness ratio has a significant effect on the inelastic displacement ratio and hence on the maximum inelastic displacement of SDOF systems.

Keywords: Inelastic displacement ratio, performance-based seismic design, displacement coefficient method , strength degradation

Introduction

The Coefficient Method of displacement is the primary nonlinear static procedure presented in FEMA 356 (ASCE, 2000). The method modifies the linear elastic response of the equivalent SDOF system by multiplying it with a series of coefficients (C_0 through C_3) to generate an estimate of the maximum global displacement (elastic and inelastic) also termed as the target displacement. The process begins with an idealized force-deformation curve (i.e., pushover curve) relating base shear to roof displacement. An effective period, T_e, is generated from the initial period, T_i, by a graphical procedure that accounts for some loss of stiffness in the transition from elastic to inelastic behavior. The effective period represents the linear stiffness of the equivalent SDOF system. When plotted on an elastic response spectrum representing the seismic ground motion, as peak acceleration, S_a, versus period, T. The assumed damping, often five percent, represents a level that might be expected for a typical structure responding in the elastic range. The peak elastic spectral displacement is directly related to the spectral acceleration by the relationship

$$\mathbf{S}_D = \frac{T_e^2}{4\pi^2} S_a \tag{1}$$

The coefficient C_0 is a shape factor (often taken as the first mode participation factor) that simply converts the spectral displacement to the displacement at the roof. The other coefficients each account for a separate inelastic effect.

Based on the evaluation summarized in FEMA 440 document and from the available research data, improvements to the Coefficient Method of FEMA 356 have been developed and are presented in the mentioned document. Recommendations include several improved alternatives for the basic ratio of the maximum displacement (elastic plus inelastic) for an elastic perfectly plastic SDOF oscillator to the maximum displacement for a completely linear elastic oscillator designated as the coefficient C_1 in FEMA 356. FEMA 440 report also recommends that the current limitations (capping) allowed by FEMA 356 to the coefficient C_1 be abandoned. In addition, a distinction is recognized between two different types of strength degradation that have different effects on system response and performance. This distinction leads to recommendations for the coefficient C_2 to

[1] Associate Research Fellow, National Center for Research on Earthquake Engineering, ytweng@ncree.org.tw

[2] Professor, Dept. of Civil Engineering, National Taiwan University, sjhwang@ntu.edu.tw

account for cyclic degradation in strength and stiffness. It is also suggested that the coefficient C_3 be eliminated and replaced with a limitation on strength.

In this study, using constant-ductility format, the coefficients C_1 and C_2 were revised and are presented. The determination of the target displacement in the simplified nonlinear static procedure (NSP) known as the Displacement Coefficient Method has been revised in this study. The target displacement, δ_t, which corresponds to the displacement at roof level, can be estimated as follows:

$$\delta_{\mathbf{t}} = C_0 C_1 C_2 S_a \frac{T_e^2}{4\pi^2} g \tag{2}$$

where C_0 is the fundamental modal participation factor, and C_1 represents the approximate ratio of the maximum displacement of an elastic-perfectly-plastic SDOF oscillator model to that of a fully elastic counterpart. The proposed modification was based from the results of the simplified dynamic analyses conducted as part of the evaluation database. The proposed relationship is a function of ductility (μ), period (T), and site class. The coefficient C_2 accounts for the change in maximum inelastic displacement for systems that exhibit cyclic degradation of stiffness and strength. The proposed modification was based from the results of the simplified dynamic analyses conducted as part of the evaluation database. In many cases, the data suggest that cyclic degradation does not increase maximum displacements. However, there are exceptions especially for short period, low strength structures.

Description of equivalent SDOF model

An elasto-plastic SDOF system with linear hardening or softening and viscous damping was used to model the structure, as shown in Fig. 1. The statistical dynamic response of this system to actual seismic records was investigated and is discussed in the next section. The dynamic equilibrium equation of an SDOF system is given by the following:

$$\mathbf{m}\ddot{\mathbf{u}} + \mathbf{c}\dot{\mathbf{u}} + \mathbf{k}_{\mathbf{T}} u = -m a_g \tag{3}$$

where **m** is the mass, **u** is the relative displacement, **c** is the damping coefficient, k_T is the tangent stiffness, and a_g is the acceleration of the ground motion, while upper dots stand for time derivatives. If the required yield force for a system with available ductility μ is denoted by f_y and the maximum force response of the corresponding linear elastic system by f_{el} (Fig. 1), the force reduction factor R can be defined as

$$\mathbf{R} = \mathbf{f}_{\mathbf{el}} / f_y \tag{4}$$

Using traditional structural dynamics theory, SDOF systems are defined here by their elastic vibration period T, ranging from 0.1 s to 3.0 s, and viscous damping ratio ξ , assumed to be 1%, 2%, 5% and 10%. The yield force f_y can be expressed in terms of the yield displacement u_y and the elastic stiffness k_{el} as

$$\mathbf{f}_{\mathbf{y}} = k_{el} \cdot u_y \tag{5}$$

while the ductility μ is defined in terms of the maximum displacement u_{max} and the yield displacement u_y, as

$$\mu = \mathbf{u}_{\mathbf{max}} / \mathbf{u}_{\mathbf{y}} \tag{6}$$

Strain hardening or softening takes place after yielding initiates. The tangent stiffness is defined as the slope $k_t = H \times k_{el}$ of the second branch of the skeleton force-displacement relationship (see Fig. 1). In this work, seven different values of the post-yield stiffness ratio, $H = k_t/k_{el}$, were examined. These are 0%, which corresponds to an elastic-perfectly plastic model, 1%, 3% and 5% for the linear hardening model, and -1%, -3% and -5% for the linear softening model. Unloadings and subsequent loadings were assumed to be parallel to the original loading curve, as shown in Fig. 1.

Finally, the inelastic displacement ratio is defined as the maximum lateral inelastic displacement u_{max} divided by the maximum lateral elastic displacement u_{el} for a system with the same mass and initial stiffness (i.e., same period of vibration) subjected to the same earthquake ground motion. This ratio is given by

$$\mathbf{IDR} = \mathbf{u}_{\mathbf{max}} / u_{el} = \mu / R \tag{7}$$

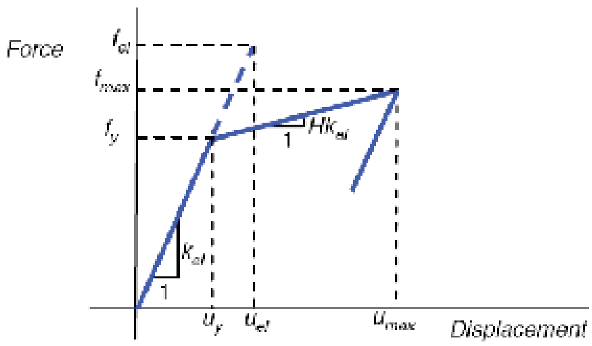

Fig. 1 Bilinear elasto-plastic model of an SDOF

As Figure 2 shows, in order to compute the coefficients C_1 and C_2, an equivalent bilinear structural pushover curve model has been proposed to consider structural cyclic strength degradation.

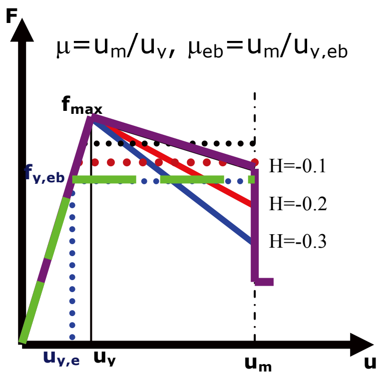

Fig. 2 Equivalent bilinear structural pushover curve model

In order to evaluate the coefficient C_2, the model shown in Figure 2 was considered. Use equal energy principle to idealize the pushover curve as a bilinear curve, and then compute the corresponding post-yield stiffness ratio H and ductility ratio. The C_2 coefficient which reveals cyclic stiffness and strength degradation effects can be computed as

$$\mathbf{IDR} = \left(\mathbf{1} - \sqrt{\mathbf{1} - \mathbf{H}}\right) \cdot \mu + \sqrt{1 - H} \qquad (8)$$

In order to verify the feasibility of Eq. (8), a total of 112 real earthquake acceleration time-histories from around the world are used in this study. These accelerograms present maximum ground acceleration greater or equal to 0:10g and are recorded at sites ranging from hard rock to soft soil conditions according to the definitions of the United States Geological Survey (USGS) site classification system (Boore 1993). More specifically, 4 groups of 28 accelerograms are examined, which correspond to:

- hard rock site conditions with shear wave velocity 750 m/s ≤ V_S (soil type A).
- soft rock or very dense soil with shear wave velocity 360m/s ≤ V_S < 750 m/s (soil type B)
- stiff soil with shear wave velocity 180 m/s ≤ V_S < 360 m=s (soil type C)
- soft soil with shear wave velocity 180 m/s > V_S (soil type D).

The complete list of these earthquakes, which was downloaded from the strong motion database of the Pacific Earthquake Engineering Research (PEER) Center. The total sample of earthquakes can be characterized as fairly broad since it ranges in terms of maximum ground acceleration between 98 and 806 cm/s^2, i.e., between 0.100g and 0.822g. The mean response elastic spectra (ξ = 5%) for the four aforementioned groups and the whole sample are presented in Fig. 3. These spectra seem to be similar to the corresponding design spectra proposed by modern seismic codes with analogous site classification systems. Furthermore, this soil classification system is quite similar to EC8 provisions (ECS, 2003) since the only difference between the EC8 and USGS categorizations has to do with the characteristic shear wave velocity of hard rock, which is greater than or equal to 800 m/s and 750 m/s, respectively.

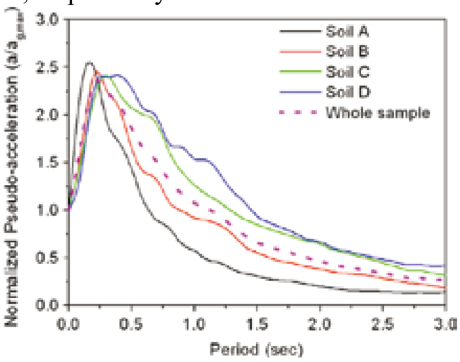

Fig. 3. Acceleration spectra for the four groups of accelerograms.

Influence of various parameters

This section examines the influence of period of vibration, force reduction factor, site conditions, post-yield stiffness ratio and viscous damping ratio on the inelastic displacement ratios. These aspects are investigated for reasons of completeness as many of them have been also studied by several authors, but in the most cases separately and seldom simultaneously. The influence of soil types is typically shown in Fig. 4. It is evident that the inelastic displacement ratios are not significantly affected by local site conditions and can be practically neglected. This characteristic is in agreement with the observations of Miranda (2000).

Figure 5 shows the influence of post-yield stiffness ratio. It is evident that the decrease of this ratio leads to a significantly higher inelastic displacement ratio value and vice versa. Finally, as one can observe from Figs. 4-5, the inelastic displacement ratios are extremely dependent on the structural period of vibration, in any case. Concluding this section, it should be noted that despite the observed influence of the most critical parameters, i.e. post-yield stiffness ratio, force reduction factors and structural period on the inelastic displacement ratios, there are many seismic design codes which ignore them in the estimations.

Conclusions

This paper proposes a new method for evaluating the inelastic displacement ratios of SDOF systems on the basis of empirical expressions obtained after extensive parametric studies. The influence of period of vibration, force reduction factor, soil type conditions and post-yield stiffness ratio (hardening and softening) is carefully examined and discussed. The main innovation of this work has to do with the quantification of the seismic sequence effect directly onto displacement demands, a problem which has not been studied in the past. A detailed study of the influence of the various parameters of the problem on the inelastic displacement ratio leads to the following conclusions:

1. The increase of force reduction factors always leads to an increase of the inelastic displacement ratio and vice versa. Furthermore, these ratio values are extremely dependent on the structural period of the SDOF system, especially in the short-period range, say up to 0.5 s. In this case, the lower the period, the higher the inelastic displacement ratio. Additionally, the decrease of post-yield stiffness ratio leads to higher displacement demands and vice versa. This effect is more pronounced for negative values of this parameter, i.e., for softening behavior.
2. The local site conditions and the viscous damping ratio influence the inelastic displacement ratio slightly, and can be

practically ignored.

3. The traditional seismic design procedure, which is essentially based on the isolated `design earthquake', should be reconsidered.

References

Federal Emergency Management Agency. Prestandard and commentary for the seismic rehabilitation of buildings. Rep. FEMA 356, Washington (DC); 2000.

Federal Emergency Management Agency. Improvement of nonlinear static seismic analysis procedures. Rep. FEMA 440, Washington (DC); 2006.

Miranda E. Inelastic displacement ratios for structures on firm sites. J Struct Eng 2000;126(10):1150-9.

Boore DM. Some notes concerning the determination of shear-wave velocity and attenuation. In: Proceedings of geophysical techniques for site and material characterization. 1993. p. 129-34.

Pacific Earthquake Engineering Research Center. PEER strong motion database. [accessed 01.03.09] http://peer.berkeley.edu/smcat.

European Committee for Standardization. Eurocode 8: Design of structures for earthquake resistance. 2003.

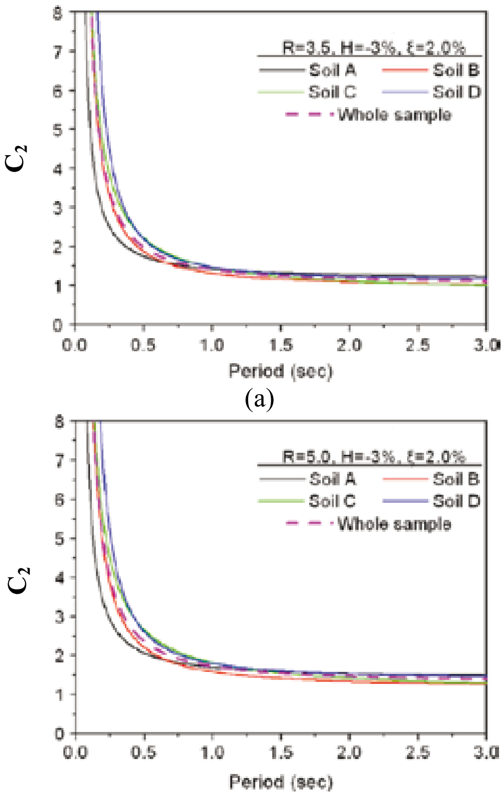

(a)

(b)

Fig. 4. Influence of local site conditions.

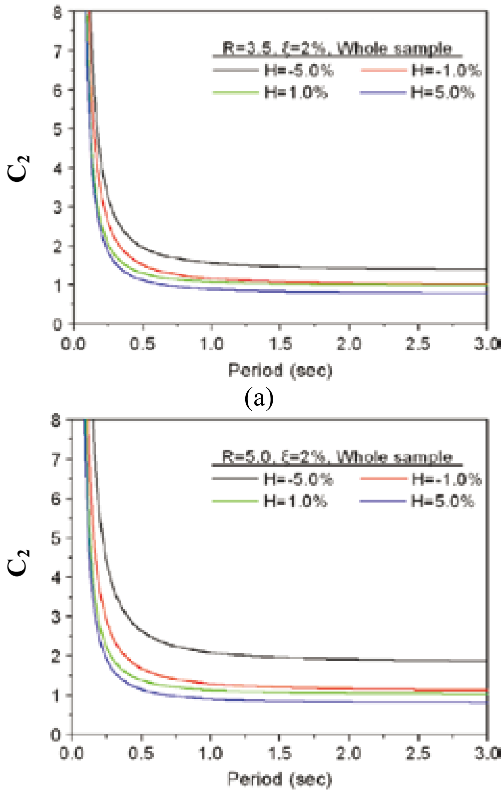

(a)

(b)

Fig. 5. Influence of post-stiffness ratio.

Establishment of Seismic Evaluation and Retrofit Data Bank of Elementary School Buildings in Taiwan

Yeong-Kae Yeh[1], Yi-Feng Chao[2], Hung-Ming Chen[2], Wei-Ko Kao[2], Wen-Cheng Shen[1], Pu-Wen Weng[1], Lap-Loi Chung[1], Wen-Yu Jean[1], Shyh-Jiann Hwang[1]

葉勇凱[1]、趙宜峰[2]、陳鴻銘[2]、高偉格[2]、沈文成[1]

翁樸文[1]、鍾立來[1]、簡文郁[1]、黃世建[1]

Abstract

Since 2003, the National Center for Research on Earthquake Engineering (NCREE) has accepted the project from the Department of Elementary Education (DEE) to establish procedure on seismic capacity upgrading in Taiwan's elementary school buildings. The said procedure can be divided into four stages, namely: (1) simple survey, (2) preliminary evaluation, (3) detailed evaluation, and (4) retrofit design with construction. The simple survey was designed to be applied by school administrators and has been applied already in Taipei city and county. Analysis of simple survey data can provide reference to determine which school buildings have doubtful seismic capacities. These selected school buildings can then be sent to the next steps for preliminary evaluation, detailed evaluation or even retrofit design with construction which will be carried out by professional engineers.

In the past few years, NCREE has set up the so-called "Seismic Information Web of School Buildings" for the requirement of DEE. This web includes collections into a one unique platform of the simple survey, preliminary evaluation, detailed evaluation, and retrofit design with construction. In this year, NCREE will assist all city and county governments to undertake simple survey, preliminary evaluation, and detailed evaluation and retrofit design with construction of elementary school buildings. And the so-called "overall school building investigation" will be processed in this year. The checklist of retrofit design with construction will be so designed such that data will be received through the network. Through the established web platform, the collected data can be provided to education departments, researchers and professional engineers to study about elementary school buildings. Therefore, the budget from the national government can be used effectively through the study of the collected data in the web.

Keywords: Seismic information web of school buildings, Seismic capacity evaluation of school buildings, Data bank of school buildings,

Introduction

In the past years the government has considered seismic capacity upgrading of school buildings as an important issue. To improve the seismic capacity of school buildings, since 2004, the Department of Elementary Education of the Ministry of Education (MOE) has supported projects of NCREE to study the procedure of seismic evaluation and retrofit of school buildings as shown in Fig. 1. From the simple surveyed data reported by the school administrators, the first sampling of school buildings with doubtful seismic capacity can be specified. Those school buildings can be set to the preliminary evaluation process which is processed by professional engineers. The school buildings which have insufficient seismic capacity from the results of preliminary evaluation will be put to detailed evaluation to identify their seismic capacities. The school buildings which lack seismic capacity will be retrofitted or rebuilt. All the

[1] National Center for Research on Earthquake Engineering, ykyeh@ncree.org.tw.

[2] Department of Construction Engineering, National Taiwan University of Science and Technology

data collected from these processes will be compiled into the seismic evaluation and retrofit data bank of elementary school buildings. The collected data can be provided to education departments, researchers and professional engineers to study about school buildings. The budget of the government can then be used effectively through the study of the collected data.

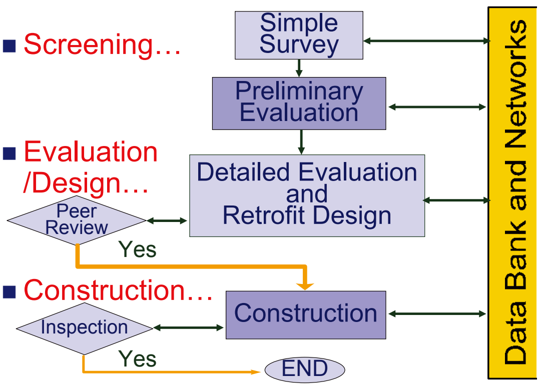

Fig. 1 Established procedure on seismic evaluation and retrofit of school buildings

Overall investigation of school buildings

In 2009, NCREE assisted MOE to execute the four-year project to upgrade the seismic capacity of high school and elementary school buildings in Taiwan. Accordingly, professional engineers will evaluate the seismic capacity of school buildings and design the retrofitting method if it is required. Engineers will submit the evaluation and retrofit data to the seismic information web of school buildings.

To move forward this project, an overall investigation of school buildings will be undertaken. This overall investigation can provide a whole picture on the present condition of school buildings. The investigation results can be compared with the data bank of seismic information web of school buildings. Then, it is hoped that the progress of the project to upgrade the seismic capacity of high school and elementary school buildings in Taiwan be understood.

The overall investigation of school buildings will be held under the cooperation of NCREE and several universities and colleges. Civil engineering students will be sent to investigate the school buildings. Major investigation items include the basic information of the school, the present conditions of school buildings and the seismic upgrading stage of the buildings.

At the moment, a total of 456 schools have the overall investigation results including 18 schools in Taipei City, 166 schools in Taipei County, 88 schools in Yunlin City and County, 96 schools in Chiayi County, 60 schools in Tainan City and County, and 28 schools in Hualien County.

Preliminary evaluation

Since December 2003, the collection of preliminary evaluation of school buildings has started. At that year, the data on preliminary evaluation included 26 schools in seven cities or countries. In 2006, the upload checklist of preliminary evaluation was established and received the data of about 1,500 schools in Taipei City and County. Until 2009, the data bank collected preliminary evaluation checklists of over nine thousand school buildings.

The method of preliminary evaluation has two versions. The first version was developed in 2003 and was modified in 2008 and served as the second version. The preliminary evaluation in Taipei City and County used the first version. Most school buildings applied in the project of MOE used the second version and its distribution is shown in Fig. 2.

Fig. 2 The distribution of school buildings which used the second version of preliminary evaluation method

Detailed evaluation and retrofit design

Detailed evaluation is the third stage of the strategy on seismic upgrading of school buildings. The detailed evaluations are executed by professional engineers to identify the seismic capacity of school buildings. The process involves more detailed and complete analysis than the preliminary evaluation. It needs to collect the structure’s blueprint, investigate the structure in person and take samples to test. These data serve as reference to evaluate the seismic capacity of the school buildings. The seismic performance requirement of the school building is due to its usage. Then the engineer will model the structure and proceed to the nonlinear static analysis using a structural analysis program. From the analysis, the performance object peak ground acceleration compared with the peak ground acceleration of the design earthquake of 475 years return period can be determined. If the performance object peak ground acceleration is smaller than the design earthquake’s acceleration, the school building needs to be retrofitted or rebuilt. If the school building satisfies the requirement of the seismic performance, the building does not need to be retrofitted.

The last stage of the strategy on seismic upgrading of school buildings is the retrofit design. This work is also executed by professional engineers. The retrofit construction is processed by a construction contractor and supervised by the original retrofit design engineer.

Table 1 Analysis results of various detailed evaluation methods

	Strength Ductility Method		Pushover Method	
	buildings	ratio	buildings	ratio
Need retrofit	207	93.24%	528	80.61%
No need retrofit	11	4.95%	75	11.45%
Suggest to rebuild	4	1.80%	52	7.94%

On November 26, 2009, the data bank has already collected detailed evaluation data of 877 school buildings. In these data, there are 222 (about 25.3%) school buildings that used the strength and ductility method for detailed evaluation. The other 655 school buildings used the pushover analysis. In general, the strength and ductility method is more conservative. It only considers the elastic behavior of the structure and the assumed ductility is considered too conservative. So nearly 93.2% of the evaluated school buildings were judged to be retrofitted or rebuilt. But for pushover analysis, only 80.6% of the evaluated school buildings have to be retrofitted or rebuilt. The analysis results of these two detailed evaluation methods are shown in Table 1. The pushover analysis is more suitable to be the tool on the detailed evaluation works. It can specify the school buildings that need retrofitting and can eventually save on budget.

Table 2 Data of supposed retrofit method in the data bank

	Proposed case 1	Proposed case 2
Adding shear walls	247	179
Adding wing walls	254	206
Adding struts	8	56
Extended columns	217	266
Enclosed steel plates	7	8
Foundation retrofit	159	155

The data bank has collected already retrofit design data of 90 school buildings as of November 26, 2009. In the data, 37 school buildings (about 41%) used the strength and ductility method to evaluate the seismic capacity of the retrofitted school buildings. The other 53 school buildings used the pushover analysis.

In the seismic data bank of school buildings, the supposed retrofit methods include adding elements, column retrofit, wall retrofit, beam retrofit, reducing weight, foundation retrofit, etc. Table 2 shows the data of supposed retrofit methods in the data bank. The extended column, adding wing walls and adding shear walls are most favorable for professional engineers.

Short courses of seismic evaluation and retrofit design of school buildings

Because most of the works on seismic upgrading of school buildings are processed by professional engineers, NCREE has held many short courses to let engineers be familiar with all the needed information on the checklists which are relevant to upload the data of preliminary evaluation, detailed evaluation, and retrofit design with construction.

Fig. 3 The short course of seismic evaluation and retrofit design of school buildings

From March to November of 2009, NCREE has held 22 short courses on seismic evaluation and retrofit design of school buildings as shown in Fig. 3. A total of 2,075 engineers from all parts of Taiwan have attended these short courses. These short courses hoped to ease on the uploading works and proceed more successfully.

Conclusions

The elementary school buildings have considerable quantities and are located everywhere in Taiwan. Most often times, the school buildings play an important role as evacuation shelters in case of disaster reduction plans. The seismic design requirement for the school buildings is higher than the ordinary buildings of about 50%. Based from the observation of the seismic disaster of historical earthquakes the elementary school buildings have suffered tremendous damages than the ordinary buildings. The lack of seismic capacity for elementary school buildings is an important problem. This research aimed to assist the government officials of cities and counties to process the works on seismic upgrading of school buildings and collect the data of seismic evaluation and retrofit design. The seismic information web of school buildings is continuously maintained and is linked to governments, engineers and researchers.

As of November 26, 2009, the seismic information web of school buildings has been visited by more than 90,000 individuals. The collected data include more than 4,000 schools, simple survey data of 12,500 school buildings, preliminary evaluation data of 10,628 school buildings, detailed evaluation data of 1,815 school buildings, and retrofit design data of 186 school buildings.

References

內政部建築研究所，「嘉義瑞里地震建築災害調查報告書」，內政部建築研究所，台北，1998 年 8 月。

羅俊雄，「一九九九年九月二十一日台灣中部集集地震初步勘災報告(二)」，國家地震工程研究中心研究報告，NCREE-99-031，台北，1999 年 11 月。

蕭江碧，「九二一集集大地震全面勘災報告－建築物震害調查－」，國家地震工程研究中心研究報告，NCREE-99-054，台北，1999 年 11 月。

許丁友、鍾立來、廖文義、邱建國、簡文郁、周德光，「國民中小學典型校舍耐震能力初步評估法」，NCREE-03-049，台北，2003 年 12 月。

蘇耕立，「台灣中小學校舍結構耐震能力初步評估方法之探討」，台灣大碩士論文，台北，2008 年 7 月。

Guidelines for Seismic Upgrading of Public School Buildings in Taiwan

Tsung-Chih Chiou[1], Shyh-Jiann Hwang[2], Lap-Loi Chung[2], Wen-Yu Jean[3], Yeong-Kae Yeh[3], Wen-Cheng Shen[1], Pu-Wen Weng[1]

邱聰智 [1] 黃世建 [2] 鍾立來 [2] 簡文郁 [3] 葉勇凱 [3] 沈文成 [1] 翁樸文 [1]

Abstract

The Ministry of Education in Taiwan promotes the project regarding the renovation or rebuilding of elementary school, junior high school, state high school and vocational high school buildings and facilities from 2009 to 2012. The project, contracted by the National Center for Research on Earthquake Engineering (NCREE), includes four-stage strategy for screening with existing school buildings, which are seismic preliminary evaluation, detailed evaluation, retrofit design and retrofit implementation. In order to promote this project successfully, NCREE proposes a series of guidelines for stages of seismic detailed evaluation, retrofit design and retrofit implementation. Three guidelines, namely, “Guideline of Detailed Seismic Evaluation for Public School Buildings”, “Guideline of Seismic Retrofit Design for Public School Buildings”, and “Guideline of Retrofit Construction Supervision for Public School Buildings” are discussed in this report. Possible problems of concern posted by school administrators were also collected and are detailed in this report in modifying the proposed standards in the future.

Keywords: school building, seismic evaluation, retrofit design, construction supervision, guideline.

Introduction

Taiwan, located in a zone of frequent earthquakes and volcanic eruptions on the so-called Ring of Fire, has to constantly face the hazard of seismic effects. For instance, in the Chi-Chi earthquake, on Sep. 21, 1999, nearly half of school buildings in Nantuo County located in the central part of Taiwan were severely damaged. Recently, earthquakes with more than 6.5 in Richter Scale occur repeatedly in the Pacific Ring of Fire region, and cause human injuries and casualties with severe damage of buildings. In addition, the China’s Wenchuan earthquake on May 12, 2008, had caused more than 7,000 school buildings to collapse and a large toll of student casualties. Therefore, various mitigation measures on the aftermath of earthquakes have been paid much attention to in numerous studies and policies for the government.

The experiences gained during the major earthquake that hit Taiwan on September 21, 1999 and on the Sichuan earthquake in 2008, made clear to everyone the importance of ensuring that school buildings must be resistant to earthquakes, and had drawn attention to the problem of school buildings being old, decrepit and vulnerable to earthquake damage, and the potential threat they pose to the safety of students and teachers. This project has been formulated in line with the government's so-called “Plan for Expansion of Investment in Public Construction to Revitalize the Economy”, further aimed to speed up the renovation and rebuilding of old and decrepit public school buildings, so as to enhance their resistance to earthquakes and ensure the safety of both students and teachers, while also improving the overall school environment.

In this project, four-stage strategy in screening existing school buildings were established, namely, seismic preliminary evaluation, detailed evaluation,

[1] Assistant Research Fellow, National Center for Research on Earthquake
[2] Division Head, National Center for Research on Earthquake
[3] Research Fellow, National Center for Research on Earthquake

retrofit design, and retrofit implementation (see Fig. 1). With the task to seismically upgrade public school buildings, the Ministry of Education entrusts this project to the National Center for Research on Earthquake Engineering (NCREE) in establishing a data bank of seismic resistance of school buildings, so as to screen the vulnerability of buildings by preliminary evaluation data, and to sort the insufficient resistance by detailed evaluation data, and then to collect the results of retrofit deign and retrofit implementation.

In order to do this project successfully, NCREE proposed a series of guidelines for each stage of seismic detailed evaluation, retrofit design, and retrofit implementation. Each of the three guidelines provides operating standards, including procedure, rules, technique, peer review, and acceptance. In the following sections, the three guidelines, named as "Guideline of Detailed Seismic Evaluation for Public School Buildings", "Guideline of Seismic Retrofit Design for Public School Buildings", and "Guideline of Retrofit Construction Supervision for Public School Buildings", are briefly introduced.

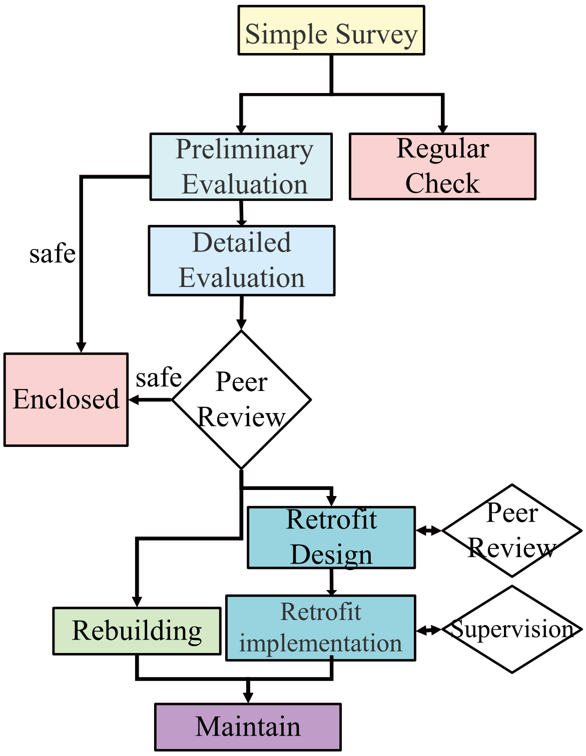

Fig. 1 Procedure of Seismic Upgrading for Public School Buildings

Guideline of Detailed Seismic Evaluation for Public School Buildings

This guideline aimed to evaluate accurately the seismic resistance of buildings, so as to sort the retrofitting method necessary in the future. The contents of this guideline include the following: Preface, Operating Procedures of Detailed Evaluation, Rules for Operating Procedure, Technical Items of Detailed Evaluation, Standard of Peer Review, and Acceptance Criteria.

■ **Operating Procedures of Detailed Evaluation**

This section shows the procedures of detailed evaluation, which indicates that the project will be managed from signing of contract to acceptance. Two examinations (peer reviews) will be held in this procedure. Finally, the evaluation result should be uploaded to the data bank. The whole procedure is shown in Fig. 2.

■ **Rules for Operating Procedure**

The rules for operating procedure include how to call examination committee, to apply uploading account, to participate in operating workshop, and to submit reports, etc.

■ **Technical Items of Detailed Evaluation**

This section discusses the technical items that provider needs to define, i.e. to make a record of user demand, to check the seismic importance factor, to choose the evaluation method, to define the seismic performance criteria, to finish the checking items of analysis, and to suggest two plans for retrofit, etc.

■ **Standard of Peer Review**

In here, the rules on how to establish the committee of peer review and of the procedure of peer review are defined. The standards for midterm and term examinations are also discussed.

■ **Acceptance Criteria**

To finalize the items required in the contract, the provider needs to upload the results of evaluation and submit a final report. The school managers will be encouraged then to check if the results of evaluation have been uploaded.

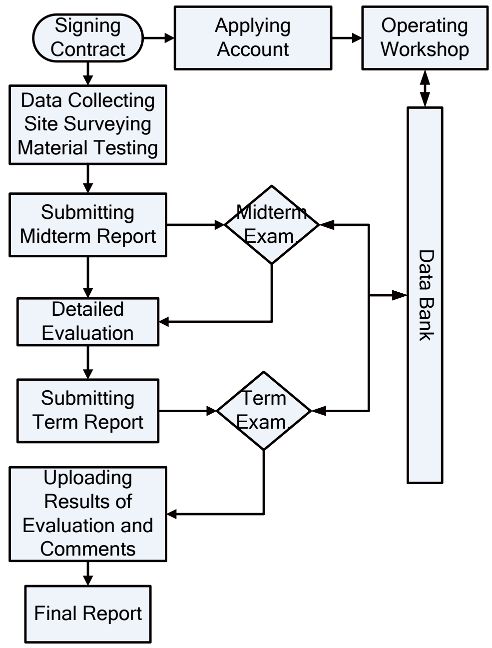

Fig. 2 Procedure of Detailed Seismic Evaluation

Guideline of Seismic Retrofit Design for Public School Buildings

This guideline aimed to effectively upgrade the seismic resistance of buildings by suitable retrofitting methods and at reasonable cost, so as to ensure the security of people using the building. The contents of this guideline include the following: Preface, Operating Procedure of Retrofit Design, Rules for Operating Procedure, Technical Items of Retrofit Design, Standard of Peer Review, and Acceptance Criteria.

■ Operating Procedure of Retrofit Design

This section shows the procedure of retrofit design. Two examinations (peer reviews) will be conducted in this procedure by the school chosen to support the session. After evaluation by NCREE, the plan of retrofit design can then pass the given examination. Finally, the designed plan should be uploaded to the data bank. The whole procedure is shown in Fig. 3.

■ Rules for Operating Procedure

The rules for operating procedure include how to call examination committee, to apply uploading account, to participate in operating workshop, to submit a report of basic plan, to finish detailed design and documentation of purchase order, and to administer supervision, etc.

■ Technical Items of Retrofit Design

This section indicates the technical items that provider needs to define, i.e. to carry out basic plan, to make a record of user demand, to carry out the seismic simulation of retrofitted structural modal, to check the seismic importance factor, to define the seismic performance criteria, to finish the checking items of analysis, and to choose the best plan for retrofit.

■ Standard of Peer Review

In this section, the rules on how to establish the committee of peer review, and of the procedure of peer review are defined. The standards for midterm and term examinations are also discussed.

■ Acceptance Criteria

In here, the provider needs to upload the details of design, to carry out the policy of energy-saving scheme and carbon reduction, and submit a final report. The school managers are also encouraged to check if the results of retrofit design have been uploaded.

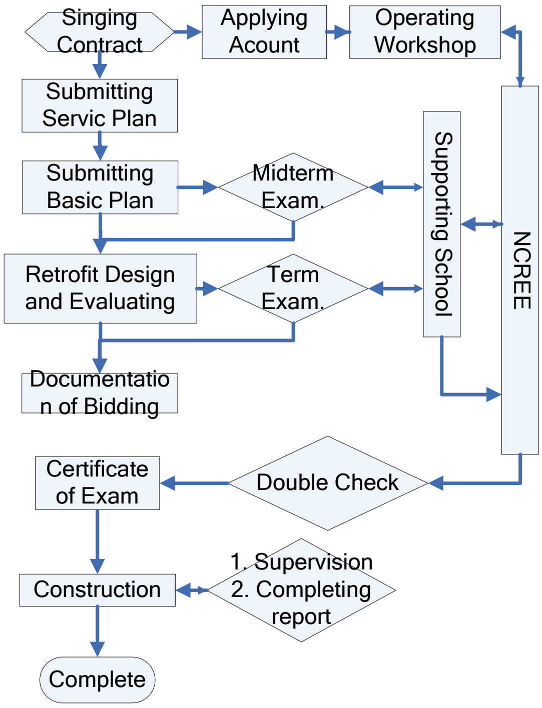

Fig. 3 Procedure of Seismic Retrofit Design

Guideline of Retrofit Construction Supervision for Public School Buildings

The whole procedure of seismic upgrading for school buildings includes seismic preliminary evaluation, detailed evaluation, retrofit design and retrofit implementation as shown in Fig. 1. However, the budget of retrofit implementation is over 90% of the total project cost thus, the quality of retrofit implementation is the key of the whole project.

This guideline aimed to ensure the quality of retrofitting construction, so as to guarantee teachers and students safety from disaster caused by earthquakes.

The policy on quality management of construction has been executed by the Government Procurement Act several years ago in Taiwan. All procurements of the retrofit implementation have to follow the “Operation Guidelines for Managing Construction Quality of Public Works”. Due to that the retrofit construction is more difficult than a new construction, and that the importance of retrofit explicitly relates to the security of teachers and students safety, the quality management of retrofit construction depends if the construction supervision can be exactly carried out in order to ensure that the construction absolutely conform to the design. Therefore, NCREE prescribed these Guidelines pursuant to the Guideline 18 of the “Operation Guidelines for Managing the Construction Quality of Public Works” amended and promulgated by the Executive Yuan Public Construction Commission (abbreviated as “PCC”).

Moreover, the content of this guideline includes

Preface, Authority and Duty of Supervised Operation, Rules for Operating Procedure, and Acceptance Criteria.

- **Authority and Duty of Supervised Operation**

This section shows the major serviced items of supervision unit and the relation of the authority and duty among agency, engineering design company, supervision unit and construction units.

- **Rules for Operating Procedure**

The rules in the supervised operating procedure includes: 1) The supervisor should execute operation on-site; 2) He shall examine the construction plan, quality plan, expected schedule, construction drawings, equipment samples and other items submitted by the supplier for examination; 3) He shall establish inspection hold points and obtaining samples for inspection on appropriate items in cooperation with the supplier; 4) He shall perform spot-checking on all of the retrofitting members one by one, and filling out spot check records; 5) The supervisor shall coordinate and integrate contract execution interface, if necessary, changing order of contract; 6) He shall take pictures or files of the key-point of work so as to be the evidences; 7) He shall supervise the execution of the following matters: site safety and hygiene, traffic maintenance, environmental protection, etc; 8) He shall examine the completion report submitted by the supplier; and, 9) He shall upload the completion report to the data bank (http://school.ncree.org.tw/school/).

- **Acceptance Criteria**

To execute the items in the contract, the supervision unit needs to examine the project completion report submitted by the supplier and have it uploaded on the website of the project (http://school.ncree.org.tw/school/). The agency is also encouraged to check if the results of completion report have been uploaded.

Conclusions

The guidelines serve as the operating standards for seismic upgrading of school buildings. Since the Ministry of Education published the guidelines in June, 2008, 9,000 buildings have finished preliminary evaluation, 2,250 buildings have finished detailed evaluation, about 500 buildings have finished retrofit design, and over 145 buildings have finished retrofit implementation as of January 2010.

In the course of executing this strategy for seismic upgrading of school buildings, all kinds of construction problems have been collected and discussed with the committee, which is composed of scholars, professional engineers, and officials. The guidelines will adopt the expert suggestions so as to solve the future problems and to speed up the renovation and rebuilding of old and decrepit public school buildings.

Preliminary Seismic Evaluation Method for Typical School Buildings in Taiwan

Keng-Li Su [1], Shyh-Jiann Hwang [2], Pu-Wen Weng[3], Tsung-Chih Chiou [3]

蘇耕立 [1]、黃世建 [2]、翁樸文 [3]、邱聰智 [3]

Abstract

Recent reconnaissance reports revealed that the low-rise reinforced concrete buildings were particularly vulnerable structures. School buildings are typical type of low-rise buildings. Although there are many researches about the seismic capacities of school buildings, in this research, three groups of model building based on true school building were established and then simplified pushover analysis was performed in calculating their seismic capacity. Also, the existing NCREE preliminary seismic evaluation method was used to analyze the same building model and corresponding comparison between preliminary seismic evaluation method and simplified pushover analysis has been made. Based on the results, recommendations were made to develop further the proposed preliminary seismic evaluation method.

Keywords: school building, preliminary seismic evaluation method, simplified pushover analysis, vertical element.

Introduction

On September 21, 1999, a major earthquake of 7.3 in Richter scale has devastated Taiwan and had caused heavy casualties and a great loss of properties. There were large numbers of low-rise reinforced concrete school buildings that had sustained severe damage or complete failure. In Taiwan, school buildings serve as place for students' classes on regular times and are turned into shelters for evacuees and rescue operations when such disaster happened. In order to make sure of the school building's function and perhaps to reduce its vulnerability to damage, the seismic capacity must be seriously considered. However, there are more than ten thousands school buildings in Taiwan. It is therefore necessary to develop a faster and simpler method to evaluate the seismic capacity of school buildings. In response, NCREE develops a preliminary seismic evaluation method. In this study, focus will be on modification of the existing parameters for the proposed evaluation.

Frame Analysis

In this research, analyses of a group of model buildings using NCREE's preliminary seismic evaluation method and simplified pushover analysis were done and comparison of results has been made. The model buildings also include the walls in the system.

NCREE's Preliminary Seismic Evaluation Method

The evaluation method[1] is based on "The seismic evaluation method for existing RC buildings" published by The Japan Building Disaster Prevention Association and "The seismic evaluation method for RC buildings" [2] from Prof. Tsai, I. C. The conditions of actual school buildings in Taiwan were also considered in the evaluation method. The basic seismic capacity can be derived based on the ratio of demand and supply. But the present conditions of the school buildings play an important role on the evaluation of their seismic capacities. The "Preliminary Seismic Evaluation Method" also accounts for structural modification factors. By combining the basic seismic capacity and the

[1] Research Assistant, National Center for Research on Earthquake Engineering.
[2] Professor, Department of Civil Engineering, National Taiwan University
[3] Assistant Researcher, National Center for Research on Earthquake Engineering.

structural modification factors, the seismic capacity index can be determined.

The main idea of the "Preliminary Seismic Evaluation Method" can be expressed as

$$\frac{V_{\mathbf{supply}}}{V_{demand}} \geq 1.0 \qquad (1)$$

where $V_{\mathbf{supply}}$ is the total shear force of the vertical member in the first floor, which is

$$V_{\text{supply}} = \beta(\tau_{BW4}A_{BW4} + \tau_{BW3}A_{BW3} + \tau_C A_C + \tau_{RCW}A_{RCW}) \qquad (2),$$

and τ_{BW4} is the ultimate unit shear force of four-sided confined brick wall, τ_{BW3} is the ultimate unit shear force of three-sided confined brick wall, τ_C is the ultimate unit shear force of RC column, τ_{RCW} is the ultimate unit shear force of RC wall. However, the stiffness of the member is totally different from each other, so the ultimate strength will not occur at the same time. In order to make the result closer to the real behavior of the structure, the reductive factor β adopted was 0.8, which is referred from, "The seismic evaluation method for existing RC buildings".

V_{demand} is from the seismic design code in Taiwan, which is defined as

$$V_{demand} = \frac{ZICW}{F_u} \qquad (3)$$

where Z is the seismic zone factor, I is the occupancy importance factor, C is the seismic force coefficient, W is the total dead load, and F_u is the reduction factor, $F_u = \sqrt{2R_a - 1}$.

$$\text{ZI} = \text{PGA} = \frac{\beta(\tau_{BW3}A_{BW3} + \tau_{BW4}A_{BW4} + \tau_c A_c + \tau_{\text{RCW}}A_{\text{RCW}})\sqrt{2\text{R}_a - 1}}{CW} \qquad (4)$$

The above formula represents the PGA evaluation of the NCREE's Preliminary Seismic Evaluation Method. In this study, PGA was considered the most important comparison point between the Preliminary Seismic Evaluation Method and the simplified pushover method.

2. Simplified pushover method

First of all, ordinary RC buildings usually have strong-beam-weak-column behavior, and the beam can be considered as a rigid body because they are confined by the floor slab. Summing up all the reasons, the deformation and shear force of the structure are all accounted for by the vertical members. Because of this, the pushover curve of the structure can be provided by the summation of load-deflection curves of all the vertical members. Tu and Tu (2005) suggested that the peak ground acceleration can be found in the demand spectrum.

The calculation of the load-deflection curve of RC column depends on different failure modes. Cindrawaty's (2007)[5] suggestion was used in this study, in which the failure mode of column was divided into four, namely: shear failure, flexural shear failure, flexural shear failure (transition zone), and flexural failure. The calculation of column load-deflection curve utilized the concept of soften strut-and-tie model, which can predict the behavior of RC column more correctly.

The calculation of load-deflection curve of RC wall in this study was referred from Ika Bali's research in 2006 of lateral force-displacement curve prediction of RC wall [6]. Considering the confinement of floor slab, most members experience double curvature deformation. Thus, this study applied this assumption in predicting the RC wall behavior.

The calculation of load-deflection curve of brick wall in this study was referred from the model provided by the Chen Y.H. (2003) [7] and from the brick wall code of Taiwan. All the assumed brick walls in this study were infilled after casting the three confined sides of brick wall.

In this study, the performance point was set at point where the strength reduced to 80% after the maximum base shear has occurred. The yield point was set at the cross point of the link of point of origin and 75% strength (before the maximum base shear has occurred) to the extended line of maximum base shear. The ductility of the structure can be calculated from performance point divided by yield point.

3. Model buildings

The model buildings were grouped to three kinds, namely: pure frame, frame with RC wall, and frame with brick wall. According to the data survey of school buildings in Taiwan, the school buildings can be classified whether there is corridor, column, or the span of one classroom. Typically, there are four classrooms in one floor. The pure frame model school building can be presented by combining all the different common characteristics of school buildings.

The cross-section of the RC column was obtained from the data survey of school buildings. So, to represent the typical school buildings in Taiwan, both the details and the cross-section of the RC column used in the model building were all based on real school buildings in the region. However, the data base do not have cases of RC wall and brick wall along the corridor, so assumption was necessary if the wall member was included in the scenario. Considering the possibility of the real situation, different wall quantities were included in this study. A total of 304 different kinds of model buildings were included.

Results and Comparison

Results of Analysis

The NCREE's Preliminary Seismic Evaluation method and the simplified pushover analysis method were both utilized to analyze those various types of model buildings. The results of analyses were compared to modify the PGA, the ultimate unit shear force, β, and R_a. In this research, the results are shown by the ratio of preliminary seismic evaluation method to simplified pushover analysis method such as the graphs in Fig. 1.

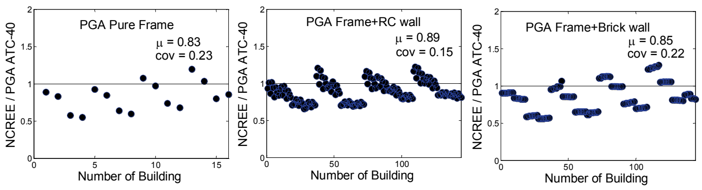

(a)Pure Frame (b)Frame with RC wall (c)Frame with brick wall

Fig. 1 Results of PGA ratio

The graphs show that NCREE's preliminary seismic evaluation method over- or under-estimates the seismic capacity of particular school building. It is because the axial load will make the ultimate column strength different. In this research, the columns were classified according to the following: classroom column, corridor column, and partition column in the brick wall. The graphs are used to find the relation between column types and storey.

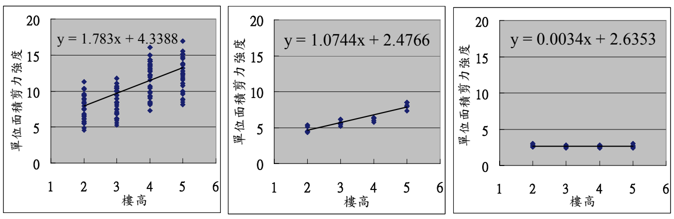

(a) Classroom Column (b) Corridor Column (c) Partition Column

Fig. 2 Relationship between column types and storey.

From the graphs in Fig. 2, the ultimate unit shear force of the three types of column are as follows:

$$\tau_{c(classroom)} = 1.8 \times story + 4 \qquad (5)$$

$$\tau_{c(carridor)} = 0.6 \times \tau_{c(classroom)} \qquad (6)$$

$$\tau_{c(partition)} = 2.6 \qquad (7)$$

In order to get a conservative result, the axial load has been ignored and it was assumed that the strength is controlled by flexure. The ultimate unit shear strength of RC wall was a fixed value, $\tau_{RCW} = 12\,kgf/cm^2$.

The ultimate shear strength of brick wall was determined according to the existing building code. The ultimate unit shear force of brick wall was $\tau_{BW3} = 2\,kgf/cm^2$ 。

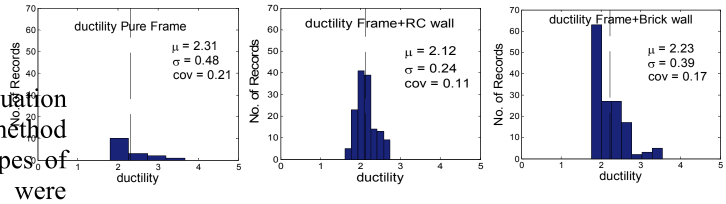

(a) Pure Frame (b) Frame with RC wall (c) Frame with brick wall

Fig. 3 Relationship between Model Building and Ductility

The graphs in Fig. 3 show that the ductility is well than the suggestion from existing preliminary seismic evaluation method. From the field test result, it can be observed that the school building has good ductility. Thus, ductility equal to 2.2 was suggested in this research.

Since the whole members in the building will have not reached the ultimate strength at the same time, the strength reduction factor, β, is needed. In this research, the strength reduction factor, β, is 0.9.

The existing preliminary seismic evaluation method used the unit weight of floor as 900 kgf/m^2 . According to the database, the unit weight of floor as suggested, for function story is 900 kgf/m^2 , for roof story is 750 kgf/m^2 .

Modification Result

After using the suggested values of the parameters in the analyses and comparing with the existing preliminary seismic evaluation method, the results are shown below.

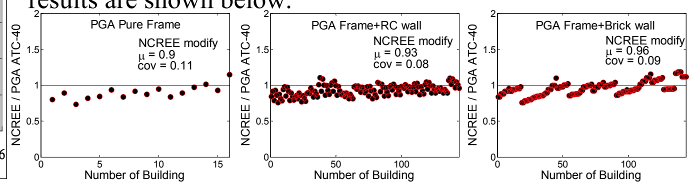

(a) Pure Frame (b) Frame with RC wall (c) Frame with brick wall

Fig. 4 Modification results of PGA Ratio

After modifying the method, the results show that the coefficient of variation is less than 0.11. Therefore, the analysis method has improved.

Conclusions

1. In the existing preliminary seismic evaluation method, the failure mode of column was pure shear failure. But the ultimate unit shear strength and the failure mode were different from the axial load. In this research, the columns were classified as classroom column, corridor column, and partition column in the brick wall. The modification results have improved the over- and under-estimation problem cause by different

storeys or different model buildings.

2. The unit shear strength of RC wall is according to the test result of RC wall frame in the laboratory. But most RC walls along the corridor in the existing building maybe a wing-wall. In order to get the conservative result, the axial load has been ignored and it was assumed that the strength is controlled by flexure. The ultimate unit shear strength of RC wall was a fixed value, $\tau_{RCW} = 12\,kgf/cm^2$.
3. The ultimate shear strength of brick wall is according to the existing building code, and the brick wall is a French style. The ultimate unit shear force of brick wall used was $\tau_{BW3} = 2\,kgf/cm^2$.
4. In this research, three types model buildings with different reduction factors were analyzed with reduction values of 0.9 to 0.99. For conservatism, the strength reduction factor, β adopted was 0.9.
5. In this study, the results on column analyses show that the failure modes are flexure failure. It means that the school buildings have well ductility. From the field test result, it can be observed also that the school buildings have well ductility. Therefore, ductility equal to 2.2 is hereby suggested.
6. According to the database, the unit weight of floor suggested are as follows: for function story is 900 kgf/m^2, and for roof story is 750 kgf/m^2.

References

1. Sheu, D. Y., Chung, L. L., Liao, W. I., Chiu, C. K., Chien, W. Y., Chow, T. K., ”Preliminary Seismic Evaluation Method for Typical Building Structures of Primary and Secondary Schools”, National Center for Research on Earthquake Engineering, NCREE-03-049, Taiwan, 2003.
2. Tsai, I. C., Huang, C. S., Tseng, Y. P., Chen, W. C., ‘Detailed Evaluation of the Seismic Capacity of a School Building with Considering Strengthening’, “Seismic Evaluation and Retrofit of Elementary School Buildings”, National Center for Research on Earthquake Engineering, Taiwan, 2000.
3. ATC, “Seismic Evaluation and Retrofit of Concrete Buildings,” ATC-40 Report, Applied Technology Council, Redwood City, California, SSC 96-01, Nov. , 1996.
4. Tu, Y. H., Tu, Y. S., “Seismic Evaluation of RC School Buildings with Simplified Pushover Analysis”, National Center for Research on Earthquake Engineering, NCREE-05-018, Taiwan, 2005.
5. Cindrawaty, L., “Seismic Capacity Assessment of Compulsory School Buildings in Taiwan”, master thesis，National Taiwan University of Science and Technology, Taiwan, 2007.
6. Ika Bali, “An Analytical Study of Lateral Load-Deflection Curves of Low-Rise RC Shear Walls and Its Application”, doctoral dissertation, National Taiwan University of Science and Technology, Taiwan, 2006.
7. Chen, Y. H., ”Seismic Evaluation of RC Buildings Infilled with Brick Walls”, doctoral dissertation, National Cheng Kung University, Taiwan, 2003.
8. Chen, Y. T., “Seismic Assessment of Compulsory School Buildings in Taiwan. “, master thesis, National Taiwan University of Science and Technology, Taiwan, 2006.

Seismic Evaluation of Reinforced Concrete Structure with Pushover Analysis

Yeong-Kae Yeh[1], Fu-Pei Hsiao[2], Wen-Cheng Shen[3],
Yao-Sheng Yang[4], and Shyh-Jiann Hwang[5]

葉勇凱[1]、蕭輔沛[2]、沈文成[3]、楊耀昇[4]、黃世建[5]

Abstract

This study utilized the capacity spectrum method suggested by ATC-40 to evaluate the seismic resistance of reinforced concrete buildings, and introduced a nonlinear analysis program as a tool to perform a precise seismic evaluation. The capacity spectrum curve is transferred from the relative curve of the base shear versus the roof displacement provided by a pushover analysis. From the pushover analysis, the seismic resistance of the structure is not only controlled by the strength but also by the deformation.

The National Center for Research on Earthquake Engineering (NCREE) had proceeded a series of static pushover experiments for school buildings, and this paper compared the experimental and analytical curves in order to verify the suggested seismic evaluation method. The results of analysis show that the proposed analytical method can simulate the strength and the actual seismic behavior of reinforced concrete buildings conservatively. Then, the seismic evaluation method suggested in this paper can provide engineers a way to perform more precise seismic evaluation.

Keywords: Seismic evaluation, pushover analysis, nonlinear hinge, ATC-40

Introduction

Taiwan is located in the so-called Circum-Pacific Ring of Fire where earthquake often occurs. Earthquakes are common experiences for people in Taiwan and being used to earthquakes they sometimes even ignore them. In the morning of September 21, 1999, the Chi-Chi earthquake awoke the people of Taiwan with its huge destruction. It taught the people regarding the importance of the seismic capacities of structures. The Chi-Chi earthquake caused nearly half of the school buildings in the central area of Taiwan to collapse or seriously damage. About 656 primary and secondary school buildings were damaged by the said earthquake. The disaster had taught the community regarding the seismic capacities of existing school buildings in Taiwan which are probably not sufficient. Due to the existence of windowsill in traditional school buildings, the short-column effect caused weak seismic capacity along the direction of the passage. Serious casualties and losses may result from the collapse of school buildings under strong earthquakes. To avoid or minimize casualties in the future earthquakes, studies on earthquakes are relevant in Taiwan. To retrofit the bad seismic performance of school buildings is one of the possible solutions to reduce the probable casualties. Before retrofitting possible low seismic capacity school buildings, their seismic capacities should be evaluated with a reliable method.

According to the capacity spectrum method proposed by ATC-40, the pushover analysis can be used to obtain the nonlinear-base-shear-to-roof -displacement relationship of school buildings which is termed as the capacity curve. The seismic capacity of buildings can be specified with the damage peak ground acceleration determined from the pushover

[1] Research Fellow, National Center for Research on Earthquake Engineering, ykyeh@ncree.org.tw
[2] Associate Research Fellow, National Center for Research on Earthquake Engineering, fphsiao@ncree.org.tw
[3] Assistant Research Fellow, National Center for Research on Earthquake Engineering, wcshen@ncree.org.tw
[4] Assistant Technologist, National Center for Research on Earthquake Engineering, yaosheng@ncree.org.tw
[5] Division Head, National Center for Research on Earthquake Engineering, sjhwang@ncree.org.tw

curve and the corresponding performance point. The accuracy of the pushover analysis is dependent on the well-defined properties of nonlinear hinges in structural elements. The load-deformation relationships of nonlinear hinges in beams and columns are discussed in this paper.

Pushover Analysis

The capacity curve from the pushover analysis is the foundation of the purposed detailed seismic evaluation method in this paper. Many commercial programs like ETABS and MIDAS can process nonlinear static analyses, also called as pushover analyses. The nonlinear response of a structure is restricted to nonlinear hinges assigned to the structural elements of the structure. These nonlinear hinges can be divided to three types: moment hinges, shear hinges, and axial hinges. As shown in Fig. 1, the mechanical parameters of a nonlinear hinge are constructed from the nonlinear part of the load-deformation curve of a structural member. For moment hinges, load Q is the moment M at the location of the moment hinge, and deformation Δ is the associated rotation angle θ of the moment hinge. For shear hinges, load Q is the lateral force V of the structural member, and deformation Δ is the associated lateral displacement δ_v of the structural member. For axial hinges, load Q is the axial force P of the structural member, and deformation Δ is the associated axial displacement δ_p of the structural member.

In the pushover analysis, the flexural rigidity of reinforced concrete beams was assumed as $0.35E_cI_g$ and the flexural rigidity of reinforced concrete columns was assumed as E_c, where $0.35E_cI_g$ is Young's modulus for concrete, and I_g is gross moment of inertia of the concrete section. In the following sections, the construction of nonlinear hinges for beams and columns are presented.

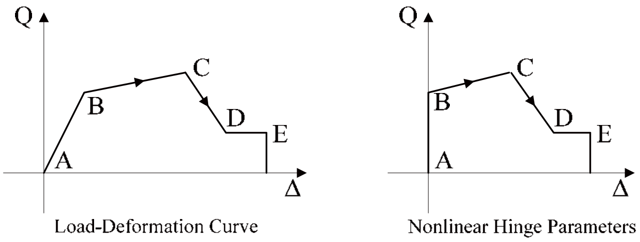

Fig. 1 Nonlinear hinge parameters

Nonlinear Hinges

Since the position of the inflection point on column or beam varies with the applied loading, the failure mode cannot be realized before the pushover analysis. Therefore, moment hinges can be set in each end of column or beam to present the flexure-shear failure mode or flexure failure mode in the pushover analysis. And shear hinge can be set in the middle of column or beam to present the shear failure mode in the pushover analysis. The engineers can define hinge properties based from data on research papers or experimental data with their experience. This paper referred on the previous lateral loading-displacement curves of column and beam, and suggestions were made to the parameters of moment hinges and shear hinges, which can serve as reference for research or design engineers. Figure 2 shows nonlinear hinge parameters of each structural component suggested in this research.

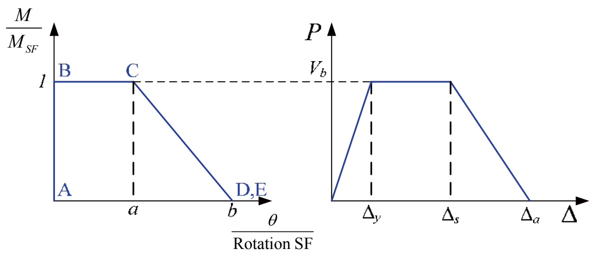

(a) Moment hinge property of RC column

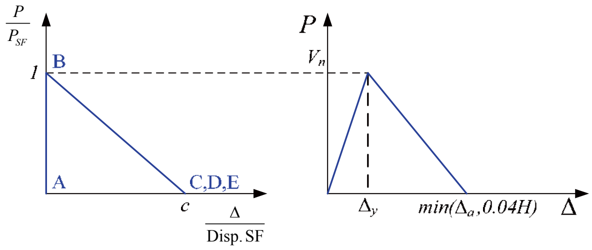

(b) Shear hinge property of RC column

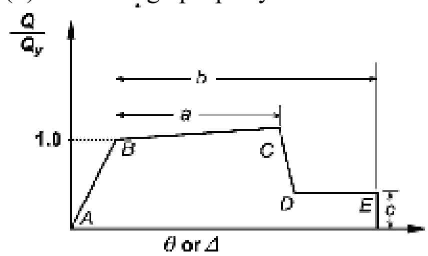

(c) Nonlinear hinge property of RC Beam suggested by ASCE 41-06

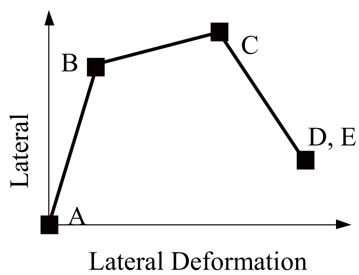

(d) Nonlinear hinge propriety of RC wall

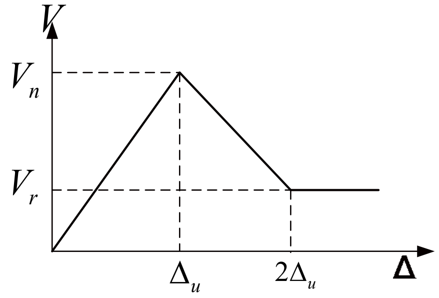

(e) Axial hinge propriety of brick wall
Fig. 2 Nonlinear hinge parameters of each structural components

Capacity Spectrum Method

The capacity spectrum method is a seismic evaluation method proposed by the Applied Technology Council in ATC-40. This method requires the derivation of the capacity curve, which can be obtained from the pushover analysis, showing the relationship of the base shear V and the roof displacement Δ_{roof} as shown in Fig. 3. To do the pushover analysis and to get the roof displacement, the numerical model of the building with nonlinear hinges was constructed, and the distribution of lateral forces as was specified as follows:

$$F_i = \left[w_i\phi_i \Big/ \sum_j w_j\phi_j \right] V \tag{1}$$

where V is the base shear; F_i is the lateral force at level i; w_i is the weight assigned to level i; and ϕ_i is the amplitude of the first mode at level i. For simplification, ϕ_i is equal to h_i the height of level i.

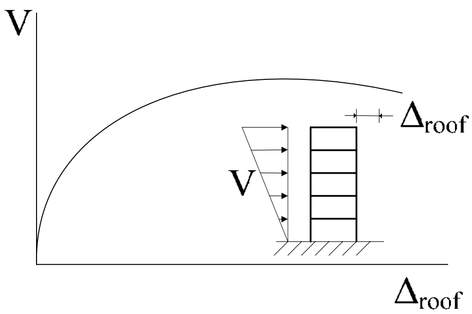

Fig. 3 Capacity curve

As shown in Fig. 4, based on the simulation of a single degree-of-freedom (DOF) oscillator, the capacity curve can be transferred into the capacity spectrum, which is the relation curve of the spectral acceleration and spectral displacement. The parameters needed in transferring the capacity curve to the capacity spectrum (S_a versus S_d) are as follows:

$$PF_1 = \sum_i w_i\phi_i \Big/ \sum_i w_i\phi_i^2 \tag{2}$$

$$\alpha_1 = \left[\sum_i w_i\phi_i \Big/ W \right] PF_1 \tag{3}$$

$$S_a = V/(\alpha_1 W) \tag{4}$$

$$S_d = \Delta_{roof} / PF_1 \tag{5}$$

where PF_1 is the modal participation factor for the first natural mode; α_1 is the modal mass coefficient for the first natural mode; W is the building dead weight plus likely live loads; Δ_{roof} is the roof displacement; S_a is the spectral acceleration; and S_d is the spectral displacement.

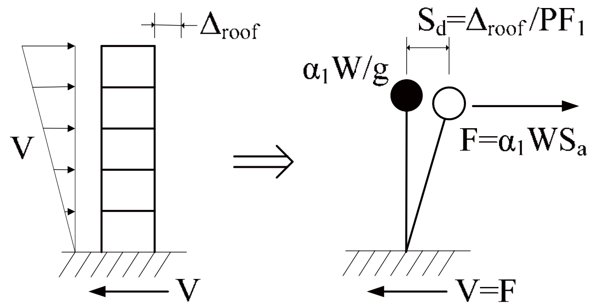

Fig. 4 Simulated single DOF oscillator

Based on the maximum allowable displacement, maximum allowable interstory drift ratio, failure of a vital structural element, or allowable degraded lateral strength, the performance point (d_p, a_p) can be set at the capacity spectrum. As shown in Fig. 5, this performance point also lies on a corresponding demand response spectrum reduced for nonlinear effects. At the performance point, the seismic capacity of the building is said equal to the seismic demand imposed on the building by the specified ground motion. The peak ground acceleration a_c of this specified ground motion can be used as a measure to specify the seismic capacity of the building.

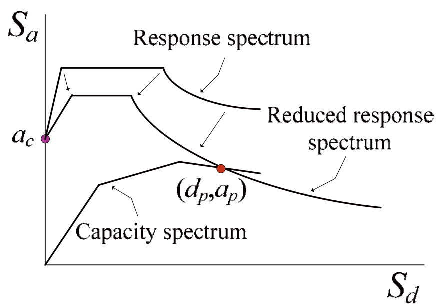

Fig. 5 Capacity spectrum and response spectrum

Comparison of Analytical and Test

Results

The research team of NCREE has hold several in situ tests of old school buildings in Taiwan, that includes Kou-Hu Elementary School, Sin-Chen Elementary School, Reui-Pu Elementary School, and Guan-Miao Elementary School, which is about to be demolished as have been the specimen of a pushover test. The specimen was tested by static lateral load and pushed to until it collapsed. The test results can be used to verify the seismic analysis model.

Figure 6 shows the comparison of analytical and experimental pushover curves of in situ test. The comparison shows that the analytical models provide conservative approximation of the pushover curve of the in situ test. In the figures, the negative slope of pushover cure has been modified by dynamic reduction factor.

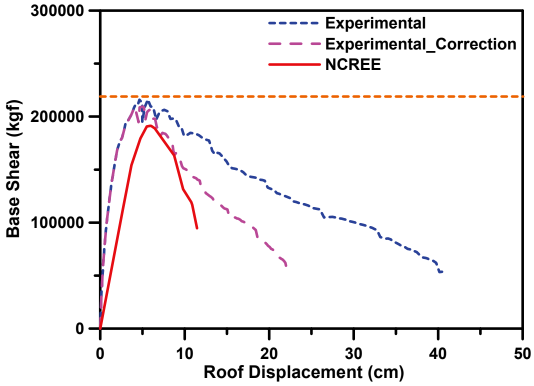

(a) Pushover curve of Kou-Hu Elementary School

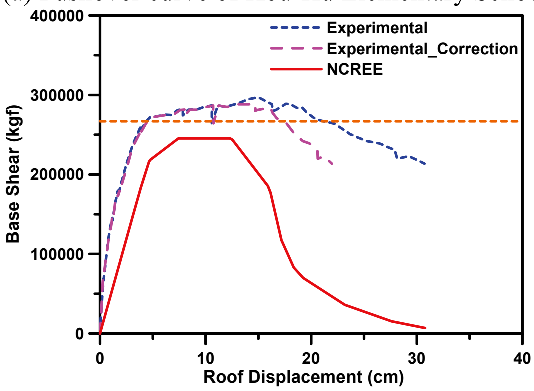

(b) Pushover curve of Sin-Chen Elementary School

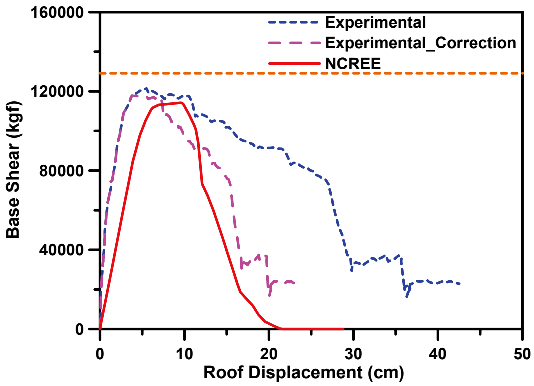

(c) Pushover curve of Reui-Pu Elementary School

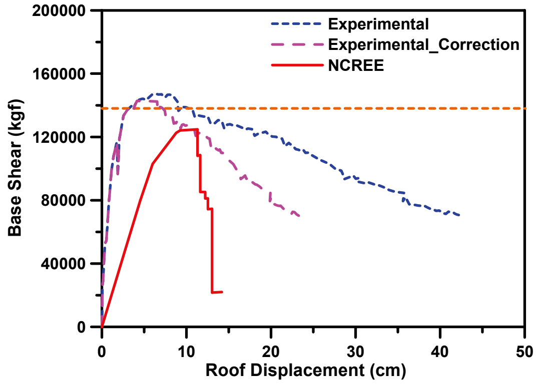

(d) Pushover curve of Guan-Miao elementary school

Fig. 6 Comparison of analytical and experimental pushover curves of in situ test

Conclusions

The detailed seismic evaluation method proposed in this paper can reasonably provide a measure to determine the seismic capacity of buildings. Through the verification made with the experiment data from in situ tests conducted by NCREE, the result from this study can provide a conservative approximation for RC school buildings. Therefore, the seismic evaluation process suggested herein can provide another sound way to evaluate precisely the seismic capacity of RC school buildings.

References

ATC (1996), Seismic Evaluation and Retrofit of Concrete Buildings, ATC-40 Report, Applied Technology Council, Redwood City, California, USA.

Elwood, K. J., and Moehle, J. P. (2005a), "Drift Capacity of Reinforced Concrete Columns with Light Transverse Reinforcement," Earthquake Spectra, Vol. 21, No. 1, pp. 71-89.

Elwood, K. J., and Moehle, J. P. (2005b), "Axial Capacity Model for Shear-Damaged Columns," ACI Structural Journal, Vol. 102, No. 4, pp. 578-587.

Test and Verification on Seismic Behavior of School Buildings

Lap-Loi Chung[1], Lai-Yun Wu[2], Chi-Hsiang Sun[3], Kuan-Hua Lien[3], Ming-Li Chang[3], Yao-Sheng Yang[3], Tsung-Chih Chiou[4], Yeong-Kae Yeh[1], Wen-Yu Jean[1], Te-Kuang Chow[4]

鍾立來 [1]、吳賴雲 [2]、孫啟祥 [3]、連冠華 [3]、張明禮 [3]、楊耀昇 [3]
邱聰智 [4]、葉勇凱 [1]、簡文郁 [1]、周德光 [4]

Abstract

Seismic performance of existing school buildings may not be sufficient based on the suggested approach of updated codes, thus development of evaluation techniques becomes timely and important. The criteria used to investigate the seismic behavior of buildings are suitable for structures with ductile design. Hence, they may not be valid for existing school buildings. In this paper, the criteria for the prediction of soft story, weak story, strong-column-weak-beam, column failure mode and joint failure for existing school buildings are studied based on experimental data. Further, the criteria for the prediction of strong-column-weak-beam and joint failure are modified to be more logical and consistent with experimental results.

Keywords: strong-column-weak-beam, nonductile structure, beam-column joint, seismic behavior

Introduction

The seismic behavior of existing school buildings is studied based on the experimental data of a full-scale, two-story and three-span reinforced concrete frame duplicated from a real school building. Soft story, weak story, strong-column-weak-beam, column failure mode and joint failure are predicted according to the criteria provided by the codes. The prediction results are then compared with the experimental ones. If difference between the results of prediction and experiment exists, modification of the criteria is proposed in this paper.

Experiments

The specimen was a full-scale, two-story and three-span reinforced concrete building structure with window sills made of bricks. The size of the frame and the detailing of the columns and beams are shown Figs. 1 and 2. By material tests, the concrete had a compressive strength of 191 kgf/cm^2, the bar No. 3 had a yielding strength of 3900 kgf/cm^2, the bar No. 6 3167 kgf/cm^2, and the bar No. 7 3701 kgf/cm^2. Axial force was applied on the top of each column by hydraulic jacks to simulate story weight. Columns C1 and C5 were loaded with 36.9 tonf, C2 and C6 42.8 tonf, C3 and C7 46.6 tonf, and C4 and C8 43.5 tonf. The numbering of columns, beams and joints is shown in Fig. 3. Cyclic loading was applied at the roof and the second floor by hydraulic actuators so that the lateral forces at the roof and the second floor was in the proportion of 2:1. After each cycle, the specimen was observed. (Chiou, et al., 2008).

The lateral displacements of the roof and the second floor at different extent of roof drift ratios are shown in Fig. 4. The hysteresis loops of the second and the first floor are ploted in Figs. 5 and 6, respectively. When the drift ratio of the roof reached 0.25%, the shear force of the second floor was 168.55kN and the story drift of the roof relative to

[1] Research Fellow, National Center for Research on Earthquake
[2] Professor, Department of Civil Engineering, National Taiwan University
[3] Student, Department of Civil Engineering, National Taiwan University
[4] Assistant Research Fellow, National Center for Research on Earthquake

the second floor was 6.64mm so the stiffness of the second floor was 25.38kN/mm. At the same time, the shear force and the story drift of the first floor were 246.21kN and 8.58mm, respectively, so the stiffness of first floor was 28.70kN/mm. The stiffness ratio of the first floor to the second floor was 113%. It indicated that no soft story was present in the specimen.

When the drift ratio of the roof reached 2.0%, the story drift of the roof relative to the second floor was 26.55mm and the story drift of the second floor relative to the first floor was 102.59mm. Therefore, almost all deformations had happened in the first floor whereas the second floor acted like a rigid body. In addition, most energy was dissipated by the first floor (Figs. 5 and 6). From these two points, weak story existed in the specimen.

As can be observed from the picture taken after the experiment (Fig. 7), the deformation of the specimen centralized at the first floor. The columns of the first floor were seriously damaged but no obvious cracks were on the beams, thus, the specimen had strong-beam-weak-column condition. In the early stage of the experiment, columns C6 and C7 (these two columns were constrained by window sills) had some flexural crack at their top and bottom. However, it turned to shear failure at the latter stage of the experiment. Therefore, the failure mode of C6 and C7 was flexural shear failure. Columns C5 and C8 had some flexural cracks at their top and bottom, thus the failure mode of C5 and C8 was flexural failure. Because of stress concentration, only joint 8 of the first floor had some small cracks at the concrete cover.

Prediction by Code

According to the Seismic Design Codes of Buildings (Ministry of Interior of Taiwan, 2005), the soft story is the story where the lateral stiffness is less than 70% of the story above; the extremely soft story is the story where the lateral stiffness less than 60% of the story above. The section and detailing of columns and beams for the first and second floors of the specimen were the same, so the lateral stiffnesses were the same too, then no soft story in the specimen according to the codes. From the results of experiment, the lateral stiffness ratio of the first floor to the second floor was 113% and no soft story existed. The prediction by codes agrees with the experimental results.

Moreover, according to the Seismic Design Codes of Buildings, the weak story is the story where the ratio of the ultimate shear strength to the design shear is less than 80% of the story above. The section and detailing of columns and beams in the first and second floors of the specimen were the same, so the ultimate shear strengths were the same. By the vertical distribution of earthquake forces, the first floor design shear was 1.5 times the second floor one. Therefore, the ratio of the ultimate shear strength to the design shear for the first floor is 67% that for the second floor. From the results of experiment, the story drift of the second floor was only 26% of the first story, so most of the deformation happened in the first floor. The ultimate shear strength of the first floor had been fully developed but not the second floor, so the first story was a weak story. The prediction by codes agrees with the experiment results.

According to ACI (ACI, 2005), the criterion of strong column and weak beam is

$$\sum M_{\mathrm{nc}} \geq 6/5 \sum M_{\mathrm{nb}} \tag{1}$$

where ΣM_{nc} is the sum of the nominal flexural strength of each column framing into joint with axial force taken into consideration; and ΣM_{nb} is the sum of the nominal moment strength of each beam framing into joint. Both joints 5 and 8 had two beams and one column. The summation of flexural strength of column was larger than 1.2 times the summation of flexural strength of beams, so joints 5 and 8 have strong-column-weak-beam condition (Table 1(a)). Both joints 6 and 7 had two beams and two columns, and the summation of flexural strength of columns was lower than 1.2 times the summation of flexural strength of beams, so joints 6 and 7 also have strong-beam-weak-column condition (Table 1(a)). As can be observed from the picture taken after the experiment (Fig. 7), all the columns of the first floor failed but not the beams, thus the specimen indeed experienced strong-beam-weak-column condition. The prediction of strong column and weak beam for joints 5 and 8 by codes was different from the experimental results. Because of weak story at the first floor, the strength of the columns in the second floor could not be developed. To be conservative, the strength of the columns in the second floor contributed to the joints are neglected. Therefore, if weak story exists, the strengths of the columns above are neglected in the prediction of strong column and weak beam. After a modification is proposed, the prediction agrees with the experimental results (Table 1(b)).

According to ACI, the shear strength V_{n} and flexural strength M_{n} of a column is calculated with the consideration of axial force. Dividing the flexural strength of the column by half of its clear height gives the lateral flexural strength V_{m} based on the assumption that the column deforms in double curvature. If the ratio of lateral flexural strength to shear strength is smaller than 0.6, the failure mode is flexural; if the ratio is between 0.6 and 1.0, the failure mode is flexural shear; if the ratio is larger than 1.0, the failure mode is shear (ASEC/SEI 41-06). According to this crtiteria, the failure mode is predicted to be flexural for columns C5 and C8, and flexural shear for columns C6 and C7. The prediction agrees with the experimental results (Table 2).

According to ACI, in strong-column-weak-beam situation, the beams develop flexural strength first.

When the beams reached the flexural strength, the tension forces of the longitudinal reinforcement and the shear forces of the columns are calculated. The difference between the sum of longitudingal reinforcement tension forces and the column shear force is the demand of the joint. If the demand is less than capacity of the joint, no joint failure occurs. For the case of the specimen, it exhibited strong-beam-weak-column condition. The procedures for the prediction of joint failure should be modified. The columns develop flexural strength first. The flexural strength is distributed to the beams according to stiffness. Similarly, the demand of the joint is calculated from the difference between the sum of reinforcement tension forces of beams and shear force of column. For both situations, strong-column-weak-beam and strong-beam-weak-column, no joint fails according to the predictions (Table 3) which match the experimental results. However, only the latter one is logical for the specimen.

Conclusions

The prediction of soft story, weak story and column failure mode by the codes agree with the experimental results. If weak story exists, the criterion of strong-column-weak-beam has to be modified such that the contribution of flexural strength by the columns above the weak story should not be taken into account. Consequently, a structure with weak story tends to exhibit a strong-beam-weak-column mode. If a structure satisfies the condition of strong-beam-weak-column, the beams have not developed their flexural strength even after column fails. Therefore, the demand of the joint is estimated at the moment when the columns reach their flexural strength.

References

Chiou, T.C., Yeh, Y.K., Chien, W.Y., Chung, L.L. & Chow, T.K. (2008). Design and Test on Seismic Retrofit for School Buildings. National Center for Research on Earthquake Engineering, Taiwan. NCREE 08-038:3-24.

Ministry of Interior of Taiwan (2005). Seismic Design Codes of Buildings, Taiwan.

ACI 318M-05 (2005). Building Code Requirements for Structural Concrete and Commentary.

American Society of Civil Engineers (ASCE), Seismic Rehabilitation of Existing Buildings, Report No. ASEC/SEI 41-06, Virginia, USA, 2007.

Table 1. Strong-column-weak-beam prediction

(a) by code

	5	6	7	8
$\sum M_{nc}$ (tf-m)	27.02	27.54	27.94	27.68
$6/5\sum M_{nb}$ (tf-m)	21.59	32.90	32.90	21.59
Strong Column Weak Beam or not	Yes	No	No	Yes

(b) proposed

	5	6	7	8
$\sum M_{nc}$ (tf-m)	13.51	13.77	13.97	13.84
$6/5\sum M_{nb}$ (tf-m)	21.59	32.90	32.90	21.59
Strong Column Weak Beam or not	No	No	No	No

Table 2. Prediction of column failure mode

	C1, C5	C2, C6	C3, C7	C4, C8
axial force N_u(tf)	36.9	42.8	46.6	43.5
flexural strength M_n(tf-m)	13.51	13.77	13.97	13.84
lateral flexural strength V_m(tf)	9.65	17.21	17.46	9.89
shear strength V_n (tf)	17.90	18.50	18.91	18.58
V_m / V_n	0.539	0.930	0.923	0.532
failure modes	flexural	flexural shear	flexural shear	flexural

Table 3. Prediction of joint failure

(a) by code

	5	6	7	8
M_{pr} (tf-m)	21.90	33.51	33.51	21.90
V_{col} (tf)	6.44	23.94	23.94	6.44
T_{beam} (tf)	45.37	68.05	68.05	45.37
$V_{ju\text{-}sc}$ (tf)	38.93	44.11	44.11	38.93
ϕV_n (tf)	68.72	68.72	68.72	68.72
check	OK	OK	OK	OK

(b) proposed

	5	6	7	8
V_{col}(tf)	9.65	17.11	17.64	9.89
M_{b1} (tf-m)	13.51	13.77	13.97	---
M_{b2} (tf-m)	---	13.77	13.97	13.84
T_{beam} (tf)	30.38	53.77	54.38	31.09
$V_{ju\text{-}sb}$ (tf)	20.73	36.66	36.74	21.20
ϕV_n (tf)	68.72	68.72	68.72	68.72
check	OK	OK	OK	OK

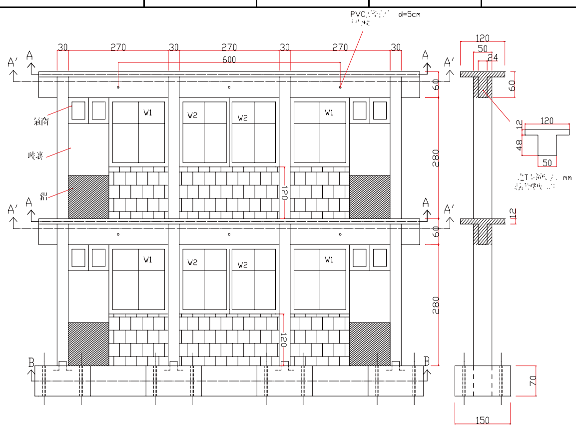

Fig. 1. Structural model

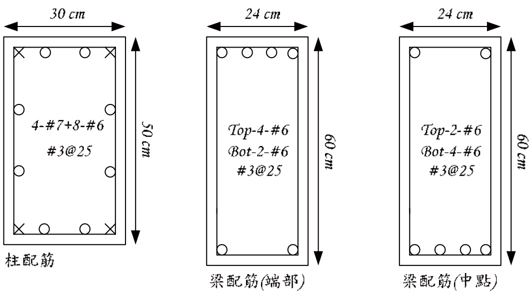

Fig. 2. Detailing of columns and beams

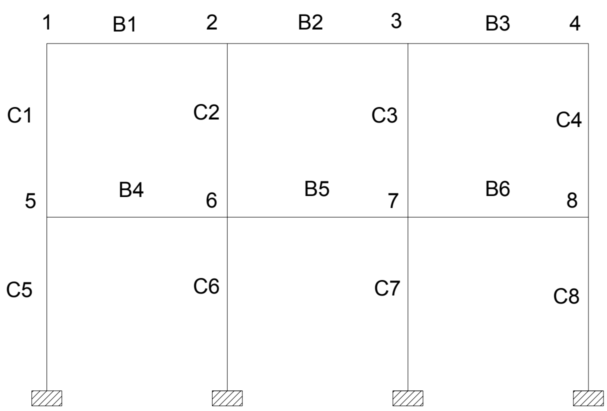

Fig. 3. Numbering of columns, beams and joints

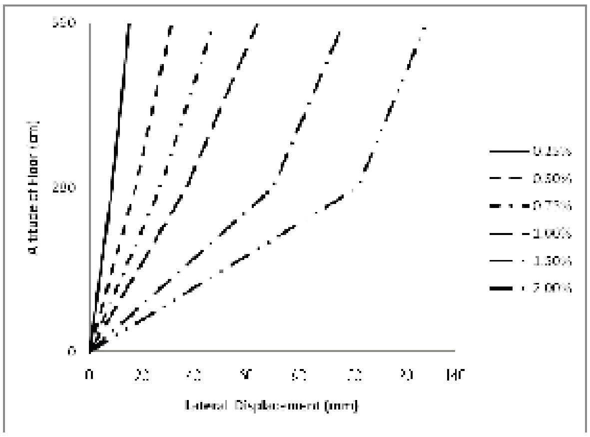

Fig. 4. Lateral displacements of floors

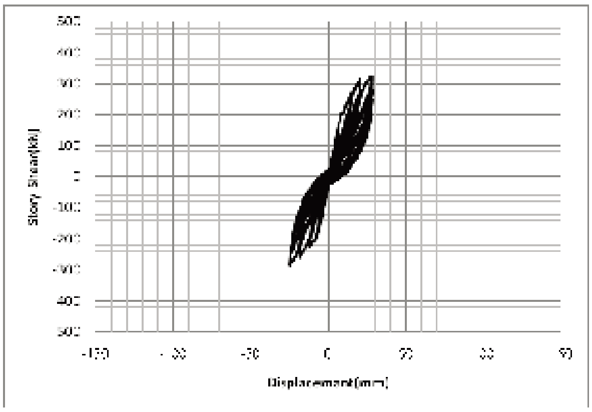

Fig. 5. Hysteresis loop of second Floor

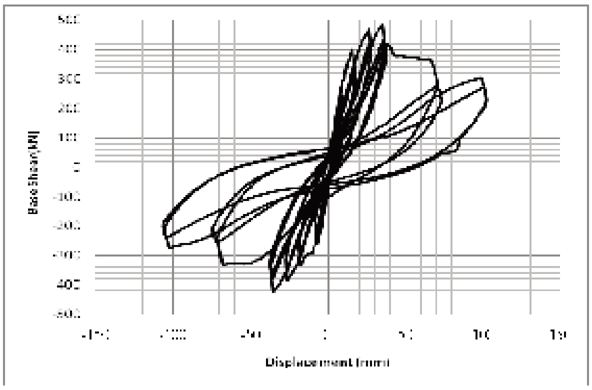

Fig. 6. Hysteresis loop of first Floor

Fig. 7. Final failure modes of specimen (displacement reset to zero)

Seismic Retrofitting Manual for Highway Bridges

Kuang-Yen Liu [1] and Kuo-Chun Chang [2]

劉光晏 [1]、張國鎮 [2]

Abstract

This paper presents a major revision of the Directorate General of Highways publication, the “Seismic Retrofitting Manual for Highway Bridges,” which was published by the Ministry of Transportation and Communications in 1999. The 2009 edition expands upon the previous publication by including procedures for performance-based seismic evaluation and retrofitting of bridges, as well as basic principles for evaluating and retrofitting scoured bridges with an exposed foundation structure. The revised manual maintains the basic format of the retrofitting process described in the 1999 manual. However, major changes were made to include current advances in earthquake engineering, field experience with retrofitting highway bridges, and the performance of bridges in recent earthquakes as well as in the 1999 Chi-Chi earthquake.

Keywords: near-fault ground motions, quasi-dynamic model, variable rupture velocities, 1992 Landers Earthquake,

Introduction

A major revision of the Directorate General of Highways publication, the “Seismic Retrofitting Manual for Highway Bridges,” which was published by the Ministry of Transportation and Communications in 1999 is detailed in this report. The 2009 edition expands upon the previous publication by including procedures for performance-based seismic evaluation and retrofitting of bridges, as well as basic principles for evaluating and retrofitting scoured bridges with an exposed foundation structure. The revised manual maintains the format of the retrofitting process described in the 1999 manual. However, major changes were made to include current advances in earthquake engineering, field experience with retrofitting highway bridges, and the performance of bridges in recent earthquakes as well as in the 1999 Chi-Chi earthquake. The revised manual is comprised of seven chapters and detailed in the succeeding paragraphs.

Chapter 1: Seismic retrofitting of highway bridges

Chapter 1 provides a complete overview of the retrofitting process including the philosophy of performance-based retrofitting, characterization of the seismic and geotechnical hazards, and summaries of recommended simplified and detailed assessment procedures, retrofit strategies, approaches and measures based on a system or component-by-component approach perspective. Performance levels PL0, PL1, PL2 and PL3 (refer to Table 1) are recommended according to bridge importance (see Table 2), safety, serviceability, and reparability (both short and long period), with a more rigorous performance being required for important, relatively new bridges (as detailed in Table 3), and a lower level for standard bridges (refer to Table 4). A higher level of performance is required for event of design earthquake than for the frequent earthquake. Table 5 shows the assessment methods according to the performance level and regularity. The topics in this chapter are detailed in the following six chapters.

Chapter 2: Seismic ground motion hazard

Chapter 2 characterizes the seismic and geotechnical hazards. Basically, the seismic demand is the same as the current manual, the “Seismic design specification of bridge structures”, published in 2009, except for disregarding the maximum considerable earthquake

[1] Associate Research Fellow, National Center for Research on Earthquake Engineering, kyliu@ncree.org.tw
[2] Director, National Center for Research on Earthquake Engineering, kcchang@ncree.org.tw

level with a 2500 return period.

Table 1 Performance matrix of the retrofitting bridge

Performance level	Safety	Serviceability	Reparability	
			Short period	Long period
PL3	Structure remains elastic and no unseating.	As same as prior to the earthquake	Simply repair	Regular repair
PL2	Limited damages and no unseating.	Repair in short time	Repair in short time by conventional approach	Repair in long time by conventional approach
PL1	Limited residual inelastic deformation and no unseating	Repair in short time with limited vehicle weight and speed	Replace or retrofit the damaged member	Close and partially rebuild the bridge
PL0	Collapse prevention and no unseating	Close and use alternative route	Tore down or partially rebuild	Tore down or partially rebuild

Table2 Important factor of the bridge

Bridge type	Importance factor
Highway bridge	1.2
Bridge is on the main route, or bridge is above important infrastructure, or bridge is the only one connection between two towns	1.2
others	1.0

Table3 Performance level for standard/regular bridge

Seismic hazard level	Published year of the Design Specification of highway bridge structures		
	1995 and 2000	1960 and 1987	Before 1960
Frequent earthquake	PL3	PL3	PL3
Design earthquake	PL2	PL1	PL0

Table4 Performance level for important bridge

Seismic hazard level	Published year of the Design Specification of highway bridge structures		
	1995 and 2000	1960 and 1987	Before 1960
Frequent earthquake	PL3	PL3	PL3
Design earthquake	PL2	PL1	PL1

Table5 Seismic assessment methods

Performance level	Regular bridge	Irregular bridge
PL3	Linear elastic/dynamic, or Nonlinear elastic/dynamic	Linear / Nonlinear dynamic
PL0, PL1, and PL2	Nonlinear elastic/dynamic	Nonlinear dynamic

Structural performance, especially nonlinear deformation capability, is mainly verified according to a design earthquake level with 475 return period, which is a design earthquake level corresponding to a peak ground acceleration of 0.4SDS; while the frequent earthquake level linearly reduces the force demand from the previous level by dividing it by 3.25. Retrofitted bridge should display good ductility under the design earthquake level and simultaneously remain elastic under the frequent earthquake level.

Chapter 3: Seismic simplified assessment methods and prioritization

Chapter 3 provides two simplified seismic assessment methods. Engineers are encouraged to carry out field investigations using the tables (Tables 6-7) provided in Method A to examine both the unseating probability and strength capacity of the bridge under study. Method B is an in-house task using fragility curve (Figs. 1-2) to determine the damage probability of a bridge in terms of collapse, severe, moderate, slight and no damage state for 12 kinds of bridges (Table 9). For method A, as shown in Table 8, there is no need to perform a detailed assessment if the score is smaller than 30 but it is mandatory to carry out a detailed assessment as described in Chapter 4 when the score is larger than 60. For the case whose score is between 30 and 60, engineers are also encouraged to do the detailed assessment to check the safety of the structure. The evaluation results from either method are applied to calculate the strength-ductility and falling index in prioritizing which bridge needs retrofitting.

Table 6 Method A - Screening table for unseating check

Item		Partition	Weight	Score
Environ-ment	Near fault	8	1/0	
	Soil category	4	1/0.67/0.33/0	
	Soil variation	2	1/0.67/0.33/0	
	Liquefaction	6	1/0.67/0.33/0	
Structural system	Difference between adjacent vibration unit	8	1/0.67/0.33/0	
	Outside cantilever with inner hinge	2	1	
	Skew angle	4	$\theta/90$	
	Slope	2	S/6	
	Curve	4	$\min(w_1, w_2)$ $w_1 = 1-(r/100)$ $w_2 = (\alpha/30)-1$	
	Foundation exposed condition	20	0~2	
Structural detail	Bearing condition	4	1/0.67/0.33/0	
	Unseating length	20	$w = \dfrac{N-N_e}{N/2} \le 1.0$	

	Unseating device	12	1/0.67/0.33/0	
	Others	4	1~4	

Table7 Method A - Screening table for strength capacity check

Item			Partition	Weight	Score
Environ-ment	Near Fault		8	1/0	
	Soil category		6	1/0.67/0.33/0	
	Liquefaction		6	1/0.67/0.33/0	
Structure system	Skew angle		4	0~1	
	Column aspect ratio		6	0~1	
	Column height ratio		4	0~1	
	Indeterminate		6	1/0.5/0	
	Foundation exposed condition		24	0~2	
Structural detail	Single /bent	Lap splice	8	1/0	
		Lateral reinforcement detailing	8	1/0.5/0	
		Cut off of longitudinal bars	4	1/0.5/0	
		Deterioration of column and foundation	8	1/0.67/0.33/0	
	Wall type	Lap splice	6	1/0	
		Longitudinal and transversal reinforcement ratio	8	1/0.5/0	
		Cut off of longitudinal bars	6	1/0.5/0	
		Deterioration of column and foundation	8	1/0.67/0.33/0	
	Steel column	Slender ratio of column steel plate	8	1/0.5/0	
		Thickness ratio of longitudinal stiffener	6	1/0	
		Location of man hole	6	1/0	
		Welding detail	8	1/0	
	Bearing condition and others		8	1	

Table8 Relationship between simplified and detailed assessment

Simplified assessment	Strength capacity or unseating		
Score	<30	30-60	>60
Require detailed assessment	No	Yes, Require detailed assessment	Yes, Require detailed assessment and retrofitting

Table9 Bridge type used in the Method B (fragility curve analysis)

Superstructure	Column	Seismic Design	Type
Simply supported	Single column	No	TYPE1C
		Yes	TYPE1S
	Column bent	No	TYPE2C
		Yes	TYPE2S
	wall	No	TYPE3C
		Yes	TYPE3S
Continuous	Single column	No	TYPE4C
		Yes	TYPE4S
	Column bent	No	TYPE5C
		Yes	TYPE5S
	wall	No	TYPE6C
		Yes	TYPE6S

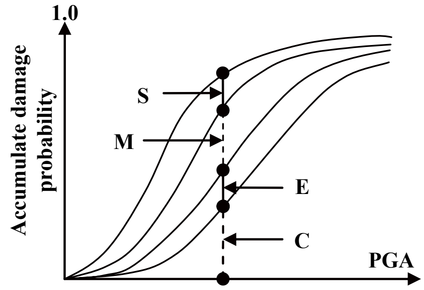

Fig.1 Fragility curve of the damaged bridge

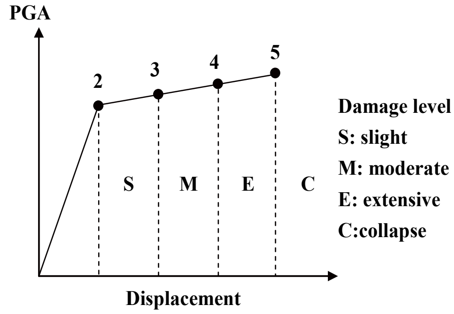

Fig. 2 Damage level

Chapter 4: Seismic detailed assessment methods for existing bridges

Chapter 4 discusses the modeling of the bridge in detail, for the superstructure, the bearing system, the substructure, and the foundation. The soil spring model for spread footings, pile foundations and caissons are also introduced since the soil profile is both required and important for any seismic evaluation. If the bridge foundations are located in the river, it is necessary to consider the scouring effect and exposed foundations. In order to estimate a reasonable behavior of the structure, the revised manual allows engineers to use either a linear static, nonlinear static, linear dynamic or nonlinear dynamic method according to the seismic hazard level and the regularity of the bridge. Among those four methods, the pushover analysis by the definition of plastic hinges shown in Fig.3 and the modified capacity spectrum method are proposed as the standard procedure to obtain the yielding and anticipated ultimate peak ground acceleration. It is recommended to apply the Kawashima model and the Mander model for bridges before and after retrofitting, respectively. The pushover curve (Fig.4) is transformed to capacity spectrum as recommend in the ATC-40, however, in stead of searching a performance point, in this manual, a revised ATC-40 procedure, without dealing with iteration and converge problem, is applied to obtain the peak ground acceleration corresponding to the top displacement of the column or girder. Since performance level, PL1 for example, has been selected as defined in Chapter1, if the PGA with respect to PL3 is smaller than SDS/3.25, the bridge need a strength retrofitting. In addition, if the seismic demand, 0.4SDS, is larger than the PGA of PL1, it is required to make ductility retrofitting.

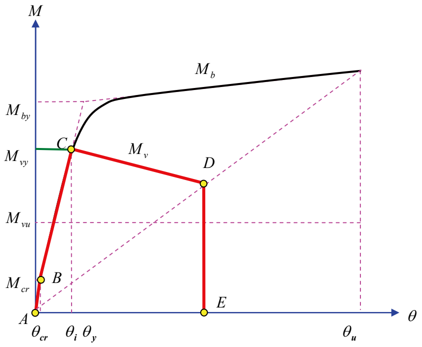

(a) shear failure

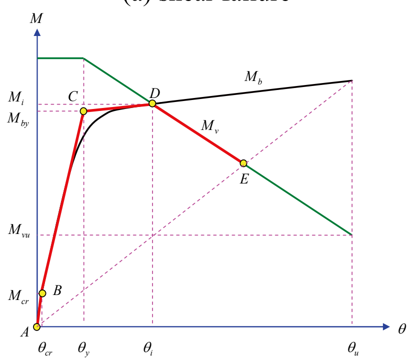

(b) flexural-shear failure

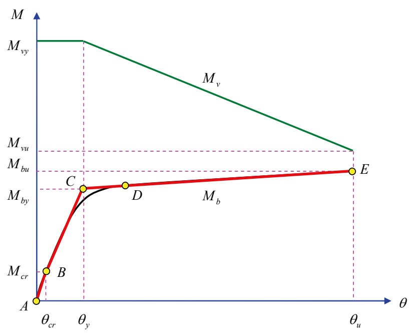

(c) flexural failure

Fig.3 Plastic hinge definition for RC column

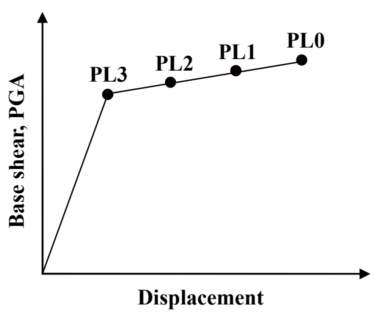

Fig.4 Pushover curve and performance curve

Chapter5: Seismic retrofitting by using system approach

Chapter 5 describes the approach to retrofit a complete bridge by following four methods: (1) equalize the inertial force distribution; (2) optimize the existing bearing system; (3) use isolation bearings; or (4) add dampers. In addition, it is important to avoid girders from falling. To prevent this, the unseating retrofitting method is introduced by extending the bearing-seat length on the cap beam if there is sufficient space, or by adding devices to prevent unseating, such as for example, restrainers connecting adjacent girders.

Chapter6: Seismic retrofitting by using component approach

Chapter 6 presents the component-by-component retrofitting approach. For the bridge columns, based on the ultimate strain theory, engineers can apply specific formulas as proposed in the notes of this manual to calculate the thickness for steel, FRP, and concrete jacketing. As a result, after retrofitting the shape of a rectangular column becomes an elliptical section to ensure that the confining stress can be developed. In addition, the design procedure for strengthening the footing can be found similar to that the design procedure referenced in the “Seismic Retrofitting Manual for Highway Structures” of the 2006, Federal Highway Administration publication. It is important to remind that the strength retrofitting of column often induces extra shear force to the foundation; therefore, adding piles or thickening the pile cap may be considered. Instead, to make a ductility retrofitting, there will be a gap between the jacketing and foundation so that to only provide the confinement on the column without inducing extra plastic shear force to the foundation.

Chapter7: Special issue on souring and exposed foundation

Chapter 7 deals with scouring-induced seismic safety evaluation and retrofitting measures. Considering the difficulties due to the variation in river channel and soil profiles, a simplified procedure using a reduction factor as a nonlinear function of the remaining length of the pile or caisson is proposed for a quick assessment of the structural performance.

References

Kuo-Chun Chang, Yi-Chao Tsai, Dyi-Wei Chang, Yu-Chi Sung, Wen-Yi Liao, Juin-Fu Chai, Hsiao-Hui Hung, Kuang-Yen Liu, Hung-Min Wu, Su-Ren Qi, Yen-Hao Chen, (2009). ″ Seismic assessment and retrofit manual for highway bridges,″ NCREE-09-028, Taipei, Taiwan.

Seismic Behavior of Bridges under Bilateral Loading Conditions II

Chi-Hung Lu [1], Kuang-Yen Liu [2] and Kuo-Chun Chang [3]

盧智宏 [1]、劉光晏 [2]、張國鎮 [3]

Abstract

This study presents a simplified approach to evaluate the displacement demand of the bridge with sliding rubber bearing system. A simplified approach is proposed based on the equivalent linear system and composite damping method to consider sliding of rubber bearing as an equivalent system damping for the whole structure. The analytical results revealed that the proposed approach can obtain good accuracy of the displacement evaluation by comparing the data from shaking table tests, especially for both the maximum and the residual displacements.

Keywords: displacement based design, equivalent linear system, bearing sliding/ friction, frictional force

Introduction

In 1999 Chi-Chi earthquake, out of 1,095 affected bridges, only seven bridges had collapsed due to surface rupture passing the bridge's location, while more than 90% of the bridges had suffered minor to none damage. It has been found based on numerical simulation and experimental studies that the sliding at the bearing provides an isolation effect to protect column from large plastic deformation. However, to deal with the friction behavior between rubber pads and bearing seat often requires more time to solve highly nonlinear equations. Therefore, a simplified approach is proposed based on the equivalent linear system and composite damping method to consider sliding of rubber bearing as an equivalent system damping for the whole structure.

Effective damping coefficient of bridge bearing considering sliding/friction mechanism

Figure 1 shows the force-displacement relationship of rubber bearing obtained from the friction coefficient tests. In practice, rubber bearings considering sliding/friction mechanism can be modeled as bilinear elements. Initial work on substitute-structure analysis was based on equating the energy adsorbed by hysteretic steady-state cyclic response to a given displacement level to the equivalent viscous damping of the substitute structure. This resulted in the following expression for the equivalent viscous damping coefficient:

$$\xi_{hyst} = \frac{A_h}{2\pi a_y D_{\max}} \tag{1}$$

where A_h is the area within one complete cycle of stabilized force-displacement response, and a_y and $D_{\max}$ are the maximum force and displacement achieved in the stabilized loops, respectively. The effective stiffness, defined as the secant slope of the peak-to-peak values in a hysteresis loop, is given by

$$K_{eff} = Q / D \tag{2}$$

where D is the anticipated bearing deformation and $Q = \mu N$ is the friction force between the rubber and concrete surface. The area of the hysteresis loop (the energy dissipated per cycle), W_D is given as

[1] Ph.D Candidate, National Taiwan University, Department of Civil Engineering, d93521020@ntu.edu.tw
[2] Associate Researcher, National Center for Research on Earthquake Engineering, kyliu@ncree.org.tw
[3] Director, National Center for Research on Earthquake Engineering, kcchang@ncree.org.tw

$$W_D = 4Q(D - D_y) \tag{3}$$

The effective damping ratio may be evaluated by

$$\xi_b = \frac{4Q(D - D_s)}{2\pi K_{eff} D^2} = \frac{2}{\pi} \times \frac{D - D_s}{D} \tag{4}$$

where D_s is the bearing deformation when the sliding/friction mechanism occurred.

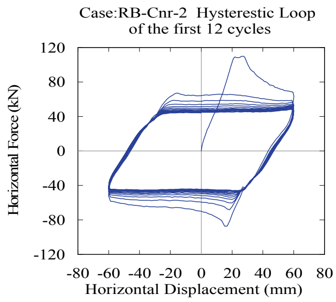

Fig.1 Hysteresis loop of a friction coefficient test (laminated rubber bearing on the concrete surface)

Linear theory of highway bridges with functional bearings

An elementary analysis for the purpose of gaining insight into the behavior of highway bridges considering bearing friction/sliding can be developed using a simple linear two-degree-of-freedom model with linear springs and linear viscous damping. Since the friction/sliding behavior is intrinsically non-linear, this analysis will be only approximate for such system, and the effective stiffness and damping will have to be estimated by some equivalent linearization process. The parameters of the model are shown in Figure 2.

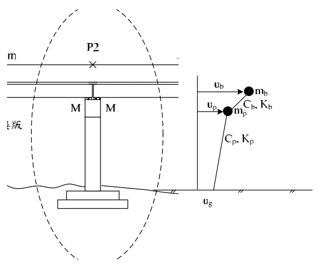

(a) Longitudinal direction

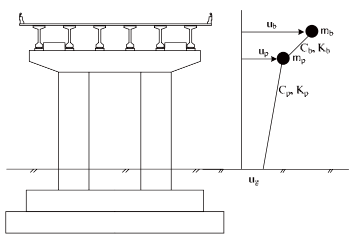

(b) Transverse direction

Fig. 2 Parameters of a simplified two degree-of-freedom bridge model

In this study, the analytical model was limited to the regular bridges such as those defined in the standard seismic design specifications of AASHTO. Bridges with abrupt changes of stiffness or mass distribution, large skew angle and intermediate expansion joints along their spans were excluded. It was assumed to be fixed at the column bases and the superstructure was presumed to be relatively rigid compared with the rubber bearings and the bridge bents.

The absolute equations of motion are:

$$m_b \ddot{u}_s = -c_b(\dot{u}_s - \dot{u}_p) - k_b(u_s - u_p) \tag{5}$$

$$m_b \ddot{u}_s + m_p \ddot{u}_p = -c_p(\dot{u}_p + \dot{u}_g) - k_p(u_p + u_g) \tag{6}$$

where m_b and m_p are the lumped masses of the bridge superstructure and substructure above and below the bridge bearing, respectively; k_p and k_b are the elastic stiffness of the bridge column and the effective stiffness of the bridge bearings, correspondingly; c_p and c_b are, respectively, the viscous damping coefficient of the bridge column and the equivalent viscous damping coefficient of the bridge bearing. For convenience, the following works with relative displacements:

$$v_b = u_s - u_g \quad \text{or} \quad u_s = v_b + u_g \tag{7}$$

$$v_p = u_p - u_g \quad \text{or} \quad u_p = v_p + u_g \tag{8}$$

where, v_p and v_s are the lateral displacements of the bent top and the bridge deck relative to the ground, respectively. In this, the equations of motion can be expressed as:

$$m_b \ddot{v}_b + (c_b \dot{v}_b - c_b \dot{v}_p) + (k_b v_b - k_b v_p) = -m_b \ddot{u}_g \tag{9}$$

$$m_p \ddot{v}_p + [-c_b \dot{v}_b + (c_b + c_p)\dot{v}_p] + [-k_b v_b + (k_b + k_s)v_s] = -m_p \ddot{u}_g \tag{10}$$

This two-degree-of-freedom system of equations can be solved directly or through modal decomposition. A modal analysis provides insight on the response of bridge system and the results will be applicable to more elaborate models. The equations (9) and (10) can be rewritten in the matrix form to develop the modes, frequencies and participation factors of the system:

$$[M]\{\ddot{V}\} + [C]\{\dot{V}\} + [K]\{V\} = -[M]\{r\}\ddot{u}_g \tag{11}$$

where

$$[M] = \begin{bmatrix} m_b & 0 \\ 0 & m_p \end{bmatrix}, \quad [C] = \begin{bmatrix} c_b & -c_b \\ -c_b & c_b + c_p \end{bmatrix}, \text{ and}$$

$$[K] = \begin{bmatrix} k_b & -k_b \\ -k_b & k_b + k_p \end{bmatrix} \tag{12-14}$$

$$\{V\}=\begin{Bmatrix} v_b \\ v_p \end{Bmatrix},\quad \{r\}=\begin{Bmatrix} 1 \\ 1 \end{Bmatrix} \tag{15)-(16}$$

Based on equation (11), the undamped natural frequencies and natural modes are given by:

$$([K]-\omega_n^2[M])\{\phi^n\}=0,\ n=1,2 \tag{17}$$

where, ω_n represents the natural frequencies ω_1 and ω_2 corresponding to the bearing mode and the structural model, and $\phi^n=\{\phi_b^n \quad \phi_p^n\}^T$ is the corresponding shape vectors. From equation (8) one can obtain the following:

$$-m_b\omega_n^2\phi_b^n+k_b\phi_b^n-k_b\phi_p^n=0 \tag{18}$$

$$-m_p\omega_n^2\phi_p^n-k_b\phi_b^n+(k_b+k_p)\phi_p^n=0 \tag{19}$$

And the following variables must be defined:

$$\omega_b^2=k_b/m_b,\quad \omega_p^2=k_p/(m_b+m_p),\ \gamma_m=m_p/(m_b+m_p)$$

$$\gamma_s=k_b/k_s,\quad \omega_b^2/\omega_s^2=\gamma_s/(1-\gamma_m) \tag{19)-(24}$$

where γ_m is the mass ratio obtained from the ratio of the lumped mass of the substructure below the bridge bearing to the sum of the lumped masses of the superstructure above the bridge bearing. Equations (18) and (19) can be rewritten, respectively, as

$$(\omega_b^2-\omega_n^2)\phi_b^n-\omega_b^2\phi_p^n=0 \tag{25}$$

$$(1-\gamma_m)\omega_b^2\phi_b^n+[\gamma_m\omega_n^2-(1-\gamma_m)\omega_b^2-\omega_p^2]\phi_p^n=0 \tag{26}$$

The characteristic equation for ω_n is

$$\gamma_m\omega_n^4-(\omega_b^2+\omega_p^2)\omega_n^2+\omega_b^2\omega_p^4=0 \tag{27}$$

Solving the above equation for the natural frequencies

$$\omega_{1,2}^2=\frac{(1-\gamma_m)}{\gamma_s}\frac{\left(1+\frac{\gamma_s}{1-\gamma_m}\right)\pm\left[\left(1+\frac{\gamma_s}{1-\gamma_m}\right)^2-\frac{4\gamma_m\gamma_s}{1-\gamma_m}\right]^{1/2}}{2\gamma_m}\omega_b^2 \tag{28}$$

The mode shape vectors corresponding to the bearing and structure modes are then determined, respectively, by

$$\{\phi^1\}=\begin{Bmatrix} 1 \\ 1-\alpha_1 \end{Bmatrix},\quad \{\phi^2\}=\begin{Bmatrix} 1 \\ 1-\alpha_2 \end{Bmatrix} \tag{29)-(30}$$

where $\alpha_1=\omega_1^2/\omega_b^2$ and $\alpha_2=\omega_2^2/\omega_b^2$. Using the approximate procedure [N], the transformation which diagonalizes the stiffness matrix is assumed to also be able to diagonalize the damping matrix. The generalized mass and damping coefficient matrices are expressed as

$$[M^*]=\{\phi^n\}^T[M]\{\phi^n\}=\begin{bmatrix} m_{11}^* & m_{12}^* \\ m_{21}^* & m_{22}^* \end{bmatrix}=\begin{bmatrix} m_b+(1-\alpha_1)^2m_p & 0 \\ 0 & m_b+(1-\alpha_2)^2m_p \end{bmatrix} \tag{31}$$

$$[C^*]=\{\phi^n\}^T[C]\{\phi^n\}=\begin{bmatrix} c_{11}^* & c_{12}^* \\ c_{21}^* & c_{22}^* \end{bmatrix}=\begin{bmatrix} \alpha_1^2c_b+(1-\alpha_1)^2c_p & 0 \\ 0 & \alpha_2^2c_b+(1-\alpha_2)^2c_p \end{bmatrix} \tag{32}$$

From the generalized masses and damping coefficients, the modal damping ratio are derived in the forms of

$$\xi_1=\frac{c_{11}^*}{2m_{11}^*\omega_1}=\frac{\alpha_1^2c_b+(1-\alpha_1)^2c_p}{2[m_b+(1-\alpha_1)^2m_p]\omega_1} \tag{33}$$

$$\xi_2=\frac{c_{22}^*}{2m_{22}^*\omega_2}=\frac{\alpha_2^2c_b+(1-\alpha_2)^2c_p}{2[m_b+(1-\alpha_2)^2m_p]\omega_2} \tag{34}$$

The viscous damping ratio of the bridge bearing ξ_b and the equivalent viscous damping ratio of the bridge column ξ_p are

$$\xi_b=\frac{c_b}{2m_b\omega_b},\quad \xi_p=\frac{c_p}{2(m_b+m_p)\omega_p} \tag{35)-(36}$$

Normally, for concrete substructures, the elastic damping ratio ξ_p is taken as 0.05, related to the critical damping. A lower value (typically 0.02) is often used for the steel substructures. Equations (33) and (34) are rewritten, respectively, as

$$\xi_1=\frac{\alpha_1^2(1-\gamma_m)\xi_b+(1-\alpha_1)^2\left(\frac{1-\gamma_m}{\gamma_s}\right)^{1/2}\xi_p}{\alpha_1^{1/2}[(1-\gamma_m)+(1-\alpha_1)^2\gamma_m]} \tag{37}$$

$$\xi_2=\frac{\alpha_2^2(1-\gamma_m)\xi_b+(1-\alpha_2)^2\left(\frac{1-\gamma_m}{\gamma_s}\right)^{1/2}\xi_p}{\alpha_2^{1/2}[(1-\gamma_m)+(1-\alpha_2)^2\gamma_m]} \tag{38}$$

The model participation factors L_1 and L_2 for the two modes are obtained by

$$L_1=\frac{\{\phi^1\}^T[M]c}{\{\phi^1\}^T[M]\{\phi^1\}}=\frac{(1-\gamma_m)+(1-\alpha_1)\gamma_m}{(1-\gamma_m)+(1-\alpha_1)^2\gamma_m} \tag{39}$$

$$L_2 = \frac{\{\phi^2\}^T[M]c}{\{\phi^2\}^T[M]\{\phi^2\}} = \frac{(1-\gamma_m)+(1-\alpha_2)\gamma_m}{(1-\gamma_m)+(1-\alpha_2)^2\gamma_m} \tag{40}$$

Thus, the basic matrix equation is reduced to the two equations below:

$$\ddot{q}_1 + 2\omega_1\xi_1\dot{q}_1 + \omega_1^2 q_1 = -L_1\ddot{u}_g \tag{41}$$

$$\ddot{q}_2 + 2\omega_2\xi_2\dot{q}_2 + \omega_2^2 q_2 = -L_2\ddot{u}_g \tag{42}$$

If the time history of the ground motion $\ddot{u}_g$ is known, then the modal components $q_1(t)$ and $q_2(t)$ can be calculated from the following:

$$q_1(t) = -\frac{L_1}{\omega_1}\int_0^t \ddot{u}_g(t-\tau)e^{-\xi_1\omega_1\tau}\sin(\omega_1\tau)d\tau \tag{43}$$

$$q_2(t) = -\frac{L_2}{\omega_2}\int_0^t \ddot{u}_g(t-\tau)e^{-\xi_2\omega_2\tau}\sin(\omega_2\tau)d\tau \tag{44}$$

Estimations of the maximum values of $q_1(t)$ and $q_2(t)$ are given by

$$|q_1|_{\max} = L_1 S_d(\omega_1,\xi_1) = L_1\frac{1}{\omega_1^2}S_a(\omega_1,\xi_1) \tag{45}$$

$$|q_2|_{\max} = L_2 S_d(\omega_2,\xi_2) = L_2\frac{1}{\omega_2^2}S_a(\omega_2,\xi_2) \tag{46}$$

Where, $S_d(\omega,\xi)$ and $S_a(\omega,\xi)$ are the displacement response spectrum and the acceleration design spectrum for the ground motion $\ddot{u}_g$ at frequency ω and damping ratio ξ, respectively. With these two modes, ϕ^1 and ϕ^2, we can write the relative displacements v_b and v_p in the form

$$v_b = q_1\phi_b^1 + q_2\phi_b^2\ ,\quad v_p = q_1\phi_p^1 + q_2\phi_p^2 \tag{47)-(48}$$

The predicted relative displacement maxima will be as follows:

$$|v_b|_{\max} = \left[(\phi_b^1 q_{1,\max})^2 + (\phi_b^2 q_{2,\max})^2\right]^{1/2} \tag{49}$$

$$|v_p|_{\max} = \left[(\phi_p^1 q_{1,\max})^2 + (\phi_p^2 q_{2,\max})^2\right]^{1/2} \tag{50}$$

Comparisons on the experimental study

The proposed equivalent linear theory was verified by the shaking table tests of a simply-supported bridge with one single span of RC deck and two steel column bents supported by four laminated rubber bearings, as shown in Fig. 3. Figure 4 shows the input ground acceleration, the East-West component of the record of 1949 EL-Centro earthquake. It has been found that the test results of maximum displacement of the column can be predicted well by the proposed method as shown in green line in Fig. 5 with PGA of 300, 500, and 700 gal, respectively.

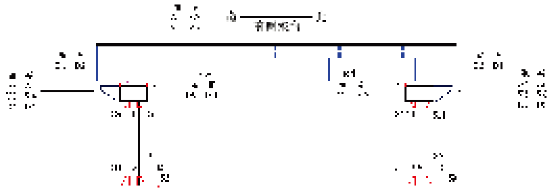

Fig.3 Test setup of the shaking table test

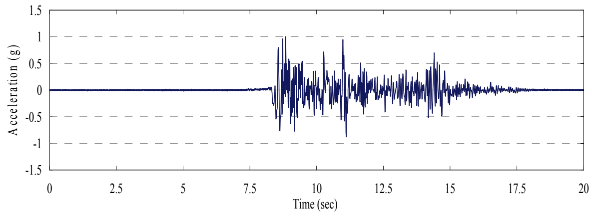

Fig.4 Input ground acceleration of EL-Centro earthquake (normalized to 1g)

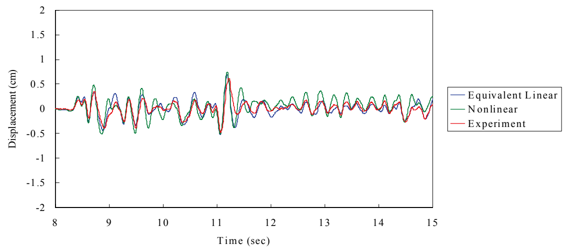

(a) PGA of 300gal

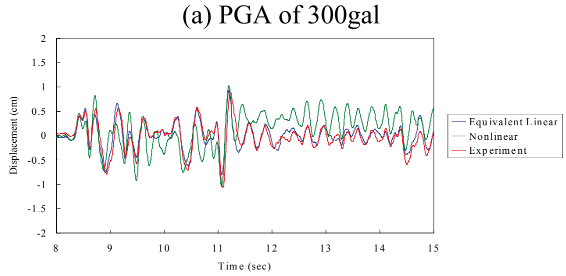

(b) PGA of 500gal

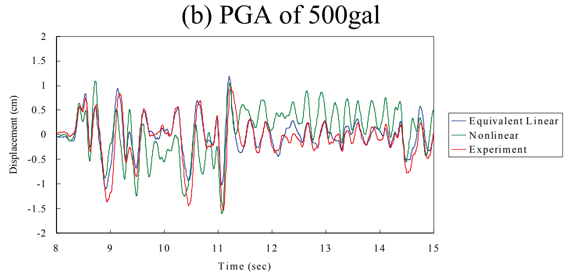

(c) PGA of 700gal

Fig.5 Comparison of the proposed method and test results from shaking table tests

References

Farzad Naeim and James M. Kelly, (1999). "Design of Seismic Isolated Structures from Theory to Practice,"John Wiley& Sons INC., New York.

Rocking Behavior of Bridge Piers with Spread Footing under Cyclic Loadings and Pseudo-dynamic Loadings

Hsiao-Hui Hung [1], Kuang-Yen Liu [2], and Kuo-Chun Chang [3]

洪曉慧 [1]、劉光晏 [2]、張國鎮 [3]

Abstract

From some of the actual engineering practices used in Taiwan, the size of spread footings was found to be exaggeratedly large due to the strict design provisions related to footing uplift. According to previous design code in Taiwan, the footing uplift involving separation of footing from subsoil is permitted only up to one-half of the foundation base area as the moment applied reaches the value of plastic moment capacity of the column. The reason for this provision is that rocking of spread footings is still not a favorable mechanism. However, recent researches have indicated that rocking itself may not be detrimental to seismic performance and in fact can act as a form of seismic isolation mechanism. In order to gain a better understanding of rocking, a series of rocking experiments were performed. Experimental data of six circular RC columns subjected to quasi-static and pseudo-dynamic loadings were presented. During the tests, columns were rested on a rubber pad to allow rocking to take place. Experimental variables included dimension of footings, strength and ductility capacity of columns, and level of the earthquake intensity applied. Results of each cyclic loading test were also compared with the benchmark test with fixed base condition. By comparing the experimental responses of specimen with different design details, the beneficial effect of rocking in reducing ductility and strength demand of columns was verified.

Keywords: rocking, cyclic loading test, pseudo-dynamic test, spread footing

Introduction

Some of the retrofitting works for actual engineering practices in Taiwan resulted to uneconomically large spread footings. This is due to the restriction of footing uplift regulated in the bridge design code. However, some researches have indicated that rocking itself can act as a form of isolation mechanism. Besides, unless the footing is very massive, some uplift on the tension edge of the spread footing during a major earthquake cannot be avoided. The analysis that is based on the assumption that footing and soil are firmly bonded to each other will show unreasonable large internal forces in columns. To retrofit or design columns and their footings based on these unreasonable large internal forces will dramatically increase the cost. Besides, the widening and strengthening of the footing to restrain footing from uplifting will also force the columns to sustain most of the seismic energy and thereby intensify the damage level to those columns. For these reasons, it is reasonable to tolerate a certain amount of uplift of the footing in design, especially for the retrofit design.

In the current design philosophy for new bridges based on strength design approach, the rocking mechanism of the footing is not allowed and is not taken into account in the analysis. This is because neglecting the effect of rocking will overestimate the seismic forces applied to the structures, and simply lean toward conservative side of design. However, with the ever growing interest in performance-based design approaches in recent years, the seismic performance becomes the key parameter for design; thus, the importance of a precise prediction of the

[1] Associate Research Fellow, National Center for Research on Earthquake Engineering, hhung@ncree.org.tw.
[2] Associate Research Fellow, National Center for Research on Earthquake Engineering, kyliu@ncree.org.tw
[3] Professor and Chairman, National Center for Research on Earthquake Engineering, kcchang@ncree.org.tw

seismic behavior of the structure is increasingly being recognized. Not considering the effect of rocking sometimes underestimates the disadvantages that may be brought by rocking, such as large lateral displacements of the deck and permanent settlement in soils, and then leans toward unsafe design. Therefore, realistically taking the effect of rocking into consideration, including the interaction among foundation, column and soil, has gradually become an important issue.

The seismic isolation effect of the rocking mechanism has been identified in many previous researches since the pioneer work performed by Housner (1963). Over the following few decades, several other articles were published on the study of rocking. Most of these earlier studies were performed by analytical approach. Recently, with the advances in experimental technique, rocking experiments became the focus of several studies, including series of tests performed on a large centrifuge by Gajan et al. (2008) and tests performed on a shaking table by Espinoza and Mahin (2006). All of these previous studies recognized the beneficial effect of rocking. However, few of them considered the coupling effect of the material nonlinearity involved with column plastic hinging and the geometrical nonlinearity resulted from footing uplift. In order to have a better understanding about the rocking mode and its role on the overall behavior of a bridge, more experimental data are still required. Therefore, in this study, six circular RC columns with different design details were constructed and subjected to a series of rocking experiments.

Simple Calculation for Rocking

In order to ensure that the objectives of the current study are possible prior to the design and construction of the experimental specimens, the basic theory on rocking mechanism was studied and a simple calculation was performed. For a column with a spread footing standing on soils, the footing will lift off the ground once its moment of resistance provided by gravity is overcome. Thus, the base moment of the foundation can be limited to the value required to induce uplift against the restraining forces due to gravity. By assuming that the underlying soil is a perfect plastic material with an ultimate stress of q_u, according to the force equilibrium, the limit value of the moment of a rigid foundation can be written as

$$M_2 = \frac{BW_T}{2}(1 - q / q_u) \qquad (1)$$

where B is the width of the footing in the direction of the bending; W_T is the total axial load applied to the footing base; q is the contact stress under the footing and equal to W_T /BL, in which L denotes the length of the footing. If we further assume that the ultimate stress of q_u is far larger than q, then the value of q/q_u in Eq. (1) can be omitted and the limit value depends only on the footing size and the total vertical force of gravity. This limitation of moment also implies that if the footing of a column is allowed to rock, the shear force and bending moment that the column has to sustain will also have an upper limit value. These upper limit values can be derived from value M_2,

$$V = \frac{M_2}{H} = \frac{BW_T}{2H}\ ; \quad M = V(H-h) = \frac{BW_T}{2H}(H-h) \qquad (2)$$

where H is the distance from the footing base to where the lateral force applied, and h is the height of the footing. Obviously, the ratio of the moment capacity of the column to the upper limit moment calculated in Eq. (2) is the key parameter for the seismic performance of the column with a spread footing.

Experimental Program

Based on the simple calculation shown in the previous section, six RC columns with two types of footing size and three types of design details in column were designed and constructed. As shown in Fig. 1, these circular columns were all 50 cm in diameter with a clear height of 2.5m and a height of footing 0.5m. Their footing sizes were either B = 140m or B = 170m. Thus, according to Eq. (2), the corresponding upper limit values of bending moment for specimens with B = 140cm (W_T= 574 kN) and B = 170 cm (W_T= 585 kN) are M= 334.8 kN-m and M = 414.4 kN-m, respectively. In order to compare the seismic performance of specimens with different ratios of the moment capacity to the upper limit moment, these test columns were reinforced with three types of design details. One with 12-D19 main reinforcements was transversely reinforced with D13 perimeter hoops spaced at 9 cm (ρ_s = 0.012), corresponding to a case with sufficient transverse reinforcements. The other two with 18-D19 main reinforcements were transversely reinforced with D13 hoops spaced at 9 cm and 18 cm, respectively. The one with the transverse reinforcements spaced at 18 cm on center represents a column with an insufficient volumetric confinement ratio (ρ_s = 0.006). The nominated material properties for these specimens are as follows: concrete compressive strength $f_c^{'}$=280 kg/cm^2; yield strength of main reinforcements F_y=4200 kg/cm^2; yield strength of transverse reinforcements F_{yh}=2800 kg/cm^2. Based on the nominated material properties, the moment strength for these specimens was also calculated. The effective yield moments for specimens with 18-D19 and 12-D19 main reinforcements are 428.3 kN-m and 329.0 kN-m, respectively.

With the combination of different footing size and design details, a total of six test columns were designed and named as CD40FS-R, CB40FS-R, CD30FS-R, CD40FB-R, CD30FB-R and CD30FB-F, as plotted in Fig. 1 and listed in Table 1. In which, characters “FS” and “FB” denote cases with a footing of smaller size (B = 140 m) and of larger size (B = 170 m), respectively. Numbers “40” and ”30” denote cases with 18-D19 and 12-D19 main reinforcements, respectively; characters “CD” and “CB” denote columns transversely reinforced with perimeter hoops spaced 9 cm and 18 cm, respectively; while "R" and "F" represent rocking base condition and fixed base condition, respectively. As such, the ratios of the moment capacity of the column to the upper limit moment M for CD40FS-R, CD40FB-R, CD30FS-R and CD30FB-R are 1.28, 1.03, 0.98 and 0.79, respectively. Specimen CB40FS-R has the same ratio as CD40FS-R.

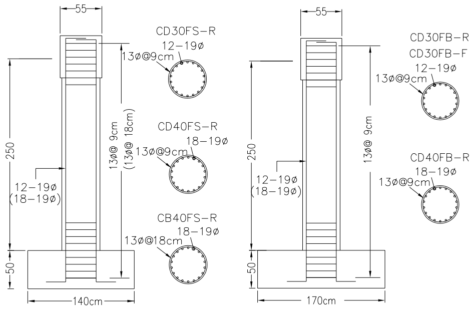

Fig. 1 As-built details of model columns

Both tests with and without the footing uplift restraint were conducted. In the case where the rocking mechanism was considered, the footings were rested on a 10 cm thick neoprene pad to simulate a spread footing standing on stiff soils. During the test, an axial load of 539 kN was applied to the test column through a tap beam to model the tributary dead load of the deck. One horizontal actuator was used to apply the lateral force to the column's top to simulate the seismic loading. The location of the applied force was 3 m from the footing base.

Table 1 Experimental test schedule

Test Specimens	Base condition	Tests
CD40FS-R	Rocking base	pseudo-dynamic tests
		cyclic loading test
	Fixed base	cyclic loading test
CD30FS-R	Rocking base	pseudo-dynamic tests
		cyclic loading test
CD40FB-R	Rocking base	pseudo-dynamic tests
		cyclic loading test
CD30FB-R	Rocking base	pseudo-dynamic tests
		cyclic loading test
CB40FS-R	Rocking base	cyclic loading test
	Fixed base	cyclic loading test
CD30FB-F	Fixed base	cyclic loading test

The test schedule is also listed in Table 1, which includes pseudo-dynamic loading test and cyclic loading test. The input ground motions for pseudo-dynamic test were two artificial earthquake accelerations. One was a code compatible medium earthquake (TH1) and the other was a code compatible design earthquake (TH2) for Nantou Pouli in Taiwan. The cyclic loading tests were performed under displacement control to a drift ratio of 7%.

Test Results and Discussions

First, specimens CD40FS-R, CD30FS-R, CD40FB-R and CD30FB-R were supported on a neoprene pad without uplift restraint and subjected to the pseudo-dynamic test of TH1. Results indicate that the uplift of footing was not significant and the plastic hinge was not formed while the columns experienced a minor earthquake; thus their results were not shown here. After the pseudo-dynamic test of TH1, these four specimens were subjected to another pseudo-dynamic test of TH2. The experimental results of the lateral force versus the lateral displacement curves and the moment versus the rotation curves are plotted in Figs. 2(a) and (b), respectively. In these moment-rotation curves, the rotations were obtained by taking the reading of the highest tiltmeter mounted on the column minus the reading of another tiltmeter mounted on the footing. Thus, the rotations in Fig. (b) were from the elastic and plastic flexure of the column only; whereas the lateral displacements given in Fig. (a) were from the elastic and plastic flexure of the column plus the rocking of the footing. By observing Fig. 2, it is evident that under the presence of a design earthquake, the plastic deformation of the columns was still not noticeable. However, at the same time, some uplift behavior already occurred since the force-displacement curves are not linear anymore yet shows a softer stiffness as the displacement increases.

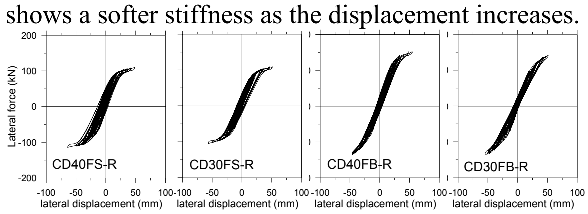

(a) Lateral load vs. displacement curves

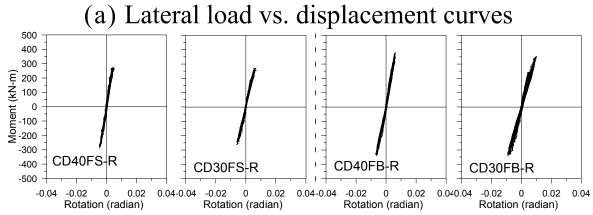

(b) Moment vs. rotation at column base.

Fig. 2 Results for pseudo-dynamic test of TH2

After the pseudo-dynamic tests, a total of eight cyclic loading tests were performed. Figs. 3-4 show the experimental results for specimens with 18-D19 main reinforcements. In these figures, the results for fixed base cases of CD40FS-F and CB40FS-F can signify the capacity of columns, as well as represent cases with massive footings. By comparing the results of CD40FS-F, CD40FB-R and CD40FS-R, it is noted that the rocking behavior becomes more pronounced as the dimension of footing decreases. Also, the maximum value of lateral forces that the column sustained decreases with the decrease in footing size. These corresponding maximum values for CD40FB-R and CD40FS-R shown in Fig. 3(a) are, respectively, around V = 160 kN and V = 130 kN. These values are close to the upper limit values calculated by Eq. (2). Besides, the maximum value of the bending moment that the column sustained decreases too, as shown in Fig. 3(b). Because the maximum values of moment sustained by CD40FB-R and CD40FS-R are less than the moment capacity of columns indicated by CD40FS-F, the moment-rotation curves for both

CD40FB-R and CD40FS-R are almost linear, implying that not much plastic deformation occurred in columns. As for the cases shown in Fig. 4 with insufficient transverse reinforcements, CB40FS-F is the benchmark test for CB40FB-R. For the rocking case of CB40FS-R, results show that the seismic force the column sustained was limited to an almost constant value around M = 320 kN-m. Because this maximum value of bending moment sustained by the column was lower than its moment capacity indicated by CB40FS-F, the corresponding moment-rotation curve shown in Fig. (b) for CB40FS-R are almost linear. Another trend which can be observed in Figs. 3 and 4 is that the response behaviors of CD40FS-R and CB40FS-R are similar, even though the responses of CD40FS-F and CB40FS-F are different. This result confirms that the ductility demand of a column can be reduced if its upper limit value of moment due to rocking is lower than the moment capacity of the column.

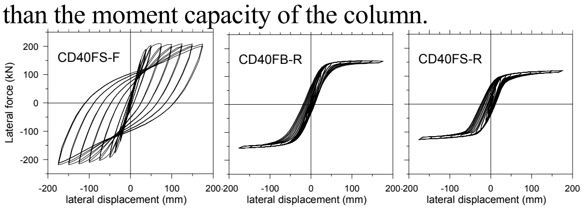

(a) Lateral load vs. displacement curves

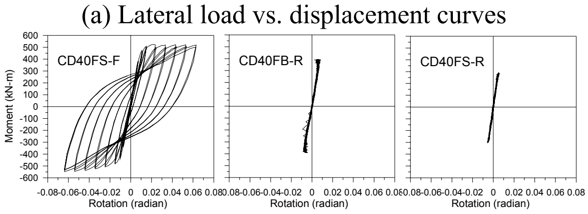

(b) Moment vs. rotation at column base.

Fig. 3 Results for cyclic loading tests for CD40xx-x

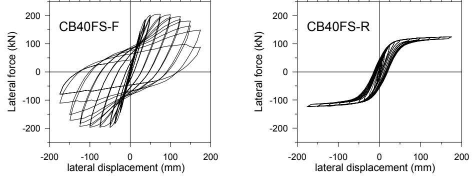

(a) Lateral load vs. displacement curves

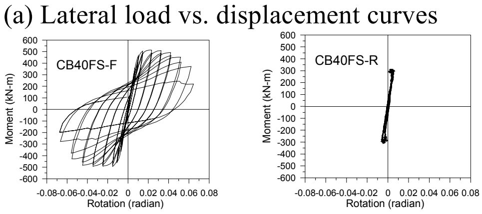

(b) Moment vs. rotation at column base.

Fig. 4 Results for cyclic loading tests for CB40xx-x

Fig. 5 plots the experimental results for specimens with 12-D19 main reinforcements. CD30FB-F was the benchmark test, representing the case with a massive footing and signifying the capacity of specimens with 12-D19 main reinforcements. The results demonstrate that with the decrease in footing size, the rocking behavior becomes more significant. Consequently, the plastic deformation occurred in the column's base becomes minor. For instance, the moment-rotation curve for CD30FS-R is almost linear, while some plastic deformation was formed in CD30FB-R. For CD30FB-R, the calculated upper limit value of moment based on Eq. (2) is 414.4 kN-m, which is higher than the moment capacity of column indicated by CD30FB-F. Therefore, before the base moment of the footing could reach its limit value, the column already yielded, and thereby the moment strength of the column governed the response behavior. On the other hand, for specimen CD30FS-R, the maximum value of bending moment sustained by column was around 320 kN-m, which is lower than the effective yield moment of CD30FB-F. Thus, the column can still remain in elastic state.

Conclusions

In this study, a series of pseudo-dynamic and cyclic loading tests of six RC columns were conducted. These experiments showed that if the footing of a column is allowed to rock, the moment that the column has to sustain can be limited to a certain value. If this limit value of moment is lower than the moment strength of the column, the plastic deformation at the column base will not be formed and the ductility demand of the column can be reduced. In addition, if the footing uplift took place, there will be a decrease in plastic deformation in the column as a result of the energy dissipation of the inelastic rocking mechanism. The extent of decrease in plastic deformation depends on the ratio of the moment capacity of column to the limit value of moment that the column sustained.

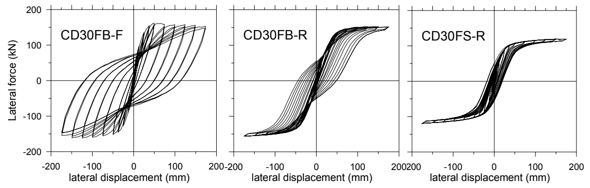

(a) Lateral load vs. displacement curves

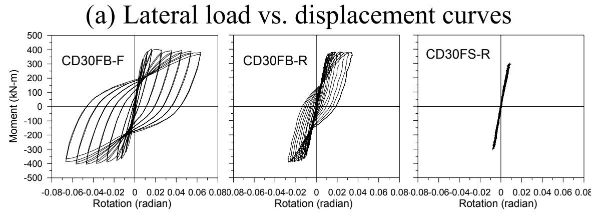

(b) Moment vs. rotation at column base

Fig. 5 Results for cyclic loading tests for CD30xx-x

References

Housner, G.W., 1963. The behavior of inverted pendulum structures during earthquakes. Bulletin of the Seismological Society of America, 53(2), 403-417.

Gajan, S. and B.L. Kutter, 2008. Capacity, settlement, and energy dissipation of shallow footings subjected to rocking. Journal of Geotechnical and geoenvironmental engineering (ASCE); 134(8), 1129-1141.

Espinoza, A. and S. Mahin, 2006. Rocking of bridge piers subjected to multi-directional earthquake excitation. Fifth National Seismic Conference on Bridge & Highways, San Francisco, CA, September 18-20.

Analytical and Experimental Studies on Seismic Behavior of Mid-Story Isolated Buildings (I)

Kuo-Chun Chang [1], Jenn-Shin Hwang [2] and Shiang-Jung Wang [3]

張國鎮 [1]、黃震興 [2]、汪向榮 [3]

Abstract

In a mid-story isolated building, the isolation system is incorporated into the mid-story rather than the base of the building. In this study, the dynamic characteristics and seismic responses of mid-story isolated buildings were investigated using a simplified three-lumped-mass structural model for which equivalent linear properties were formulated. Moreover, the adverse effect arising from the coupling of higher modes on the seismic responses of a mid-story isolated building was clarified. A simple method to guarantee the mid-story isolation design against the coupling of higher modes attributed to the improper design of the substructure and superstructure was deduced and is presented in this report. Besides, the structural models with their isolation system located at the base and other stories were fabricated and tested to investigate the discrepancies between the seismic responses of base-isolated and mid-story isolated buildings. Based on the analytical and test results, the irrationalities of adopting the equivalent lateral force procedure for the mid-story isolation design are discussed. The most rigorous situation for the displacement demand of the isolation system should be carefully considered and will be further studied.

Keywords: mid-story seismic isolation, higher mode, modal coupling, equivalent linear system, equivalent lateral force procedure

Introduction

The excellent performance of seismically isolated buildings during the 1994 Northridge earthquake and 1995 Kobe earthquake has encouraged the adoption of seismic isolation design for structural protection in the past two decades. The application of seismic isolation design in Taiwan has also been extensive after the 1999 Chi-Chi earthquake (Chang et al., 2009). Among the increasing practical applications of seismic isolation design, the mid-story isolation design, in which the isolation system is typically installed on the top of the first story of a building, is recently gaining popularity because it can satisfy both architectural concerns of aesthetics and functionality. More importantly, it can enhance the construction feasibility at highly populated areas where installing the isolation system beneath the base of a building is extremely difficult if the building separation and the property lines are of particular concerns.

The existing seismic isolation design guidelines are tailored for base-isolated buildings rather than for mid-story isolated buildings. In current practice, the preliminary design of mid-story isolated buildings usually follows the equivalent lateral force procedure provided for base-isolated buildings, assuming that the substructure is sufficiently stiff or rigid. In order to gain insight into the seismic responses of mid-story isolated buildings, this study aimed to investigate the dynamic characteristics and seismic behavior of mid-story isolated buildings. In addition, the shaking table tests on the scaled down steel structural models with the mid-story isolation systems composed of high damping bearings (HDRB) were performed to verify the analytical results and to probe the discrepancy between the seismic responses of base-isolated and mid-story isolated structures. Based on the analytical and experimental studies, the irrationalities of adopting the equivalent lateral force procedure for the mid-story isolation design are discussed.

[1] Director General, National Center for Research on Earthquake Engineering, kcchang@ncree.org.tw.
[2] Deputy Director General, National Center for Research on Earthquake Engineering, jshwang@ncree.org.tw.
[3] Assistant Researcher, National Center for Research on Earthquake Engineering, sjwang@ncree.org.tw.

Equivalent Linear Analysis

All structural elements, except the isolation system, in the analytical model were assumed to remain elastic under earthquake excitations. Besides, the hysteretic behavior of seismic isolation system was represented by an equivalent linear model composed of effective stiffness and equivalent damping ratio.

(1) Simplified Three-Lumped-Mass Structural Model for Mid-Story Isolated Buildings

Referring to the simplified structural model for base-isolated buildings proposed by Kelly (1990), a mid-story isolated building may be represented by a simplified three-lumped-mass structural model, composed of the superstructure, isolation system and substructure, as shown in Fig. 1. The mass ratios and "nominal frequencies" of the substructure, isolation layer and superstructure are defined as

$$r_{sub} = m_{sub} / m_{iso} \text{ and } r_{sup} = m_{sup} / m_{iso} \quad (1)$$

$$\omega_{sub} = \sqrt{k_{sub} / m_{sub}},\ \omega_{iso} = \sqrt{k_{iso} / (m_{iso} + m_{sup})} \text{ and } \omega_{sup} = \sqrt{k_{sup} / m_{sup}} \quad (2)$$

where m_{sub}, m_{iso} and m_{sup} are the seismic reactive masses of the substructure, isolation layer (or super-floor) and superstructure, respectively; k_{sub} and k_{sup} are correspondingly the elastic lateral stiffnesses of the substructure and superstructure; and k_{iso} is the effective lateral stiffness of the isolation system. The component damping ratios ξ_{sub}, ξ_{iso} and ξ_{sup} can be expressed by the mass ratios and nominal frequencies in which ξ_{sub} and ξ_{sup} are the viscous damping ratios of the substructure and superstructure, respectively; and ξ_{iso} is the equivalent viscous damping ratio of the isolation system. The equation of motion corresponding to the simplified three-lumped-mass structural model in terms of story drifts can be rewritten in a more useful and generalized form.

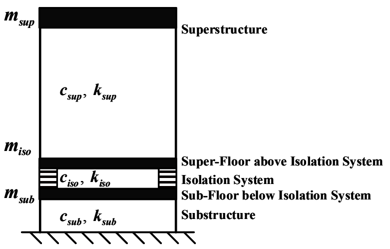

Fig. 1 Simplified three-lumped-mass structural models for mid-story isolated buildings

The fundamental modal natural frequency ω_1 may be very close to the isolated frequency ω_{iso} and is well separated from the residual modal natural frequencies if k_{sub} and k_{sup} are much greater than k_{iso}. Defining $\varepsilon_1 = \omega_{iso}^2/\omega_{sub}^2$ and $\varepsilon_2 = \omega_{iso}^2/\omega_{sup}^2$ and assuming ε_1 and ε_2 are of an order equal to or less than 10^{-1}, the first mode shape of story drifts can be approximated by substituting ω_{iso} for ω_1. Moreover, the first modal damping ratio ξ_1 can be obtained based on the classical damping assumption as follows:

$$\xi_1 \approx \frac{\xi_{iso}}{\left(1 + \frac{2(1+r_{sup})}{r_{sub}}\left(\frac{\omega_{iso}}{\omega_{sub}}\right)^2 + \frac{2r_{sup}}{1+r_{sup}}\left(\frac{\omega_{iso}}{\omega_{sup}}\right)^2\right)} \quad (3)$$

and the first modal participation mass ratio L_1 can be determined by

$$L_1 \approx \frac{r_{sub} + 2(r_{sub} + r_{sup} + 1)\left(\frac{\omega_{iso}}{\omega_{sub}}\right)^2 + \frac{2r_{sub}r_{sup}}{1+r_{sup}}\left(\frac{\omega_{iso}}{\omega_{sup}}\right)^2}{(1 + r_{sub} + r_{sup})\left(\frac{r_{sub}}{1+r_{sup}} + 2\left(\frac{\omega_{iso}}{\omega_{sub}}\right)^2 + \frac{2r_{sub}r_{sup}}{(1+r_{sup})^2}\left(\frac{\omega_{iso}}{\omega_{sup}}\right)^2\right)} \quad (4)$$

It is seen that ξ_1 and L_1 may be significantly affected by the masses and stiffnesses of the substructure and superstructure. If k_{sub} and k_{sup} are much greater than k_{iso} such that $\omega_{iso}/\omega_{sub}$ and $\omega_{iso}/\omega_{sup}$ are sufficiently small, and m_{sup} is larger than m_{sub} (i.e. $r_{sup} > r_{sub}$), it is reasonable to assume that the first vibration mode is the isolation mode and the effective damping ratio is equal to ξ_1.

(2) Coupling of Higher Modes

To study the condition in which the coupling of higher modes (Koh and Kobayashi, 2004) occurs in the simplified structural model (i.e. $\omega_2 \approx \omega_3$), ω_1 was assumed to be approximated by ω_{iso} and was well separated from the higher modal natural frequencies. It has been found that the coupling of higher modes is unavoidable in the mid-story isolation design if the values of $\omega_{sub}/\omega_{iso}$, $\omega_{sup}/\omega_{iso}$, r_{sub} and r_{sup} are chosen carelessly to satisfy the following equation:

$$(\omega_{sub}/\omega_{iso}) = (\omega_{sup}/\omega_{iso})\sqrt{1+r_{sup}} \text{ or } \omega_{sub} = \omega_{sup}\sqrt{1+r_{sup}} \quad (5)$$

It is obvious that the above equation is a linear function of ω_{sub}, ω_{sup} and r_{sup} and can be calculated easily. Besides, the condition in which the coupling of higher modes occurs is independent of ω_{iso}.

Parametric Study

A series of parametric studies with various mass ratios were conducted. The inherent viscous damping ratio of 5% was assumed for the superstructure and substructure, while the equivalent damping ratio of 20% was presumed for the isolation system. The effective period of the isolation system was assumed to be 2.0 seconds or $\omega_{iso} = \pi$. The comparison between ω_1 and ω_{iso} with various frequency ratios $\omega_{sub}/\omega_{iso}$ and $\omega_{sup}/\omega_{iso}$ is shown in Fig. 2. It is seen that to assume $\omega_1 \approx \omega_{iso}$ is reasonable when both ω_{sub} and ω_{sup} are much higher than ω_{iso}. In addition, it is obvious from the figure that $\omega_{sub}/\omega_{iso}$ has a more significant influence than $\omega_{sup}/\omega_{iso}$ on ω_1. ξ_1 varying with $\omega_{sub}/\omega_{iso}$ and $\omega_{sup}/\omega_{iso}$ is illustrated in Fig. 3. It is seen that ξ_1 is proportional to $\omega_{sub}/\omega_{iso}$, $\omega_{sup}/\omega_{iso}$ and r_{sub} and gradually approaches ξ_{iso} when $\omega_{sub}/\omega_{iso}$ and $\omega_{sup}/\omega_{iso}$ become larger. Furthermore, $\omega_{sub}/\omega_{iso}$ has a more significant influence than $\omega_{sup}/\omega_{iso}$ on ξ_1. L_1

varying with $\omega_{sub}/\omega_{iso}$ and $\omega_{sup}/\omega_{iso}$ is illustrated in Fig. 4. It is seen that the increases in r_{sub} and $\omega_{sub}/\omega_{iso}$ result in the reduction of L_1. $\omega_{sub}/\omega_{iso}$ has a more significant effect than $\omega_{sup}/\omega_{iso}$ on L_1. Furthermore, L_1 becomes nearly a constant when $\omega_{sub}/\omega_{iso}$ is larger.

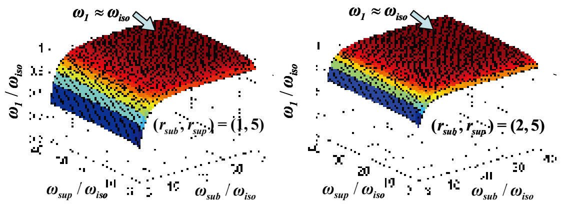

Fig. 2 ω_1 with various $\omega_{sub}/\omega_{iso}$ and $\omega_{sup}/\omega_{iso}$

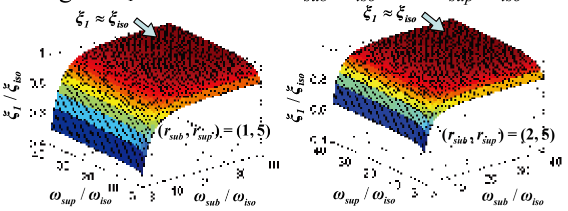

Fig. 3 ξ_1 with various $\omega_{sub}/\omega_{iso}$ and $\omega_{sup}/\omega_{iso}$

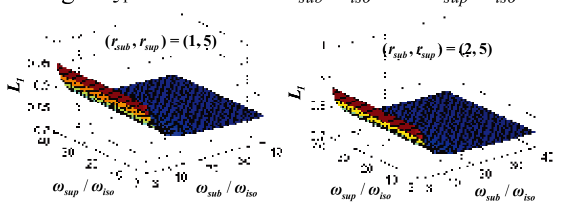

Fig. 4 L_1 with various $\omega_{sub}/\omega_{iso}$ and $\omega_{sup}/\omega_{iso}$

It is seen from Fig. 5 that the third modal participation mass ratio L_3 is nearly zero in the frequency ratio region where the second modal participation mass ratio L_2 is effective and vice versa. The increases of r_{sub} and $\omega_{sub}/\omega_{iso}$ result in the increases of the higher modal participation mass ratios. In between the two frequency ratio regions where either the second or the third mode is effective, there exists a frequency ratio bandwidth in which the coupling of higher modes occurs. Outside the modal coupling zone, the effective higher mode will be either the second mode or the third mode. Besides, corresponding to the effective higher mode categorized in Fig. 5, the modal natural frequency nearly coincides with ω_{sub}, i.e. $\omega_2 \approx \omega_{sub}$ or $\omega_3 \approx \omega_{sub}$.

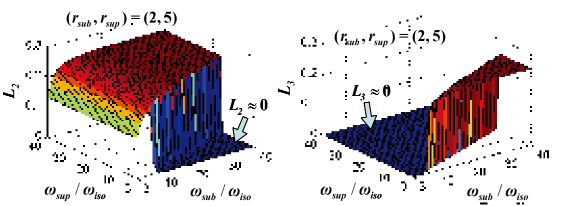

Fig. 5 Higher modal participation mass ratios with various $\omega_{sub}/\omega_{iso}$ and $\omega_{sup}/\omega_{iso}$

The seismic responses were calculated using response spectrum analyses. It is found that the maximum inertia force exerting at the substructure is primarily attributed to the higher modal responses rather than the fundamental modal response. Therefore, the calculation of design force of the substructure (or the base shear force) should carefully consider the contribution of higher mode responses. The maximum inertia forces acting at the super-floor and superstructure are mainly attributed to the first modal inertial forces. However, significant response amplifications can be noticed when $\omega_{sub}/\omega_{iso}$ and ω_{sup}/ω_{is} fall within the frequency ratio bandwidth in which the coupling of higher modes occurs, as shown in Fig. 6.

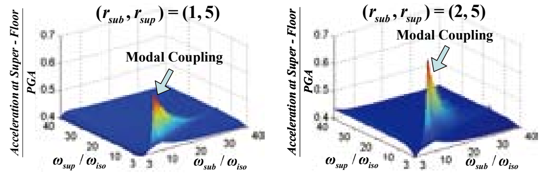

Fig. 6 Maximum acceleration response at super-floor with various $\omega_{sub}/\omega_{iso}$ and $\omega_{sup}/\omega_{iso}$

Experimental Study and Numerical Validations

The superstructures of three seismically isolated structural models, Specimens A, B and C, as shown in Fig. 7, were all identical but, respectively, isolated at the base of the superstructure, the top of a one-story substructure, and the top of another two-story substructure. The four floors from bottom to top of the superstructure were sequentially denoted as SUP-1, SUP-2, SUP-3, and ROOF. In addition, the floor of the substructure of Specimen B was denoted as SUB-1 and the two floors from top to bottom of the substructure of Specimen C were sequentially denoted as SUB-1 and SUB-2. The isolation system was composed of four HDRBs. Three earthquake records, denoted as 921TCU047, I-ELC270 and KJM000, were selected for earthquake inputs of the uniaxial shaking table tests.

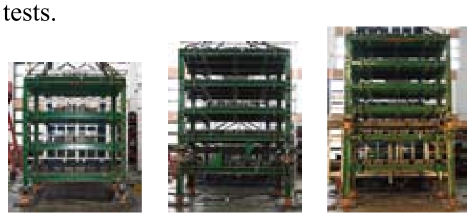
Fig. 7 Photos of Specimens A, B and C

The modal quantities of all specimens can be identified by the system realization using information matrix (SRIM), as summarized in Table. 1. The first modal participation mass ratio of Specimen B is higher than that of Specimen C, which is reasonable since the first modal participation mass ratio is increased with a higher $\omega_{sub}/\omega_{iso}$. The mid-story isolation design has more significant participation of higher modes and less fundamental modal damping ratio than the base isolation design, in particular, when the isolation system is at a higher story.

Table. 1 Identified modal quantities of all specimens under 921TCU047 with PGA of 1.19g

Test Specimen		A	B	C
Modal Natural Period (sec)	1^{st} mode	0.71	0.82	0.90
	2^{nd} mode	0.11	0.11	0.22
	3^{rd} mode	-	0.09	0.13
	4^{th} mode	-	-	0.04

Modal Participation Mass Ratio (%)	1st mode	99.88	77.16	67.63
	2nd mode	0.01	2.41	14.96
	3rd mode	-	19.51	2.73
	4th mode	-	-	8.52
Modal Damping Ratio (%)	1st mode	17.92	16.70	13.74
	2nd mode	2.54	2.24	8.07
	3rd mode	-	7.00	3.33
	4th mode	-	-	3.40

It can be seen from test results that the mid-story isolation design without the coupling of higher modes reveals the excellent seismic performance since the story drift response is still dominated by the isolation layer and the acceleration responses transmitted to the superstructure can be reduced effectively. Besides, the maximum deformation response of the isolation system is increased when the isolation system is installed at a higher story. It is because that the fundamental modal damping ratio becomes smaller with a more flexible substructure. In addition, the significant phase lag existing between the displacement responses at the superstructure and substructure due to the higher mode contribution may not be negligible.

The force and displacement responses vertically distributed along Specimen C at different moments are depicted in Figs. 8 and 9, respectively. It can be seen that there exists a phase lag of almost 180 degrees between the inertia force responses acting at the substructure and superstructure when the peak seismic responses occur at the superstructure and isolation system. Besides, when the peak seismic responses occur at the substructure, the inertia force responses acting at the superstructure are very limited compared with those at the substructure, and a phase lag of larger than 90 degrees is observed between the inertia force responses acting at the substructure and superstructure. When the maximum deformation of the isolation system and peak shear force response across the isolation system occur, a phase lag of larger than 90 degrees existing between the displacement responses at the superstructure and substructure of Specimen C is observed in Fig. 9.

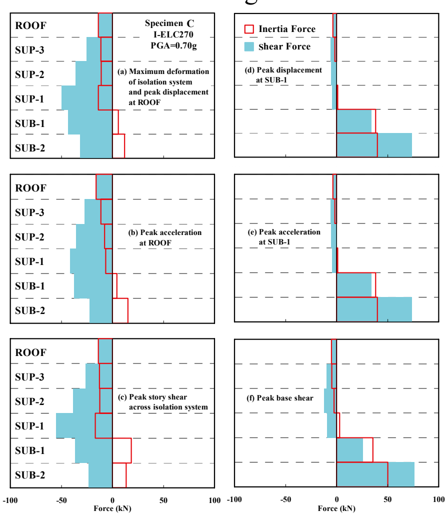

Fig. 8 Vertical distributions of force responses of Specimen C at different instants under I-ELC270 with PGA of 0.70g

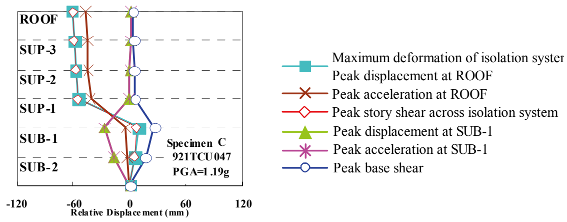

Fig. 9 Displacement responses of Specimen C at different instants under 921TCU047 with PGA of 1.19g

Conclusions

1. The mass and stiffness of the substructure are more important than those of the superstructure in affecting the dynamic characteristics of a mid-story isolated building.
2. The maximum inertia forces acting at the super-floor and superstructure are mainly attributed to the first modal inertial forces. However, the contribution of higher mode responses to the inertia force at the substructure is significant such that the design of substructure should carefully consider the higher mode contribution.
3. The coupling of higher modes results in enlarged acceleration responses at the super-floor.
4. A mid-story isolated building can be pictured as a vertically irregular building with a soft story. Therefore, the most rigorous situations should be considered carefully for the design demands of such building.
5. As an alternative to the equivalent lateral force procedure, the modal response spectrum analysis may be applicable for the preliminary design of mid-story isolated buildings (Ramirez et al., 2000).

References

Chang K.C., Hwang J.S. and Wang S.J. (2009), “Applications of Seismic Isolation and Energy Dissipation Systems to Buildings in Taiwan”, Proceedings of the JSSI 15th Anniversary International Symposium on Seismic Response Controlled Buildings for Sustainable Society, Tokyo, Japan.

Kelly J.M. (1990), “Base Isolation: Linear Theory and Design”, Earthquake Spectra. 6(2), 223-244.

Koh T. and Kobayashi M. (2004), “Analytical Study of Modal Coupling Effect on Mid-story Isolation System by Eigen Value Analysis and Random Vibration Analysis”, Summaries of Technical Papers of Annual Meeting, Architectural Institute of Japan.

Ramirez O.M., Constantinou M.C., Kircher C.A., Whittaker A.S., Johnson M.W. and Gomez J.D. (2000), “Development and evaluation of simplified procedures for analysis and design of buildings with passive energy dissipation systems”, Report No. NCEER-00-0010, National Center for Earthquake Engineering Research, State University of New York at Buffalo, New York.

Experimental Study on the Seismic Performance of Medical Equipment in Hospitals

Juin-Fu Chai [1] and Fan-Ru Lin [2]

柴駿甫 [1]、林凡茹 [2]

Abstract

Considering the great quantity and variations of medical equipment in large hospitals, the simplified evaluation and seismic design methods for medical buildings should be efficient and accurate. Thus, this study aimed to determine the seismic performance of different categories of medical equipment and to verify the application of the existing simplified evaluation and design methods for such equipment. According to the results of shaking table tests on the modeled specimens of medical equipment, the simplified evaluation and seismic design forms were modified to be applicable for free-standing medical equipment.

Keywords: freestanding medical equipment, shaking table test, simplified evaluation form, simplified seismic design

Introduction

Due to the interruption of traffic after earthquakes, it is necessary that medical equipment and medicine supplies of a hospital within the affected area should be self-sufficient for at least 72 hours. However, from the experiences of the Hanshin-Awaji earthquake in Japan (1995) and the Chi-Chi Earthquake in Taiwan (1999), medical equipment (e.g. medicine cabinets and x-ray machines) was damaged seriously, and hence it resulted to significant shortage of emergent medical capacities of hospitals. Currently, the Department of Health (DOH) in Taiwan has completed the simplified evaluation of seismic capacity, electrical and mechanical systems of DOH hospitals, but the specific seismic capacity of various medical equipment was not considered yet. For large hospitals, a lot of medical equipment is attached to different types of structures with miscellaneous attachment types. Therefore, both the efficiency and accuracy should be considered for the simplified evaluation of seismic capacity and simplified seismic design of medical equipment.

In cooperation with a large hospital (hereinafter referred to as N Hospital) in the southern part of Taiwan, this study used survey questionnaire to head nurses for the critical categories of medical equipment after a catastrophic earthquake. Vulnerable items of questionnaire results were selected then by simplified evaluation forms. The simplified design forms were presented for non-destructive seismic restraint devices as well. The evaluation and seismic design forms were verified and modified according to pull-out tests and shaking table tests.

Survey of Critical Medical Equipment

To simplify the evaluation range of equipment, at first, critical medical spaces were chosen according to SB 1953 and N Hospital managers' opinion. Critical medical spaces in N Hospital included Emergency Room, Pharmacy, PET Center, Hemodialysis Room, Operating Room, Department of Nuclear Medicine, Department of Radiation Oncology, Department of Anesthesiology, and Department of Radiology.

The critical medical equipment items with higher vulnerability during earthquakes were chosen from the results of questionnaires and from criterion stated in TBC and ASCE7-05, and the simplified evaluation form was then filled out for any selected item. Items identified as 'seismic evaluation required' or with

[1] Research Fellow, National Center for Research on Earthquake Engineering, chai@ncree.org.tw

[2] Assistant Research Fellow, National Center for Research on Earthquake Engineering, frlin@ncree.org.tw

overturning or rocking responses, as shown in Table 1, should be strengthened by seismic-restraint devices.

Table 1 Simplified evaluation results of Department of Radiology

Medical Space	Department of Radiology				
Basic characteristics	illustration				
No.		01	02	03	04
Equipment Name	Please fill the identifiable name	**X-Ray**	CT Scan	MRI	PACS
Category	Referred to Appendix 1	25	22	22	25
Position (Floor number)	Fill -1~-3 if at B1F~B3F / Fill R1~R2 if at R1F~R2F	1	1	1	1
Position of Equipment	Referred to Appendix 3	2	1	1	1
Position of Attachments	Referred to Appendix 3	2	1	1	4
Installation method	Referred to Appendix 2	1	0	0	9
Number of supports	If equipment is attached at 4 points, fill "4"				4
Weight	equipment except piping(kgf)	720	1137	4460	X
Equipment Size (m)	equipment except piping				
1. length		3.08	2.31	1.88	0.95
2. width		1.11	0.79	1.67	0.61
3. height (included contents)		2.9	1.78	2.4	1.91
The height of the highest point of equipment (included contents)(m)		2.9	1.78	3	1.91
Equipment against the wall (Y or N)		N	N	N	N
flexible connections with other equipment (Y or N or U)	If it's individual, please fill "U"	Y	Y	Y	Y
Results	"N" represents needn't to evaluate, "Y" represents need to evaluate	Y	Y	Y	Y
	Response of freestanding Equipment	Rocking	Rocking	Rocking	Overturning

Seismic Design for Medical Equipment

After filling out the simplified evaluation form, the reaction of each support of medical equipment can be automatically calculated by MS Excel software. According to [1] and ACI 318- 02 [2], as shown in Table 2, a simplified design form for post-installed anchorage was presented to guide designers or constructors. Based on the design parameters (e.g. number of anchors at each support, anchor size, and embedded depth), the attachments of equipment can be designed to satisfy the specified seismic demands.

In Table 2, the seismic-restraint device of medical equipment is supposed to be post-install anchors. However, most supports of medical equipment are not designed with bolt holes in advance and it is unlikely to drill holes at the shell of equipment. In view of this situation, a seismic design form of non-destructive seismic-restraint devices for medical equipment was presented (Table 3).

Pull-out and Shaking Table Tests

Based on survey questionnaires and simplified evaluation for medical equipment at each critical medical space in N Hospital, medical equipment can be classified into three categories according to its type of attachment, namely, freestanding items (e.g. Safety Cabinet), wheel movable items (e.g. medical trolley, Pharmaceutical refrigerator, mass infuser, Hyperbaric Oxygen Capsule, Dialysis machine), and desktop items (e.g. Gamma Counter). Meanwhile, more vulnerable medical equipment in each category was subjected to shaking table tests. Non-destructive seismic-restraint devices, such as brakes, adhesive belts (such as Thumb Lock) and z-shape stoppers, were designed for equipment according to its daily use. As shown in Fig. 1, tensile strength of adhesive and clasp belts were confirmed by pull-out tests.

Table 2 Simplified anchorage design form

Nonstructural Component	Medical Equipment			
Basic characteristics	illustration			
No.		03	05	06
Equipment Name	Please fill the identifiable name	Safety Cabinet	Refrigerator	Hyperbaric Oxygen Capsule
Results	"N" represents needn't to evaluate, "Y" represents need to	Y	Y	Y
	Response of freestanding Equipment	Rocking	Rocking	Rocking
Horizontal seismic design force for each attachment (kgf)		166.32	216.00	1526.07
Vertical seismic design force for each attachment (kgf)		83.16	108.00	763.03
Number of attachments		3	2	4
Number of attachments in short side		1	1	2
Number of anchors in one attachment		2	3	4
Spacing of anchors in one attachment	(in) It needn't be filled if only one anchor in a attachment.	5	2	2
Anchor size	(M8 M10…)	M8	M8	M8
Anchor embedded depth	(in)	2	2	2
Concrete strength of structure (f'_c)	(psi)	2000	2000	2000
(V/Va)^(5/3)+N/Na^(5/3)<=1.0		0.40	0.63	0.99
Seismic capacity of attachments is enough or not		OK	OK	OK
Shear Force in one attachment (Vu)	(kgf)	55.44	108	381.5174312
Tensile Force in one attachment (Tu)	(kgf)	139.7663235	276.75	355.3167661
Normal Force in one attachment (Nu)	(kgf)	523.6905882	462.9350649	852.8416514

Table 3 Seismic design form of non-destructive seismic restraint devices

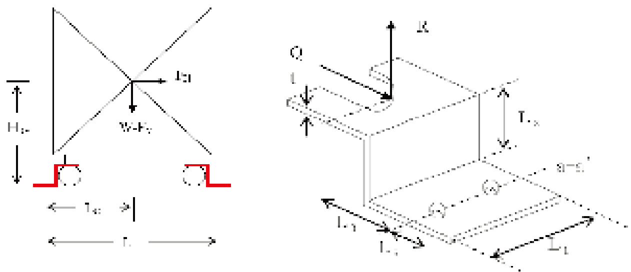

Nonstructural Component	Medical Equipment			
Basic characteristics	illustration			
No.		03	05	06
Equipment Name	Please fill the identifiable name	Safety Cabinet	Refrigerator	Hyperbaric Oxygen Capsule
Width (L1)	(cm)	130	125	16
Height (L2)	(cm)	12	15	16
Distance from Anchor to Support (L3)	(cm)	7	6	16
Distance from edge to Anchor (L5)	(cm)	2.5	4	8
Height of Mass Center (hG)	(cm)	350	106	87
Horizontal Distance between Mass Center and attachments (LG)	at short side of equipment (cm)	38	38	40
Distance between attachments (L)	at short side of equipment (cm)	76.5	77	80
Allowable bending stress of Stopper material (fb)	If unkown, 2400(kgf/cm2)	2400	2400	2400
Anchor size	(M8 M10…)	M8	M8	M8
Thickness of Stopper plate (cm)		0.15	0.19	1.45
Tensile Force of Anchor Bolt (kgf/each)		265.56	230.63	203.04
Shear Force of Anchor Bolt (kgf/each)		27.72	36.00	95.38
(V/Va)^(5/3)+N/Na^(5/3)<=1.0		1.01	0.41	0.25
Seismic capacity of Stopper is enough or not Equation 1： If Vua≦0.2φVn ， φNn ≧ Nua Equation 2： If Nua≦0.2φNn ， φVn ≧ Vua Equation 3：(Vua /φVn)^(5/3)+(Nua /φNn)^(5/3)≦1.0		OK	OK	OK
Design Results	Thickness of Plate (cm)	0.5	0.5	1.5
	Anchor Bolt Size / embedded depth	M8 / 2 in.	M8 / 2 in.	M8 / 2 in.

Because of the extremely high price of medical equipment, it was modeled by square pipe and steel plate for the shaking table test, except medical trolley and electrical stimulator. As shown in Figs. 2 to 5, the size, weight and support types of equipment was actually modeled according to the *in situ* survey. The input excitation that is compatible with the Required Response Spectrum as specified by AC-156 can be determined from the time histories of floor response acceleration at ChiaYi Potz Hospital in Chi-Chi Earthquake (Fig. 6). The amplitude of input time histories was scaled linearly to three levels, i.e. small earthquake and design earthquakes with S_{DS} of 0.5 and 0.8. Most locations of the critical medical equipment items in N Hospital were from B1F (basement one floor) to 3F (third floor). Therefore, shaking table tests were classified into two groups according to their location.

For the equipment items without seismic-restraint devices, most responses in shaking table tests were quite consistent with the response identified by the simplified evaluation form (i.e. fixed well, rocking, sliding or overturning)

Fig. 1 Pull-out tests for adhesive and clasp belts

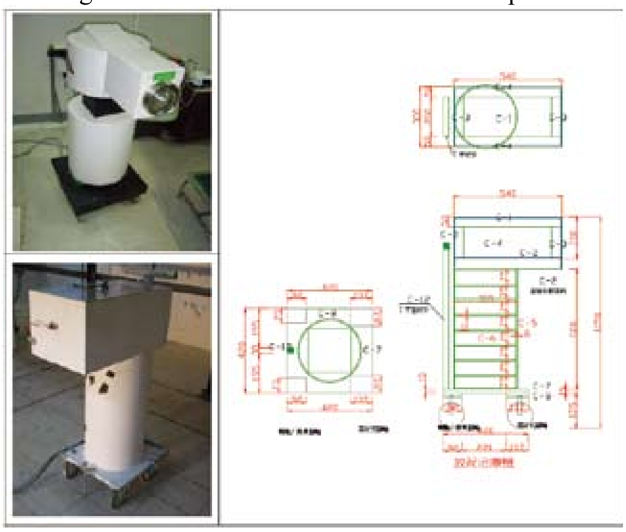

Fig. 2 Micro-Selectron specimen

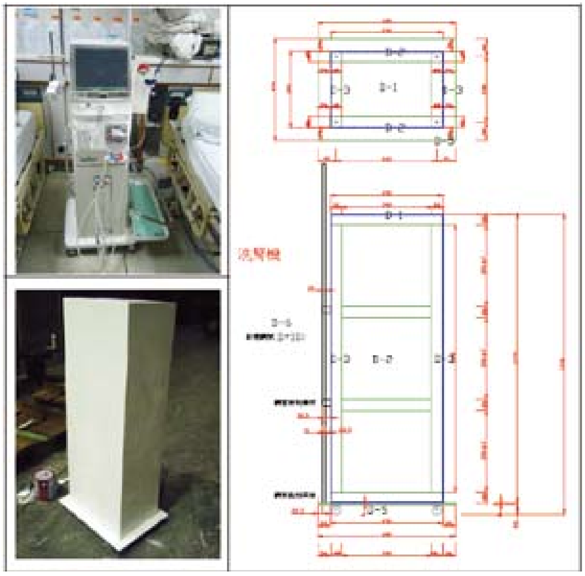

Fig. 3 Dialysis machine specimen

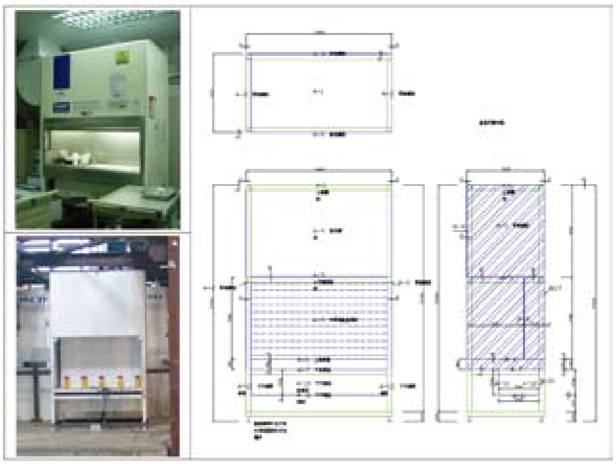

Fig. 4 Safety Cabinet specimen

Fig. 5 Pharmaceutical refrigerator specimen

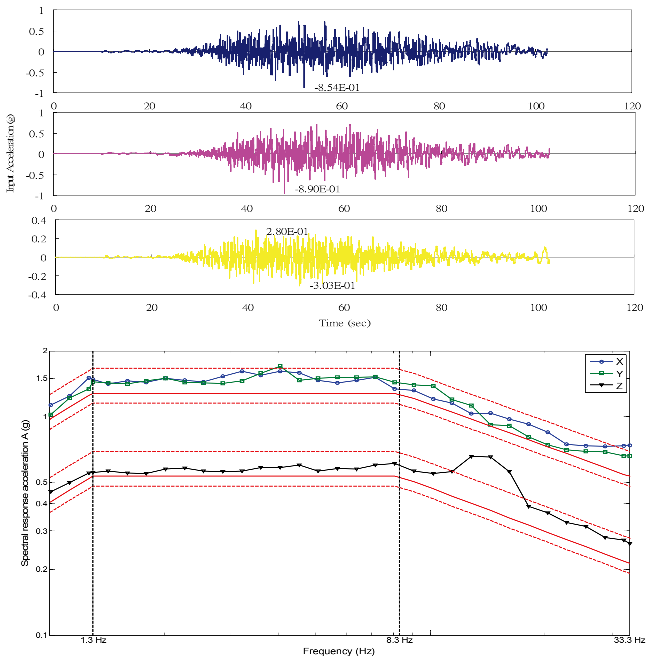

Fig. 6 Input Accelerations and Test Response Spectrum (S_{DS}=0.8, 1/3 to building height)

From test results, it can be observed that seismic-restraint devices efficiently decreased displacement responses and possibilities of overturning or bumping with other items. However, restraint devices would inevitably increase the acceleration responses of equipment items. Take Dialysis Machine and Mass Infuser as examples, as shown in Fig. 7, Thumb Lock or belt devices can decrease the amount of sliding displacement, but result in a sharp increase of response acceleration because of the impact force. Besides, fundamental frequencies of medical equipment with restraint become generally higher than those without any restraint (Fig. 9).

To reduce impact force and to avoid resonance of internal components in medical equipment, using ductile restraint devices or adding energy-dissipating devices (such as rubber pads) are suggested.

Conclusions

In this study, basic features of critical medical equipment in nine medical spaces in N hospital were surveyed and classified into three attachment types, i.e. wheel movable, freestanding, and desktop ones. According to the results of questionnaires and simplified evaluation forms, nine vulnerable medical equipment items were chosen for shaking table tests. Non-destructive seismic-restraint devices were also proposed for each equipment item. Test results revealed that restraint devices actually contribute to decrease displacement response, but it also increases acceleration response of the equipment. Besides, damages of adhesive layer between restraint devices and equipment or anchors at partition wall appeared under larger earthquakes. Therefore, the pull-out strength of partition wall and the adhesive strength of non-destructive devices might be the next research subjects for seismic design of medical equipment.

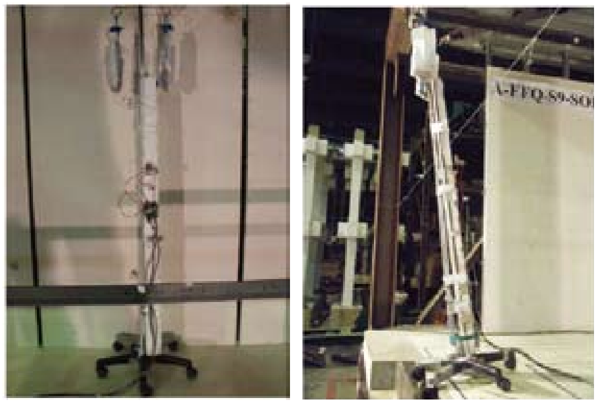

Fig. 7 Test results of Mass Infuser with (left) or without (right) seismic restraint devices

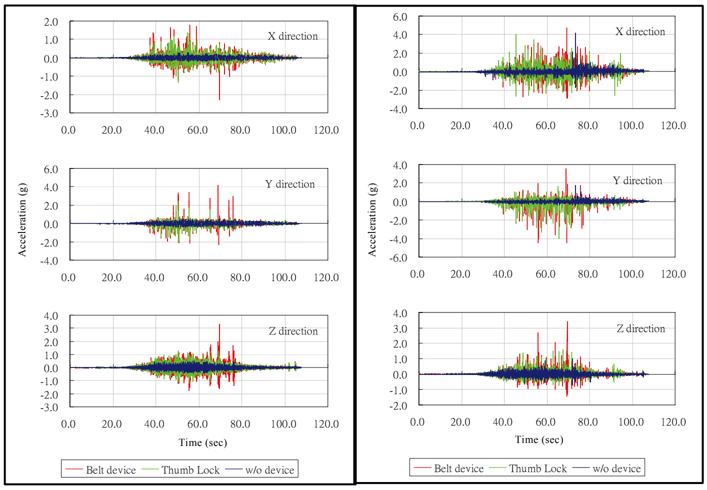

Fig. 8 Acceleration Responses of Dialysis Machine (left) and Mass Infuser (right)

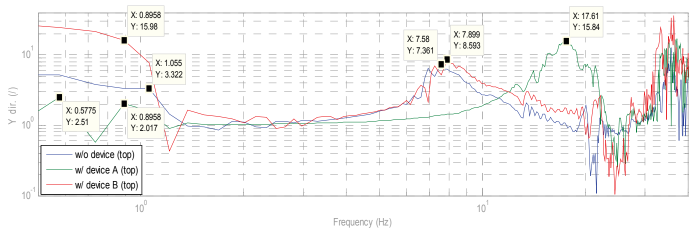

Fig. 9 Transfer functions at top of Safety Cabinet

References

Chai, J.-F., Yao George C. and Lin, Fan-Ru, (2008). "Simplified Study on the Seismic Design of Nonstructural Components in a Hospital", NCREE, Taiwan, NCREE-09-018 (in Chinese).

ACI Committee 318, (2002). "Building Code Requirements for Structural Concrete (ACI 318-02) and Commentary (ACI 318R-02)," American Concrete Institute, Detroit.

Experimental Study on Seismic Performance of Equipment with Vibration Isolation Devices

Jenn-Shin Hwang [1] , Shiang-Jung Wang [2] and Min-Fu Chen [3]

黃震興 [1]、汪向榮 [2]、陳閔富 [3]

Abstract

The seismic performance of a building depends not only on the seismic capability of its structural components but also on the seismic capability of important equipment and nonstructural facilities inside the building. In order to maintain the desired functionality of a building during or after a major earthquake event, the important equipment and nonstructural facilities have to be always functional. In current practice, the important equipment, such as mechanical and electrical equipment, is usually mounted on the vibration isolation devices which are originally designed to prevent vertical vibration produced by the mounted equipment from transmitting to the building. However, these vibration isolation devices usually possess lower horizontal stiffness. If the natural frequencies of the building and the equipment with vibration isolation devices are too close during an earthquake event, there may have resonance that will cause severe displacement responses of vibration isolation devices and may even lead to serious collapse of the mounted equipment. For this reason, the dynamic hysteretic behavior and seismic capability of the commonly used vibration isolation devices were thoroughly investigated in this study through a series of shaking table tests.

Keywords: Mechanical and electrical equipment, vibration isolation device, seismic performance

Introduction

This study aimed to explore the seismic performance of electronic equipment mounted on the commonly used vibration isolation devices through a series of shaking table tests. A steel frame mounted with suitable mass blocks was used to simulate electronic equipment and its weight in this study. The artificial input excitations were compatible with the floor spectrum which was made in accordance with the regulations specified in AC156. Based on the test results, the dynamic hysteretic behavior and seismic capability of the vibration isolation devices can be thoroughly investigated.

The past investigations indicate that the dominant failure mode of most vibration isolation devices is the pop-up condition of the inside spring, as presented in Fig. 1. It can be deduced that, in addition to insufficient strength of the vibration isolation device itself, the significant overturning behavior due to inappropriate arrangement of the equipment mounted on vibration isolation devices (e.g. improper aspect ratios) may result in the failure mode aforementioned.

Fig. 1 Damaged vibration isolation devices due to earthquake.

Experimental Study

Two commonly used types of vibration isolation

[1] Deputy Director General, National Center for Research on Earthquake Engineering, jshwang@ncree.org.tw.

[2] Assistant Researcher, National Center for Research on Earthquake Engineering, sjwang@ncree.org.tw

[3] Assistant Researcher, National Center for Research on Earthquake Engineering, mfchen@ncree.org.tw

devices in practice, denoted as Type A and Type B, as shown in Fig. 2, were studied in the shaking table tests. The coil springs of Type A and Type B devices are identical. Two screws and two zincked semicircle plates in both sides of the coil springs of Type A and Type B devices, respectively, can freely move (within $\pm 5mm$ approximately) in the horizontal direction before an impact occurs. Two horizontal directions (X and Y) and one vertical direction (Z) of the test specimen (a steel frame mounted with mass blocks) equipped with four vibration isolation devices were subjected to a series of uniaxial earthquakes, as depicted in Fig. 3. The longitudinal and transverse directions of Type A and Type B devices were installed corresponding to X and Y directions of the test specimen. The input acceleration started at 30% of the original artificial earthquake and continued with 30% increase until any of the vibration isolation devices are damaged apparently (i.e. 30%, 60%, 100%, 120% and 150% of the original artificial earthquake).

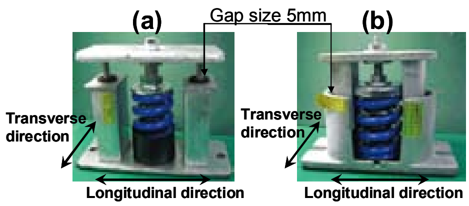

Fig. 2 Commonly used vibration isolation devices (a) Type A; and (b) Type B.

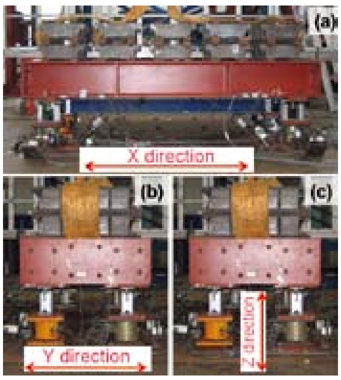

Fig. 3 The test specimen installed on the shaking table subjected to uniaxial earthquakes (a) X direction; (b) Y direction; and (c) Z direction.

Experimental Results

The acceleration histories, hysteresis loops and dominant failure modes of test specimens equipped with Type A and Type B devices subjected to X, Y and Z directional earthquakes are described as follows.

The maximum input peak accelerations in the uniaxial tests along X and Y directions are about 1.0 and 0.7g, respectively. Corresponding to the maximum input earthquakes, the measured acceleration responses transmitted to the test specimen equipped with Type A (Type B) devices in X and Y directions are 1.3g (1.66g) and 3.0g (2.0g), respectively. The acceleration histories are illustrated in Fig. 4.

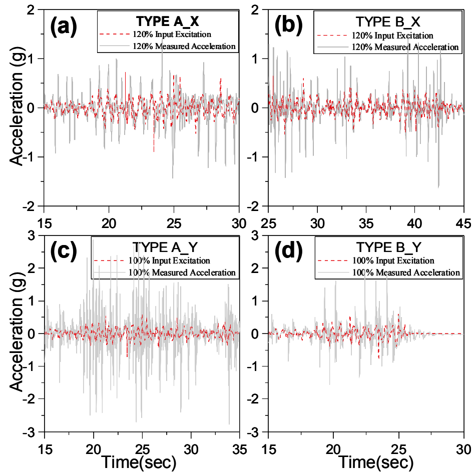

Fig. 4 Input and transmitted acceleration histories of test specimens equipped with Type A and Type B devices in X and Y directions.

When the test specimen equipped with Type A devices was subjected to X directional earthquakes, the significant plastic deformation of two screws in both sides of the coil spring can be observed. Once the screws were fractured, the lateral force was resisted by the coil spring only and the seismic damage potential to the test specimen may be induced by the severe deformation of the coil spring, as shown in Fig. 5(a). The hysteresis loop of one Type A device in X direction is depicted in Fig. 5(c). Moreover, when the test specimen equipped with Type B devices was subjected to X directional earthquakes, the zincked semicircle plates in both sides of the coil spring revealed the superior restrained capability in X direction such that there is no significant deformation of the coil spring, as shown in Fig. 5(b). The hysteresis loop of one Type B device in X direction is depicted in Fig. 5(d).

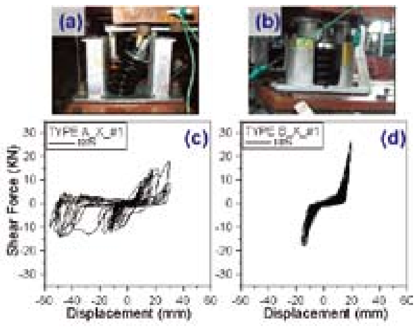

Fig. 5 Dominant failure modes and hysteresis loops of Type A and Type B devices subjected to X directional earthquakes.

It should be noted that the overturning behavior is more significant when the test specimen is subjected to Y directional earthquakes. This is because the aspect ratio of the test specimen in Y direction is much larger than that in X direction. When the test specimen equipped with Type A devices was subjected to Y directional earthquakes, the screws in both sides of the coil spring provided the restrained capability in Y and Z directions. The significant overturning behavior leads to the fracture of the screws. Since there is no stopper for the coil spring in Y direction, the pop-up condition of the coil spring occurred eventually, as shown in Fig. 6(a). The hysteresis loop of one Type A device in Y direction is depicted in Fig. 6(c). Moreover, when the test specimen equipped with Type B devices was subjected to Y directional earthquakes, the zincked semicircle plates in both sides of the coil spring revealed the superior and limited restrained capabilities in Y and Z directions, respectively. The significant overturning behavior results in the unbalanced force exerting on the coil spring and the severe axial deformation of the coil spring, as shown in Fig. 6(b). The hysteresis loop of one Type B device in Y direction is depicted in Fig. 6(d).

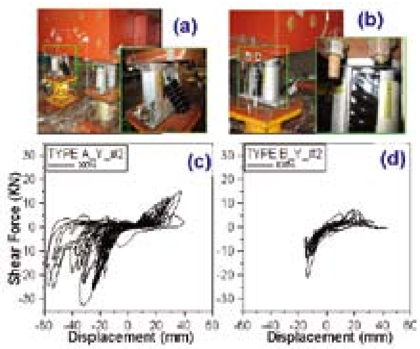

Fig. 6 Dominant failure modes and hysteresis loops of Type A and Type B devices subjected to Y directional earthquakes.

When the test specimen equipped with Type A devices was subjected to Z directional earthquakes, the screws in both sides of the coil spring provided the restrained capability in Z direction such that the axial stiffness can be enhanced obviously, as shown in Fig. 7(a). Moreover, when the test specimen equipped with Type B devices was subjected to Z directional earthquakes, only the coil spring sustained the vertical force since there is no restraint in Z direction. The relationship between axial force and axial deformation of one Type B is depicted in Fig. 7(b).

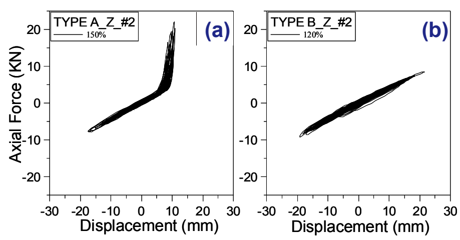

Fig. 7 Relationship between axial force and axial deformation for Type A and Type B devices subjected to Z directional earthquakes.

Discussions

The ratio of the peak acceleration response transmitted to the test specimen to the peak earthquake input is defined as "Acceleration Response Ratio (ARR)", as given in Equation (1). Besides, the ratio of the peak displacement response of the vibration isolation device to the free movable distance without any restraint (i.e. $\pm 5mm$ in Type A and Type B devices) is defined as "Displacement Response Ratio (DRR)", as given in Equation (2). Since there is no restraint in Z direction for Type B devices, the test results under Z directional earthquakes are excluded for the following discussion of DRR. Moreover, when the test specimen is subjected to X or Y directional earthquakes, the overturning angle can be calculated based on the arctangent of the vertical displacement response of the boundary vibration isolation device to the horizontal displacement response of the boundary vibration isolation device plus the horizontal distance between the centroid of the test specimen and the boundary vibration isolation device. When the test specimen is subjected to Z directional earthquakes, the overturning angle can be calculated based on the arctangent of the difference between the vertical displacement responses of the vibration isolation devices installed at two boundaries to the horizontal distance between the two vibration isolation devices. It can be found that when the test specimen equipped with Type A or Type B devices is subjected to X or Z directional earthquakes, the overturning angles are less than 1 degree. However, when the test specimens equipped with Type A and Type B devices are subjected to Y directional earthquakes, the overturning angles are 2 to 6 degrees and 2 to 20 degrees, respectively.

$$ARR = \frac{|\pm AR|_{\max}}{|\pm IA|_{\max}} \qquad (1)$$

where $|\pm AR|_{\max}$ is the peak acceleration response transmitted to the test specimen; and $|\pm IA|_{\max}$ is the peak earthquake input.

$$DRR = \frac{|\pm DR|_{\max}}{|Gap\ Size|} \qquad (2)$$

where $|\pm DR|_{\max}$ is the peak displacement response of the vibration isolation device; and $|Gap\ Size|$ is the free movable distance without any restraint (i.e. $\pm 5mm$ in Type A and Type B devices).

It can be seen from Figs. 8(a) and 8(b) that under X directional earthquakes, the increase in the earthquake input results in the reduction of ARR for the test specimen equipped with Type A devices, while ARR of the test specimen equipped with Type B devices is proportional to the scale of earthquake inputs. Furthermore, when test specimens equipped with Type A and Type B devices are subjected to Z directional earthquakes, ARR values are proportional to the scales of earthquake inputs, as presented in Figs. 8(e) and 8(f).

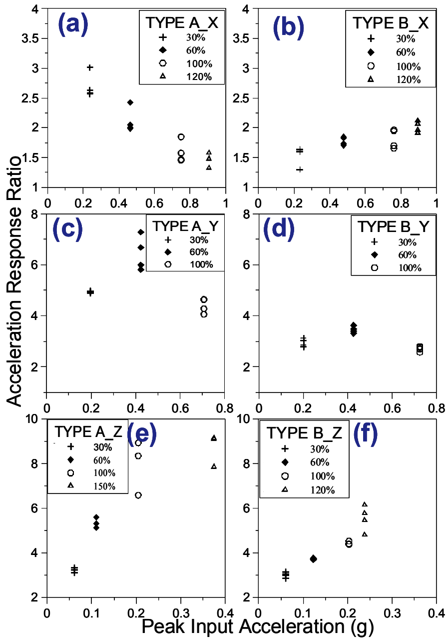

Fig. 8 ARR values of test specimens equipped with Type A and Type B devices under X, Y and Z directional earthquakes.

DRR<1, DRR=1 and DRR>1 represent that the restraint is not engaged, the restraint works exactly and the restraint is engaged, respectively. As shown in Fig. 9, DRR values are proportional to the scales of earthquake inputs.

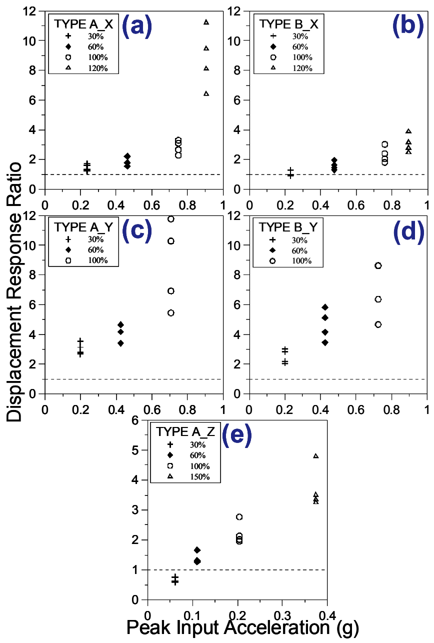

Fig. 9 DRR values of test specimens equipped with Type A and Type B devices under X, Y and Z directional earthquakes.

Conclusions

1. When the test specimen is subjected to X directional earthquakes, the overturning behavior is very limited since the test specimen in X direction possesses a smaller aspect ratio. Furthermore, the energy dissipation capacity of Type A devices is superior to that of Type B devices. It can be found from the comparison of ARR values under X directional earthquakes that, the increase in earthquake inputs results in the reduction of acceleration responses transmitted to the test specimen equipped with Type A devices, while the acceleration response transmitted to the test specimen equipped with Type B devices is proportional to the scale of earthquake inputs.
2. When the test specimen is subjected to Y directional earthquakes, the overturning behavior is really significant since the test specimen in Y direction possesses a larger aspect ratio. It is worthy of noting that the overturning behavior of the test specimen equipped with Type A devices can be suppressed effectively compared with the test specimen equipped with Type B devices due to the restrained capability in the vertical direction. Furthermore, it can be found from the comparison of ARR values under Y directional earthquakes that, with the same earthquake inputs, the peak acceleration response transmitted to the test specimen equipped with Type B devices is smaller than that with Type A devices.
3. It can be found from the comparison of DRR values under X and Y directional earthquakes that, with the same earthquake inputs, the peak displacement response of the vibration isolation devices in Y direction is much severer than that in X direction. It is because that the test specimen in Y direction possesses a larger aspect ratio. The test results indicate that the seismic damage potential to the mounted equipment may be induced by the severe displacement response of vibration isolation devices.

References

Saeed Fathali, and Andre Filiatrault, (2007) “Experimental Seismic Performance Evaluation of Isolation / Restraint Systems for Mechanical Equipment, Part1: Heavy Equipment Study”, MCEER-07-0007.

Hwang J.S., and Chen M.F. (2008), “A Study on Cyclic Loading Tests of Vibration Isolations Mechanical/Electrical Equipment”,Taiwan.

Hwang J.S., and Chen Y. (2009), “Cyclic Behavior of Vibration Isolation Systems of Mechanical/Electrical Equipment”,Taiwan.

Implementation of Bio-informatics on Structural Health Monitoring

Chang-Hung Ku [1] and Tzu-Kang Lin [2]

Abstract

A structural health monitoring (SHM) mobile module based on bioinformatics is studied in this paper. An eight-story down-scale steel building located at the shaking table of the National Center for Research on Earthquake Engineering (NCREE) was used as the testing benchmark structure. In order to create a mobile SHM prototype as well as providing a platform for application on future control system, the system was developed by utilizing both advanced software and hardware in the related field.

Keywords: Structural health monitoring, mobile module, bio-informatics

Introduction

This study aimed to design, build and test a mobile SHM system that can be used easily. Considering the mobility of the SHM system and the goal to meet the expected performance, appropriate software, hardware interface and wireless transmission system were selected as the fundamental elements. To verify the feasibility of the SHM prototype system, a series of experiments has been conducted on the eight-story down-scale benchmark specimen at NCREE. The experimental data will also be established as a reliable reference for SHM system development.

The selection of hardware

The main part of the hardware is composed of a CompactRIO system with FPGA system, reconfigurable chassis, hot-pluggable type I/O modules, and LabView Real-Time (RT) System. The platform is expected to process real-time monitoring control. This embedded technology can access low-level hardware resources wide open to rapidly develop independent or discrete control system.

Through the graphical programming design tool, the mobile type SHM system can be designed and optimized on different embedded monitoring projects for specific applications. As shown in Figs.1 and 2, As the FPGA system and the Real-Time system can operate independently for parallel computing, the execution efficiency of entire SHM system can be easily enhanced.

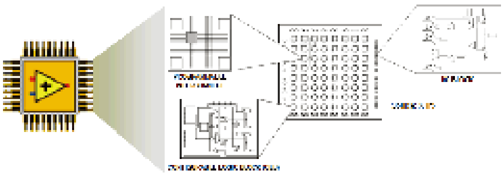

Fig. 1 The concept of FPGA system

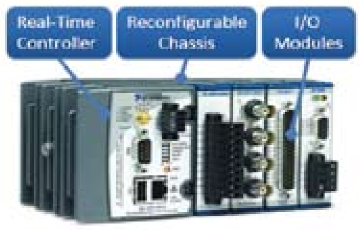

Fig. 2 The Real-Time controller

The Wireless Transmission System

The WirelessPlug MA8-9i GPRS/CDMA communication platform providing a wireless solution on Machine to Machine application including the MA8-9i wireless platform and software Plug Master of central server was used in this research. The RS-232／RS-485 interface of industrial standard which can be connected directly with industrial acquisition equipment was utilized for data transmission.

[1] Undergraduate student, National Taiwan University Civil Engineering, b95501031@ntu.edu.tw

[2] Associate Research Fellow, National Center for Research on Earthquake Engineering, tklin@ncree.org.tw

Mobile SHM Prototype

To implement the SHM concept in practice, a SHM prototype detection system has been developed. As shown on the left side in Fig. 3, three hot-pluggable type modules including the sensing input module, GPS module, and the data storage module were integrated to form the prototype system. Meanwhile, by using the customized rectangular tin on the prototype system, power for the sensing unit can be easily provided, and the sensor may operate normally to become a relay station to collect the data required. As designed, the micro-vibration data will first be measured by the sensor deployed and then be transmitted through the input module to the built-in microprocessor. Both acceleration and velocity of the structure can be measured simultaneously to evaluate the health condition of the structure. In addition, different SHM prototype systems can be extended to SHM network by connecting network wires between each prototype system.

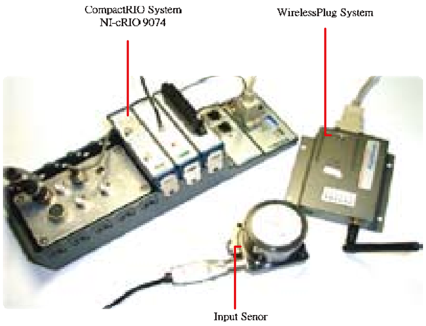

Fig. 3 The Prototype

The SHM Software

The software of this SHM system can be divided into two parts as the Onsite Program shown in Fig. 4 and the Demonstration Program shown in Fig. 5.

As mentioned above, the On-site program is then divided into four parts as shown in Fig. 4 including the Data Pre-Processing, the Coefficient Extracting Module, the Health Condition Diagnosis, and GPRS & Wireless Module.

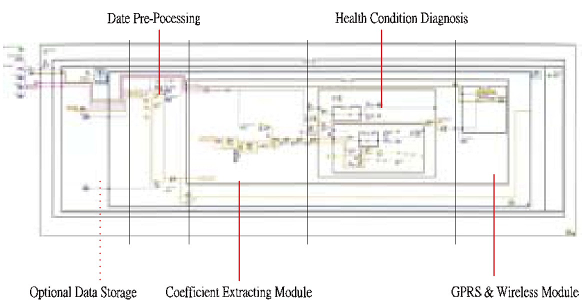

Fig. 4 The Onsite Program

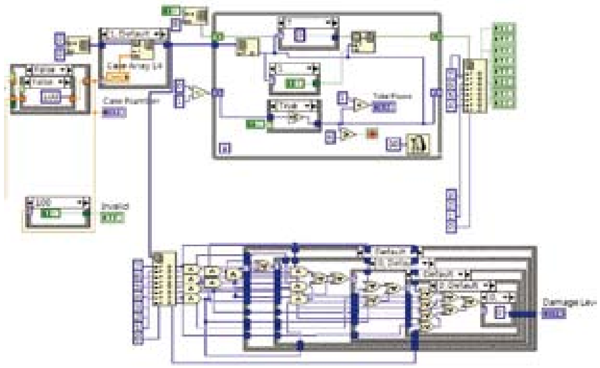

Fig. 5 The Demonstration Program

The Pre-Processing program is composed of three parts including the collection of the input data, the design of the digital filter, and the settings of the data size for SHM processing. By using the Pre-Processing program, the unnecessary noise from the ambient environment can be successfully avoided to ensure the accuracy of the input data.

In this study, the sample rate of the data was selected as 200Hz, and the filter was chosen as band-passed filter to filter out the unwanted high and low frequency set as 90Hz and 0.1Hz, respectively. The errors caused by the voltage conversion between the analog and digital signals can also be eliminated to collect the proper data required while the accuracy of the data is also guaranteed. The setting and selecting of filter parameters is indicated in Fig. 6.

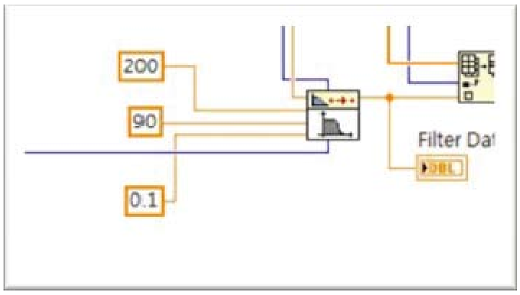

Fig. 6 The Data Pre-Processing

The Coefficient Extracting module was designed based on the specific SHM algorithm developed for the monitoring objective, the eight-story down-scale steel structure. In this study, the AR-ARX model was first established and then implemented by codes written with the LabView program, and the settings of the order required is shown in Fig. 7. By using the Coefficient Extracting module, the time history of the structure response can be quickly transformed into the AR-ARX array form and the damage condition of the structure can be evaluated by comparing with the deposited database in the next stage.

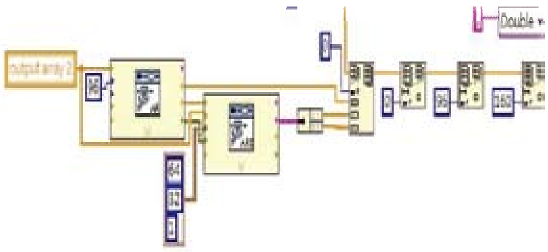

Fig. 7 Coefficient Extracting Module

The Naïve Bayes-based SHM algorithm was applied in Fig. 8. By comparing the AR-ARX array calculated from the previous block with the stored database, the occurrence probability of all 19 damage cases was estimated by a designated loop, and the structural damage condition and location can be easily determined. The detail of the Health Condition Diagnosis module is shown in Fig. 8.

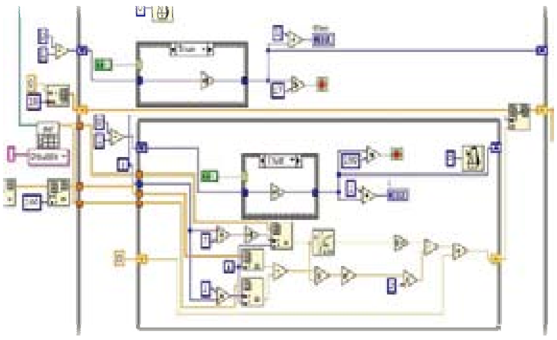

Fig. 8 Coefficient Extracting Module

In order to achieve the goal of real-time monitoring after determining the damage condition and location, the GPRS Module was utilized to transfer the data back to the monitoring server. For the purpose of the safe-transmission of data and the accuracy of reception, data transmission is transmitted with encryption. In this study, the skill to encrypt and decrypt is achieved by adding an AA string in the beginning of the data transmitted. Signals are received once the AA string is detected, and the result is displayed. The details of the transmitter and receiver software are shown in Figs. 9 & Fig. 10.

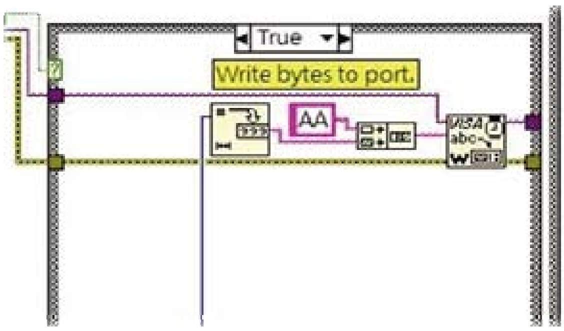

Fig. 9 The Transmitter

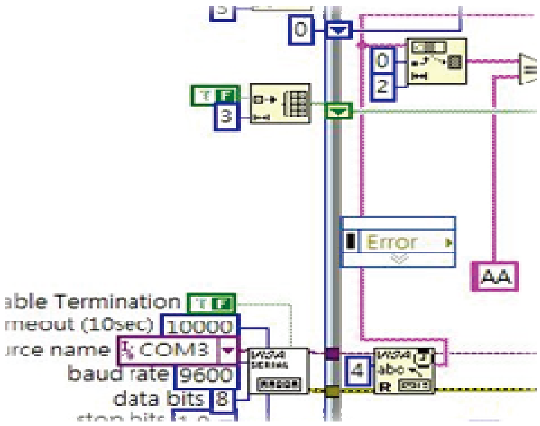

Fig. 10 The Receiver

In order to test the performance and the consistency between the software and hardware of the SHM prototype, an experimental verification was arranged. The scaled-down six-story steel building mounted on the shaking table at NCREE was again used as the practical testing structure. The structural damage was simulated by loosening four bolts on the third floor, which is damage case 4, and then the ambient vibration response measured by the sensor of the roof was analyzed by the on-site SHM prototype for testing. By comparing the AR-ARX array obtained from the micro-vibration data with the database deposited in the SHM system, the results of the structural health condition can be evaluated immediately.

The real-time monitoring result is shown in Fig. 11 where the SHM results can be determined every 20 seconds on the left side of the figure. The numbers shown in the panel represent the classification result. To avoid false alarm in practical application, the SHM algorithm was designed to operate three times per 60 seconds to determine the damage condition and location of the structure which is shown on the right side of Fig. 11. The damage level of the structure, which is either none, slight, moderate, severe, ultimate, or nonlinear is shown in the middle of the figure. Furthermore, not only the real-time structural damage can be monitored by the mobile type SHM system, but the software parameters can also be remotely controlled. This flexible monitoring design can make the SHM system optimal to fit all kinds of conditions and evaluate the structural damage immediately. The high mobility and prompt execution concepts of the proposed mobile SHM prototype can then be finally implemented.

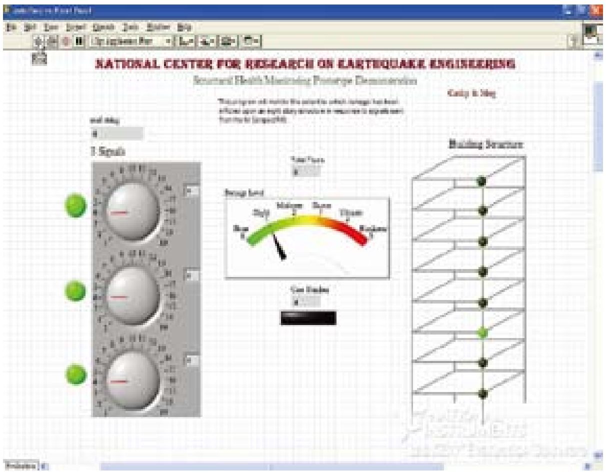

Fig. 11 The Real-Time Monitoring Interface

Conclusions

In this study, a SHM prototype was designed, developed, and verified on real structures. Advanced software and hardware were integrated. The result has demonstrated the feasibility of the proposed SHM system in practice.

References

Straser, E. and Kiremidjian, A.S., "A Modular Wireless Damage Monitoring System for Structures," The John A. Blume Earthquake Engineering Center Technical Report No. 128, Department of Civil and Environmental Engineering, Stanford University, Stanford, California, 1998.

Sohn, H., and Farrar, C. R., "Damage Diagnosis Using Time Series Analysis of Vibration Signals," Journal of Smart Materials and Structures, 10(3), pp. 446-451(2001).

Keller, A. D., Schummer, M., Hood, L., Ruzzo, W. L.,"Bayesian Classification of DNA Array Expression Data," Department of Computer Science and Engineering, University of Washington, Technical Report UW-CSE-2000-08-01, Seattle (2000).

Cyclic Test of a Coupled Steel Plate Shear Wall Substructure

Keh-Chyuan Tsai [1], Jing-Tang Chang [2], Chao-Hsien Li [3] and Chih-Han Lin [4]

蔡克銓 [1]、張景棠 [2]、李昭賢 [3]、林志翰 [4]

Abstract

This research aimed to investigate the seismic behavior and design of the Coupled Steel Plate Shear Wall (C-SPSW). A prototype six-story C-SPSW building was designed based on the model building code. A 40% scale specimen was constructed as the bottom two-and-half-story substructure of the six-story C-SPSW prototype. The reduced scale sub-structural specimen was cyclically tested using the Multi-Axial Testing System (MATS) at the National Center for Research on Earthquake Engineering (NCREE). In addition to the cyclic lateral forces, the constant vertical loading and cyclic overturning moments were applied on the specimen simultaneously. The test results show that the C-SPSW specimen behaved in a ductile manner and dissipated significant amounts of hysteresis energy during the cyclic loadings. Finally, based on the experimental results, the implications in the capacity design for the bottom boundary column are discussed.

Keywords: Steel Plate Shear Wall , Coupled Steel Plate Shear Wall, Coupling Beam, Capacity Design

Introduction

Steel plate shear wall (SPSW) has seen increased usage in North America and Asia in recent years. An SPSW is composed of a structural frame and infill steel plates. The beams and columns surrounding the infill panels are named as boundary beams and boundary columns, respectively. SPSW can effectively resist horizontal earthquake forces by allowing the development of diagonal tension field action after the infill plate buckles in shear. The energy is then dissipated through the cyclic yielding of the infill plates in tension. However, infilling the steel plate into the structural frame would conflict with the architectural demand for doorways. In a tall and slender SPSW, the significant overturning moments will result in high axial force demands in the boundary columns. Moreover, the tall SPSWs likely behave in the flexure-dominated deformation mode under the lateral forces. It would cause the steel plates in the top stories of the wall to fail in developing the plastic tension field action. Thus, this research proposed Coupled Steel Plate Shear Wall (C-SPSW) as a solution to the application of SPSW in high-rise building.

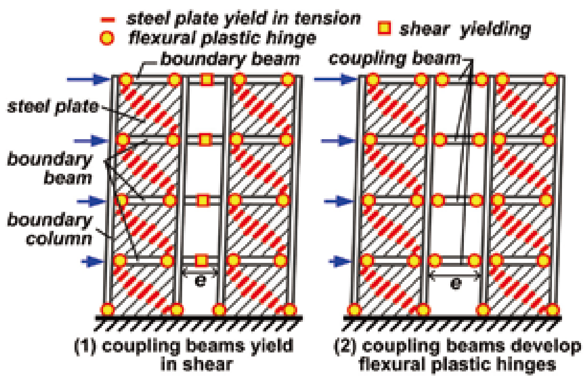

Fig. 1 Plastic mechanism of the C-SPSW

As shown in Fig. 1, a C-SPSW consists of two or more SPSWs in series coupled by the coupling beams between the walls at the story levels. The coupling beams restrain the individual cantilever action of each wall by forcing the system to work as composite

[1] Professor, National Taiwan University, Former Director, National Center for Research on Earthquake Engineering, kctsai@ncree.org.tw

[2] Former Master Student, National Taiwan University, r96521232@ntu.edu.tw

[3] Assistant Research Fellow, National Center for Research on Earthquake Engineering, chli@ncree.org

[4] Assistant Research Fellow, National Center for Research on Earthquake Engineering, hanklin@ncree.org

section. The total stiffness of a C-SPSW exceeds the summation of its individual wall stiffness.

Plastic Mechanism of C-SPSW

For the Reinforced Concrete Coupled Shear Wall, which is commonly seen in practice, the desired plastic mechanism consists of flexural yielding in the coupling beams and at the base of the wall. However, when a C-SPSW develops plastic mechanism under lateral forces, as shown in Fig. 1, the infill plates at all stories develop the plastic tension field and the plastic hinges forms on the coupling beams, boundary beams and the column bases. The difference in plastic mechanism between RC and steel coupled shear wall prevents the extension of the research results for concrete systems to the steel systems.

By extending the current seismic provisions (AISC, 2005) for the link beam of the eccentrically-braced frame to the prediction for the yielding mechanism of the coupling beam, the coupling beam will yield in shear when its length, *e*, is smaller than $1.6M_p/V_p$, where M_p and V_p are the plastic flexural strength and plastic shear strength of the coupling beam, respectively; and the coupling beam will develop flexural plastic hinges at its both ends when $e > 2.6\ M_p/V_p$.

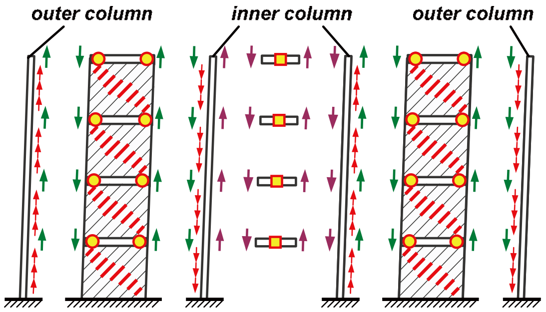

Fig. 2 Schematic of the calculation of the ultimate axial forces in the columns

As shown in Fig. 2, when a C-SPSW is subjected to the lateral forces, the ultimate axial forces on the outer columns come from the plastic panel forces and shears of the boundary beams. For the inner columns, the axial forces due to the coupling beams are opposite to those from the steel plates and boundary beams. Thus, the ultimate axial forces in the inner columns will be less than those in the outer columns.

Design of Prototype 6-story C-SPSW

A prototype 6-story C-SPSW building was designed based on the model building code and some design recommendations from the past researches. The site is located at the east zone of the Chiayi City in Taiwan. As shown in Fig. 3(a), the floor dimension is 54 m × 28 m. The total height is 24 m. The first story has a height of 5 m and the others are 3.8 m high. In the longitudinal direction, there were four six-bay moment resisting frames (MRF). In the transverse direction (the direction of interest here), there were two C-SPSW frames (located on the middle bays of the frame lines B and F) acting as the primary lateral force resisting system. As shown in Fig. 3(b), each C-SPSW is composed of two 3.5 m wide SPSWs and 3 m long coupling beams between the SPSWs.

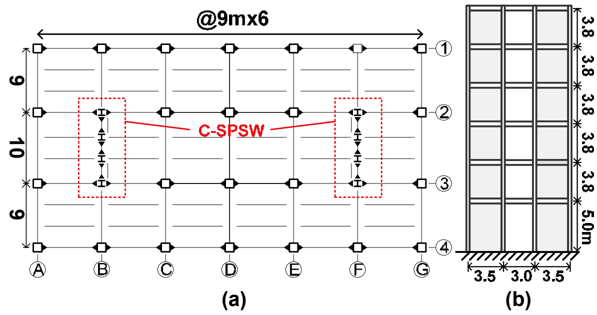

Fig. 3 (a) Floor plane of the 6-story prototype building and (b) elevation of the C-SPSW

The analytical strip model (Thorburn *et al.*, 1983) of the C-SPSW was constructed to check that the whole structure remains elastic under the code pre-scribed load combinations. The coupling beams were designed to be shear links. The selection of the boundary beams was based on the capacity design method proposed by Vian and Bruneau (2005). The determination of the boundary column was based on the capacity design method proposed in this research. The design objective was to limit the plastic hinge on the compressed bottom column to form within the lowest quarter column height. The proposed flexural demand M_d for the bottom boundary column is:

$$M_d = \left[\frac{(3\lambda-1)}{16(\lambda+1)} + \frac{1}{96}\right]\omega_{ch1}h_1^2 \qquad (1)$$

The λ is the ratio of moment due to the frame sway action at the top end to that at the bottom end of the compressed bottom column. The h_1 and ω_{ch1} are the column height and the horizontal component of the yielding panel forces in the 1st story, respectively. The calculations of λ and ω_{ch1} were introduced in the past research. (Tsai *et al.*, 2010)

Test Specimen Design and Test Program

Using the 6-story C-SPSW prototype as a basis, a 40% scale specimen was constructed as the bottom 10.5 m high substructure of the original C-SPSW. The region of the substructure contains the lowest tow stories and the bottom half third story of the original structure (shown in Fig. 4). The infill plates were 3.5 mm thick low yield strength (LYS) steel (measured F_y = 220MPa). All the boundary elements and coupling beams were made of A572 Grade 50 steel. The design results of the test specimen are shown in Fig. 5. The Reduced Beam Section (RBS) detailing was employed at the ends of the boundary beams. The infill plates were welded at the edges to the boundary elements using 7 mm thick fishplate connection details.

In order to simulate the effects of the upper structure acting on the substructure, as illustrated in Fig. 4, the specimen was subjected to the cyclic lateral forces F_H, the cyclic overturning moments M_{OT}, and the constant vertical loadings P_V representing the gravity load effects. The specimen was tested using the Multi-Axial Testing System (MATS) at the National Center for Research on Earthquake Engineering (NCREE). The specimen was set upside down in the MATS. The base beam of the specimen was mounted on the cross beam of MATS. The top boundary of each SPSW was connected with a transfer beam. The column top ends were pin-connected with the transfer beam ends; and the top steel plate was welded to the transfer beam using the fishplate connection. The mid-span of transfer beam was pin-supported on the platen. A lateral support system was constructed on the platen and the reaction frame (A-frame) of MATS. Lateral supports were provided at each beam-to-column joint for both the boundary beams. Thus, the unbraced length of the columns was equal to the story height.

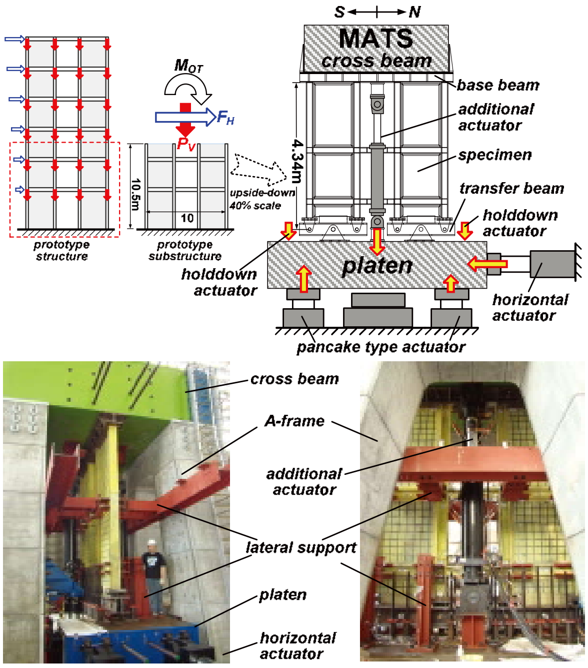

Fig. 4 Schematic of the substructure and test setup

The actuator system applied forces on the platen. Two horizontal actuators were employed to apply the lateral displacement on the specimen. Two cycles of 0.1%, 0.2%, 0.3%, 0.5%, 0.75%, 1.0%, 1.5%, 2.0%, 3.0%, 4.0% and 5.0% radian roof drifts were imposed sequentially on the specimen. The vertical actuators can be classified into 3 categories: (1) two rows of pancake-type actuators pushing the bottom of the platen. The difference in the applied forces between the two rows of actuators induced the overturning moment effects on the platen; (2) two hold-down actuators which were mounted on the A-frame of MATS and pushing on the top of the platen; and (3) two additional actuators which were anchored between the platen and the cross beam. The additional actuators pushed the platen downward. The resultant forces of these vertical actuators applied a constant vertical force (P_V=1400 kN). The relationship between the resultant moment M_{OT} of these vertical actuators and the lateral forces F_H applied by horizontal actuators is: $M_{OT} = F_H \times$ (2.51m). The relationship is calculated based on the assumption that the vertical distribution of the lateral forces acting on the original 6-story building is con- stant during the cyclic loading. The vertical distribution of the lateral forces was determined from the recommendations of the current Taiwan's seismic code.

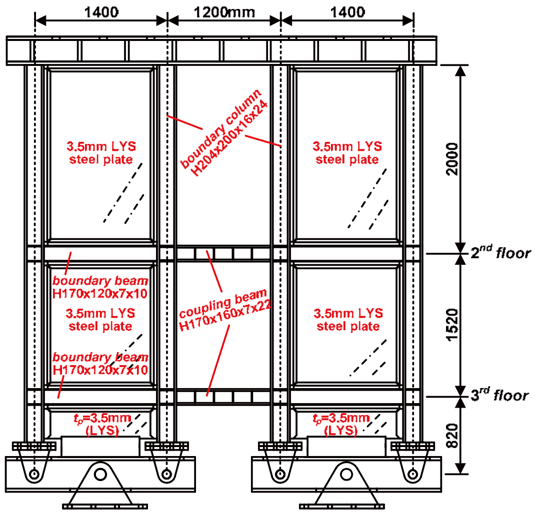

Fig. 5 Schematic of the test specimen

Test Results and Design Implications

Fig. 6 illustrates the force versus displacement relationship of the specimen. The C-SPSW specimen exhibited an excellently ductile behavior and dissipated significant amount of hysteresis energy during the cyclic loading test. The lateral and vertical load-carrying capacities did not notably deteriorate when the overall drift of the specimen reached 5% rad. The expected plastic mechanism was developed. The procedure of the test is stated in the following two paragraphs.

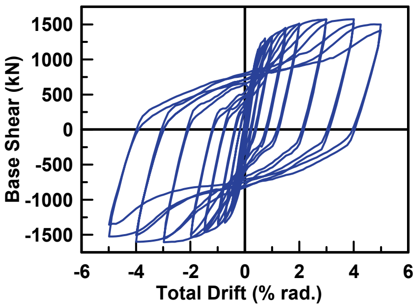

Fig. 6 Force versus displacement relationship of the specimen

The visible local buckling of the infill plates occurred at 0.3% rad. drift level. At a roof drift of 0.5% rad., the infill plates and the coupling beam web slightly yielded. The specimen initiated the notable hysteresis behavior at the 0.75% rad. drift level. At a roof drift of 1.0% rad., the fillet weld between the fishplate and the transfer beam in the 3rd story of the southern SPSW started to tear. In addition, a lot of horizontal yield lines appeared on the whitewash on the outer flanges of the outer column. It suggested that the flange yielded in axial force. At the drift level of 1.5% rad., the yielding of the column became more severe. The flaking of the whitewash was found at the outer flanges of the inner columns and at the webs of the outer columns.

At the 2.0% rad. roof drift, the fishplate was torn away from the transfer beam at the 3rd story of the southern SPSW. Notable flaking of the whitewash was found at the column webs. The locations of the flaking indicated that plastic zones on the inner columns' webs concentrated at the column base. In contrast, the plastic zones on the outer columns' webs spread over a wider region which is located at 50 to 80 mm away from the column base. At a roof drift of 3.0% rad., the flange local buckling developed at the RBSs of the boundary beams. As the roof drifts increased to 4% and 5% rad., the flange and web local buckling of the RBSs of the boundary beams became more severe. Except for the fracture of the weld between the fishplate on the transfer beam and the 3rd story infill plate of the northern SPSW, no other notable fracture occurred.

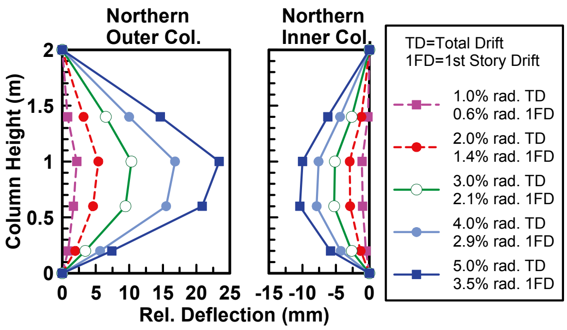

Fig. 8 Residual pull-in deflections of the 1st story columns in the northern SPSW after the various drift levels

Fig. 8 shows the relative deflections of the 1st story columns in northern SPSW when the lateral forces approached zero during the second cycle of the various drift levels. The relative deflection was obtained by subtracting the deflection due to the rigid body motion from thee total deflection. The relative deflection can be utilized to estimate the inward flexural deformation of the column induced by the panel forces. It can be found that residual "pull-in" deformations on the outer column were much larger than those on the inner column. This should be attributed to that the axial forces in the outer column were much higher, thus, the flexural strength of the outer column is smaller due to the axial-flexural interaction effect. However, form the Fig. 7, it can be found that the maximum residual deflection of the 1st story outer column was about 10 mm (=h_1/200) after the specimen had suffered two cycles of 3.0% rad. roof drift (2.1% rad. 1st story drift). The 1/200 of the story height can serve as the deflection index limiting the development of large secondary forces in the columns (Ellingwood, 2003). Moreover, the past test (Tsai et al. 2006) has shown that peak story drift a well-designed SPSW specimen during the collapse prevention level (2/50 hazard level) earthquake was about 2.0 to 2.5% rad. The test result suggests that, as the plastic hinge on the compressed bottom column form within the lowest quarter column height, the residual pull-in deflection of the column would not cause a severe second order effect after a collapse prevention level earthquake.

Conclusions

The test results show that the C-SPSW specimen behaved well in the cyclic test. The limited residual pull-in deflections of the columns suggest that the proposed capacity design for the boundary column could be a choice of design in the practice. Further design issues of C-SPSW will be explored based on the test results and additional analytical studies.

References

AISC. "Seismic Provisions for Structural Steel Buildings", American Institute of Steel Construction (AISC), Inc. 2005.

Ellingwood, B. "Serviceability Guidelines for Steel Structures", Engineering Journal Article (AISC). 2003.

Thorburn, L.J., Kulak, G.L., and Mont- gomery. C.J. "Analysis of Steel Plate Shear Walls", Structural Engineering Report No. 107, Department of Civil Engineering, University of Alberta, Edmonton, Alberta, Canada. 1983.

Tsai, K.C., Li, C.H., Lin, C.H., Tsai, C.Y. and Yu, Y.J. "Cyclic Tests of Four Two-story Narrow Steel Plate Shear Walls. Part 1: Analytical Studies and Specimen Design" Earthquake Engineering and Structural Dynamics. 2010. (accepted)

Tsai, K.C., Lin, C.H., Lin, Y.C., Hsieh, W.D and Qu, B. "Substructural Hybrid Tests of A Full Scale 2-Story Steel Plate Shear Wall." Technical Report NCREE -06-017, National Center for Research on Earthquake Engineering, Taipei, Taiwan, 2006. (in Chinese)

Vian D. and Bruneau, M. "Steel Plate Shear Walls for Seismic Design and Retrofit of Building Structures" Technical Report MCEER-05-0010, Multidisciplinary Center for Earthquake Engineering Research, Buffalo, NY, USA. 2005.

Structural Health Monitoring and Simulation of RC Frames Subjected to Shake Table Excitations

Wen-I Liao [1]

廖文義 [1]

Abstract

Structural health monitoring of reinforced concrete (RC) structures under seismic loads has recently attracted attention in the earthquake engineering research community. In this paper, a piezoceramic-based device called "smart aggregate" was used for the health monitoring of RC frame structures under earthquake excitations. Four RC moment frames instrumented with smart aggregates were tested using a shake table. The distributed piezoceramic-based smart aggregates embedded in the RC structures were used to monitor the health condition of the structures during the tests. The sensitiveness and effectiveness of the proposed piezoceramic-based approach were investigated and evaluated by analyzing the measured responses. The displacement ductility demand of the structural members was calculated and compared with the damage index determined from the health monitoring technology using the smart aggregate. The comparison has shown that the damage index is compatible with the calculated ductility demand.

Keywords: piezoceramic, smart aggregate, health monitoring, RC moment frame

Introduction

There are two major categories of piezoelectric based health monitoring: 1) The impedance-based approach, in which the impedance of piezoelectric transducers can be applied to the health monitoring of concrete structures (Sun et al. 1995, Ayres et al. 1998, Tseng and Wang 2004), and 2) Vibration-based health monitoring approach, in which the wave-propagation properties are studied to detect and evaluate the cracks and damages inside the concrete structures (Okafor et al. 1996, Saafi and Sayyah 2001, Song et al., 2007, Liao et al., 2008).

In this paper, piezoelectric based-smart aggregates were developed to form a distributed intelligent sensor network in perform structural health monitoring for concrete structures after earthquake excitation. Through a series of shaking table tests of four one-story two-bay reinforced concrete frames subjected to different level of base excitation, the local damage status was identified from the response measurements. The ground motion record TCU082 from the 1999 Taiwan Chi-Chi earthquake was used as the excitation source for the shake table under different acceleration levels. On the other hand, the simulation of nonlinear dynamic behavior of the RC member is important for predicting the response of the structure before an earthquake. A simple but accurate method is proposed in this paper for the simulation of the responses of the RC frames when subjected to earthquake excitations. The displacement ductility demand of the structural members calculated by the proposed method was compared with the damage index determined from the health monitoring technology using the smart aggregate. The comparison has shown that the damage index has a good agreement with the calculated ductility demand.

Experimental Setup

Four 1-story 2-bay reinforced concrete frames RCF2, RCF3, RCF4 and RCF5, designed with Taiwan Building Code, were constructed under identical design details and construction qualities. Each frame was tested on the NCREE's shaking table with different intensity levels of earthquake excitation. Figure 1 shows the dimension of the RC frame structure. Figure 2 shows the test setup on the shake table. Each span of the frame is 2 m and the height is 2.3 m. Dead load (lead ballistic) of 4 t was added to

[1] Associate Professor, National Taipei University of Technology, wiliao@ncree.org.

the top of the floor of the specimens RCF2-RCF4, and 5.5 t was added to the specimen RCF5 to ensure a significant inertia force on the frame. The cross section of the column and the beam were 20x20 cm and 16x20 cm, respectively. The rebar arrangement of the central column was 8-#4 longitudinal steel rebars with #3@10cm stirrup, and 4-#4 longitudinal steel rebars with #3@10cm stirrup for side columns. The average concrete strength was 210 kg/cm^2. The average yielding stresses for rebar was 4100 kg/cm^2. The foundation was designed to remain elastic when the failure of the reinforced concrete column or beam occurs. The horizontal displacements and response acceleration of the walls were measured by LVDTs and accelerometers, respectively. Furthermore, to prevent the accidental torsional motion of the concrete frame, lateral supporting steel frame were equipped in the four corners of concrete slab. The steel roller was designed to be located between the concrete slab and the supporting frame to reduce the friction force. The input ground acceleration history for all tests was the E-W component of the TCU082 station of the 1999 Taiwan Chi-Chi earthquake (denoted as TCU082EW). The first fundamental frequency of the frame in longitudinal direction was designed to be about 6.0 Hz. White noise excitations were also applied to these tested structures before and after the earthquake excitation from the shaking table. As shown in Table 1 each RC frame was tested with different intensity levels of ground excitation.

Table 1 Measured and identified four test frames from the test results.

Specimen	Excitation Name	Input PGA (gal)	Identified frequency (Hz)
RCF2	White noise	27	6.0
	TCU082	840	
	White noise	31	3.0
RCF3	White noise	24	6.0
	TCU082	1310	
	White noise	36	2.1
RCF4	White noise	30	6.0
	TCU082	1186	
	TCU082	668	
	White noise	33	2.1
RCF5	White noise	30	5.1
	TCU082	1248	
	White noise	30	2.0

The adopted smart aggregate of this study was proposed by Song *et al.* (Song *et al.*, 2007). It was fabricated by embedding a water-proof coated piezoceramic patch into a small concrete block as shown in Figure 3. This configuration offers protection to the fragile piezoceramic patches. The smart aggregates were embedded at the desired distributed locations before the casting. Figure 4 shows the embedded locations of smart aggregates in the tested column. The adopted smart aggregates sensing unit has the advantages of low cost and active sensing. Active sensing means one smart aggregate is actively excited by a desired wave form so that other distributed smart aggregates detect the responses. By analyzing the sensor signals, many important properties of the structures can be monitored and evaluated.

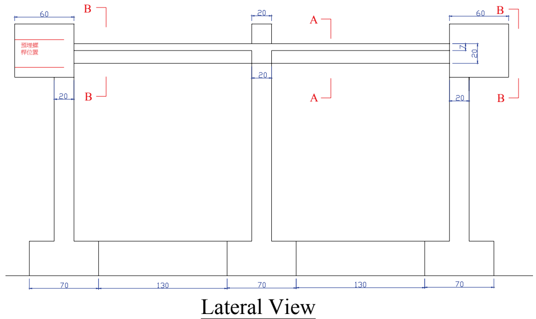

Fig. 1 Configuration of the test RC frame.

Fig. 2 Photo of test setup.

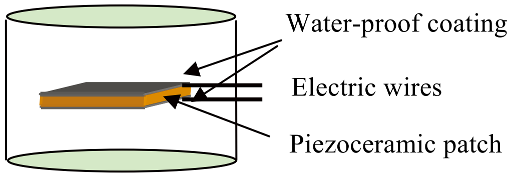

Fig. 3 Fabricated smart aggregates.

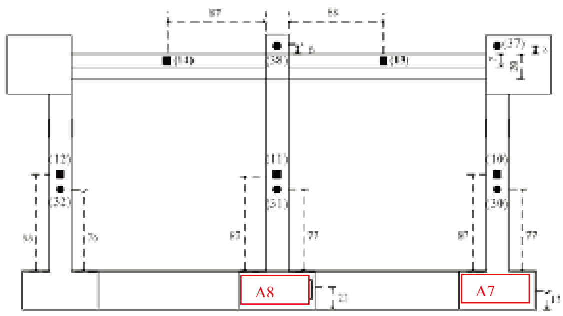

Fig. 4 Locations of smart aggregates.

Health Monitoring

The energy of smart aggregate sensor is calculated as

$$E = \int_{t_0}^{t_f} u^2 dt \tag{1}$$

where t_0 is the starting time, t_f is the finish time, and u is the sensor voltage. The energy vector for the healthy data is E_h. The energy vector for the damage status at time index i is defined as E_i. The damage index at time index i is defined as

$$I = \frac{|E_h - E_i|}{E_h} \tag{2}$$

The proposed damage index represents the transmission energy loss caused by damage. When the damage index is close to 0, it means the structure is in a healthy state. When the damage index is greater than a certain threshold, it means damage has appeared. In this case, the greater the index, the more serious the damage is. When the damage index is very close to 1, it means the concrete structure is near failure. A Sensor-History Damage Index Matrix (SHDIM) $M_{m\times n}$ is defined as

$$M_{m\times n} = \left[I_{i,j}\right]_{m\times n} \quad (i=1,\cdots m \text{ and } j=1,\cdots n) \tag{3}$$

where the matrix element at the i^{th} row and the j^{th} column, $I_{i,j}$, is the damage index of the i^{th} smart aggregate at the time of the j^{th} test (i.e. i is the sensor index, j is the time index); m is the total number of smart aggregates and n is the total number of tests. The damage status at different locations at different test time of the concrete specimen can be represented by a 3-dimensional damage index matrix plot.

The severity of the damage at RCF5 is more than the damage at RCF2. After the shake table tests, the smart aggregates were utilized for the structural health monitoring of the concrete column. The PZT-A8 shown in Figure 4 behaved as an actuator with excitation frequencies 1 kHz and 5 kHz; PZT sensors located in the column and beam behaved as sensors. The damage index matrix proposed was utilized in the structural health monitoring of tested RC frames. The damage index matrix of sensors is shown in Fig. 5. The sensor numbers were as according to the description of Fig. 4. From the damage index matrix shown in Fig. 5, the damage index values of each PZT sensor have an increased trend that related to the inertia force of the RC frames. This shows the effectiveness of the proposed damage index matrix to evaluate the severity of the damage at different frames.

Simulation of the Nonlinear Behaviors of Frames

A finite element model was established by using SAP2000 in the simulation of the dynamic behavior of the RC frame structure when subjected to different levels of earthquake ground excitations. In the simulated model of the RC frame, the beam and column were modeled as the linear elastic element with a nonlinear link at the ends of the element; the cracking moment, yielding moment, ultimate moment strength and corresponding curvatures were obtained by the software XTRACT. The hysteretic model for the analysis is the Takada model. The effective moment of inertia of the beam-column element adopted herein is the average of the cracked and uncracked moment of inertia. Figure 6 shows the simulated displacement time histories at the slab of the test RC frames and in comparison with those results measured in the test. From these figures, it cab be seen that the simulated method proposed in this study can accurately predict the maximum displacement and residual displacement of RC frame structures. The damage state of each member is important as well as the whole behavior of the structure. Ductility demand is a suitable and common index to represent the damage state of beam-column members. Table 2 shows the ductility demand of columns C1, C2 and C3 of RC frames. The comparison of calculated ductility demand and the damage index obtained by smart aggregates is shown in the table. The increasing trend of the damage index is consistent with the trend of calculated ductility demand. This demonstrates again the effectiveness and accuracy of the health monitoring by smart aggregates.

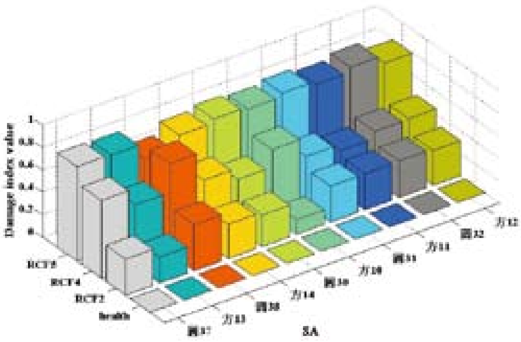

(a) excitation frequency=1 kHz

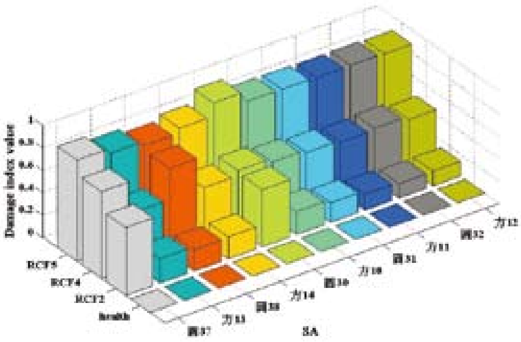

(b) excitation frequency=5 kHz

Fig. 5 Damage index matrix of sensors.

Conclusions

In this paper, a smart aggregate-based sensor network has been applied to the health monitoring of concrete frames under different levels of intensity of earthquake excitation. From the experimental results, the smart aggregate-based sensors can monitor and predict the health status of the tested frame through the proposed damage index matrix. The smart aggregate-based sensor has the potential to be implemented to real concrete structures to enhance safety. A method was proposed for the simulation of the responses of the RC frames subjected to earthquake excitations. The displacement ductility demand of the structural members was calculated and compared with the damage index determined from the health monitoring by smart aggregates. The comparison has shown that the damage index is compatible with the calculated ductility demand.

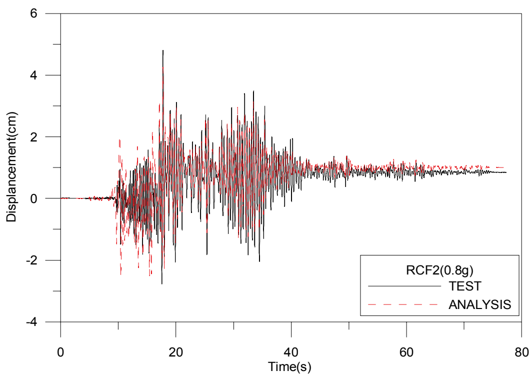

(a) RCF2

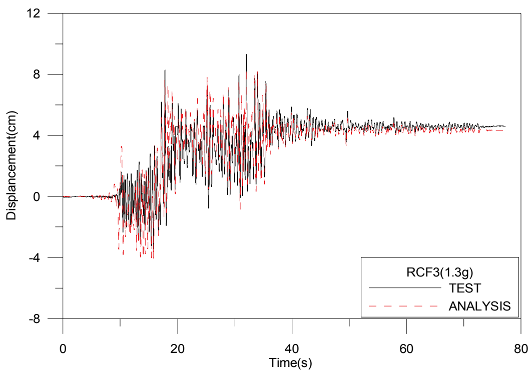

(b) RCF3

Fig. 7 Simulated displacements and test displacements of RC frames.

References

Sun F. P., Chaudhry Z, Rogers C A and Majmundar M. (1995), "Automated real-time structure health monitoring via signature pattern recognition", Proceedings of the SPIE -Smart Structures and Materials Conferences, vol. 2443, pp. 236-247

Ayres J.W., Lalande F., Chaudhry Z. and Rogers C., (1998), "Qualitative impedance-based health monitoring of civil infrastructures", Smart Materials and Structures, vol.7, no. 5 , 1998, pp. 599-605

Liao W.I., Gu H, Olmi C, Song G, and Mo Y.L., "Structural Health Monitoring of a Concrete Column Subjected to Shake Table Excitations Using Smart Aggregates", 2008 ASCE Earth & Space Conference, March 3-5, 2008, Long Beach, CA, USA.

Tseng K. K. and Wang, L., (2004), "Smart piezoelectric transducers for in situ health monitoring of concrete", Smart Materials and Structures, vol. 13, no. 5, 2004, pp.1017-1024.

Okafor A.C., Chandrashekhara and Jiang Y.P. (1996), "Delamination prediction in composite beams with built-in piezoelectric devices using modal analysis and neural network", Smart Materials and Structures, vol. 5, no. 3, pp. 338-347

Saafi M. and Sayyah T.(2001), "Health monitoring of concrete structures strengthened with advanced composite materials using piezoelectric transducers", Composites Part B: Engineering, vol. 32, no.4, pp. 333-342

Song G., Gu H., Mo Y. L., Hsu T., and Dhonde H., (2007) "Concrete structural health monitoring using embedded piezoceramic transducers", Smart Materials and Structures, vol. 16, pp. 959-968.

XTRACT, software for Cross-sectional X Structural Analysis of Components", 2006, TRC/Imbsen Software Systems.

Wilson E.L., "SAP2000 Analysis Reference", 2002, Computer sand Structures, Inc, Berkeley, California, USA.

Table 2(a) Damage index and ductility demand of columns(1 kHz)

specimen / column	RCF2		RCF4	
	Damage index	Ductility demand	Damage index	Ductility demand
C1(Pzt32)	0.418	1.203	0.444	1.837
C2(Pzt31)	0.410	1.276	0.439	1.909
C3(Pzt30)	0.385	1.213	0.453	1.861

Table 2(b) Damage index and ductility demand of columns(5 kHz)

specimen / column	RCF2		RCF4	
	Damage index	Ductility demand	Damage index	Ductility demand
C1(Pzt32)	0.134	1.203	0.505	1.837
C2(Pzt31)	0.170	1.276	0.506	1.909
C3(Pzt30)	0.151	1.213	0.560	1.861

Structural Health Monitoring of Arch Dam using Seismic and Ambient Data

Jian-Huang Weng[1] Chin-Hsiung Loh[2] and Pei-Yang Lin[3]

翁健煌[1]、羅俊雄[2]、林沛暘[3]

Abstract

This paper presents the system identification of the Fei-Tsui arch dam using the recorded seismic data and ambient vibration data. The modal properties of the dam under different reservoir water levels were identified using the recorded seismic data from 84 earthquake events. Considering the spatial variability of input excitation, both multi-input and single-input system models were employed in the input/output subspace identification. The regression curves between the natural frequencies and the reservoir water level were developed from the statistical analysis of identification results. In order to compare the current behavior of the dam to its past, an ambient vibration experiment was performed and the output-only stochastic subspace identification method was used to identify the current modal properties of the dam. Finally, a safety evaluation was made by pointing the current identification result on the developed regression curve. Furthermore, the comparison between different identification algorithms in this study was made. From the stability diagram of the identification, the output-only stochastic subspace identification (using ambient data) provides clearer system characteristics than the input/output subspace identification (using seismic data). Discussion on the single-input model and the multi-input model for subspace identification is also made in this study.

Keywords: Structural Health Monitoring, System Identification, Fei-Tsui Arch Dam, Ambient Vibration

Introduction

Monitoring technology plays an important role in securing the integrity of structural system and maintaining the longevity of the structure. It consists of three aspects: (1) instrumentation with sensors, (2) methodologies for obtaining meaning information concerning the structural health monitoring, and (3) early warning from the measured data. Various methods based on the dynamic and static tests have been applied in addressing the structural health monitoring and damage identification. One important problem in the seismic safety analysis of dams is the evaluation of the hydrodynamic-forces-induced reservoir-dam interaction during strong earthquakes. Generally, the damage of structure such as dam may be detected from the variation of structural features; however, these features may be affected by the changing environmental conditions such as reservoir's water level and temperature. Around the world, very few major dams had enough seismic response data for developing the safety evaluation guideline of dams. The problem is even more complicated in case of concrete arch dam because of the geometry of the dam's cross-section. Therefore, continuous monitoring as well as seismic monitoring of an arch dam becomes one of the important objectives in conducting safety assessment of the dam.

In this study the discrete-time system identification of Taiwan's Fei-Tsui arch dam, using both the recorded seismic data and the ambient vibration data were studied. Discussions are made on the results of the conducted study.

Description of the Fei-Tsui Arch Dam

The sections of Fei-Tsui arch dam is shown in Fig. 1. The level of the water in the reservoir normally varies between elevation of 170 m and 120 m. The local temperature normally varies between 50 °F to 86 °F. According to previous research, the reservoir level is the most important factor in changing the dynamic features of the arch dam. Therefore, the relationship between reservoir water level and features must be clarified and regressed before the structural health monitoring of the arch dam.

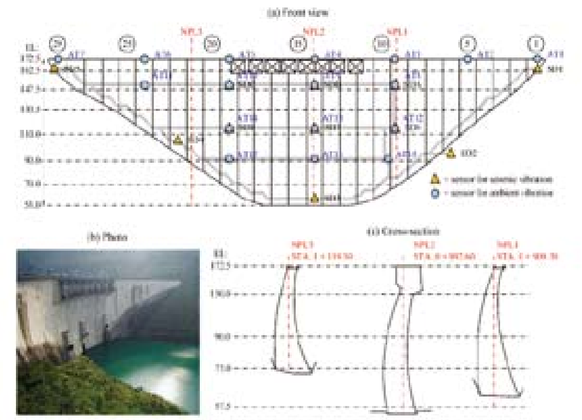

Fig. 1 The Fei-Tsui arch dam; (a) Front view, (b) Photograph, (c) Cross-sections at NPL1, NPL2 and NPL3.

System Identification from Seismic Data

To monitor the dynamic properties of the dam during earthquake, eleven tri-axial accelerometers were deployed in the Fei-Tsui dam as shown in Fig. 1(a). The strong motion accelerometers in Fei-Tsui dam were upgraded in 1998. The strong motion records of 84 earthquakes collected after the upgrade in 1998 (from 1999 to 2008) were chosen and used in this study. The most intense of these earthquakes occurred on March 31, 2002 and it was called as the 331 Earthquake in Taiwan. The recorded PGA of 331 Earthquake was up to 0.028g which is greater than 921 Chi-Chi Earthquake (0.025g). The strong motion instrumentation of Fei-Tsui arch dam includes eleven GeoSIG AC-63 tri-axial accelerometers on the dam body since 1998. The analogue signals were digitized by using a 16-bit ADC and the corresponding sampling rate is 200Hz. The specification of the accelerometer is shown in Table 1.

AC-63 tri-axial accelerometer		VSE-15D velocity sensor	
Full-scale	*± 2 g*	Full-scale	*± 0.1 m/s*
Type	*Force balanced accelerometer*	Type	*Force balanced accelerometer*
Sensitivity	*10V/g*	Sensitivity	*1000V/m/s*
Dynamic Range	*> 120 dB*	Dynamic Range	*approximately 140 dB*
Bandwidth	*DC ~ 100 Hz*	Bandwidth	*0.2 ~ 100 Hz*
Damping	*70 % of critical*	Damping	*100.% of critical*

Table 1 Specification of tri-axial accelerometer and VSE-15D velocity sensor.

Numerical model of the arch dam

According to the previous research of Loh et al. (2000), the input ground motion for the Fei-Tsui arch dam was found to be varied along the abutment of the dam and it has been suggested that the dam should be considered as a multi-input system for system identification. As long as the ground motion was measured at finite locations (SD1~SD5), the dam was naturally considered as a dynamic system with multiple support excitations [5]. The equation of dynamic equilibrium for such a system can be written in partitioned form:

$$\begin{bmatrix} \mathbf{m} & \mathbf{m_g} \\ \mathbf{m_g}^T & \mathbf{m_{gg}} \end{bmatrix}\begin{Bmatrix} \ddot{\mathbf{u}}^t \\ \ddot{\mathbf{u}}_g \end{Bmatrix}+\begin{bmatrix} \mathbf{c} & \mathbf{c_g} \\ \mathbf{c_g}^T & \mathbf{c_{gg}} \end{bmatrix}\begin{Bmatrix} \dot{\mathbf{u}}^t \\ \dot{\mathbf{u}}_g \end{Bmatrix}+\begin{bmatrix} \mathbf{k} & \mathbf{k_g} \\ \mathbf{k_g}^T & \mathbf{k_{gg}} \end{bmatrix}\begin{Bmatrix} \mathbf{u}^t \\ \mathbf{u}_g \end{Bmatrix}=\begin{Bmatrix} \mathbf{0} \\ \mathbf{p_g} \end{Bmatrix} \quad (1)$$

The total displacement vector now contains two parts: (1) $\mathbf{u_g}$ includes the DOFs of the supports (such as SD1~SD5); and (2) $\mathbf{u^t}$ includes all DOFs of the dam except the DOFs of the supports. For earthquake loading, it can be observed that only the support forces $\mathbf{p_g}$ are applied to the system. Eq. (1) then can be rewritten by focusing on the dynamic displacements $\mathbf{u}$ on the DOFs of the dam:

$$\mathbf{m\ddot{u}} + \mathbf{c\dot{u}} + \mathbf{ku} = \mathbf{p_{eff}} \quad (2)$$

where the effective earthquake forces is:

$$\mathbf{p_{eff}} = -(\mathbf{m\ddot{u}^s} + \mathbf{m_g\ddot{u}_g}) - (\mathbf{c\dot{u}^s} + \mathbf{c_g\dot{u}_g}) \quad (3)$$

where $\mathbf{u^s} = \mathbf{u^t} - \mathbf{u}$ is the quasi-static displacement. Eq. (3) can be further simplified by considering two "possible" assumptions for real application: (1) small damped system; and (2) lump mass system. Based on the first assumption, the damping force is relatively smaller than the inertia force thus it can be neglected. For the second assumption, the non-diagonal term $\mathbf{m_g}$ will be a null matrix and therefore can be dropped. After the simplifications of the effective earthquake forces, Eq. (2) can be rewritten as:

$$\mathbf{m\ddot{u}} + \mathbf{c\dot{u}} + \mathbf{ku} = -\mathbf{m\iota\ddot{u}_g} \quad (4)$$

where $\iota = -\mathbf{k^{-1}k_g}$ is the influence matrix because it describes the influence of support displacements on the structural displacements. Eq. (4) defines a numerical model for a dynamic system with multiple support excitations. On the other hand, the input ground motion was assumed to be uniform and one of the records from SD1~SD5 has been selected to be the representative ground motion. The motion equation will be simpler than Eq.(4) base on assumption of uniform input:

$$\mathbf{m\ddot{u}} + \mathbf{c\dot{u}} + \mathbf{ku} = -\mathbf{m1\ddot{u}_g} \quad (5)$$

where $u_\mathbf{g}$ is a scalar of the uniform input and $\mathbf{1}$ is a vector with each element equal to unity. A multi-support excitation system may use more input excitations to model the non-uniform input ground motions but it also needs to discrete the boundary of the dam in order to get the equivalent earthquake forces. And also, there are two assumptions needed to be satisfied for the simplification of effective earthquake forces in Eq. (3). As for the single-input system, there is only one assumption that should be satisfied but this assumption is not "completely" true for real applications.

Input/output subspace identification

The input/output subspace identification algorithm starts from the continuous-time state space model, which is a different form of the motion equation:

$$\dot{\mathbf{x}} = \mathbf{A_c x} + \mathbf{B_c \ddot{u}_g} + \mathbf{w} \quad (6)$$

$$\ddot{\mathbf{u}}^t = \mathbf{Cx} + \mathbf{v} \quad (7)$$

where

$$\mathbf{x}=\begin{bmatrix}\mathbf{u}\\ \dot{\mathbf{u}}\end{bmatrix};\mathbf{A}_c=\begin{bmatrix}\mathbf{0} & \mathbf{I}\\ -\mathbf{m}^{-1}\mathbf{k} & -\mathbf{m}^{-1}\mathbf{c}\end{bmatrix};\mathbf{B}_c=\begin{bmatrix}\mathbf{0}\\ -\boldsymbol{\iota}\end{bmatrix};$$
$$\mathbf{C}=[-\mathbf{m}^{-1}\mathbf{k}\quad -\mathbf{m}^{-1}\mathbf{c}]$$

$\mathbf{w}$ is the process noise due to disturbances or modeling error and $\mathbf{v}$ is the measurement noise due to disturbances or sensor noise. It is assumed that they are zero mean and white vector sequences. In Eqs. (6) and (7), the inputs of this system are the absolute accelerations of all supports $\ddot{\mathbf{u}}_g$ and the outputs are the absolute accelerations of all degree-of-freedoms (DOFs) of the dam $\ddot{\mathbf{u}}^t$. The basic concept of subspace algorithms is exploitation of the state as a finite-dimensional interface between the past part and the future part. First, the input and output data are arranged into the Hankel matrices. Then projection theorem is employed to extract the observability matrix $\boldsymbol{\Gamma}_i$:

$$\mathbf{Y}_f/_{\mathbf{U}_f}\mathbf{W}_p=\boldsymbol{\Gamma}_i\mathbf{X}_f^d \tag{8}$$

After extracting the observability matrix using singular value decomposition, the system parameters $\mathbf{A}_c$ and $\mathbf{C}'$ can now be computed easily. Finally, the natural frequencies and mode shapes of the dam can be identified.

For the multi-input case, the absolute acceleration records at stations SD1, SD2, SD3, SD4 and SD5 were defined as the input excitations. The absolute acceleration records at SD6, SD7, SD8, SDA, SDB and SDC were defined as the outputs. In order to consider the canyon phenomenon, either SD1 or SD5 was chosen as the uniform input in the single-input case and the outputs are the same as above. The identification results of 331 Earthquake are presented as stability diagrams and shown in Fig. 2.

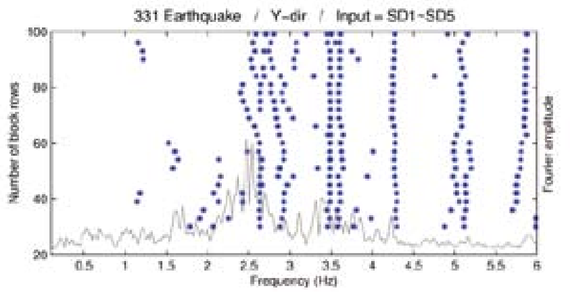

Fig. 2 Stability diagrams of the multi-input case using seismic data of 331 Earthquake.

Following the subspace identification, the stability diagram describes the identified modal frequencies under different choice of the number of block row. Including 331 Earthquake, a total of 84 earthquake events (from 1999 to 2008) were used to identify the modal frequencies under different reservoir water level. Finally, the relationships between the reservoir water level and modal frequencies were developed and regressed by using the curve fitting tool. As shown in the Fig. 3, the modal frequency can be calculated from the reservoir level according to the general power-2 function:

$$f(x)=ax^b+c \tag{9}$$

where $f(x)$ is the modal frequency (in Hz) and x is the corresponding reservoir level. It is observed that the modal frequencies of dam decreases when the reservoir level increases.

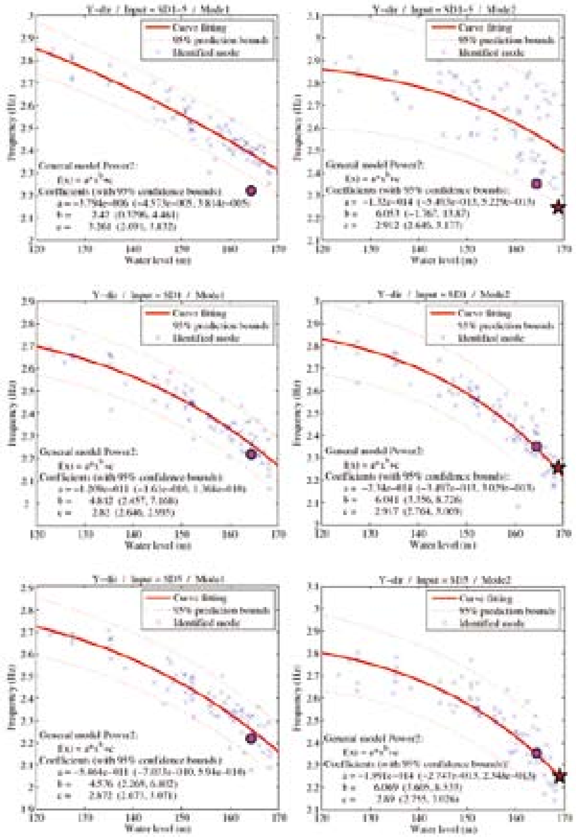

Fig. 3 Regression analysis of the relationship between reservoir level and natural frequencies of the Fei-Tsui arch dam. (☆ points the result from force vibration test; ○ points the result from ambient vibration test).

System Identification from Ambient Data

An ambient vibration test was conducted in the dam on October 30, 2009, and the corresponding reservoir water level was 164.0 m. There were 17 positions selected as measurement locations of the ambient vibration tests (AT1~AT17 as shown in Figure 1(a)). It required four steps to complete the ambient vibration test to cover all the desirable measurement points. For ambient vibration tests, a total of eight VSE-15D velocity sensors were used at the same time. Table 1 shows the specification of the sensor. It must be noted that the resolution of the sensor for ambient vibration test is 10^{-8} g and the resolution of AC-63 accelerometer is about 10^{-5} g.

Output-only stochastic subspace identification

Stochastic subspace identification algorithm was used to the ambient vibration data. This method computes the state space model of the stochastic system using output data. A stochastic system is similar to Eqs. (6) and (7) but its inputs are zero mean, white vector sequences denoted as $\mathbf{w}$ and $\mathbf{v}$:

$$\dot{\mathbf{x}} = \mathbf{A}_c\mathbf{x} + \mathbf{w} \tag{10}$$

$$\bar{\mathbf{u}}^t = \mathbf{C}\mathbf{x} + \mathbf{v} \tag{11}$$

The white noise excitation is the most important assumption of this theory which is somehow the difficulty of the ambient vibration test. The computation procedures of stochastic subspace identification are very similar to the general subspace identification expect for the application of orthogonal projection defined as follows:

$$\frac{\mathbf{Y_f}}{\mathbf{Y_p}} = \mathbf{\Gamma_i}\hat{\mathbf{X}}_\mathbf{f} \tag{12}$$

Following the procedure in subspace identification, the stability diagrams of the system identification from each step can be attained, as shown in Fig. 4. These stability diagrams from each test step clearly mark out the locations of the dam's natural frequencies and the results are consistent with the dominant frequencies of the Fourier spectrum of the responses.

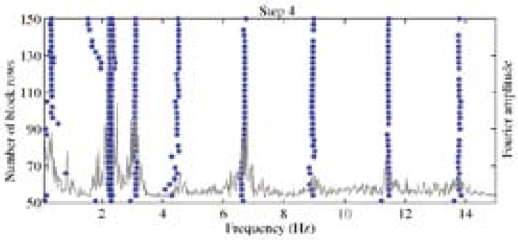

Fig. 4 Stability diagram from stochastic subspace identification.

The global mode shapes can also be determined from the measurement of each data set. Figure 5 shows the global mode shapes from ambient vibration test and the mode shapes estimated using seismic response data of 331 Earthquake are also shown.

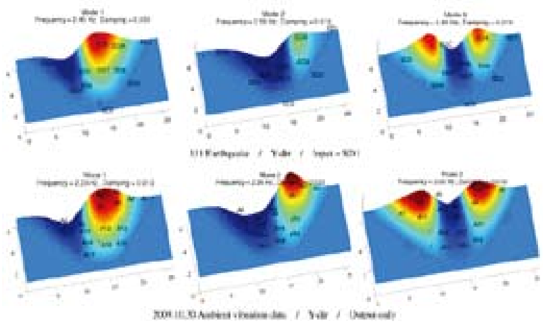

Fig. 5. Mode shapes of Fei-Tsui arch dam identified from seismic vibration data (SD1 input case) and ambient vibration data.

Conclusions

Based from the results, the analysis of ambient vibration data will have a significant effect on the improvement of the stability diagram by means of using the stochastic subspace identification. In order to compare the accuracy of multi-input and single-input identifications, the result from ambient vibration test was plotted as a circle (see Fig. 3). Another result from the forced vibration test was also plotted as the star in the same figure. This force vibration data are quoted from reference [1] which shows the first two modal frequencies (i.e. 2.26 Hz and 3.02 Hz). The regression curves from single-input identification accurately fit the results from both ambient vibration test and force vibration test.

A brief conclusion can be made further based on the discussed comparisons. The output-only stochastic subspace identification has been found to be a more reasonable approach in identifying the modal properties of the arch dam. Moreover, it can be suggested that ambient vibration measurement system may be a better solution for monitoring the dynamic characteristics of dam yet, it needs continuous recording of ambient vibration to conform the reliability of the said approach.

References

1. Loh, C. H. and Tou, I. C. (1995) "A system identification approach to the detection of changes in both linear and non-linear structural parameters," *Earthq. Engrg. Struct.* Dyn. 24,8597.
2. Darbre, G.R., de Smet, C.A.M., and Kraemer, C. (2000) "Natural frequencies measured from ambient vibration response of the arch dam of Mauvoisin." *Earthquake Engineering and Structural Dynamics*, 29, 577-586.
3. Loh, C.H., and Wu, T.S. (1996). "Identification of Fei-Tsui arch dam from both ambient and seismic response data." *Soil Dynamics and Earthquake Engineering*, 15, 465-483.
4. Loh, C.H., and Wu, T.C. (2000). "System identification of Fei-Tsui arch dam from forced vibration and seismic response data." *J. Earthquake Engineering*, 4(4),511-537.
5. Chopra, A.K. (2001) . *Dynamics of structures – Theory and applications to earthquake engineering*, 2nd ed, Prentice Hall, New Jersey, 384-388.
6. Van Overschee, P., De Moor, B. (1996) *Subspace identification for linear systems : Theory - Implementation – Applications*, Kluwer, Dordrecht.

Benchmark Building Model for Structural Control and Damage Identification

Hung-Wei Chiang[1] Pei-Yang Lin[2] and Chin-Hsiung Loh[3]

江宏偉[1]、林沛暘[2]、羅俊雄[3]

Abstract

This paper presents the benchmark building model for structural control and damage identification. The three-storey benchmark building model (almost full scale) was designed, simulated in FEM and been tested on the shaking table. With the modular design concept, various type of structures (with or without bracing, stiffness eccentric, earthquake excitations) were studied. The structural parameters, mathematical model, simulation results and shaking table test data were collected in the data bank. The data bank is open to public and can be used to develop and verify the system identification and damage detection algorithms. At the same time, the benchmark building model was used as the benchmark problem for the structural control system. The modular bracing system can fit various types of control devices. Different control devices and control algorithms can be applied to perform back-to-back comparison of the control systems. The design detail, connection of the control device, responses of the bare frame and the passive controlled responses are shown in this study. All these data is open to public, and researchers can use it to develop and verify their control system. Moreover, this study aimed to propose the benchmark models and support the development of structural control and damage identification.

Keywords: benchmark model, Structural Control, Damage Identification

Introduction

During the last decade, several benchmark structural control models have been developed through the sponsorship of the ASCE Committee on Structural Control and the International Association of Structural Control and Monitoring (IASCM). The main objective of developing these models has been the standardized evaluation of the performance of various control systems/ algorithms when applied to different structural systems. An extensive analysis of benchmark structural control problems formed the basis for a special issue of Earthquake Engineering and Structural Dynamics. Recently, the well-defined analytical benchmark problems have also been developed for bridge structures subjected to seismic excitation through the sponsorship of the ASCE Structural Control Committee.

This study aimed to propose the benchmark models and support the development of structural control and damage identification. To achieve this objective, a serious FEM analysis was done to get a suitable design of the benchmark building structure which can provide suitable and obvious nonlinear behavior under the capacity of the shaking table at the National Center for Research on Earth quake Engineering (NCREE). After the structural element was designed, the modular concept was introduced to the construction of the benchmark model. More structural types (such as stiff eccentric, soft floor, torsion coupling, rapid switch column, etc.) can provide more information to be used and be stored on the data bank. As a result, the modular design make

[1] Research Assistant Fellow, National Center for Research on Earthquake Engineering.
[2] Research Fellow, National Center for Research on Earthquake Engineering.
[3] Professor, Department of Civil Engineering, National Taiwan University.

the benchmark model be transformed into different structural types and allowed the model to have nonlinear behavior. Since all the nonlinear behaviors were concentrated on the rapid-switch column, the shaking table tests were done in series and rapidly. All the structural parameters, mathematical model, simulation results and shaking table test data were collected in the data bank, thus researchers can use it for free to develop and verify their damage identification algorithms.

Furthermore, the benchmark model for structural control was designed and tested on the shaking table. In the past four years, various kinds of control devices have been tested on this benchmark model. This study wanted to achieve its main objective, i.e. to set analytical benchmark models based on large experimental models allowing researchers in structural control to test their algorithms and devices and to directly compare the results. Thus, both the bare frame and the passive controlled benchmark structure were tested and all the tests data were collected in the data bank. Researchers on structural control system can use the stored data to develop their established control system and have it correlated with others.

Design of the Benchmark Building Model

To obtain the real structural responses of the full-scale structure, the benchmark model was designed. There were several design points considered: 1) The benchmark model needs to have obvious nonlinear behavior under the capacity of the shaking table in NCREE (Size: 5m x 5m, Load: 50tons, PGA: 2g); 2) The benchmark model must be adjusted to fit various structural types easily and quickly; 3) The nonlinear elements must be easily changeable; and 4) The dead load of the benchmark model must reflect realistic loading. According to these points, serious FEM simulations were done through the "ABAQUS" program. Finally, the three-storey benchmark model was designed to be 3m long, 2m wide, and 3m high for each story, with a total structural height of 9m. The mass of each floor (including the columns) was 6 tons and the total mass was 18 tons. The size of columns was selected as H150x150x7x10 and the size of beams was H150x150x7x10.

The corresponding frequencies and mode shapes are shown in Fig. 1. The elements which have nonlinear deformation under various PGA levels of excitation (El Centro NS) are listed in Table 1.

Mode 1: Freq.=1.0778 Hz　　Mode 2: Freq.=1.400 Hz

Fig. 1 The mode shape and modal frequencies from the FEM.

Table 1 Nonlinear deformation under various PGA levels of excitation.

El Centro	Strong-Axis	Weak Axis
100 gal	None	None
200 gal	None	Column: 2F(C11,20), 1F(C21,30)
300 gal	None	Column: 3F(C1), 2F(C11,20), 1F(C21,30)
500 gal	Beam: 2F(B2001), 1F(B3001) Column: 1F(C30)	Column: 3F(C1,C10), 2F(C11,20), 1F(C21,30)

Shaking Table Tests for Damage Identification

After the benchmark model was designed and simulated in the FEM simulation, two benchmark modes were build according to the design plots shown in Fig. 2, and been tested on the shaking table in NCREE. Seven structural types were tested on the shaking table tests as shown in Fig. 3.

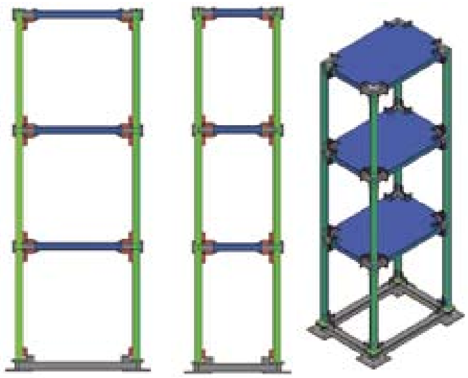

Fig. 2. Front-view, side-view and 3D-view of the three-stories benchmark model

Benchmark model A: The long-direction was the strong direction of the column. The linear tests (El Centro, ChiChi/TCU076, ChiChi/TCU082, and white noise) were done first and then the nonlinear tests (nonlinear excitation cases : 300、500 、1000、1500、1000、1200gals El Centro NS; The white noise tests were done before and after the nonlinear test.).

Benchmark B: The longitudinal direction is the weak direction of the column. The linear tests (El Centro, ChiChi/TCU076, ChiChi/TCU082, and white noise) were done first followed by the nonlinear tests (nonlinear excitation cases: 100、1000、500、300、100gals ChiChi/TCU082 NS; the white noise tests were done before and after the nonlinear test.). The test cases were listed in Table 2.

Benchmark C1: The longitudinal direction is the weak direction of the column. Only the linear tests (El Centro, ChiChi/TCU076, ChiChi/TCU082, and white noise) were done. For each excitation, both 50 gals and 100 gals of intensities were tested.

Benchmark C2: The longitudinal direction is the weak direction of the column. The bracing system (L150x150*2) was installed as shown in Fig. 3 to simulate the stiff eccentric condition. Only the linear tests (El Centro, ChiChi/TCU076, ChiChi/TCU082, and white noise) were done. For each excitation, both 50 gals and 100 gals of intensities were tested.

Benchmark C3: The longitudinal direction is the weak direction of the column. The bracing system (L150x150*2) was installed as shown in Fig. 3 to simulate the soft floor condition (2F). Only the linear tests (El Centro, ChiChi/TCU076, ChiChi/TCU082, and white noise) were done. For each excitation, both 50 gals and 100 gals of intensities were tested.

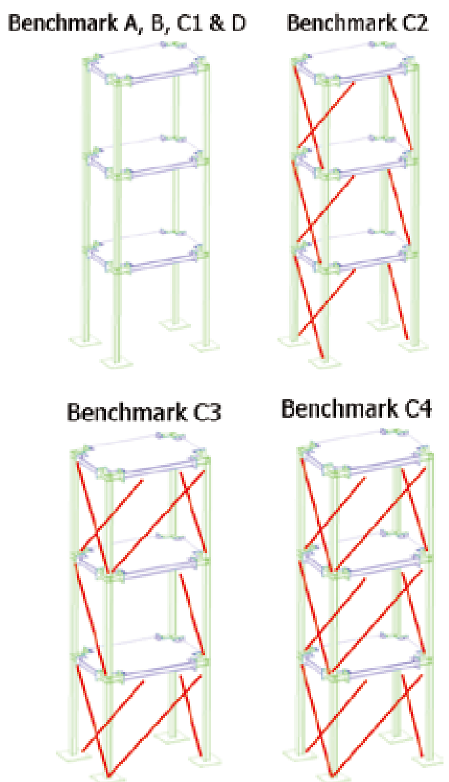

Fig. 3. Structural types of the three-storey benchmark model.

Benchmark C4: The longitudinal direction is the weak direction of the column. The bracing system (L150x150*2) was installed as shown in Fig. 3 to simulate the full brace condition. Only the linear tests (El Centro, ChiChi/TCU076, ChiChi/TCU082, and white noise) were done. For each excitation, both 50 gals and 100 gals of intensities were tested.

The sensor arrangement of the shaking table test is shown in Fig. 4. The displacement, velocity, acceleration, and strain of the column were measured. All the test data were collected and stored in the databank. In addition to the original data, the data bank also provided the simple drawing of the structural responses and the FFT amplitude.

Benchmark D: The longitudinal direction is the weak direction of the column. The linear tests 1 (El Centro, ChiChi/TCU076, ChiChi/TCU082, and white noise) were done first followed by the linear tests 2, where which the column in the 1st floor had a weak points, were done with the same excitation cases. Lastly, the nonlinear tests (nonlinear excitation cases: 100、1000、500、300、100gals ChiChi/TCU082 NS; the white noise tests were done before and after the nonlinear test.) were performed.

Table 2. List of the test cases of Benchmark model B in the shaking table test.

Test No.	Excitation case	PGA (ideal)	Direction
B1	Random	50	X-dir. / Weak Dir.
B2	Random	100	X-dir. / Weak Dir.
B3	El Centro NS	50	X-dir. / Weak Dir.
B4	El Centro NS	100	X-dir. / Weak Dir.
B5	ChiChi/TCU076/NS	50	X-dir. / Weak Dir.
B6	ChiChi/TCU076/NS	100	X-dir. / Weak Dir.
B7	ChiChi/TCU082/NS	50	X-dir. / Weak Dir.
B8	ChiChi/TCU082/NS	100	X-dir. / Weak Dir.
B9	Random	50	Y-dir. / Strong Dir.
B10	Random	100	Y-dir. / Strong Dir.
B11	El Centro NS	50	Y-dir. / Strong Dir.
B12	El Centro NS	100	Y-dir. / Strong Dir.
B13	ChiChi/TCU076/NS	50	Y-dir. / Strong Dir.
B14	ChiChi/TCU076/NS	100	Y-dir. / Strong Dir.
B15	ChiChi/TCU082/NS	50	Y-dir. / Strong Dir.
B16	ChiChi/TCU082/NS	100	Y-dir. / Strong Dir.
B17	ChiChi/TCU082/NS	100	X-dir. / Strong Dir.
B18	Random	50	X-dir. / Strong Dir.
B19	ChiChi/TCU082/NS	1000	X-dir. / Strong Dir.
B20	Random	50	X-dir. / Strong Dir.
B21	ChiChi/TCU082/NS	500	X-dir. / Strong Dir.
B22	Random	50	X-dir. / Strong Dir.
B23	ChiChi/TCU082/NS	300	X-dir. / Strong Dir.
B24	Random	50	X-dir. / Strong Dir.
B25	ChiChi/TCU082/NS	100	X-dir. / Strong Dir.
B26	Random	50	X-dir. / Strong Dir.

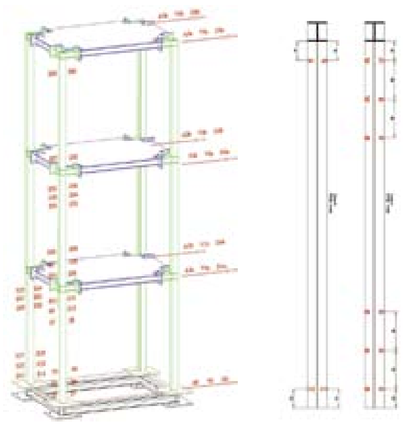

Fig. 4. Sensor arrangement of the three-stories benchmark model.

Shaking Table Tests for Structural Control

To expand the usage of the benchmark model, the three-storey benchmark building model was also used as the standard reference problem for the structural control system. The modular bracing system can fit various types of control devices. Different control devices and control algorithms can use it to perform back-to-back comparison of control systems. The design details, connection of the control devices, and responses of the bare frame and the passive controlled responses are shown in this study. All the data were made available to the public, and even researchers can utilize them to develop and verify their control systems.

To install the control devices for the structural responses induced by earthquake excitations, a strong middle bracing system was designed as shown in Fig. 5. The element size of the middle bracing was selected as H200x200. The modular design detail made the possible use of various kinds of control devices. Various control devices were install onto the benchmark model and been tested on the shaking table tests. Figure 6 shows the photos of the shaking table test of the three-storey benchmark structure with passive damper in the first story. All test results and performance tests of the control devices were collected and stored in the databank. The researchers can use these data and the original data of the benchmark model to perform possible back-to-back comparison of their control systems. In addition, the semi-active controllable MR damper manufactured by NCREE was tested too. Researchers can use the mathematical models (provided in the data bank) of the benchmark model and the nonlinear MR damper to simulate their semi-active control algorithms. The succeeding shaking table tests of the semi-active control system can be done through the international cooperation program.

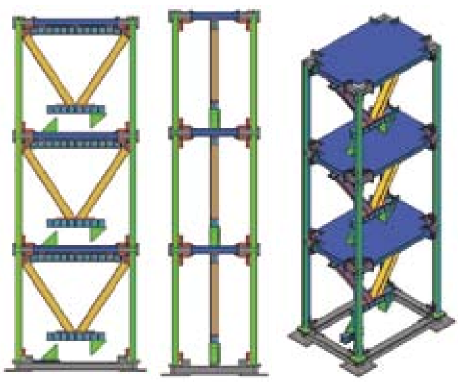

Fig. 5. Front-view, side-view and 3D-view of the three-stories benchmark model

Fig. 6. Photos of the three-story benchmark structure with passive damper in the fist story.

Conclusions

This paper presents the benchmark building model for structural control and damage identification. The design procedure, test cases, sensor arrangements and materials of the databank were illustrated. Both the benchmark model for system identification and structural control were presented. The databank include the structural parameters, shaking table test results of various structural types performance test results of the control device, mathematical model of the benchmark model and the control devices and the test results of the benchmark model with control systems. Not only the raw data, but also the simple drawings of the test data were provided.

References

S.J. Dyke. D. Bernal, J.L. Beck, and C. Ventura, An Experimental Benchmark Problem in Structural Health Monitoring, Third International Workshop on Structural Health Monitoring, Stanford, CA, September 12–14, 2001.

E. A. Johnson, H. F. Lam, L. S. and J. L. Beck, Phase I IASC-ASCE Structural Health Monitoring Benchmark Problem using Simulated Data, Journal of Engineering Mechanics, Vol. 130, No. 1, January 2004, pp. 3-15

Silian Lin1, Jann N Yang1 and Li Zhou2 , Damage identification of a benchmark building for structural health monitoring, 2005 Smart Material Structure. 14 S162-S169

C. H. Loh and C. H. Liu, “Application of model-based damage identification to a seismically loaded structure,” International Workshop on Structural Health Monitoring, Stanford University, Palo alto, USA, September, 2005.

Loh, C. H. Lynch, J.P., et al. “Experimental Verification of Wireless Sensing and Control System for Structural Control Using MR-Dampers,” Earthquake Engineering & Structural Dynamics, Vol.36, No.10, August 2007, 1303-1328

D. A. Shook, P. N. Roschke, P. Y Lin, C. H. Loh, “GA-optimized fuzzy logic control of a large-scale building for seismic loads,” Engineering Structure, March, 2007

Damping Identification of Cable Vibration with and without MR Dampers

Shieh-Kung Huang[1] Chin-Hsiung Loh[2] and Pei-Yang Lin[3]

黃謝恭 [1]、羅俊雄 [2]、林沛暘 [3]

Abstract

Vibrations of stay cable under specific loading, such as wind loading and heavy rainfall, always induced large vibration amplitude which may lead to first passage failure or fatigue failure of cable. Therefore, vibration control using passive or semi-active control devices had been used. The objective of this study is to investigate the dynamic characteristics of stayed cable with and without dampers from laboratory experiments. First, the relationship between the cable tensile force and vibration frequencies were examined, and comparison of the result with string theory, the flat taut string theory, axially-loaded beam theory, and M. Irvine's theory was made. Estimation of cable damping ratio was then conducted using the free vibration data of the cable. Methods including logarithmic decrement method, half-power bandwidth method, Ibrahim time domain method and wavelet transform method were used to extract damping ratio. Comparison on the estimated cable damping with and without damper is finally discussed. The result provides valuable information on the cable control using passive or semi-active devices.

Keywords: MR Damper, Magneto-Rheological, Damping Ratio, Cable Control

Introduction

Because of economic advantages and aesthetic qualities, cable-stayed bridges have been increasing popularity over the last three decades. However, vibrations of stay cables under specific loading always induced large vibration amplitude. For example, moderate wind (speed of 10 to 20 m/s) and light rain would cause a large vibration (on the order of 1 to 2 m). This phenomenon is well- known as a rain-wind vibration, and has been observed from a number of cable-stayed bridges [1, 2]. The extremely low inherent damping in such cable, typically in the order of a fraction of percent [3], is insufficient to eliminate this vibration. Sometimes, it may lead to fatigue in the cables and their anchors. To reduce these vibrations, many researchers have investigated several solutions, such as adding crossing ties/spacers, treating cable surface with different techniques, or providing mechanical dampers. However, it is commonly recognized that the vibrations can be eliminated by providing mechanical dampers [4, 5].

Magneto-Rheological damper (MR damper) are made from MR fluids, which typically consist of micron-sized, magnetically polarizable particles dispersed in a carrier medium such as water, oil or silicone. Most conveniently, it can achieve the required forces in a few milliseconds for transition. Therefore, the MR dampers have been widely used to increase the damping of cable in many researches. In order to design MR dampers for stay cables, it is necessary to study experimentally the dynamic properties of those cables with and without dampers. This report concentrates on the tests of stay cable, aimed at identifying the dynamic characteristics and comparing the damping performance. The free vibration response data of the stay cable as well as the force vibration responses were used to identify the amplitude-dependent natural frequencies and damping ratios of stay cable with and without damper. From the results, these realistic model parameters can be generated for research on cable control.

Formulations of Cable Vibration

[1] Research Assistant Fellow, National Center for Research on Earthquake Engineering.

[2] Professor, Department of Civil Engineering, National Taiwan University.

[3] Research Fellow, National Center for Research on Earthquake Engineering.

Considering an inclined cable with a damper transversely attached at a location x_d away from the lower end, as shown in Fig. 1, for numerical analysis, the stay cable typically has some assumptions that: (i) the cable has a uniform cross-section; (ii) the sag-to-length ratio is small and the tension-to-weight ratio is high; and (iii) the cable vibrates only in the xy-plane and the vibration can be negligible in the x-direction. Irvine [6] recommended a simple procedure for the effect of inclination that only the component perpendicular to the cable chord is used in evaluation, as shown in Fig. 1b. Therefore, the governing equation can be described by the following partial differential equation of motion:

$$\begin{aligned} EI\frac{\partial^4 v}{\partial x^4} - T\frac{\partial^2 v}{\partial x^2} + \frac{\lambda^2 T}{L^3}\int_0^L v\,dx + c\frac{\partial v}{\partial t} \\ + m\frac{\partial^2 v}{\partial t^2} = f - f_d\,\delta(x - x_d) \end{aligned} \tag{1}$$

where $v = v(x,t)$ is transverse deflection due to vibration; EI is flexural rigidity; $T = T_h/\cos\theta$ is tension force; c is the inherent damping coefficient; m is mass per unit length; $f = f(x,t)$ refers to load applied on cable; f_d refers to force of attached damper; $\delta(.)$ is Dirac delta function; λ^2 is the sag-extensibility parameter expressed as

$$\lambda^2 = \left(\frac{mgL\cos\theta}{T}\right)^2 \frac{LEA}{TL_e} \tag{2}$$

$$L_e = \int_0^L \left[(dy/dx)^2 + 1\right]^{3/2} dx = L\left[1 + \frac{(mgL\cos\theta/T)^2}{8}\right] \tag{3}$$

The transverse deflection due to vibration can be presented by separation of variables as

$$v(x,t) = \phi(x)\,q(t) \tag{4}$$

where $\phi(x)$ and $q(t)$ is time-independent and the time-dependent components of $v(x,t)$, respectively. Therefore, the Eq. (1) can be solved using finite difference method (Tabatabai et al. [7, 8]) or Galerkin method (Pacheco et al. [9]).

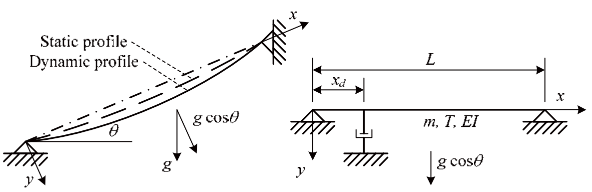

(a) (b)

Figure 1. Inclined cable with mechanical damper

Experimental Setup

To study the effect of MR damper on stay cables, a scaled-down cable was designed and constructed at the National Center for Research on Earthquake Engineering (NCREE) in Taipei, Taiwan. This scaled-down cable has adjustable tension force to change its dynamic characteristics, and can install MR damper to mitigate cable's vibration.

Figure 2 shows the schematic diagram of experimental cable, the specimen has one steel strand with seven steel wires suspended between two anchors. The cross-sectional area is 140 mm^2 and the yielding stress is 1,670 N/mm^2. In addition, the suspended cable was 13.5m in length, and each end was anchored to the reaction wall or strong floor since these ends were considered fixed. The two ends were inclined by about 26 degrees. To maintain a similar dynamic characteristic with the prototype of stay cable, 19 sets of mass block were attached to the suspended cable. Each mass block is 16 kg in weight. Furthermore, to apply an adjustable tension force to the cable, the lower end went through a hydraulic jack before anchoring.

One MR damper was connected perpendicularly to the stay cable on 10% of total length form lower end, and used to advance damping ratio of cable specimen. This MR Damper (RD-1005-3) was provided by LORD Corporation. The maximum output force of the damper is 3kN, maximum input voltage is 0.8V, maximum input current is 2.0A, and the stroke is +/-20mm. Performance test of a damper was conducted under random stroke with constant voltage. and plotted in Fig. 3. The force-displacement and force-velocity relationships of the MR damper under different applied voltages are clearly shown in this figure, and two important properties should be noted here. One is that the dissipated energy increases as provided voltage increases (as shown in Fig. 3a). Another is the initial stiffness and Coulomb friction (as shown in Fig. 3b).

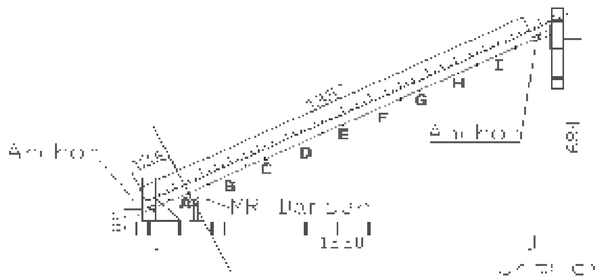

Figure 2. Schematic diagram of cable specimen

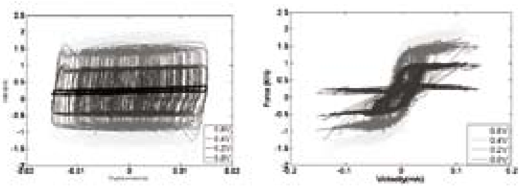

(a) (b)

Figure 3. Voltage dependent force-displacement and force-velocity relationship of MR damper

Dynamic Characteristics of CABLE

Theoretically, the natural frequency of a stay cable can be estimated based on several theories, such as the flat taut string theory, axially loaded beam theory, and

Irvine's theory [6]. Also, it can be evaluated using finite difference method and Galerkin method. Experimentally, a force is applied to the middle node of a stay cable to generate free vibration responses. The first natural frequencies under different tensile forces are shown in Fig. 4. The theoretically estimated natural frequencies are also presented in this figure. Because the flat taut string theory, axially loaded beam theory, ABAQUS, and Galerkin method do not consider the phenomenon well known as "modal crossover" [6], the natural frequencies increase linearly as the tension force. Considering modal crossover, Irvine's theory estimated natural frequencies by solving these equations:

$$\tan\left(\frac{\boldsymbol{\omega}}{2}\right)=\frac{\boldsymbol{\omega}}{2}-\left(\frac{4}{\lambda^2}\right)\left(\frac{\boldsymbol{\omega}}{2}\right)^3 \qquad \boldsymbol{\omega}=2\pi f L\sqrt{\frac{m}{T}} \quad (5)$$

where λ is the sag-extensibility parameter, which is proportional to the ratio of the axial stiffness to the geometric stiffness. In addition, Galerkin method is a well proposed method for cable control research because this method can efficiently reduce the dimension of matrix, and the finite difference method is more accurate while sag-to-length ratio is a little larger (on the order of 0.5%). Fortunately, both methods are more accurate if sag-to-length ratio is diminished.

Generally, damping ratio is the most critical parameter to be estimated in a dynamic system. There exist many methods in estimating damping ratio. Logarithmic decrement method and half-power bandwidth method are classical methods. Ibrahim time domain method calculates damping ratio by minimizing error between the mathematical model and physical model [12]. Hilbert transform method evaluates damping ratio according to the decay of envelopes [13, 14]. Wavelet transform method extracts damping ratio from wavelet coefficients of free vibration responses [15, 16]. Figure 5 shows damping ratios extracted from free vibration responses (only the result of wavelet transform method was considered here). The said figure represents that damping ratio slightly increased when vibration amplitude decreased. To examine the nonlinear property of cable inherent damping, the results of four different initial displacements, including 10mm, 15mm, 20mm, and 25mm, are shown in Fig. 5a. Then, the damping ratios under different tension forces are shown in Fig. 5b. Apparently, the damping ratio increased as tension force decreased. In the case of 16kN, the damping ratio averages 3.3%, but it averages 1.2% in the case of 45kN.

Those results indicate that a stay cable provides higher damping value when vibration amplitude is smaller, and provides smaller damping value when vibration amplitude is larger. This is very unique

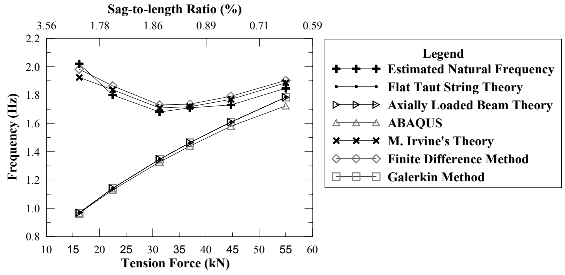

Figure 4. Estimated nature frequency of stay cable using different approaches

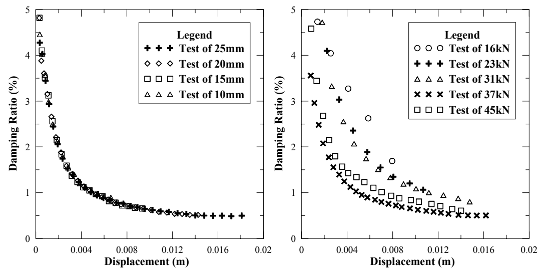

(a) (b)

Figure 5. Estimated damping ratio of cable with respect to the vibration amplitude

because a stay cable should have a high damping ratio to dissipate energy while vibration amplitude is large. Therefore, the MR Damper must provide additional damping in mitigating vibration.

Damping With and Without MR Damper

To provide additional damping on the stay cable, the MR damper with constant voltage (to act as a passive control device) was attached at node 'A' in Fig. 2. Again, estimated damping ratio is shown in Fig. 6. Different from the previous subsections, the damping ratio is larger when vibration amplitude is larger when the MR damper was added. It solved the problem that the cable has insufficient inherent damping to dissipate vibration energy, especially when it has large vibration amplitude. In Fig. 6, the '--' can represent the damping provided by MR damper, and the ' ' represented the damping of cable, as shown in Fig. 6b. It is clear that MR damper always provides higher damping while the vibration amplitude is large. While the vibration amplitude reduced, the MR damper stopped dissipating energy, and allowed the cable diminishes vibration alone. In this test, the MR damper provides about 2% damping ratio to the stay cable.

Pacheco et al. (1993) proposed universal curve using Galerkin method to design an optimum damper [9]. However, finding optimum MR damper is difficult because the said universal curve has been developed based on an idealized cable and damper by ignoring factors such as cable sag, flexural rigidity of the cable, nonlinear cable damping, stiffness of the damper, or nonlinear damper characteristics. Figure 7 shows the first mode damping ratio on large vibration amplitude (over than 1 cm in these tests). Since the voltages are increased, the initial stiffness and

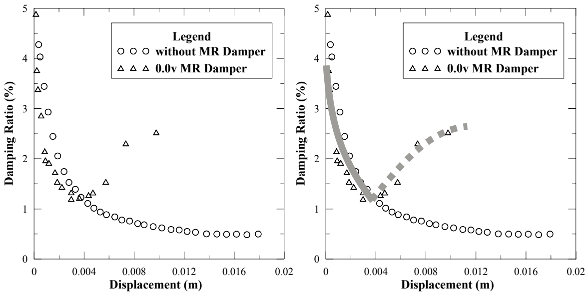

(a) (b)

Figure 6. Comparison on the estimated damping ratio with and without MR damper

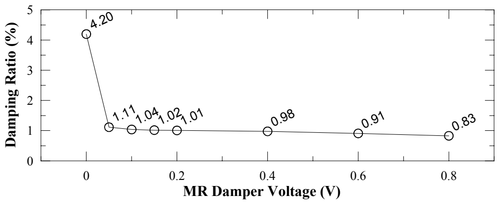

Figure 7. Estimated damping ratio with MR damper

Coulomb friction are so obvious that the MR damper will lock up the cable which may increase the natural frequency of the cable and might reduce the damping ratio of the cable.

Conclusions

In this report, the estimation of damping ratio of stay cable was used and examined. From experimental test results, it shows that the estimated damping ratio of stay cable decreases as the vibration amplitude increases. Hence, using damper has been an effective means in suppressing vibration's amplitude. MR damper can provide considerable damping force and has a wide range of dynamic response. Especially, it can reduce cable vibration under a variety of excitation frequencies. The reduction effect is extraordinarily good for the resonance case. Although MR damper is a good choice in increasing cable damping so as to reduce the cable vibration, there also exists a damper current saturation in which the reduction effect will be kept equal with increased current. Additionally, the stiffness of stay cable will increase with the installation of MR damper, because MR damper has an initial stiffness.

References

1. M. Matsumoto, N. Shiraishi, and H. Shirato. 1992. "Rain-wind Induced Vibration of Cables of Cable-stayed Bridges," *J. of Wind Engrg. and Industrial Aerodyn.*, 41-44, 2011-2022.
2. O. Flamand. 1995. "Rain-wind Induced Vibration of Cables," *J. of Wind Engrg. and Industrial Aerodyn.*, 57, 353-362.
3. H. Yamaguchi, and M. Ito. 1997. "Mode-dependence of Structural Damping in Cable-stayed Bridges," *J. of Wind Engrg. and Industrial Aerodyn.*, 72, 289-300.
4. R. E. Christenson, B. F. Spencer, and E. A. Johnson. 2006. "Experimental Verification of Smart Cable Damping," *J. of Engrg. Mech.*, 132(3), 268-278.
5. X. Y. Wang, Y. Q. Ni, J. M. Ko, and Z. Q. Chen. 2005. "Optimal Design of Viscous Dampers for Multi-mode Vibration Control of Bridge Cables", *Engrg. Struct.*, 27, 792-800.
7. A. B. Mehrabi, and H. Tabatabai. 1998. "Unified Finite Difference Formulation for Free Vibration of Cables," *J. of Struct. Engrg.*, 124, 1313–1322.
8. H. Tabatabai, and A. B. Mehrabi. 2000. "Design of Mechanical Viscous Dampers for Stay Cables," *J. Bridge Engrg.*, 5(2), 114-123.
9. B. M. Pacheco, Y. Fujino, and A. Sulekh. 1993. "Estimation Curve for Modal Damping in Stay Cables with Viscous Damper," *J. Struct. Eng.*, 119(6), 1961–1979.
10. E. A. Johnson, G. A. Baker, B. F. Spencer, and Y. Fujino. "Mitigating Stay Cable Oscillation using Semiactive Damping," *Smart Struct. and Matls. 2000*, *Proc. of SPIE*, 3988, 207-216.
11. E. A. Johnson, G. A. Baker, B. F. Spencer, and Y. Fujino. 2007. "Semiactive Damping of Stay Cables," *J. of Engrg. Mech.*, 133(1), 1-11.
12. A.M. Iglesias. "Investigating Various Modal Analysis Extraction Techniques to Estimate Damping Ratio," Master's Thesis, Mechanical Engineering, Virginia Polytechnic Institute and State University.
13. M. Feldman. 1994. "Non-linear System Vibration Analysis Using Hilbert Transform, I. Free Vibration Analysis Method `Freevib'," *Mech. Syst. Signal Process.*, 8(2), 119–127.
14. M. Feldman. 1994. "Non-linear System Vibration Analysis Using Hilbert Transform, II. Forced Vibration Analysis Method `Forcevib'," *Mech. Syst. Signal Process.*, 8(3), 309–318.
15. W. J. Staszewski. 1997. "Identification of Damping in MDOF Systems using Time-scale Decomposition", *J. of Sound and Vibration*, 203(2), 283-305.
16. M. Ruzzene, A. Fasana, L. Garibaldi, and B. Piombo. 1997. "Natural Frequencies and Dampings Identification using Wavelet Transform: Application to Real Data", *Mech. Syst. and Signal Process.*, 11(2), 207-218.

Shaking Table Test of Semi-active Mass Damping System using MR Damper

Pei-Yang Lin[1]

林沛暘

Abstract

A semi-active mass damping system (SMD) utilizing magnetorheological (MR) damper is proposed in this paper. This study aimed to integrate the reliable characteristic of the traditional tuned mass damper (TMD) and the superior performance of the active mass damper (AMD). A full-size three-story steel building was used as the benchmark structure to verify the proposed damper's performance in both the numerical simulation and shaking table tests. To predict accurately the behavior of the MR dampers, a series of performance tests with various excitation and command voltages were done. According to the performance test data, a modified Bouc-Wen model was identified and has been used to represent the nonlinear behavior of the MR damper. Unlike the clipped-optimal control, the LQR with the continuous-optimal control, which can generate the continuous varying command voltage, was used to calculate online the optimal command voltage to the MR damper. Both numerical simulation and shaking table test results demonstrated the superior mitigation ability of the proposed SMD. In addition, the control effect of the proposed SMD system is compatible to the traditional bracing system with passive dampers. The proposed SMD system provides an alternative solution and can be implemented easily during construction.

Keywords: Semi-active control, MR damper, shaking table test

Introduction

Over the last decade, the concept of semi-active tuned mass dampers (STMD) has been widely discussed. The idea of the STMD is to apply and integrate the advantages from both the TMD and the ATMD, thereby optimizing the frequency and the damping ratio in an adaptive and reliable manner. Based on this premise, a large amount of research was conducted that offers protection for civil structures [1~8]. The research by T. Pinkaew [9] proved that the utilization of STMDs can be equivalent to increasing the TMD's mass in the structure, which is the main constraint in designing a TMD system [10]. Even though all the numerical studies have shown satisfactory results for the STMD [11~13], one basic condition has always been assumed in the research, i.e. the stiffness and the damping of the STMD must be varied in a reasonably short period of time. This has proven to be the bottleneck on the use of the STMD.

A series of researches including investigation and simulation of the MR damper, as well as applying specific MR dampers to control an isolated structure were conducted by the authors. Kim et al [14] proposed a neuro-fuzzy model to describe the behavior of a hybrid system with friction pendulum system (FPS) bearings and MR damper. Different control algorithms were then compared in order to offer strong protection to the main structure. Moreover, the possibility of utilizing resettable semi-active stiffness dampers was also investigated [15]. Although the results have shown that the utilization of MR dampers can provide a vastly superior next generation control system, however, the MR dampers were mainly considered as bracing-type equipment and may not be feasible to practice when a large amount of MR damper is needed.

A semi-active mass damping system (SMD) using MR dampers is proposed in this paper. With the implementation of varying the stiffness and the damping of the MR damper in a short interval, the mass block on the top of the structure does not need to be tuned precisely in advance as the aforementioned STMD system while satisfactory control result can still be achieved. The remainder of this paper is organized as follows. First, the main concept of the proposed system was described. Next, in order to precisely evaluate the behavior of the MR damper used in the research and to guarantee its application the performance test result of a specific MR damper was compared with the numerical model developed. Then, a numerical analysis and experimental verification were carried out to demonstrate the performance of the proposed SMD system. Summary and conclusions were drawn in the final section.

Performance Test of MR Dampers

The primary concept of the smart SMD is to suppress the response of the main structure by sacrificing as much as possible the reaction of the mass added on top of the building. To achieve this goal, the stroke of the MR damper used serves as the most critical point in the system. A designated MR damper (7kN/300mm) manufactured by the National Center for Research on Earthquake Engineering (NCREE) was used in this research. The basic property of the MR damper is shown in Table 1.

The robust numerical model of the MR damper in describing its hysteresis behavior under arbitrary excitation is essential for the development of the smart system. Unlike the previous neuro-fuzzy model proposed by the authors [14], a modified Bouc-Wen model was developed in this study for both the theoretical and the experimental stages. According to the previous studies by Spencer et al. in 1997[16], the Bouc-Wen model is suitable to describe the nonlinear behavior of the MR damper. To simplify the mathematical model, a modified Bouc-Wen model, as shown in Equations (1) and (2), was used. Four parameters (C, α, βandγ) were used to express the performance of the MR damper under a fixed command voltage.

$$F_{MR}(t) = C * \dot{x}(t) + z(t) \tag{1}$$

$$\dot{z}(t) = \alpha * \dot{x}(t) + \beta|\dot{x}(t)||z(t)| + \gamma\dot{x}(t)|z(t)|^2 \tag{2}$$

where F_{MR} represents the force, and $\dot{x}(t)$ represents the velocity of the MR damper.

Generally the nonlinear curve fitting method is used to find the relationship between the model parameters and the command voltages. However, the time required as well as the complex coefficients make this method impractical. Therefore, this study simplified the relationship between the model parameters and the command voltage using a new technique of interpolation. First, the performance test data of the MR damper with random displacement and seven constant voltage levels (0, 0.2, 0.4, 0.6, 0.8, 1 and 1.2 V) were used to identify the individual model parameters (C, α, β and γ) for each constant command voltage level. These parameters can be identified using Matlab/Optimization toolbox [17]. The identified model parameters of the seven constant voltage levels are shown in Table 1. The theoretical force of the MR damper with command voltage different from these seven levels can then be obtained by interpolating the model parameters from the two adjacent levels it locates.

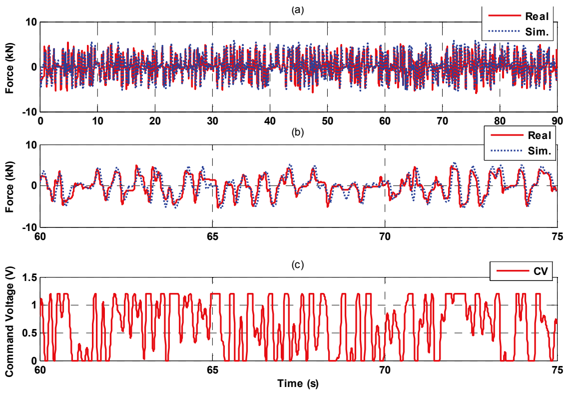

Figure 1. Comparison of the real and the simulated MR damper force in the performance test (random displacement and random voltage): (a) the whole history; (b) the time history 60~75 sec; (c) command voltage to the MR damper

The numerical model of the MR damper established was verified through a performance test of the MR damper at NCREE. A banded white noise (0-5Hz) was used as the velocity and voltage of the MR damper. Ninety seconds of damping force were recorded, and the result is shown in Figure 1 where subplot (a) shows the time history of the damping force; subplot (b) focuses on the period between 60 to 75 seconds; and subplot (c) indicates the given command voltage. The numerical simulation, shown in red color, substantially matches the measured response in blue color, and the peak values and phases of the damping force can be expressed precisely by the proposed method. This result strongly supports the understanding that the modified Bouc-Wen model can be applied in the present study.

Semi-active control algorithm of the SMD System

A four degree-of-freedom (DOF) model was used to express a three-story structure representing a typical low-rise building with rolling pendulum system (RPS) and MR damper in this research. The first three fundamental frequencies of the main structure were set to 1.085, 3.277, and 5.165 Hz, and the mass on the first and second floor was 6t (m1, m2). The total mass of m3 and m4 was also set to 6t, where m4 is the tunable mass block of the control system. The stiffness and period of the RPS used in this study were 1.049 kg/mm and 2.77 s.

To offer a strong protection to the structure, a special control algorithm combining the LQR method and a continuous–optimal control concept was proposed. In this study, the most common active control algorithm, the LQR method, was used to calculate the optimal control force with designated control objectives to make the SMD system both simpler and more flexible. Meanwhile, unlike the previous developed neural network-based MR damper model, the continuously-optimal control concept was utilized to transfer the desired control voltage from the optimal active control force obtained and to improve the time-consuming and extrapolation problems. To reach this goal, seven modified Bouc-Wen models with different constant voltages were built to form the database for a comparison. Seven damper forces calculated from these voltages were compared to the optimal control force. The command voltage was then interpolated proportionally from the two adjacent MR damper models it located. The LQR method with the continuous–optimal control concept will be able to provide an easy and stable way in calculating the suitable command voltage in each time step. The traditional LQR control algorithm was used to calculate the desired control force (active control force). Then, the continuous–optimal control was used to translate the desire control force to the command voltage in driving the MR damper.

Shaking Table Test of the SMD System

The feasibility of implementing the proposed system in practice was verified through a shaking table test conducted at NCREE. A full-size three-story steel structure measuring 3m (length) x 2m (width) x 3m (height) in each floor with the MR damper on the roof was used to form the four degree-of-freedom model in the theoretical analysis. In order to approach the assumption of a shear-type structure, the beams and the columns of the specimen were constructed using H-beams measuring 150mm x 150mm x 7mm x 10mm while the floor thickness was set as 25mm and was welded on extremely strong diaphragms. Additional blocks with a mass of 3.5 tons were mounted on every floor to satisfy the requirement of fundamental frequency. The first three fundamental frequencies of the main structure were set to 1.085, 3.277, and 5.165 Hz. The mass of the SMD system was 2 tons. The SMD system combined the Rolling Pendulum System (RPS) and semi-active controlled MR damper. The stiffness and period of the RPS used in this study were 1.049 kg/mm and 2.77 seconds, respectively. The set-up is shown in Fig. 2.

A traditional instrumentation system was deployed for the specimen to measure the response of the structure during earthquake excitation. As shown in Fig. 2, the absolute displacement, velocity, and acceleration of each floor of the main structure as well as the reaction of the MR damper were recorded by the linear variable differential transformer (LVDT) for comparison. The stroke of the MR damper was carefully monitored to avoid any collision between the MR damper and the specimen. The optimal control voltage was calculated by the embedded Simulink/dSPACE code [18] with the necessary feedback signals and then sent to the MR damper. The Control flow-chart of the smart SMD system is shown in Fig. 2.

Fig. 2: Set-up of the three-storey benchmark structure (left) and control flow-chart of the SMD damping system (right).

Four diverse earthquakes including the 1940 El Centro earthquake (NS direction), the 1995 Kobe earthquake, the TCU 068 site record, and the TCU129 site record in the 1999 Chi-Chi earthquake, representing the typical far-field and near-fault earthquakes, were used to examine the practical performance of the smart SMD system. For each testing case, the PGA value started from 50 gal with increments of 50 gal until the maximum allowable stroke of the MR damper, set to be 12 cm in the experiment, was reached. To demonstrate the advantage of applying the smart system, all four control modes comprising of the UC (uncontrolled structure), PMD (passive mass damper / max. power of MR damper), PMD-off (passive mass damper / power-off of MR damper), and the SMD (Semi-active mass damper / semi-active controlled MR damper) were executed. The experimental data were collected by the data acquisition system for further comparison.

The overall presentation of the four modes under different PGA levels of the El Centro earthquake is illustrated in Fig. 6. It should be noted that the red line, which is the PMD-off mode, can be treated as a failure mode of SMD. Apparently, the blue line, which represents the performance of the proposed SMD method, occupies the lowest position under almost every PGA value. This trend proves that the MR damper can be manipulated smartly by the proposed control algorithm with an average improvement of 40-50% from the uncontrolled state. Moreover, a 20-30% efficiency increase over the PMD system can be easily achieved by this robust control system.

Figure 4. Overall presentation of all modes under different PGA levels of the El Centro earthquake.

Conclusions

A smart SMD system using MR dampers is proposed in this research. To integrate the robustness of the traditional TMD and the superb control performance of the AMD systems, the frictionless

RPS and the MR damper were used to compose the smart system while using a full-scale three-story building as the benchmark structure. To predict accurately the behavior of the designated large-stroke MR damper, a numerical representation combining the modified Bouc-Wen model and interpolation technique was established. Seven sets of the parameters describing the relationship between the velocity and the damping force under fixed voltages were used to form the database. The damping force with arbitrary velocity and voltage was then calculated by the interpolated coefficients. The MR damper model was verified by the performance test of the MR2005 damper in NCREE. The result has shown that both the time history and the hysteresis loop of the MR damper can be estimated correctly by the numerical model. A smart control algorithm combining the LQR method and the continuous–optimal control concept was developed with the success of the MR damper model. To offer an objective-oriented control outcome, all floor responses including relative displacement, relative velocity, and absolute acceleration of the benchmark structure were considered in the performance index of the LQR method. The command voltage was then calculated by the continuous–optimal control concept by interpolating between the best two voltage levels. The proposed smart SMD theory was verified by two typical earthquakes. The numerical simulation demonstrated that the structural response can be alleviated satisfactorily by the smart SMD system.

References

1. Frahm H. Device for damping of bodies. U.S. Patent No. 989, 958, 1911.
2. Ormondroyd J, Den Hartog JP. The theory of the dynamic vibration absorber. Transactions of the ASME 1928; APM-50-7: 9–22.
3. Brock JE. A note on the damped vibration absorber. Journal of Applied Mechanics, ASME 1946; 13: A-284.
4. Mackriell, L.E.; Kwok, K.C.S.; Samali, B. Critical mode control of a wind-loaded tall building using an active tuned mass damper Engineering Structures, v 19, n 10, Oct, 1997, p 834-842
5. Qu, Z.-Q.; Shi, Y.; Hua, H. A reduced-order modeling technique for tall buildings with active tuned mass damper Earthquake Engineering and Structural Dynamics, v 30, n 3, March, 2001, p 360-362
6. Chang, C.C.; Yang, Henry T.Y. Control of buildings using active tuned mass dampers Journal of Engineering Mechanics, v 121, n 3, Mar, 1995, p 355-366
7. Loh, Chin-Hsiung; Chern, Wen-Yung Seismic effectiveness of active tuned mass dampers for the control of flexible structures Probabilistic Engineering Mechanics, v 9, n 4, 1994, p 225-234
8. M.Sakamoto, T.Kobori, T.Yamada, M.Takahashi, Practical applications of active and hybrid response control systems and their verifications by earthquake and strong wind observations, Proceedings of First World Conference on Structural Control, Los Angeles, CA,USA,1996.
9. Pinkaew, T.; Fujino, Y. Effectiveness of semi-active tuned mass dampers under harmonic excitation Engineering Structures, v 23, n 7, July, 2001, p 850-856
10. Den Hartog JP. Mechanical Vibrations (3rd edition). McGraw-Hill: New York, 1947.
11. Ricciardelli, Francesco; Occhiuzzi, Antonio; Clemente, Paolo Semi-active Tuned Mass Damper control strategy for wind-excited structures
Journal of Wind Engineering and Industrial Aerodynamics, v 88, n 1, Nov, 2000, p 57-74
12. Yang, Runlin; Zhou, Xiyuan; Liu, Xihui Seismic structural control using semi-active tuned mass dampers Earthquake Engineering and Engineering Vibration, v 1, n 1, June, 2002, p 111-118
13. Setareh, M. Use of semi-active tuned mass dampers for vibration control of force-excited structures Structural Engineering and Mechanics, v 11, n 4, April, 2001, p 341-356
14. Hyun-Su Kim, Paul N Roschke, Pei-Yang Lin, Chin-Hsiung Loh, "Neuro-fuzzy model of hybrid semi-active base isolation system with FPS bearing and MR damper", Engineering structures 28, 2006, PP947-958,
15. Yang, J. N., Bobrow, J., Jabbari, F., Leavitt, J., Cheng, C. P., and Lin, P. Y., " Full-Scale Experimental Verification of Resetable Semi-Active Stiffness Dampers ", Journal of Earthquake Engineering and Structural Dynamics, 36, PP1255-1273, 2007
16. Spencer B F, Dyke S J, Sain M K, Carlson J D, "Phenomenological model for magnetorheological dampers", J. of Engr. Mech. Am. Soc. Civil Eng. 123, 230-252, (1997).
17. MATLAB, User's Guide, The MathWorks, Inc.: Natick, MA 01760, 1992.
18. dSPACE Release 4.2, Solution for control, 2005 dSPACE GmBH, Germany

Semi-active Control of Variable Stiffness Isolation System

Kuan-Hua Lien [1] Lap-Loi Chung[2] Lai-Yun Wu[3] and Lyan-Ywan Lu[4]

連冠華 [1]、鍾立來 [2]、吳賴雲 [3]、盧煉元 [4]

Abstract

Passive isolation system may not work well if seismic excitation is other than the design earthquake. Active isolation system may work well under different earthquakes but it is expensive. Hence, semi-active isolation is a solution. In this paper, the "leverage-type stiffness controllable isolation system" (LSCIS) with simple control algorithm is studied. The algorithm is designed under a far-field earthquake but the LSCIS device also works well under various intensities of the far-field and near-fault earthquakes. Both structural base shear and LSCIS displacement are suppressed.

Keywords: semi-active control, variable stiffness isolation system, leverage-type stiffness controllable isolation system (LSCIS)

Introduction

Although isolation systems can reduce structural response under seismic excitation, they may increase isolated displacements during near-fault earthquakes. Adding passive dampers can certainly reduce isolated displacements, but it may result in increased isolated forces. Since the parameters of the passive isolation system are fixed, it may not be that effective under earthquakes other than the design one. The problem may be solved by active isolation system but requirements of higher cost and higher power are the disadvantages. Therefore, semi-active isolation system is a solution to overcome the disadvantages of passive and active isolation systems (Narasimhana, et al., 2005 & Sahasrabudhe, et al., 2005).

The purpose of this study is to investigate the "leverage-type stiffness controllable isolation system", (The LSCIS was proposed by Lu, et al., 2008; Lu, et al., 2009). The stiffness of the isolation system is adjusted by varying the position of the lever fulcrum. Simple control algorithm is proposed such that the position of the lever fulcrum is determined from the displacement and velocity of the LSCIS device. The control algorithm is designed under far-field earthquake and the feasibility of the LSCIS device is further investigated under various intensities of far-filed and near-fault earthquakes.

Motion Equation of Structure with LSCIS Device

The model of structure with LSCIS device is shown in Fig. 1. The super-structure in the figure is assumed a single-degree-of-freedom (SDOF) system to focus on the performance of the LSCIS system. LSCIS device consists of telescopic lever and its fulcrum, spring, and roller. The fulcrum of the lever is constrained in the X-direction and can move at any desired position in the Y-direction by a force F_p. The ends of telescopic lever are only free to move in the X-direction. When the fulcrum of the lever moves downward, the device offers decreased stiffness of LSCIS device; and when the fulcrum of the lever moves upward, the device offers increased stiffness of LSCIS device. The LSCIS device develops variable restoring force due to the position of the fulcrum of the lever and friction force due to roller and telescopic lever.

When an LSCIS device is attached to a structure

[1] Ph.D. candidate, Department of Civil Engineering, National Taiwan University, d95521004@ntu.edu.tw
[2] Research Fellow, National Center for Research on Earthquake Engineering, chung@ncree.org.tw
[3] Professor, Department of Civil Engineering , Nation Taiwan University, lywu@ntu.edu.tw
[4] Professor, Department of Construction Engineering, National Kaohsiung First University of Science and Technology, lylu@ccms.nkfust.edu.tw

subjected to external disturbances, $\ddot{x}_g(t)$, it becomes a two-degree-of-freedom system. The equation of motion for the nonlinear system can be expressed as

$$\mathbf{M}\ddot{\mathbf{x}}(t)+\mathbf{C}\dot{\mathbf{x}}(t)+\mathbf{K}\mathbf{x}(t)+\mathbf{B}_0\left[\Delta u_r(t)+u_f(t)\right]=-\mathbf{M}\mathbf{E}_0\ddot{x}_g(t) \quad (1)$$

where $\mathbf{x}(t)=\begin{bmatrix} x_s(t) & x_b(t)\end{bmatrix}^T$; $\mathbf{M}=\begin{bmatrix} m_s & 0 \\ 0 & m_b\end{bmatrix}$; $\mathbf{C}=\begin{bmatrix} c_s & -c_s \\ -c_s & c_s\end{bmatrix}$; $\mathbf{K}=\begin{bmatrix} k_s & -k_s \\ -k_s & k_s+k_{r0}\end{bmatrix}$; $\mathbf{B}_0=\begin{bmatrix}0 & 1\end{bmatrix}^T$; $\mathbf{E}_0=\begin{bmatrix}1 & 1\end{bmatrix}^T$; $\mathbf{x}(t)$ is the displacement vector of the system; $\mathbf{M}$, $\mathbf{C}$ and $\mathbf{K}$ are the mass, damping and stiffness matrices of the system, respectively; m_s, c_s and k_s are the mass, damping coefficient and stiffness of the SDOF structure, respectively; m_b and k_{r0} are the mass and the spring stiffness of LSCIS device, respectively; $x_s(t)$ and $x_b(t)$ are the displacements of the structure and LSCIS device, respectively; $\Delta u_r(t)$ and $u_f(t)$ are the controllable restoring force and friction force provided by the LSCIS device, respectively; and $\mathbf{B}_0$ and $\mathbf{E}_0$ are the internal loading vector and external loading vector, respectively. The equations of motion, Eq. (1), can be expressed as a first-order differential equation in state space,

$$\dot{\mathbf{z}}(t)=\mathbf{A}\mathbf{z}(t)+\mathbf{B}\left(\Delta u_r(t)+u_f(t)\right)+\mathbf{E}\ddot{x}_g(t) \quad (2)$$

where $\mathbf{z}_{4\times1}(t)=\begin{bmatrix}\mathbf{x}(t)\\ \dot{\mathbf{x}}(t)\end{bmatrix}$; $\mathbf{A}_{4\times4}=\begin{bmatrix}\mathbf{0} & \mathbf{I}\\ -\mathbf{M}^{-1}\mathbf{K} & -\mathbf{M}^{-1}\mathbf{C}\end{bmatrix}$; $\mathbf{B}_{4\times1}=\begin{bmatrix}\mathbf{0}\\ -\mathbf{M}^{-1}\mathbf{B}_0\end{bmatrix}$; $\mathbf{E}_{4\times1}=\begin{bmatrix}\mathbf{0}\\ -\mathbf{E}_0\end{bmatrix}$.

The solution of Eq. (2) can be expressed in discrete-time fashion as first-order difference equation,

$$\mathbf{z}[k+1]=\mathbf{A}_d\mathbf{z}[k]+\mathbf{B}_d\left(\Delta u_r[k]+u_f[k]\right)+\mathbf{E}_d\ddot{x}_g[k] \quad (3)$$

where $\mathbf{z}[k]=\mathbf{z}(k\Delta t)$; $(\mathbf{A}_d)_{4\times4}=e^{\mathbf{A}\Delta t}$; $(\mathbf{B}_d)_{4\times1}=\mathbf{A}^{-1}(\mathbf{A}_d-\mathbf{I})\mathbf{B}$; $(\mathbf{E}_d)_{4\times1}=\mathbf{A}^{-1}(\mathbf{A}_d-\mathbf{I})\mathbf{E}$; $\Delta u_r[k]=\Delta u_r(k\Delta t)$; $u_f[k]=u_f(k\Delta t)$; $\ddot{x}_g[k]=\ddot{x}_g(k\Delta t)$.

The controllable restoring force $\Delta u_r[k]$ and the friction force $u_f[k]$ are given as follows,

$$\Delta u_r[k]=\Delta k_r[k]x_b[k],\quad \Delta k_r[k]=\frac{2Lx_p[k]}{\left(0.5L-x_p[k]\right)^2}k_{r0} \quad (4a,b)$$

$$u_f[k]=\min\left(\left|\tilde{u}_f[k]\right|,u_{f,\max}\right)\mathrm{sgn}(\tilde{u}_f[k]),$$
$$\tilde{u}_f[k]=-(\mathbf{D}_v\mathbf{B}_d)^{-1}\mathbf{D}_v\left(\mathbf{A}_d\mathbf{z}[k]+\mathbf{B}_d(\Delta u_r[k])+\mathbf{E}_d\ddot{x}_g[k]\right),$$
$$u_{f,\max}=\mu(m_s+m_b)g \quad (5a,b,c)$$

where $\Delta k_r[k]$ is the controllable stiffness of LSCIS device; $x_p[k]$ is the displacement from the fulcrum of the lever; L is the length of the lever; $\tilde{u}_f[k]$ is the assumed friction force in the stick state; $\mathbf{D}_v=[0\ \ 0\ \ 0\ \ 1]$; $u_{f,\max}$ is the maximum friction force; and μ is the total friction coefficient of the roller and the telescopic lever.

Semi-active Control Algorithm

Based on Eq. (4b), the stiffness of LSCIS device is controllable by varying the fulcrum displacement. A simple semi-active control algorithm is proposed so that the fulcrum displacement is linearly related to the product of the displacement and velocity of LSCIS device,

$$x_p[k]=Gx_b[k]\dot{x}_b[k] \quad (6)$$

Substituting fulcrum displacement $x_p[k]$ from Eq. (6) to Eq. (4a) leads to the following equation

$$\Delta u_r[k]=\left[\frac{G2Lx_b^2[k]}{\left(0.5L-Gx_b[k]\dot{x}_b[k]\right)^2}k_{r0}\right]\dot{x}_b[k] \quad (7)$$

where the term inside the bracket is positive and variable so that the sign of the variable restoring force is the same as the velocity of the isolation system and energy is dissipated; and G is the feedback gain which is determined by minimizing a certain performance index J,

$$J=\alpha\frac{\max(|m_s\ddot{x}_s[k]|)}{\max(|m_s\ddot{x}_{sp}[k]|)}+(1-\alpha)\frac{\max(|x_b[k]|)}{\max(|x_{bp}[k]|)} \quad (8)$$

where α is the weighting factor, $\alpha=0\text{-}1$; $m_s\ddot{x}_s[k]$ and $m_s\ddot{x}_{sp}[k]$ are the base shear of the structure with semi-active and passive control, respectively; and $x_{bp}[k]$ is the displacement of LSCIS device with passive control.

Numerical Verification

Numerical simulations are performed for a structure isolated with LSCIS device. The system parameters of the structure and LSCIS device are summarized in Table 1. Both passive and semi-active cases are considered. The fulcrum of the lever is fixed under passive control while the position of the fulcrum is varied according to Eq. (6) under semi-active control. External disturbances used in the simulation are El Centro earthquake with peak ground acceleration (PGA) 3.42 m/sec^2, Chi-Chi earthquake (TCU068) with PGA 5.02 m/sec^2 and Kobe earthquake with PGA 6.17 m/sec^2. The effectiveness of the LSCIS system is investigated under far-field and near-fault earthquakes.

The optimal feedback gain G is 2.5940 determined by direct search technique (Wright, 1995) such that the performance index J with weighting factor $\alpha = 0.6$ is minimized under El Centro earthquake. The structural base shear is reduced from 29.98 N under passive control to 27.79 N under semi-active control while the isolated displacement is reduced from 0.180 m to 0.112 m. By using the same feedback gain, LSCIS device is also found effective under near-fault earthquakes, Chi-Chi and Kobe as listed in Table 2. Both reductions in structural base shear and isolated displacement can be achieved. The performance of LSCIS device under El Centro and Chi-Chi earthquakes are shown in Fig. 2 and Fig. 3. By varying the intensities of the earthquakes, the effectiveness of the semi-active control is better than that of the passive control in both the structural base shear and isolated displacement (Fig. 4 and 5). The superiority of the semi-active control over the passive control increases with the intensity of the earthquakes.

Conclusions

Semi-active control with simple algorithm of LSCIS device is successfully verified numerically. The displacement of the lever fulcrum is simply calculated from the displacement and velocity of LSCIS device. Even though the feedback is determined by minimizing the performance index under the far-field earthquake, the LSCIS device is found effective under various intensities of the far-field and the near-fault earthquakes. Significant suppression in structural base shear and LSCIS displacement can be achieved.

References

Lu, L.Y., Lin, G. L. and Kuo, T. C. (2008), "Stiffness Controllable Isolation System for Near-fault Seismic Isolation", *Engineering Structures* 30: 747-765.

Lu, L.Y., Hsu, C.C. and Yeh, S.W. (2009), "A leverage-type semi-active isolation system for seismic structures in near-fault regions", *Journal of the Chinese Institute of Civil and Hydraulic Engineering. accepted May 15, 2009.(in Chinese)*

Narasimhana, S. and Nagarajaiah, S. (2005), "A STFT Semiactive Controller for Base Isolated Buildings with Variable Stiffness Isolation Systems", *Engineering Structures* 27: 514-523.

Sahasrabudhe, S. and Nagarajaiah, S. (2005), "Effectiveness of Variable Stiffness Systems in Base isolated Bridges Subjected to Near-fault Earthquakes: An Experimental and Analytical Study", *Journal of Intelligent Material Systems and Structures* 16:743-756.

Wright, M.-H., (1995), "Direct search methods: once scorned, now respectable in numerical analysis", *Pitman Research Notes in Mathematics, Addison Wesley Longman Limited*, 191-208.

Table 1 System parameters for numerical simulation

System	Item	Value
Super-structure	Structural mass (m_s)	16 kg
	Structural stiffness (k_s)	568000 N/m
	Damping coefficient(c_s)	6000 N-sec/m
	Frequency(ω_s)	30 Hz
	Damping ratio(ζ_s)	100 %
LSCIS device	Mass (m_b)	28 kg
	Stiffness of spring (k_{r0})	438 N/m
	Friction coefficient(μ)	0.008
	Length of lever(L)	0.274 m
	Controllable stiffness $\Delta k_r[k]$	(-0.8 to 0.5) k_{r0}

Table 2 Performance of LSCIS device

Structural response	Earthquakes	Passive control	Semi-active control
Maximum isolated displacement (m)	El Centro	0.180	0.112
	Chi-Chi	0.778	0.357
	Kobe	0.348	0.141
Maximum structural base shear (N)	El Centro	29.98	27.79
	Chi-Chi	125.20	86.65
	Kobe	56.67	34.94

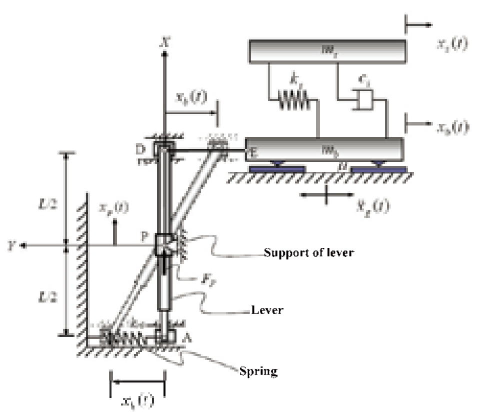

Fig. 1 Structure with LSCIS device

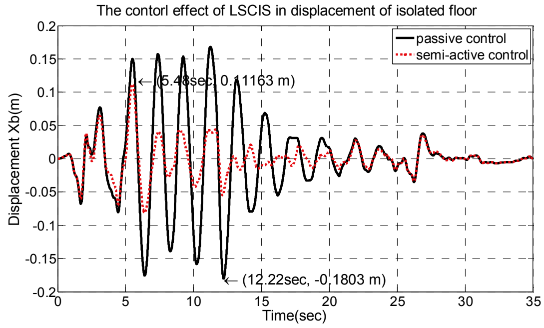

(a) Isolated displacement

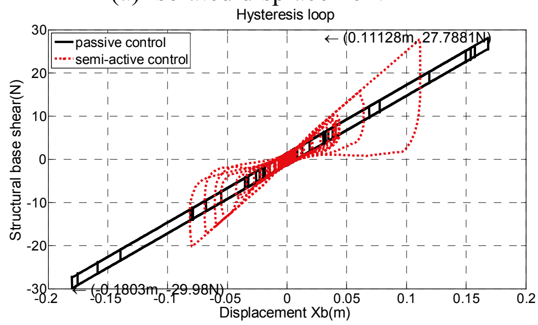

(b) Structural base shear

Fig. 2 Performance of LSCIS device under El Centro earthquake

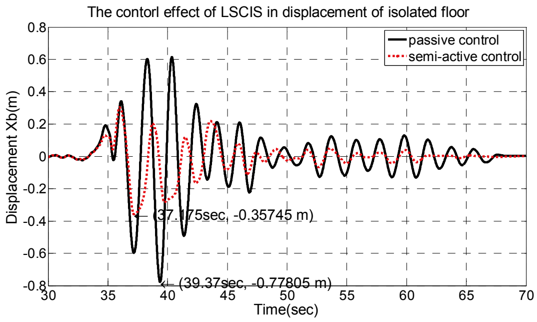

(b) Isolated displacement

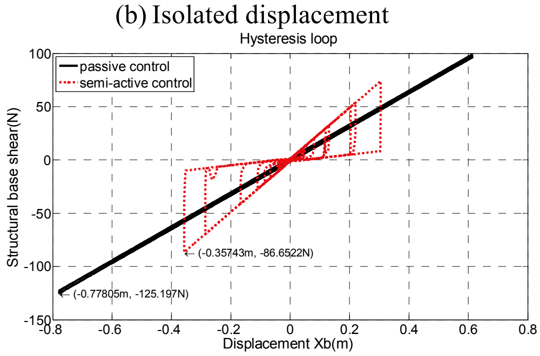

(b) Structural base shear

Fig. 3 Performance of LSCIS device under Chi-Chi earthquake (TCU068)

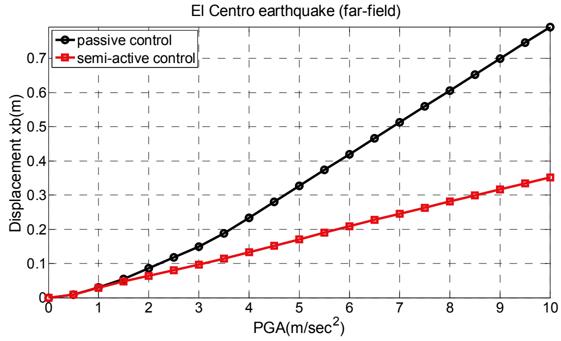

(a) Maximum isolated displacement

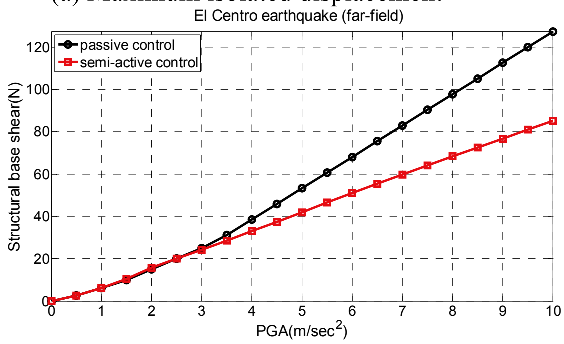

(b) Maximum structural base shear

Fig. 4 Maximum response of LSCIS device under El Centro earthquake

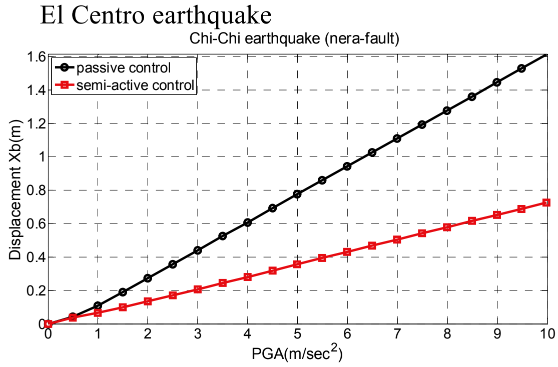

(a) Maximum isolated displacement

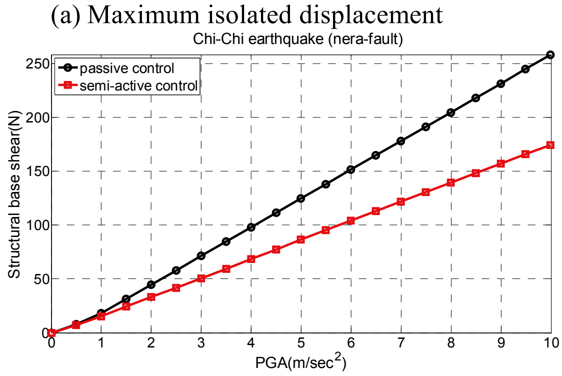

(b) Maximum structural base shear

Fig. 5 Maximum response of LSCIS device under Chi-Chi earthquake (TCU068)

Study on Dynamic Behavior of Nonlinear Rolling Isolation System with Viscous Damping

Lap-Loi Chung[1] Cheng- Hsin Hsieh[2] Cho-Yen Yang[3] Lai-Yun Wu[4]
Hung- Ming Chen[5]

鍾立來 [1]、謝姃馨 [2]、楊卓諺 [3]、吳賴雲 [4]、陳鴻銘 [5]

Abstract

Resonance may be induced in linear isolation system under near-fault earthquake. In this paper, nonlinear rolling isolation system with viscous damping is investigated. The equation of motion of the nonlinear system is derived by using Lagrange's equation. Numerical simulation is conducted for the nonlinear isolation system and the corresponding linear system under far-field and near-fault earthquakes. With the presence of viscous damping, the systems show better isolation effect in both acceleration ratio and maximum displacement regardless the isolation system is linear or nonlinear, and the earthquake is far-field or near-fault. When the damping coefficient is relatively small, the nonlinear isolation possesses much better performance over the linear one under near-fault earthquake. When the damping coefficient becomes larger, the performance of the linear isolation system is closer to that of the nonlinear one.

Keywords: isolation, nonlinear, eccentricity, damping, rolling, structural dynamics

Introduction

Some researches showed that the vibration period of many conventional isolation systems are 2 to 3 seconds which is close to the predominant period of near-fault earthquake, and thus resonance may occur (Sahasrabudhe and Nagarajaiah 2005). For this reason, nonlinear isolation systems are developed to avoid resonance. The frequency of nonlinear isolation system is not fixed, so it can keep the structure from resonance. The elliptical rolling is an example of a nonlinear isolation (Jangid and Londhe 1998). In this study, an eccentric rolling system (Chung et al. 2009) with viscous damping is investigated (Fig. 1). First, the equation of motion of the system is derived using Lagrange's equation. Then, the numerical study on forced vibration of the system is conducted. Finally, the dynamic behavior of this nonlinear rolling system is realized.

Equation of Motion

A block of mass m is pin connected to a disk with radius of R and the eccentric length from pin to center is αR (Fig. 1). Using Lagrange's equation, the nonlinear behavior of the isolator (Fig. 1) with viscous damper can be expressed as

$$\frac{d}{dt}\left(\frac{\partial L}{\partial \dot{q}_i}\right)-\frac{\partial L}{\partial q_i}=Q_i^N=-f_d\cdot R=-c\cdot(R\dot{\theta})\cdot R\neq 0 \tag{1}$$

The equation of motion of the nonlinear system can be expressed as:

[1] Research Fellow, National Center for Research on Earthquake Engineering, chung@ncree.org
[2] Master Student, Department of Civil Engineering, National Taiwan University, r97521249@ntu.edu.tw
[3] PhD. Student, Department of Construction Engineering, National Taiwan University of Science and Technology, D9405004@mail.ntust.edu.com
[4] Professor, Department of Civil Engineering, National Taiwan University, lywu@ntu.edu.tw
[5] Associate Professor, Department of Construction Engineering, National Taiwan University of Science and Technology, hungming@mail.ntust.edu.tw

$$
\begin{aligned}
&(mR^2 + m\alpha^2 R^2 - 2m\alpha R^2 \cos\theta)\ddot{\theta} + m\alpha R^2 \sin\theta \cdot \dot{\theta}^2 \\
&+cR^2\dot{\theta} + mg\alpha R \sin\theta = -\left[mR - m\alpha R\cos\theta\right]\ddot{X}_g
\end{aligned} \tag{2}
$$

where θ is the rolling angle; α is the eccentricity of the pin to the radius of the disk; g is the gravity acceleration; and $\ddot{X}_g$ is the ground acceleration.

If the rolling angle is small enough, $\sin\theta \cong \theta$ and $\cos\theta \cong 1$. The linearized frequency (f_0) and linearized damping ratio (ξ) are, respectively, given as:

$$
\begin{aligned}
f_0 &= \frac{1}{2\pi}\sqrt{\frac{mg\alpha R}{mR^2 + m\alpha^2 R^2 - 2m\alpha R^2}} \\
&= \frac{1}{2\pi(1-\alpha)}\sqrt{\frac{\alpha g}{R}}
\end{aligned} \tag{3}
$$

$$
\begin{aligned}
\xi &= \frac{cR^2}{2\sqrt{(mR^2 + m\alpha^2 R^2 - 2m\alpha R^2)(mg\alpha R)}} \\
&= \frac{c}{2m(1-\alpha)}\sqrt{\frac{R}{\alpha g}}
\end{aligned} \tag{4}
$$

Numerical Simulation

Forced vibration method provides result that is closer to the actual state as often experienced in civil engineering. In isolation, the idea is to decrease the response of the superstructure. The responses of mass block in horizontal absolute acceleration are discussed in this paper. The effect of isolation can be compared by acceleration ratio (r_a) which is defined as the ratio between maximum absolute acceleration of the mass block and the maximum ground acceleration,

$$
r_a = \frac{\left|\ddot{X}_H(t) + \ddot{X}_g(t)\right|_{\max}}{\left|\ddot{X}_g(t)\right|_{\max}} \tag{5}
$$

The mass of the block $m = 1$ (ton) and the radius of the isolator $R = 1$ (m). The excitation used is Chi-Chi (TCU102) earthquake (Fig. 2) which is a near-fault earthquake with peak ground acceleration 2.98 (m/sec^2) and the dominant frequency range is 0.37 to 0.77 Hz. Eccentricity $\alpha = 0.3$ is selected for the isolator because its linearized frequency 0.390 Hz (calculated from Equation 3) falls into the dominant frequency of the earthquake. Different linearized damping ratios (0.1, 0.2 and 0.3) are simulated to study the effect of damping on the isolation. Using the same damping coefficients, the corresponding linear systems are simulated to compare the efficiency of nonlinear and linear isolation systems.

When the damping coefficient (c) is 0.240 N-s/m, the acceleration ratio is 0.7836 for the nonlinear isolation system and 1.4311 for the linear system (Table 1(a)). The maximum displacement is 0.4883 m for the nonlinear isolation system and 0.7078 m for the linear one (Table 1(b)). When the damping coefficient (c) is 0.720 N-s/m, the acceleration ratio is reduced from 0.8379 for the linear isolation system to 0.7732 for the nonlinear one (Table 1(a) and Fig. 3) and the maximum displacement is decreased from 0.3993 m to 0.3530 m (Table 1(b) and Fig. 4). Regardless of the value of the damping coefficient, the nonlinear system possesses better isolation performance.

The behavior of the isolation systems is further studied by applying El Centro earthquake (Fig. 5) which is a far-field earthquake with peak ground acceleration 3.35 (m/sec^2) and the dominant frequency ranges from 1.1 to 2.2 Hz.

When the damping coefficient (c) is 0.240 N-s/m, the acceleration ratios are 0.3694 and 0.4853 for the nonlinear and linear isolation systems (Table 1(a)), respectively. The maximum displacements are 0.2100 and 0.2693 m (Table 1(b)) for the nonlinear and linear isolation systems, respectively. When the damping coefficient (c) is 0.720 N-s/m, the acceleration ratio is reduced from 0.3453 for the linear isolation system to 0.2733 for the nonlinear one (Table 1(a) and Fig. 6) and the maximum displacement is decreased from 0.1753 m to 0.1106 m (Table 1(b) and Fig. 7). It shows that the nonlinear isolation system performs better than the linear one in both acceleration ratio and maximum displacement.

Conclusions

The paper presents the dynamic behavior of nonlinear isolator with viscous damping. With viscous damping, the systems show better isolation effect in both acceleration ratio and maximum displacement regardless of the type of the isolation system (linear or nonlinear), and of the type of earthquake (far-field or near-fault). When the damping coefficient is relatively small, the nonlinear isolation possesses much better performance over the linear one under near-fault earthquake. When the damping coefficient becomes larger, the performance of the linear isolation system is closer to that of the nonlinear one as detailed in Table 1(a) ~ (c).

References

Jangid RS, Londhe YB. Effectiveness of elliptical rolling rods for base isolation. Journal of Structural Engineering 1998; 124:469-472.

Sahasrabudhe S, Nagarajaiah S. Experimental study of sliding base-isolated buildings with magnetorheological dampers in near-fault earthquakes. Journal of Structural Engineering 2005; 131:1025-1034.

Chung L.L., Yang C.Y., Chen H.M. and Lu L.Y.. Dynamic behavior of nonlinear rolling isolation system. Struct. Control Health Monit 2009;16:32-54.

Table1. Comparison between responses of nonlinear and linear isolation ($\alpha = 0.3$)

(a) Acceleration ratio of mass block

Chi-Chi	Acceleration ratio (r_a)	
c(N-s/m)	**Nonlinear**	**Linear**
0.240	0.7836	1.4311
0.480	0.7447	0.9809
0.720	0.7732	0.8379
El Centro	Acceleration ratio (r_a)	
c(N-s/m)	**Nonlinear**	**Linear**
0.240	0.3694	0.4853
0.480	0.2997	0.3987
0.720	0.2733	0.3453

(b) Max. displacement response of mass block

Chi-Chi	Max. relative disp.(m)	
c(N-s/m)	**Nonlinear**	**Linear**
0.240	0.4883	0.7078
0.480	0.3928	0.4775
0.720	0.3530	0.3993
El Centro	Max. relative disp.(m)	
c (N-s/m)	**Nonlinear**	**Linear**
0.240	0.2100	0.2693
0.480	0.1455	0.2135
0.720	0.1106	0.1753

(c) Max. absolute acceleration response of mass block

Chi-Chi	Max. abs. acc.(m/s^2)	
c(N-s/m)	**Nonlinear**	**Linear**
0.240	2.3382	4.2701
0.480	2.2220	2.9269
0.720	2.3072	2.5001
El Centro	Max. abs. acc.(m/s^2)	
c(N-s/m)	**Nonlinear**	**Linear**
0.240	1.2383	1.6266
0.480	1.0045	1.3366
0.720	0.9161	1.1574

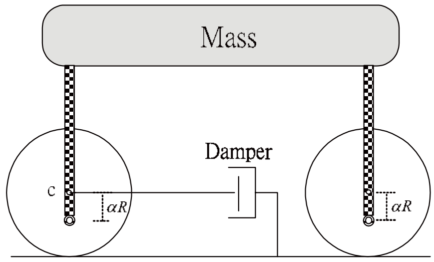

(a) Position without displacement

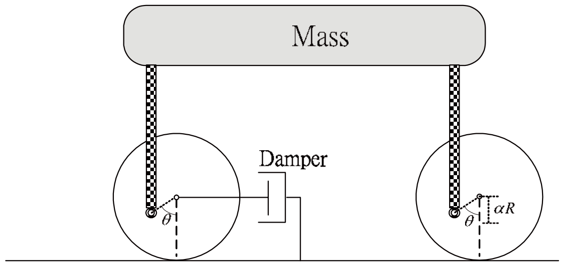

(b) Position with displacement

Fig. 1. Nonlinear rolling isolation system

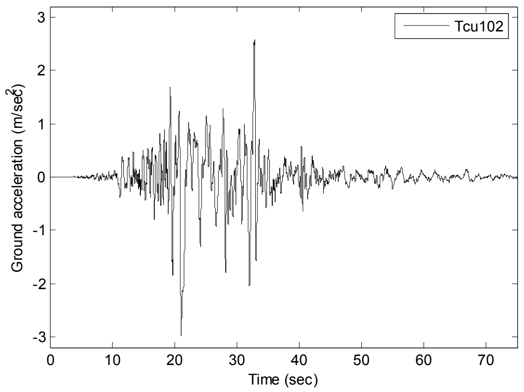

Fig. 2. Chi-Chi earthquake acceleration

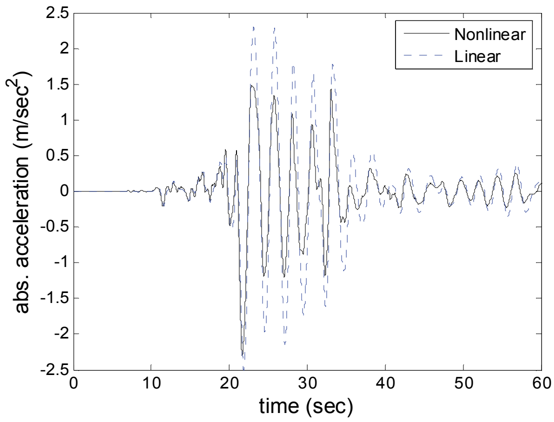

Fig. 3. Mass block acceleration (Chi-Chi)

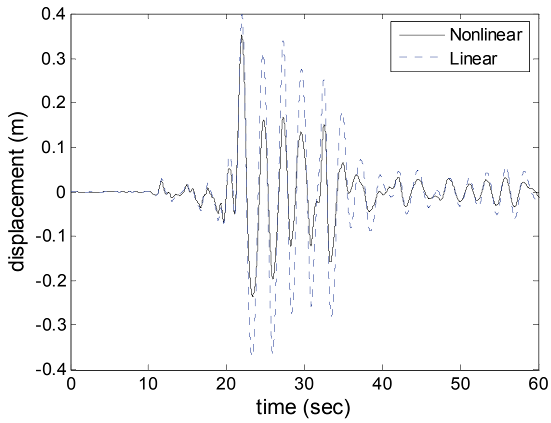

Fig. 4. Mass block displacement (Chi-Chi)

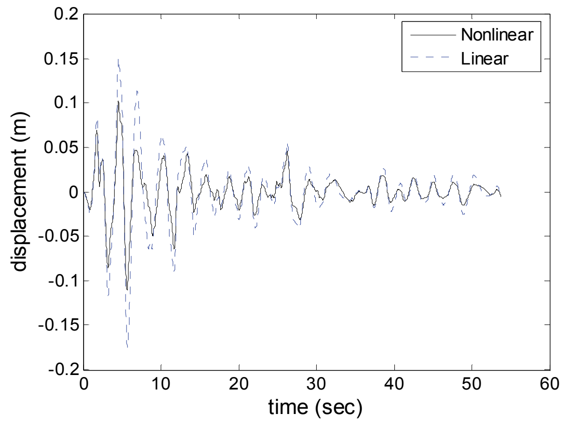

Fig. 7. Mass block displacement (El Centro)

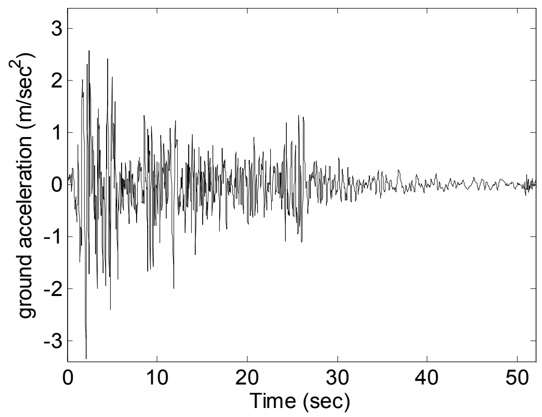

Fig. 5. El Centro earthquake acceleration

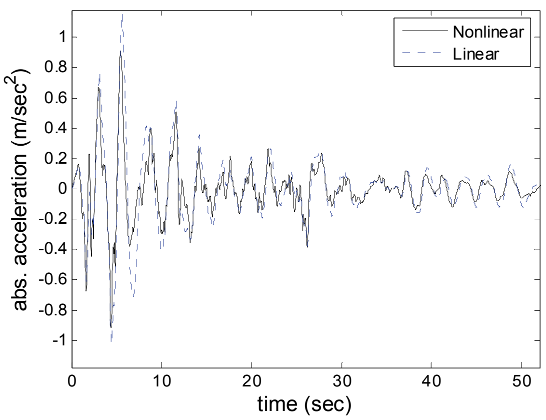

Fig. 6. Mass block acceleration (El Centro)

Optimal Design Formulae for Nonlinear Tuned Mass Dampers

Lap-Loi Chung[1] Lai-Yun Wu[2] Hsu-Hui Huang[3] and Mei-Chun Lin[4] and Kuan-Hua Lien[4]

鍾立來 [1]、吳賴雲 [2]、黃旭輝 [3]、林美君 [4]、連冠華 [4]

Abstract

The present study aims at developing optimal design formulae of nonlinear tuned mass damper (TMD) for damped main systems under the acceleration response quantity being minimized. Direct search technique is used to obtain the optimum damping coefficient and tuning frequency ratio of a nonlinear TMD system for which the response of a damped single degree-of-freedom main system subjected to white-noise random excitation is minimized. Optimal design formulae for these optimum parameters are then obtained by a sequence of curve-fitting techniques. The feasibility of the proposed optimal design formulae is illustrated numerically by using Taipei 101 structure implemented with TMD.

Keywords: optimal, design formulae, tuned mass damper (TMD), nonlinear

Introduction

A tuned mass damper (TMD) is a device consisting of a mass, a spring, and a dashpot attached to a structure to attenuate the dynamic response of the structure. The frequency of the damper is tuned to a particular structural frequency so that when that frequency is excited, the damper will resonate out of phase with the structural motion, dissipating input energy by the damper inertia force acting on the structure. The parameters that affect the response of the main system are the damping coefficient and the tuning frequency ratio of the TMD system. Maximum reduction in a response is attained when these parameters are at their optimum values. However, optimal design formulae for the linear tuned mass damper (TMD) are well developed, but those for the nonlinear TMD are still ongoing.

The present study, therefore, aims at developing optimal design formulae for nonlinear TMD for damped main systems under the acceleration response quantity being minimized. Direct search technique is used to obtain the optimum damping coefficient and tuning frequency ratio of a nonlinear TMD system for which the response of a damped single-degree-of-freedom main system subjected to white-noise random excitation is minimized. Optimal design formulae for these optimum parameters are then obtained by a sequence of curve-fitting techniques. The feasibility of the proposed optimal design formulae is illustrated numerically by using the Taipei 101 structure implemented with nonlinear TMD.

Motion Equation of Structure with Nonlinear TMD

When a nonlinear TMD is attached to a single-degree-of-freedom (SDOF) structure, as shown in Fig. 1, it becomes a 2DOF system. The equation of motion of the nonlinear system can be expressed as

$$\mathbf{M}\ddot{\mathbf{x}}(t)+\mathbf{C}\dot{\mathbf{x}}(t)+\mathbf{K}\mathbf{x}(t)=\mathbf{b}f_{\mathrm{d}}(t)+\mathbf{b}f_{\mathrm{r}}(t)+\mathbf{e}w(t) \quad (1)$$

where $\mathbf{x}(t)=\begin{bmatrix} x_{\mathrm{d}}(t) \\ x_{\mathrm{s}}(t)\end{bmatrix}$; $\mathbf{M}=\begin{bmatrix} m_{\mathrm{d}} & 0 \\ 0 & m_{\mathrm{s}}\end{bmatrix}$;

$\mathbf{C}=\begin{bmatrix} 0 & 0 \\ 0 & c_{\mathrm{s}}\end{bmatrix}$; $\mathbf{K}=\begin{bmatrix} 0 & 0 \\ 0 & k_{\mathrm{s}}\end{bmatrix}$; $\mathbf{b}=\begin{bmatrix} -1 \\ 1\end{bmatrix}$; $\mathbf{e}=\begin{bmatrix} 0 \\ 1\end{bmatrix}$;

$\mathbf{x}(t)$ is the displacement vector of the system; $\mathbf{M}$, $\mathbf{C}$ and $\mathbf{K}$ are the mass, damping and stiffness

[1] Research Fellow, National Center Research on Earthquake Engineering, chung@ncree.org
[2] Professor, Department of Civil Engineering, National Taiwan University, lywu@ntu.edu.twDoctor,
3 Ph. D., Department of Civil Engineering, National Taiwan University, d93521004@ntu.edu.tw
4 Graduate Student, Department of Civil Engineering, National Taiwan University

matrices of the system; $\mathbf{b}$ and $\mathbf{e}$ are TMD internal loading and structural external loading vectors, respectively; $x_d(t)$ and $x_s(t)$ are displacements of the TMD and the structure, respectively; m_d and m_s are the respective masses of the TMD and structure; c_s is the damping coefficient of the structure; k_s is the stiffness of the structure; $f_d(t)$ and $f_r(t)$ are the damping force and restoring force, respectively; $w(t)$ is the external disturbances.

The solution of motion equation can be expressed in discrete-time fashion as first-order difference equation,

$$\mathbf{z}[k+1]=\mathbf{A}_d\mathbf{z}[k]+\mathbf{b}_d f_d[k]+\mathbf{b}_d f_r[k]+\mathbf{e}_d w[k] \qquad (2)$$

where $\mathbf{z}[k]=\begin{bmatrix}\mathbf{x}[k]\\ \dot{\mathbf{x}}[k]\end{bmatrix}$; $\mathbf{A}_d=e^{\mathbf{A}\Delta t}$;

$\mathbf{b}_d=\mathbf{A}^{-1}(\mathbf{A}_d-\mathbf{I})\mathbf{B}$; $\mathbf{e}_d=\mathbf{A}^{-1}(\mathbf{A}_d-\mathbf{I})\mathbf{E}$;

$f_d[k]=f_d(k\Delta t)$; $f_r[k]=f_r(k\Delta t)$;

$\mathbf{A}=\begin{bmatrix}\mathbf{0} & \mathbf{I}\\ -\mathbf{M}^{-1}\mathbf{K} & -\mathbf{M}^{-1}\mathbf{C}\end{bmatrix}$; $\mathbf{B}=\begin{bmatrix}\mathbf{0}\\ \mathbf{M}^{-1}\mathbf{b}\end{bmatrix}$;

$\mathbf{E}=\begin{bmatrix}\mathbf{0}\\ \mathbf{M}^{-1}\mathbf{e}\end{bmatrix}$

The damping force $f_d[k]$ obeys a nonlinear viscous damping law, and restoring force $f_r[k]$ obeys a linear law given by

$$f_d[k]=c_d\left|\mathbf{D}_2\mathbf{z}[k]\right|^{\nu}\operatorname{sgn}(\mathbf{D}_2\mathbf{z}[k]) \qquad (3)$$

$$f_r[k]=k_d\mathbf{D}_1\mathbf{z}[k] \qquad (4)$$

where k_d is the stiffness of TMD; c_d is the damping coefficient of the TMD with dimension of mass $\cdot$ length$^{1-\nu}$ $\cdot$ time$^{\nu-2}$; ν is the power law exponent of viscous damping of TMD; $\mathbf{D}_1=\begin{bmatrix}1 & -1 & 0 & 0\end{bmatrix}$; $\mathbf{D}_2=\begin{bmatrix}0 & 0 & 1 & -1\end{bmatrix}$.

Optimal Design Formulae

In this paper, the performance index J is considered as the acceleration ratio, thus J is defined as:

$$J=\sum_{k=0}^{k_1}\mathbf{z}^{T}[k]\mathbf{D}^{T}\mathbf{D}\mathbf{z}[k]+2\mathbf{z}^{T}[k]\mathbf{D}^{T}Ew[k]+E^{2}w^{2}[k] \qquad (5)$$

where $\mathbf{D}=\begin{bmatrix}0 & -\omega_s^2 & 0 & -2\xi_s\omega_s\end{bmatrix}$; $E=1/m_s$; ω_s and ξ_s are the natural frequency and damping ratio of the structure.

The mass ratio R_m, frequency ratio R_f and non-dimensional damping coefficient χ of the nonlinear TMD are, respectively, defined as：

$$R_m=m_d/m_s,\quad R_f=\sqrt{k_d/(k_sR_m)} \qquad (6)$$

$$\chi=c_d/(m_sf_s\left|\dot{x}_s\right|^{1-\nu}_{\text{max, without TMD}}) \qquad (7)$$

where $\left|\dot{x}_s\right|_{\text{max, without TMD}}$ is the maximum velocity value for the main system without TMD.

It is extremely difficult to determine the exact closed-form expressions for optimum nonlinear TMD parameters. However, explicit mathematical expressions that correspond to the optimum parameters of nonlinear TMD system obtained by numerical searching technique are useful for engineering applications. Five white-noise wind forces, three structural damping ratios ξ_s (0, 2 and 5%), four mass ratios R_m (2, 3, 4 and 5%) and three damping exponents ν (0.5, 1 and 2) are used to determine the optimum parameters by direct search technique (Wright, 1995). A curve-fitting scheme is adopted to develop the optimum design formulae for non-dimensional damping coefficient and frequency ratio of nonlinear TMD,

$$\begin{aligned}\chi^{\text{opt}}=&[(0.20+3.48\xi_s-0.25\xi_s^2)+\\&(-6.94-8.06\,\xi_s+0.74\xi_s^2)\nu+\\&(25.52+10.47\xi_s-1.62\xi_s^2)\nu^2]R_m^2+\\&[(0.75-0.19\xi_s+0.02\xi_s^2)+\\&(0.42+0.23\xi_s-0.03\xi_s^2)\nu+\\&(-0.55-0.04\xi_s+0.01\xi_s^2)\nu^2]R_m\end{aligned} \qquad (8)$$

$$\begin{aligned}R_f^{\text{opt}}=R_m\exp[&(-1.0097-0.0004\xi_s)\ln(R_m)+\\&(-0.0497-0.0007\xi_s)]\end{aligned} \qquad (9)$$

Numerical Verification

The Taipei 101 holds the title as the world's second tallest building at 508 m. Because the TMD is hung from the 92nd floor, in order to turn the structure into an SDOF structure, the first mode shape is normalized such that the component at the 92nd floor is unity. After model reduction, the first modal mass m_s is 5371.7 $\text{tonf-sec}^2/\text{m}$, the first modal frequency f_s is 0.14251 Hz, and the first modal stiffness $k_s=m_s(2\pi f_s)^2$ is 4306.8 tonf/m. It is assumed that the first modal damping ratio ξ_s is 2% so that the first modal damping coefficient can be obtained as $c_s=2m_s(2\pi f_s)\xi_s=192.39$ tonf-sec/m

(Table 1 and Wu, et al., 2005).

The Taipei 101 structure is excited by external wind force with return period of half a year (Fig. 2). The mass of the TMD for the Taipei 101 is 660 ton, the heaviest in the world so that the mass ratio R_m is 1.25% ($m_d = 67.278$ tonf-sec^2/m). The spherical mass is supported by a sling of eight steel cables. Eight viscous dampers act like shock absorbers when the sphere shifts. The viscous damper is nonlinear of damping power law exponent $\nu = 2.0$ with damping coefficient c_d 1,000 kN-(sec/m)^2. Each damper is 3.1m in length and inclines 60 degrees with the floor. It can provide at most 1,000 kN of damping force. The mass is able to move 1.5 m in any direction. This gold-colored orb can be viewed from restaurants, bars and observation decks between the 88th and 92nd stories. The length of the pendulum for the TMD is determined from the TMD stiffness which is in turn determined by the frequency ratio. The frequency ratio R_f is 0.9855, computed from the equation proposed by Sadek, et al., 1997.

Optimum design parameters for the nonlinear TMD from the direct search method and the optimal design formulae are listed in Table 2. Optimal frequency ratio (R_f^{opt}) from the design formula is 1.025 times that from the direct search method, but optimal damping coefficient (c_d^{opt}) from the design formula is 2.00 times that from the direct search method. Maximum displacement and acceleration of the main system with TMD from design formulae are, respectively, 1.042 and 0.983 times those from the direct search method (Figs. 3 and 4). It is observed from the acceleration ratios that the effectiveness of both TMDs designed from the direct search method and the design formulae are similar since the effectiveness is sensitive to frequency ratio and not that sensitive to damping coefficient. The relative displacement of the TMD from design formulae (0.1756m) is smaller (Fig. 5) but the damping force of the TMD from design formulae (35.647kN) is larger compared with the TMD from the direct search method (0.2264m and 28.885kN) (Table 2 and Fig. 6).

Conclusions

In this paper, optimal design formulae for a TMD with nonlinear viscous damping are developed. Given structural damping ratio, maximum structural velocity without TMD, mass ratio and damping exponents, optimal design parameters (non-dimensional damping coefficient and frequency ratio) can be computed from the proposed formulae. The feasibility of the proposed optimal design formulae is illustrated numerically by using Taipei 101 structure implemented with nonlinear TMD.

References

Wright, M.H. (1995), "Direct search methods: once scorned, now respectable in numerical analysis", Pitman Research Notes in Mathematics, Addison Wesley Longman Limited, 191-208.

Wu, L.Y., Chung, L.L., Chen, J.C., Huang, G.L. (2005), "Control simulation for Taipei 101 with wind excitation", 7th Conference on Structural Engineering. (in Chinese)

Sadek F., Mohraz B., Taylor A.W., Chung R.M. (1997), "A method of estimating the parameters of mass dampers for seismic applications", *Earthquake Engineering & Structural Dynamics* 26:617-635.

Table 1 Taipei 101 SDOF parameters

parameters	value
Mass(m_s)(tonf-sec^2/m)	5371.7
TMD Mass(m_d) (tonf-sec^2/m)	67.278
Stiffness(k_s)(tonf/m)	4306.8
Damping ratio(ξ_s)	0.02
Frequency f_s (Hz)	0.1425

Table 2 Taipei 101 optimum parameters

	Without TMD	Direct search	Design formulae
Frequency ratio (R_f^{opt})	—	0.97091	0.9950
damping coefficient (c_d^{opt}) ($\mathrm{kN}\cdot(\frac{\mathrm{sec}^2}{\mathrm{m}^2})$)	—	693.31	1386.6
Acceleration ratio (R_a)	—	0.70212	0.7347
Maximum displacement (m)	0.087	0.0600	0.0625
Maximum acceleration (m/sec^2)	0.073	0.04999	0.0491
Maximum relative displacement for TMD (m)	—	0.2264	0.1756
Maximum damping force for TMD (kN)	—	28.885	35.647

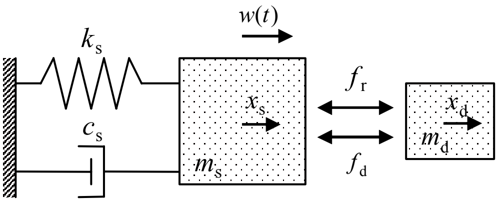

Fig. 1 System model of nonlinear TMD attached to SDOF structure.

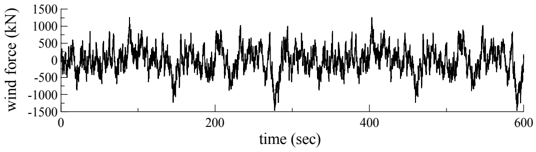

Fig. 2 External wind force with return period of half a year.

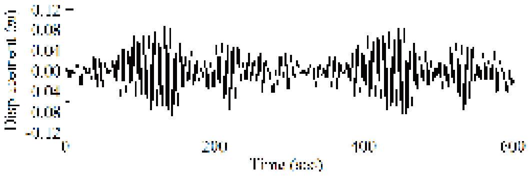

(a) Without TMD

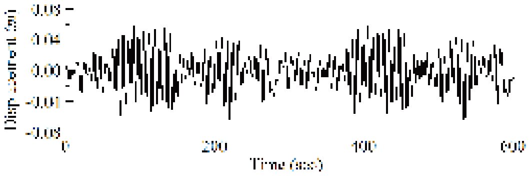

(b) Design formulae

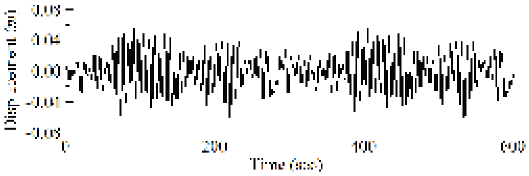

(c) Direct search

Fig. 3 Displacement time history for Taipei 101

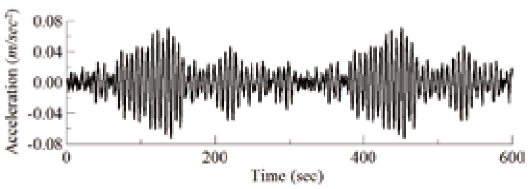

(a) Without TMD

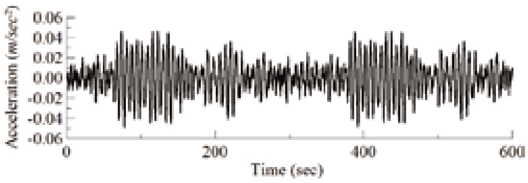

(b) Design formulae

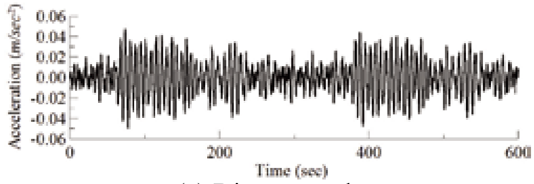

(c) Direct search

Fig. 4 Acceleration time history for Taipei 101

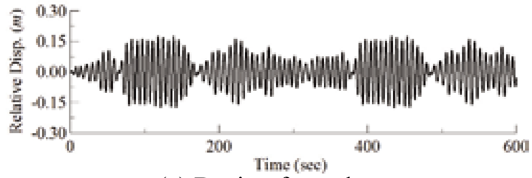

(a) Design formulae

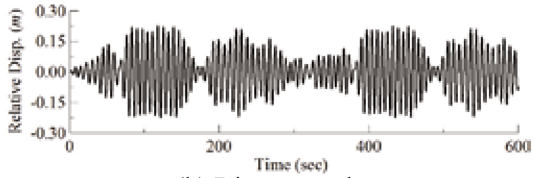

(b) Direct search

Fig. 5 Relative Displacement time history for TMD

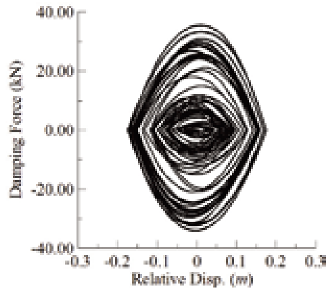

(a) Design formulae

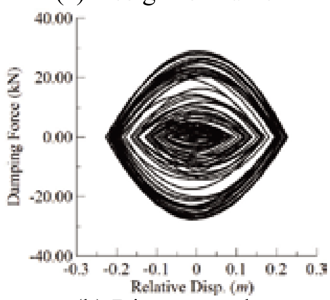

(b) Direct search

Fig. 6 Hysteresis loop for Taipei 101

Optimal Design of Friction Pendulum System Type Tuned Mass Damper

Lap-Loi Chung [1] Lai-Yun Wu [2] Hsuan-Hung Chen [3] Mei-Chun Lin [4] and Kuan-Hua Lien [5]

鍾立來 [1]、吳賴雲 [2]、陳宣宏 [3]、林美君 [4]、連冠華 [5]

Abstract

In this paper, an optimal design of a structure implemented with a friction pendulum system (FPS) type tuned mass damper (TMD) is proposed. The FPS typed TMD has these properties: (1) the mass slides on the spherical surface so that the space to accommodate the FPS type TMD is much less than the suspension type; (2) restoring force is provided by the spherical surface so that no extra spring is needed; and (3) vibration energy is dissipated by the friction mechanism of the interface between the mass and the spherical surface. Numerical simulation method is proposed for the structure implemented with FPS type TMD. The optimal design parameters (frequency ratio and friction coefficient) of the TMD are found by direct search method. The feasibility of the proposed TMD is illustrated by adopting the Taipei 101 as a model implemented with FPS type TMD. Subjected to design wind force with return period of half a year, the requirement of comfort is satisfied.

Keywords: structure control, tuned mass damper (TMD), nonlinear, friction pendulum system

Introduction

A tuned mass damper (TMD) is a device consisting of a mass, a spring, and a dashpot attached to a structure to attenuate the dynamic response of the structure. The frequency of the damper is tuned to a particular structural frequency so that when that frequency is excited, the damper will resonate out of phase with the structural motion, thus dissipating input energy by the damping mechanism of the device. In this paper, an optimal design of a structure implemented with an FPS type TMD is proposed (Mokha, et al., 1991). Restoring force is provided by the spherical surface of the TMD when the mass slides away from the lowest point of the spherical surface. Small angle of sliding is assumed so that the restoring force is linear (Tsopelas, et al., 1996). Energy is dissipated due to the nonlinear friction force of the contact interface between the mass and the sliding surface. At first, by employing the first order state-space equation transferred from the motion equation of a structure implemented with a FPS type TMD, the discrete-time state-space equation by which the time history analysis can be conducted is derived (Chung, et al., 2008). The direct search method is used to obtain the optimal design parameters of FPS type TMD. Finally, as an example, the structural response of the Taipei 101 implemented with an FPS type TMD subjected to the design wind force is simulated, and the feasibility is studied.

Motion Equation of Structure with FPS Type TMD

After an FPS type TMD is attached to the SDOF (single-degree-of-freedom) structure subjected to external disturbances, $w(t)$ (Fig. 1), it becomes a 2DOF (two-degree-of-freedom) system. The equation of motion of the system can be expressed as

$$\mathbf{M}\ddot{\mathbf{x}}(t)+\mathbf{C}\dot{\mathbf{x}}(t)+\mathbf{K}\mathbf{x}(t)=\mathbf{b}u(t)+\mathbf{E}_1 w(t) \qquad (1)$$

where $\mathbf{x}(t)=\begin{bmatrix} x_d(t) \\ x_s(t) \end{bmatrix}$; $\mathbf{M}=\begin{bmatrix} m_d & 0 \\ 0 & m_s \end{bmatrix}$; $\mathbf{C}=\begin{bmatrix} 0 & 0 \\ 0 & c_s \end{bmatrix}$;

[1] Research Fellow and Adjunct Professor, Center Research on Earthquake Engineering, chung@ncree.org
[2] Professor, Department of Civil Engineering, National Taiwan University, lywu@ntu.edu.tw
[3] Master, Department of Civil Engineering, National Taiwan University, r95521212@ntu.edu.tw
[4] Master Student, Department of Civil Engineering, National Taiwan University, r97521235@ntu.edu.tw
[5] Ph.D. Candidate, Department of Civil Engineering, National Taiwan University, d95521004@ntu.edu.tw

$\mathbf{K}=\begin{bmatrix} k_d & -k_d \\ -k_d & k_d+k_s \end{bmatrix}$; $\mathbf{b}=\begin{bmatrix} -1 \\ 1 \end{bmatrix}$; $\mathbf{E}_1=\begin{bmatrix} 0 \\ 1 \end{bmatrix}$; $\mathbf{x}(t)$ is the displacement vector of the system; $\mathbf{M}$, $\mathbf{C}$ and $\mathbf{K}$ are the mass, damping and stiffness matrices of the system; $x_d(t)$ and $x_s(t)$ are the displacements of the TMD and the main system; m_d and m_s are the masses of the TMD and the main system; c_s is damping coefficient of the main system; k_d and k_s are stiffnesses of the TMD and the structure; $u(t)$ is the friction force; and $\mathbf{b}$ and $\mathbf{E}_1$ are TMD internal loading and structural external loading vectors, respectively.

The equation of motion shown in Eq. (1) is conveniently expressed as a first-order differential equation in state space,

$$\dot{\mathbf{z}}(t)=\mathbf{A}\mathbf{z}(t)+\mathbf{B}u(t)+\mathbf{E}w(t) \tag{2}$$

where

$\mathbf{z}(t)=\begin{bmatrix} \mathbf{x}(t) \\ \dot{\mathbf{x}}(t) \end{bmatrix}$; $\mathbf{A}=\begin{bmatrix} \mathbf{0} & \mathbf{I} \\ -\mathbf{M}^{-1}\mathbf{K} & -\mathbf{M}^{-1}\mathbf{C} \end{bmatrix}$; $\mathbf{B}=\begin{bmatrix} \mathbf{0} \\ \mathbf{M}^{-1}\mathbf{b} \end{bmatrix}$; $\mathbf{E}=\begin{bmatrix} \mathbf{0} \\ \mathbf{M}^{-1}\mathbf{E}_1 \end{bmatrix}$

The solution of Eq. (2), can be expressed in discrete-time fashion as a first-order difference equation

$$\mathbf{z}[k+1]=\mathbf{A}_d\mathbf{z}[k]+\mathbf{B}_d u[k]+\mathbf{E}_d w[k] \tag{3}$$

where

$\mathbf{z}[k]=\begin{bmatrix} \mathbf{x}[k] \\ \dot{\mathbf{x}}[k] \end{bmatrix}$; $\mathbf{A}_d=e^{\mathbf{A}\Delta t}$; $\mathbf{B}_d=\mathbf{A}^{-1}(\mathbf{A}_d-\mathbf{I})\mathbf{B}$; $\mathbf{E}_d=\mathbf{A}^{-1}(\mathbf{A}_d-\mathbf{I})\mathbf{E}$;

Assume that the kinetic friction coefficient is equal to the maximum static friction coefficient. The friction force can be expressed as

$$u[k]=\mu N \tag{4}$$

where $N=m_d g$ is the normal force of the contact interface; and g is the acceleration of gravity.

Assume that the k+1 step of the TMD relative velocity is zero (non-slip state), then the friction force of the k step can be estimated as

$$\hat{u}[k]=-\left(\mathbf{d}_1{}^T\mathbf{B}_d\right)^{-1}\mathbf{d}_1{}^T\left(\mathbf{A}_d\mathbf{z}[k]+\mathbf{E}_d w[k]\right) \tag{5}$$

While the friction force is less than the maximum static friction force $\hat{u}[k]<\mu N$, the FPS type TMD is in the stick state and the friction force can be expressed as

$$u[k]=\hat{u}[k] \tag{6}$$

While the friction force is larger than the maximum static friction force $\hat{u}[k]\geq\mu N$, the FPS type TMD is in the sliding state and the friction force can be expressed as

$$u[k]=\mu m_d g \tag{7}$$

Structural acceleration can be expressed as

$$\ddot{\mathbf{x}}[k]=\begin{bmatrix} -\mathbf{M}^{-1}\mathbf{K} & -\mathbf{M}^{-1}\mathbf{C} \end{bmatrix}\mathbf{z}[k]+\mathbf{M}^{-1}\mathbf{b}u[k]+\mathbf{M}^{-1}\mathbf{E}_1 w[k] \tag{8}$$

Numerical Verification

Currently, the Taipei 101 holds the title of world's second tallest building at 508 m. Because the TMD is hung from the 92nd floor, in order to turn the structure into an SDOF structure as shown in Table 1, the first mode shape is normalized such that the component at the 92nd floor is unity. After model reduction, the first modal mass m_s is $5371.7\ \text{tonf-sec}^2/\text{m}$, the first modal frequency f_s is 0.14251 Hz, and the first modal stiffness $k_s=m_s(2\pi f_s)^2$ is 4036.8 tonf/m. It is assumed that the first modal damping ratio ξ_s is 2% so that the first modal damping coefficient can be obtained as $c_s=2m_s(2\pi f_s)\xi_s=192.4$ tonf-sec/m (Wu, et al., 2005). The parameters are normalized to be dimensionless as, respectively,

$$R_m=m_d/m_s \tag{9}$$

$$R_f=f_d/f_s \tag{10}$$

$$R_a=\sqrt{J_{\text{control}}(\ddot{x}_n[k])/J_{\text{without control}}(\ddot{x}_n[k])} \tag{11}$$

where R_m and R_f are the mass ratio and frequency ratio, respectively; and R_a is acceleration ratio.

The Taipei 101 is turned into an SDOF structure and implemented with a FPS type TMD. The mass of the TMD is $m_d=67.146\ \text{tonf-sec}^2/\text{m}$ so that the mass ratio is 1.25%. The Taipei 101 structure is excited by external wind force with return period of half a year (Fig. 2). The optimal design parameters are computed by the direct search method such that the acceleration ratio is minimized. The results are $R_f=1.0190$, $R_a=0.6888$ and $\mu=0.0011$. The performance of direct search method and 3-D diagram method are shown in Table 2. Furthermore, the 3-D variation of the performance index R_a against the TMD design parameters, R_f and μ, is plotted (Fig. 3). The optimal design parameters found by the graph of 3-D variation are very close to those by the direct search method. The structural acceleration and the TMD relative displacement time histories are plotted (Figs. 4 and Fig. 5, respectively). The structural acceleration of Taipei 101 without FPS type TMD is 6.54 gal and 4.15 gal with FPS type TMD. The degree of vibration suppression in the structural acceleration is 36.54 %. The maximum relative displacement of TMD is 0.3147m. Hysteresis loop of friction force against relative displacement for the TMD is shown in

Fig. 6 and the maximum friction force is 0.7904tonf.

Conclusions

In this study, the feasibility of FPS type TMD is verified by the numerical simulation. The discrete-time state-space equation for SDOF structure implemented with a FPS type TMD is derived so that time history analysis can be conducted. Optimal design parameters (frequency ratio and friction coefficient) of TMD are obtained by direct search method such that the performance index (acceleration ratio) is minimized. The optimal results are further confirmed by the 3-D plot. The feasibility is illustrated numerically by using the Taipei 101 structure as a model implemented with FPS type TMD. With the implementation of the TMD, the requirement of comfort is satisfied.

References

Mokha, A.S., Constantinou, M.C., Reinhorn, A.M., & Zayas, V. (1991), "Experimental study of friction pendulum system isolation system", *Journal of Structural Engineering* 117, 1201-1217.

Tsopelas, P., Constantinou, M.C., Kim, Y.S., & Okamoto S. (1996), "Experimental study of FPS system in bridge seismic isolation", *Earthquake Engineering & Structural Dynamics* 25, 65-78.

Chung, L.L., Wu, L.Y., Chen, H.H., Huang, H.H. Chang, C.H. & Lin, T.H. (2008), Optimal Design of Friction Pendulum System Typed Tuned Mass Damper, NCREE 08-018. (in Chinese)

Wu, L.Y., Chung, L.L., Chen, J.C., Huang, G.L. (2005), Control simulation for Taipei 101 with wind excitation. 7th Conference on Structural Engineering. (in Chinese)

Table 1 Taipei 101 SDOF parameters

parameters(unit)	value
Mass m_s (ton-sec^2/m)	5371.7
Damping c_s (tonf-sec/m)	192.4
Stiffness k_s (tonf/m)	4306.8
Damping ratio ξ_s	0.02
frequency f_s (Hz)	0.1425

Table 2 Performance of direct search method and 3-D diagram method

	Direct search	3-D diagram
Frequency ratio R_f	1.0190	1.0231
Frictional coefficient μ	0.0011	0.0012
Objective function ratio R_a	0.6888	0.6889

Table 3. Results of Taipei 101 model (dynamic analysis)

$R_m = 1.25\%$	Without TMD	With FPS TMD
Frequency ratio (R_f)	—	1.0190
Friction coefficient (μ)	—	0.0011
Acceleration ratio (R_a)	—	0.6888
Peak Acceleration (cm/sec^2)	6.54	4.15
TMD relative displacement (cm)	—	31.47
Friction force (tonf)	—	0.79

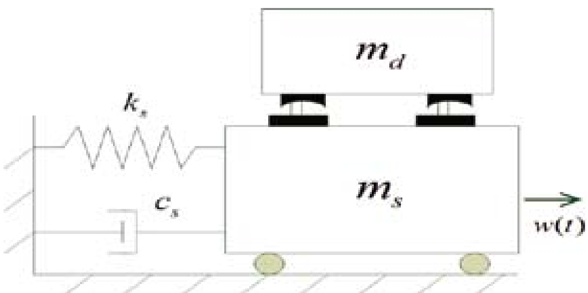

Fig. 1 System model of FPS type TMD

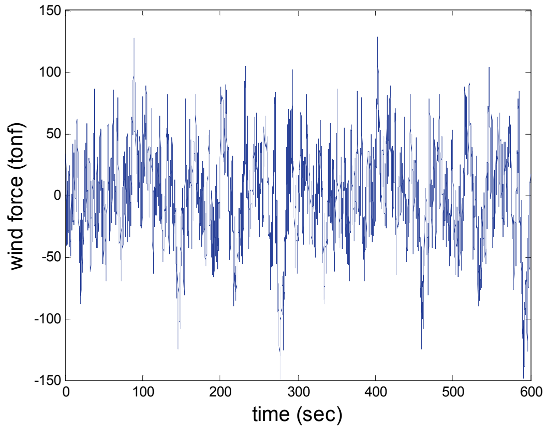

Fig. 2 External designed wind force attached to SDOF structure.

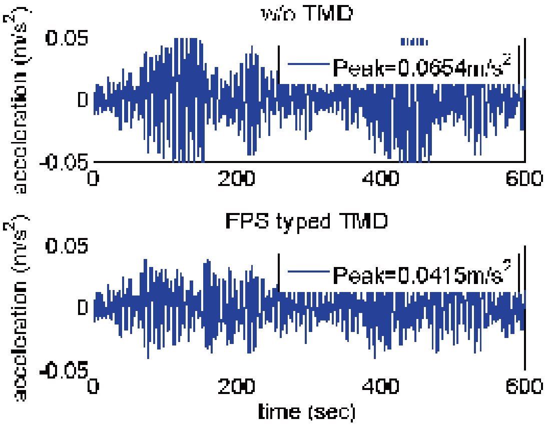

Fig. 4 Structural acceleration time history

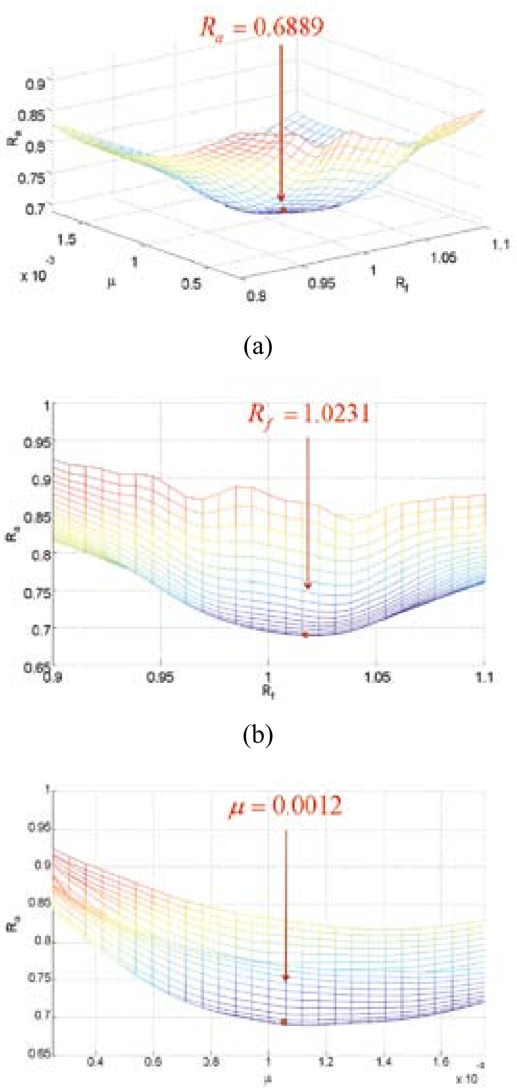

(a)

(b)

(c)

Fig. 3 3-D variation of acceleration ratio (R_a)

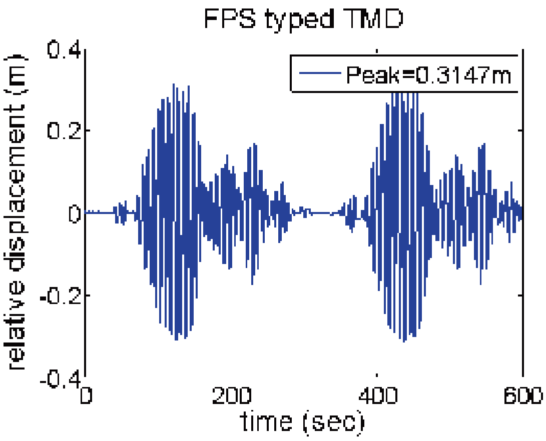

Fig. 5 TMD relative displacement time history

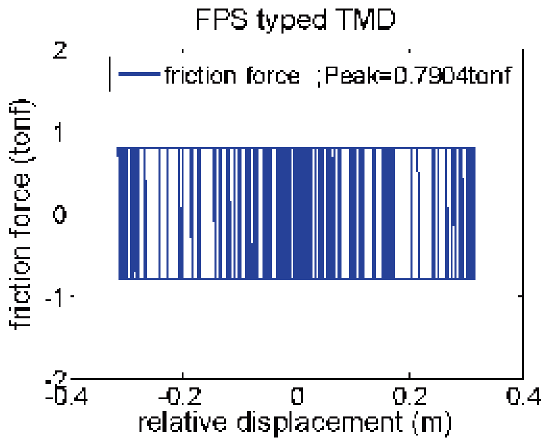

Fig. 6 Hysteresis loop of friction force

Semi-active Control of Isolation System with Variable Friction

Cho-Yen Yang [1] Lap-Loi Chung [2] Hung-Ming Chen [3] Lyan-Ywan Lu [4]

楊卓諺 [1]、鍾立來 [2]、陳鴻銘 [3] 、盧煉元 [4]

Abstract

Many researches have shown that a passive isolation system can effectively reduce seismic responses of structures. Passive isolation systems are simple and reliable but it is not adaptive under excitations different from the design one. For this reason, an active isolation system can be implemented to make an isolation system be adaptive. But there is another disadvantage in active isolation system, that is, it needs much energy for the actuator. The semi-active isolation system is a compromise between passive and active one. The piezoelectric smart isolation system (PSIS) composes of an isolation stage and a piezoelectric friction damper (PFD). In this research, a simple control law is proposed. The control force, which is the normal force of PFD, is proportional to the exponent power of the absolute velocity of isolation platform. It is simple, and full-state feedback is not required. From numerical simulation, the proposed control law is found to be more effective and efficient than passive isolation system.

Keywords: semi-active, isolation, friction, piezoelectricity

Introduction

A passive isolation system could be ineffective when the system is subjected to near-fault earthquake (Jangid 2005, Nagarajaiah & Sahasrabudhe 2005). The semi-active control is a good compromise between passive and active control systems. The feasibility of piezoelectric smart isolation system (PSIS) has been proven by numerical and experimental studies (Lu and Lin 2008). There are many control theories for semi-active control, in this study, a simple controller has been proposed. The controller needs only the measurement of velocity in the isolation platform. The controller output is proportional to the absolute velocity of platform with a power parameter ν by a gain parameter G. The optimal parameters are chosen by simulation of the system under far-field earthquake. Those optimal cases are re-simulated under near-fault earthquake. The isolation performance can be compared by a performance index which involves with base shear of the structure and maximum displacement of isolation platform.

Equation of Motion

Fig. 1 shows the mechanism of PSIS. The spring provides the restoring force of isolation sliding platform. The piezoelectric friction damper is the control device. There are two friction forces in this system, one is the friction between the sliding block and the guide rail (u_i) and another is the friction between the friction damper and the friction bar (u_d). Those two friction forces provide the energy dissipation of the isolation system. The equation of motion is as follows:

[1] PhD. Student, Department of Construction Engineering, National Taiwan University of Science and Technology, D9405004@mail.ntust.edu.tw

[2] Research Fellow, National Center for Research on Earthquake Engineering, chung@ncree.org.tw

[3] Associate Professor, Department of Construction Engineering, National Taiwan University of Science and Technology, hungming@mail.ntust.edu.tw

[4] Professor, Department of Construction Engineering, National Kaohsiung First University of Science and Technology, lylu@ccms.nkfust.edu.tw

$$\mathbf{M}\ddot{\mathbf{x}}(t)+\mathbf{C}\dot{\mathbf{x}}(t)+\mathbf{K}\mathbf{x}(t)=\mathbf{B}_1(u_d(t)+u_i(t))+\mathbf{E}_1 w(t) \qquad (1)$$

$$\mathbf{M}=\begin{bmatrix} m_s & 0 \\ 0 & m_b \end{bmatrix},\ \mathbf{C}=\begin{bmatrix} c_s & -c_s \\ -c_s & c_s \end{bmatrix},\ \mathbf{K}=\begin{bmatrix} k_s & -k_s \\ -k_s & k_s+k_i \end{bmatrix},$$

$$\mathbf{x}(t)=\begin{Bmatrix} x_s(t) \\ x_b(t) \end{Bmatrix},\ \mathbf{B}_1=\begin{Bmatrix} 0 \\ 1 \end{Bmatrix},\ \mathbf{E}_1=\begin{Bmatrix} -m_s \\ -m_b \end{Bmatrix},\ w(t)=\ddot{x}_g(t)$$

Eq. (1) shows a 2-DOF system if the isolated equipment in Fig. 1 is replaced by a SDOF structure. m_s, c_s and k_s are the mass, damping coefficient and stiffness of structure, respectively. m_b and k_i are the mass and stiffness of the isolation platform, respectively. In this system, the normal force of PFD ($N(t)$) is controllable. The Coulomb friction model is used here for the two friction forces (u_i and u_d).

$$\begin{cases} |u_i(t)| \le \mu_i(m_s+m_b)g & \text{if } \dot{x}_b(t)=0 \\ u_i(t)=\mu_i(m_s+m_b)g\,\mathrm{sgn}(\dot{x}_b(t)) & \text{if } \dot{x}_b(t)\ne 0 \end{cases} \qquad (2)$$

$$\begin{cases} |u_d(t)| \le \mu_d N(t) & \text{if } \dot{x}_b(t)=0 \\ u_d(t)=\mu_d N(t)\,\mathrm{sgn}(\dot{x}_b(t)) & \text{if } \dot{x}_b(t)\ne 0 \end{cases} \qquad (3)$$

μ_i and μ_d are the two friction coefficients for guide rail and PFD, respectively. From the above two equations (Eq. (2) and (3)), the problem is the determination of the real friction forces in each time step. Here, the shear balance method can be adopted to build a numerical model in predicting the two friction forces.

The controller in this study is defined as follows:

$$N(t)=G|\dot{x}_b(t)|^{\nu} \qquad (4)$$

The normal force ($N(t)$) is proportional to the absolute velocity of isolation platform with power to ν by a gain parameter G. The normal force is always greater than zero that is why absolute velocity is taken for the controller.

Numerical Simulation

Before numerical simulations are conducted, a performance index is defined as:

$$J=\alpha R_s+(1-\alpha)R_d \qquad 0\le\alpha\le 1 \qquad (5)$$

where $R_s=\dfrac{\max(m_s\ddot{x}_{s,abs}(t))_{semi-active}}{\max(m_s\ddot{x}_{s,abs}(t))_{passive}}$ and

$$R_d=\frac{\max(x_b(t))_{semi-active}}{\max(x_b(t))_{passive}}$$

R_s is the ratio of base shear for the isolated structure and R_d is the ratio of maximum displacement in isolation platform. In isolation problem, the base shear of the isolated object must not be the only focus but also the maximum displacement of isolation platform. The low base shear or acceleration of structure is expected but the displacement of isolation layer should not be too large. The weighting factor α defines which physical quantity, base shear or platform displacement, is concerned more. Some parameters of the system in numerical simulation are listed as follows: $m_s=75\,\text{(kg)}$, $m_b=75\,\text{(kg)}$, $\xi_s=100\%$, $\omega_s=20\,\text{(Hz)}$, $k_i=1000\,\text{(N/m)}$, $\mu_i=0.009$, $\mu_d=0.09$ and $\alpha=0.5$. ξ_s and ω_s are the damping ratio and natural frequency of the isolated structure, respectively. Both the two parameters are assigned in large value to consider the isolated object as a rigid body. The frequency of the isolator is 0.41 (Hz).

In numerical simulation, the optimal gain G (N/(m/sec)$^{\nu}$) should be determined. The isolation system is simulated under far-field earthquake, El Centro earthquake, and the optimal G is searched in the range of 0 to 50000 with interval 10 by Eq. (5). Five cases for the power parameter ν, 0, 0.5, 1, 1.5, 2 and 2.5, are considered.

The optimization results of G are listed in Table 1a. The performance index becomes larger with the increases in both G and ν. In Table 1a, it is easy to observe that the optimal choice in two parameters is $G=1140\,\text{(N/(m/sec))}$ and $\nu=0$ with $J=0.369$. But, this case can be thought as optimal passive isolation because $\nu=0$ results a constant normal force. After those optimal parameters are obtained, the same feedback gains are used to do re-simulation for all the cases subject to near-fault earthquake, Chi-Chi TCU102 (Fig. 2). The maximum normal force and performance index with respect to G are shown in Table 1b.

The semi-active case with $\nu=0.5$ and $G=2570\,\text{(N/(m/sec)}^{0.5})$ is chosen for the semi-active controller. The results are shown in Fig. 3. From Figs. 3a and 3b, the responses of passive control system are relatively very large under a near-fault earthquake. But, the responses are smaller for semi-active case. In Fig. 3c, the normal force is a little bit large but it is not over 20000 (N) which is the maximum force generated by PFD. The hysteretic loop (Fig. 3d) shows that the semi-active isolation can reduce both the base shear and platform displacement. The comparison is also listed in Table 2. The semi-active control can reduce the base shear of structure, especially in Chi-Chi earthquake from 586.4 N (passive) to 200.8 N (semi-active). The displacement of isolation platform (0.28 (m)) is smaller than in the passive case (1.16 (m)).

Conclusions

Based on the simulation results, the semi-active isolation system is indeed adaptive when the system is under very different excitations. Even though the controller is designed under far-field earthquake, the proposed controller in this study is still found to be effective under near-fault earthquake. The controller is so simple that only the platform velocity should be measured.

References

Jangid, R.S. 2005. Optimal Friction Pendulum System for Near-fault motions. Engineering Structures 27: 349-359.

Lu, L.Y. & Lin, G.L. 2008. A Theoretical Study on Piezoelectric Smart Isolation System for Seismic Protection of Equipment in Near-fault Areas. Journal of Intelligent Material and Structures 20: 217-232.

Nagarajaiah, S. & Sahasrabudhe, S. 2005. Experimental Study of Sliding Base-Isolated Buildings with Magnetorheological Dampers in Near-fault Earthquakes. Journal of Structural Engineering 131: 1025-1034.

Table 1a. Optimal G with corresponding J under El Centro earthquake.

ν	0	0.5	1	1.5	2	2.5
Min(J)	0.369	0.370	0.418	0.462	0.496	0.532
Optimal G	1140	2570	5180	9210	15180	35820

Table 1b. Performance of PSIS under Chi-Chi earthquake.

ν	0	0.5	1	1.5	2	2.5
G	1140	2570	5180	9210	15180	35820
J	0.330	0.291	0.264	0.250	0.243	0.235
$N(t)_{max}$	1140	1911	2612	3100	3475	3867

Table 2. Comparison of passive and semi-active ($G = 2570, \nu = 0.5$) isolations

Excitation	El Centro		Chi-Chi (TCU102)	
System type	Passive	Semi-active	Passive	Semi-active
$\max(x_s(t))$ (m)	0.25	0.05	1.16	0.28
$\max(m_s \ddot{x}_{s,\text{abs}}(t))$ (N)	131.0	71.9	586.4	200.8
$\max(x_b(t))$ (m)	0.25	0.05	1.16	0.28
$\max(N(t))$ (N)	—	1406	—	1911

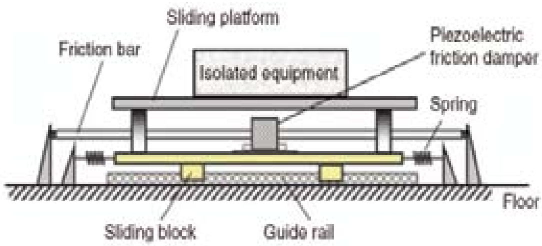

Fig. 1. Schematic diagram of PSIS.

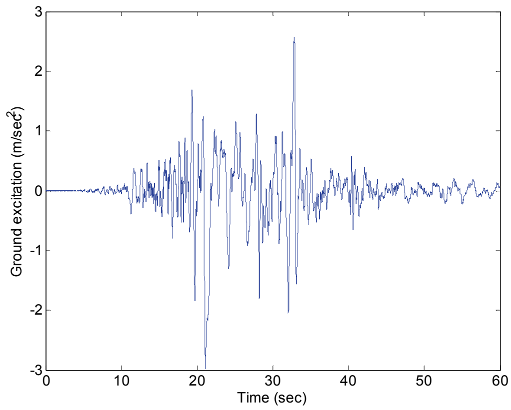

Fig. 2. Chi-Chi earthquake (TCU102).

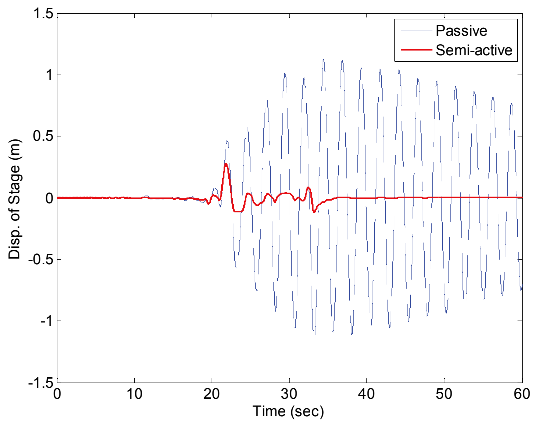

Fig. 3a. Displacement time history of platform.

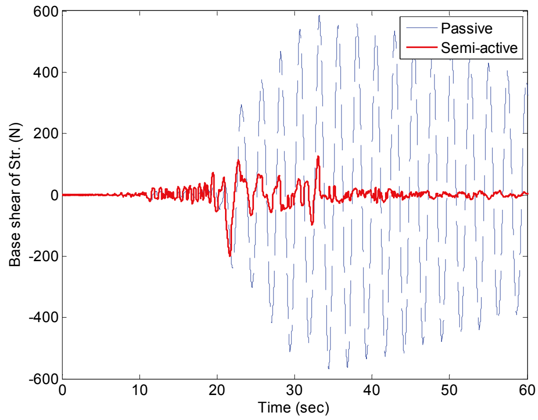

Fig. 3b. Base shear time history of structure.

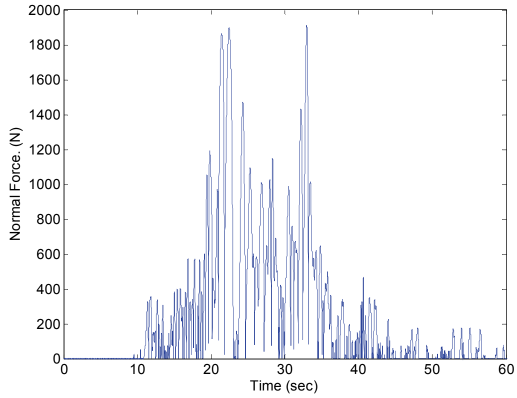

Fig. 3c. Time history of normal force.

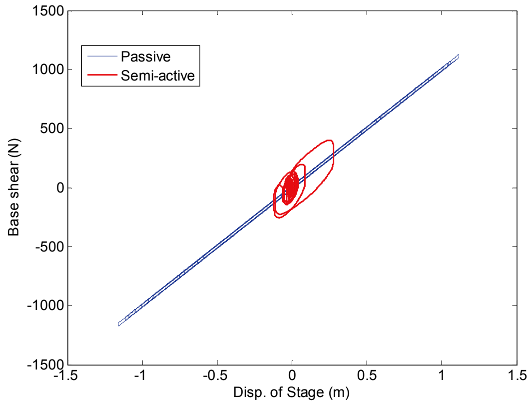

Fig. 3d. Hysteretic loop.

Simple Assessment Method for Ductility Capacity of a Fixed-Head Pile

Jiunn-Shyang Chiou[1], Cheng-Hsing Chen[2] and Yu-Ching Tsai[3]

邱俊翔 [1]、陳正興 [2]、蔡煜青 [3]

Abstract

This study develops simple equations to estimate the displacement ductility capacity of a fixed-head pile. The basic form of the equations is derived based on an ideal model of a semi-infinite pile with bilinear moment-curvature property in Winkler-type soils to relate the displacement capacity of the pile with the pile-soil system parameters and the formulation is modified for the effect of soil nonlinearity. Through this model, the displacement ductility capacity of the pile can be explicitly expressed in terms of the pile-soil system parameters, including the sectional over-strength ratio, curvature ductility capacity, and the ratios of characteristic coefficients of the pile-soil system. A series of numerical nonlinear pushover cases of full pile-soil models are conducted to calibrate and validate the proposed equations. Finally, a set of simple equations for the ductility capacity of the pile are built.

Keywords: Ductility capacity, piles, plastic hinge.

Introduction

Fixed-head piles usually experience a large flexural curvature demand at the pile head when subjected to large seismic loading since the pile head is restrained by a slab or a pile cap. In this case, it is cost-effective to design piles as ductile structures to absorb earthquake energy instead of elastic structures which are normally assumed in conventional design. When the ductile behavior of a pile is considered in design, the displacement ductility capacity of the pile will be an important concern.

Many methods have been developed to estimate the displacement ductility capacity. Those methods have regarded the curvature ductility capacity as an important factor. For instance, Chai (2002) employed the concentrated plastic-hinge model with a constant plastic-hinge length to build a relationship between the displacement ductility of extended pile-shafts and the curvature ductility of the pile section. Song et al. (2005) also adopted the concentrated plastic-hinge model to study the similar relationship for fixed-head piles.

In additional to the curvature ductility capacity, Chiou et al. (2009a) found that the over-strength ratio of a section (the ratio of ultimate moment to yield moment) is another important factor to the displacement ductility capacity, but the aforementioned methods ignore its effect.

The above assessment methods for the ductility capacity of fixed-head piles have not contained the influence of the over-strength ratio and there might be other influencing factors that are not identified. Therefore, this study attempts to re-confirm the important factors to the displacement ductility capacity for the fixed-head pile and to develop an assessment method to include their influences. The cohesive soil is taken as an illustrative soil stratum. This study uses a simple ideal model to derive the relationship of the ductility capacity of the pile to the parameters of the pile-soil system. From this model, simple equations about the ductility capacity for the linear and nonlinear soils can be built. Finally, a number of numerical pushover cases are conducted to calibrate and validate the proposed equations.

[1] Associate Research Fellow, National Center for Research on Earthquake Engineering, jschiou@ncree.org.tw
[2] Professor, Department of Civil Engineering, National Taiwan University, chchen2@ntu.edu.tw
[3] Doctoral Candidate, Department of Civil Engineering, National Taiwan University

Ductility Capacity of a Long Pile in Winkler Soils

1. Pile in elastic soil

In order to derive the ductility capacity equation of a pile, a simple ideal model is constructed as shown in Fig. 1(a). A semi-infinite pile with fixed-head condition is embedded in the uniform elastic soil of Winkler-type whose stiffness is constant with depth. The sectional moment-curvature property of the pile is assumed to be a bilinear curve which is defined by a yield point (M_y, κ_y) and an ultimate point (M_u, κ_u), as shown in Fig. 1(b). The nonlinear sectional property of the pile can be characterized by its curvature ductility capacity μ_κ and over-strength ratio ω, which are defined as

$$\mu_\kappa = \frac{\kappa_u}{\kappa_y} \tag{1}$$

$$\omega = \frac{M_u}{M_y} \tag{2}$$

Based on the model constructed above, the moment-displacement response at the pile head when subjected to a lateral loading will have the shape as shown in Fig. 1(c). Then, the displacement ductility capacity of the pile μ_Δ can be defined as

$$\mu_\Delta = \Delta_u / \Delta_y \tag{3}$$

where Δ_u is the ultimate displacement at the pile head when its moment reaches M_u and Δ_y is the yield displacement at the pile head when its moment reaches M_y.

Through theoretical derivation, the displacement ductility capacity can be expressed as

$$\mu_\Delta = \omega + \frac{\beta}{2\lambda_L} \cdot (1 - \frac{1}{\omega}) \cdot (\mu_\kappa - \omega) \tag{4}$$

where λ_L is the coefficient between the ultimate pile-head shear and moment, defined as $H_u/(2M_u)$ and β is the characteristic coefficient of the linear pile-soil system, which is defined as

$$\beta = \sqrt[4]{\frac{E_s}{4EI}} \tag{5}$$

where E_s is the subgrade reaction modulus and EI is the elastic flexural rigidity of the pile.

From Eq. (4), it can be clearly seen that the ratio β/λ_L, the over-strength ratio ω, and the curvature ductility capacity μ_κ are the influencing factors to the displacement ductility capacity of the pile. Since λ_L can be theoretically derived to be related to β, Eq. (5) can be further reduced as

$$\mu_\Delta = \sqrt{\omega + \mu_\kappa(\omega - 1)} \tag{6}$$

From Eq. (6), it is interesting to note that, for the linear soil, the ductility capacity of a pile is purely contributed by the over-strength ratio and curvature ductility capacity of the pile section.

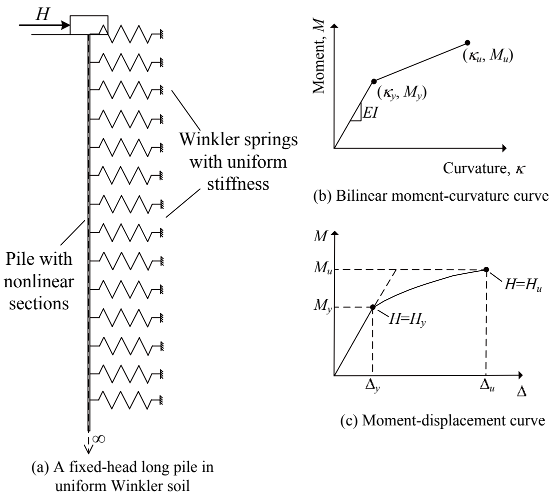

Fig. 1 Ideal model

2. Pile in Nonlinear Soil

When the pile is in the nonlinear soil, the soil may enter nonlinear state during lateral loadings. The degree of soil nonlinearity depends on how much the pile displacement exceeds the soil yield displacement. Since Eq. (4) is derived for a pile embedded in the linear soil, its formulation has to be modified as shown in Eq. (7) below when the effect of soil nonlinearity is considered.

$$\mu_\Delta = \omega + \frac{\beta_y^2}{2\beta_u \lambda_{NL}} \cdot (1 - \frac{1}{\omega}) \cdot (\mu_\kappa - \omega) \tag{7}$$

where β_y and β_u are the equivalent characteristic coefficients of the pile-soil system in the state of the pile yielding and the formation of the pile-head plasticity, respectively; λ_{NL} represents the characteristic coefficient that relates the ultimate moment and shear at the pile head, defined as $H_u/(2M_u)$.

Define a ratio to examine the change in the ductility capacity due to the soil nonlinearity by comparing Eq. (4) to Eq. (7) as follows

$$\alpha = \frac{\mu_{\Delta,NL} - \omega}{\mu_{\Delta,L} - \omega} = \frac{\beta_y^2}{\beta_u \beta} \frac{\lambda_L}{\lambda_{NL}} \tag{8}$$

where $\mu_{\Delta,L}$ and $\mu_{\Delta,NL}$ denote the displacement ductility capacities for the case of the linear soil and nonlinear soils, respectively. It should be noted that λ_L and λ_{NL} may be different since the ultimate lateral loads in the cases of linear and nonlinear soils may be different.

Since the range that the soil responds nonlinearly in the state of pile yielding is normally none or slight, β_y can be approximated to be β. Then, Eq. (8) can be further approximately expressed as

$$\alpha \approx \frac{\beta}{\beta_u}\frac{\lambda_L}{\lambda_{NL}} \tag{9}$$

From Eq. (9), it can be seen that α will be larger than one since β/β_u and λ_L/λ_{NL} will be larger than one due to the soil nonlinearity. It can be seen that the ductility capacity of a pile in nonlinear soils may be larger than that in linear soils due to the soil nonlinearity.

Therefore, to consider the effect of soil nonlinearity on the displacement ductility capacity, α can be used to modify the displacement ductility capacity for the linear soil, that is

$$\mu_\Delta = \omega + \alpha(-\omega + \sqrt{\omega + \mu_\kappa(\omega - 1)}) \tag{10}$$

where α is regarded as a modification factor which is displacement-dependent due to the degree of soil nonlinearity. Since it does not have a theoretical value, the following section will adopt a statistical approach to build an empirical relation for α from a series of pushover data.

Calibration and Verification

From the above derivations, the significant factors to the displacement ductility capacity of the pile are extensively discussed and Eqs. (6) and (10) are developed to estimate the displacement ductility capacity. However, the parameter α in Eq. (10) has not been determined. Therefore, this study will conduct a number of nonlinear pushover analyses of full pile-soil models to determine the parameter α and demonstrate the applicability of Eqs. (6) and (10).

1. Analysis model and Parameters

The case analyses assume a fixed-head pile of length 25m embedded in cohesive soils as shown in Fig. 2. The Winkler-beam model is applied to analyze the pushover curves for different specified parameters of the pile-soil system, with consideration of nonlinearity of the pile and the soil. The Winkler-beam model uses the beam elements to simulate the pile and adopts a series of independent springs to model the soil reactions. As shown in Fig. 1(b), the moment-curvature response of the pile section is assumed to be a simplified bilinear curve. The nonlinear behavior of the pile is simulated by the distributed plastic hinge model. In this model, many plastic hinges are distributed along the pile shaft for simulating the plasticity propagation in the pile. For the detailed description of this model, one can refer to Chiou et al. (2009b). The nonlinear *p-y* relation for the cohesive soil model is assumed to be elastic-perfectly-plastic, as shown in Fig. 3, in which the subgrade reaction modulus E_s is assumed uniform with depth and the profile of the ultimate soil resistance proposed by Reese et al. (1975) is adopted.

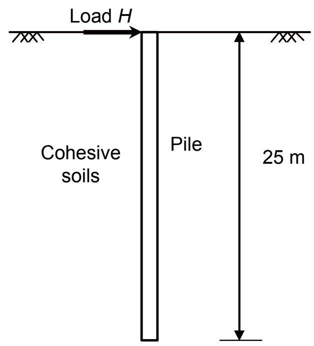

Fig. 2. Pile-soil model for case analyses

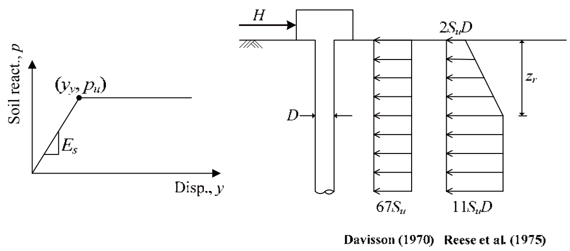

Fig. 3. *p-y* model for cohesive soils

Table 1. Analysis cases

Case	D (m)	$P/(f_c'A_g)$	ω	μ_κ	S_u (kN/m^2)
1	1	0	1.2	16	80
2	1	0.1	1.2	16	80
3	1	0.2	1.2	16	80
4	1	0.1	1.05	16	80
5	1	0.1	1.4	16	80
6	1	0.1	1.6	16	80
7	1	0.1	1.2	14	80
8	1	0.1	1.2	18	80
9	1	0.1	1.2	20	80
10	1	0.1	1.2	16	20
11	1	0.1	1.2	16	150
12	0.6	0.1	1.2	16	80
13	1.5	0.1	1.2	16	80

Pushover cases as listed in Table 1 are conducted. Parameters include the pile diameter D, the axial load level $P/(f_c'A_g)$, the over-strength ratio ω, the curvature ductility capacity μ_κ, and the undrained shear strength S_u. Note that the axial load level $P/(f_c'A_g)$ is varied to change the flexural rigidity of the pile.

According to the analysis parameters specified in Table 1, the pushover analyses are performed to obtain the pile-head pushover curves. Accordingly, the displacement ductility capacities for all the cases can be determined.

2. Determination of α

To obtain α in Eq. (10), the ductility capacity values from all the pushover cases are chosen to establish an empirical relationship for α. A non-dimensional relationship of α versus Δ_u/y_y is constructed as shown in Fig. 4, in which Δ_u is the pile-head ultimate displacement and y_y is the soil yield displacement y_y at the top soil layer. An approximate trend of Eq. (11) as shown below is employed to fit the data points in Fig. 4.

$$\alpha = 1 + 0.0528(\Delta_u / y_y - 1) \leq 1.26 \quad \text{for } \Delta_u > y_y \qquad (11)$$

For $0<\Delta_u/y_y<1$, the soil behaves linearly and therefore α in this range is set to one.

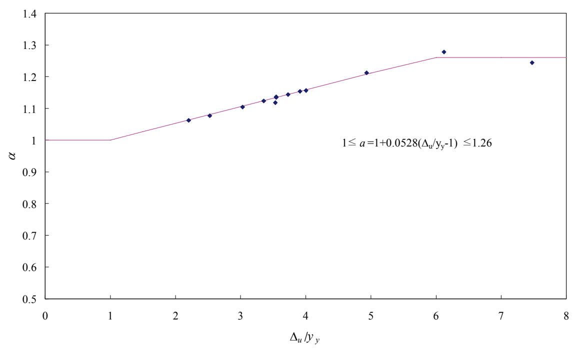

Fig. 4. α versus Δ_u/y_y

4. Performance of Eqs. (6) and (10)

Fig. 5 compares the capacities from Eqs. (6) and (10). Eq. (6) underestimates the capacities and provides the least estimates. Eq. (10), which additionally considers the effect of soil nonlinearity, gives consistent capacities to those from the pushover curves.

Conclusions

From the ideal model, the controlling factors to the ductility capacity of the fixed-head pile in cohesive soils include the curvature ductility capacity, over-strength ratio, and the ratios of the characteristic coefficients of the pile-soil system.

For a fixed-head pile in linear soils, its ductility capacity is completely controlled by its sectional curvature ductility and over-strength ratio, as in Eq. (6). This equation provides the least estimate for the ductility capacity of the pile. For a pile in the nonlinear soils, a modification factor is introduced to modify the ductility capacity for the case of a pile in the linear soil as shown in Eq. (10) for the possible effect of soil nonlinearity.

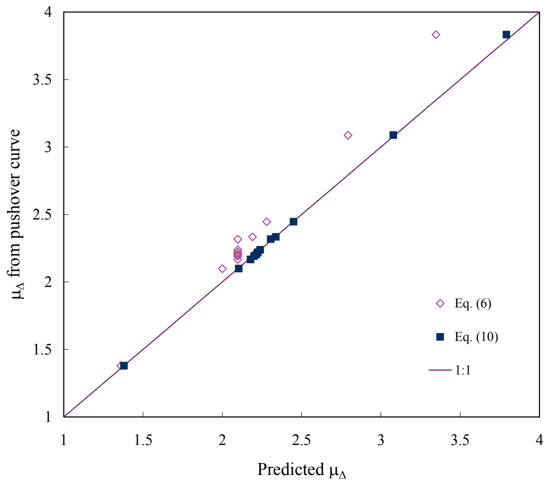

Fig. 5. Simple equations for cases 1-13

References

Chiou, J.S, Chen, C.H., and Tsai, Y.C. (2009a). "Ductility capacity of fixed-head reinforced concrete piles," under review, Soils and Foundations.

Chiou, J.S., Yang, H.H., and Chen, C.H. (2009b). "Use of plastic hinge model in nonlinear pushover analysis of a pile," Journal of Geotechnical and Geoenviromental Engineeering, 135(9), 1341-1346.

Chai, Y. H. (2002). "Flexural strength and ductility of extended pile-shafts. I: Analytical model," Journal of Structural Engineering, 128(5), 586-594.

Davisson, M.T. (1970). "Lateral load capacity of piles." High. Res. Rec., No. 39, 25-48.

Reese, L.C., Cox, W.R., and Koop, F.D. (1975). "Field testing and analysis of laterally loaded piles in stiff clay," Proceedings, 7th Annual Offshore Technology Conference, Vol. 2, Houston, Texas, 672-690.

Song S.T., Chai, Y. H., and Hale, T. H. (2005). "Analytical model for ductility assessment of fixed-head concrete piles," Journal of Structural Engineering, 131(7), 1051-1059.

Lateral Load and Shaking Table Tests on Model Pile in Saturated Sand Specimen

Tzou-Shin Ueng[1], Chia-Han Chen[2], Cheng-Hsing Chen[3] and Wei-Lun Tai[4]

翁作新 [1]、陳家漢 [2]、陳正興 [3]、戴偉倫 [4]

Abstract

To study the behavior of soil-pile interaction for a pile foundation in saturated sand under earthquake shakings, a series of lateral loading tests and shaking table tests were conducted on the instrumented model pile within a saturated Vietnam sand specimen inside the laminar shear box at the National Center for Research on Earthquake Engineering (NCREE). The model pile, 1.60 m in length, was made of aluminum alloy with an outer diameter of 101.6 mm and a thickness of 3 mm. The pile tip was fixed at the bottom of the laminar shear box to simulate the condition of a pile foundation embedded in the rock or within a firm soil stratum. Strain gauges and accelerometers were installed on the pile surface to observe the behavior of the pile during shaking. The near-field and far-field soil responses, including pore pressure changes, accelerations, and settlements were also measured. Unidirectional and multi-directional shaking table tests were performed on the model pile in the shear box with and without soil. The shakings included sinusoidal and recorded earthquake accelerations. The results of this study can be used for the design of pile foundations under seismic loadings.

Keywords: lateral loading test, shaking table test, liquefaction, model pile

Introduction

Pile foundations have suffered extensive damage in saturated soils in many large earthquakes such as 1964 Niigata Earthquake, 1989 Loma Prieta Earthquake, 1995 Kobe Earthquake and 1999 Chi-Chi Earthquake. There were pile foundation failures because of the loss of soil supports and excessive lateral loading. Many studies on soil-structure interaction have been performed in order to understand the mechanism of the dynamic responses of foundations in a saturated soil under earthquake loading. The results of these studies provide the bases for evaluation of the mitigation methods for liquefaction hazard and aseismic design for structures with pile foundations in a liquefiable ground.

Lateral loading tests in the field or in the laboratory and shaking table tests on model piles within soil specimens, under either 1 g or centrifugal conditions, have been used to investigate the pile behaviors and soil-pile interaction in saturated soils (e.g., Chen et al., 1998; Rollins et al., 2005; Ashford et al., 2006; Dobry and Abdoun, 2001, 2003; Tokimatsu et al., 2005). These tests are mostly under one-dimensional shaking and cannot consider the effect of multidirectional shaking on the pile foundations. Besides, the inertial effect caused by the superstructure and the kinematic loading imposed by the surrounding ground cannot be separately identified and understood. This research used the large biaxial laminar shear box developed at NCREE as the soil container and the instrumented model pile was installed inside the shear box filled with saturated sand. Static and cyclic lateral loading tests on the model pile were conducted utilizing the reaction wall at NCREE to acquire the basic pile properties and soil-pile interaction under simple conditions. The biaxial shear box with the model pile in a saturated sand specimen was then placed on the shaking table at NCREE; one- and multi-directional sinusoidal and recorded

[1] Professor Emeritus, Department of Civil Engineering, National Taiwan University.
[2] Assistant Researcher, National Center for Research on Earthquake Engineering, chiaham@ncree.org.tw
[3] Professor, Department of Civil Engineering, National Taiwan University.
[4] Graduate Student, Department of Civil Engineering, National Taiwan University.

earthquake accelerations were applied from the shaking table. The soil, pile responses and their interaction under these types of shakings were studied.

Model Piles and Sand Specimen

The model pile was made of an aluminum alloy pipe, 1.60 m in length, with an outer diameter of 101.6 mm, a wall thickness of 3 mm and EI = 77.62 kN-m^2. Resistance-type stain gauges were placed on the pile surface to measure bending strains of the model pile. At each depth, two pairs of stain gauges were mounted on opposite sides of the pile in X- and Y-directions. There are 10 different depths with 15 cm spacing along the pile axis. Vertical acceleration arrays along the pile were also set up on the model pile in X- and Y -directions for acceleration measurements. The pile was fixed at the bottom of the shear box to simulate the condition of a pile foundation embedded in rock or within a firm soil stratum. Up to 6 steel disks were fixed at the top of the aluminum pile to simulate various conditions of the superstructure. Each steel disk weighs about 37.10 kg. The model pile with instrumentation inside the shear box was set up before preparation of the sand specimen, as shown in Figure 1.

Fig. 1 Instrumented model pile with 6 steel disks on its top.

We used clean fine silica sand from Vietnam for the sand specimen inside the laminar shear box. This sand has been used in the shaking table tests for liquefaction studies at NCREE (Ueng et al., 2006). The maximum and minimum void ratios are 0.887~0.912 and 0.569~0.610, respectively. The sand specimen was prepared using the wet sedimentation method after the placement of the model pile and instruments in the shear box. The sand was rained down into the shear box filled with water to a pre-calculated depth. The size of sand specimen is 1.880 m × 1.880 m in plane and about 1.40 m in height before shaking tests. The saturation of the specimen was checked by the P-wave velocity measurements across the specimen horizontally. Details of the sand specimen preparation and the mechanism of the biaxial laminar shear box were described in Ueng et al. (2006).

Lateral Loading Tests

In order to evaluate the basic properties of the model pile and the soil-pile interaction under simple loading conditions, lateral loading tests on the model pile with and without saturated sand specimen inside the shear box were conducted. As shown in Fig. 2, the tests were performed using two hydraulic jacks affixed on the reaction wall and on the rigid frame individually to apply the displacement-controlled loading at the top of the model pile. The displacement of the pile top was limited to less than 10 mm to keep the pile deformation within the elastic range.

Fig. 2 Lateral loading test on the model pile in a saturated sand specimen

A triangular wave with the velocity of 0.0667 mm/sec was used in the static loading series. Loading and unloading cycles were applied to evaluate the elastic and hysteretic behavior of the model at place with and without the surrounding soil. In the cyclic loading tests, sinusoidal displacement-controlled loadings were applied with amplitude ranging from 1 to 10 mm at frequencies varying from 0.5 to 4 Hz. Ten cycles of loading were applied in each test. In addition, the 2D trajectories (e.g. circle and ellipse) were also applied to the model pile to evaluate the 2D responses of the model pile in the static and cyclic loading tests.

During the loading tests, the displacements at the top and different depths (for tests without sand) of the pile were measured. Strains (on four sides of the pile) and accelerations at different depths on the pile and pore water pressure changes and accelerations at various locations in soil specimen were measured. The heights of sand surface especially near the pile were also measured after each test.

Shaking Table Test

Shaking table tests were first conducted on each model pile without sand specimen to evaluate the dynamic behavior of the pile itself. Sinusoidal and white noise accelerations with amplitudes from 0.03 to 0.075 g were applied in X- and Y-directions. The model pile within the saturated sand specimen was then tested under one- and multi-directional sinusoidal shakings (1~24 Hz) and recorded earthquake accelerations with amplitudes ranging from 0.03 to 0.15 g. White noise accelerations were also applied in both X- and Y-directions to investigate the behavior of the model pile and the sand specimen after every several shakings. Figure 3 shows a shaking table test of the model pile in the saturated sand specimen.

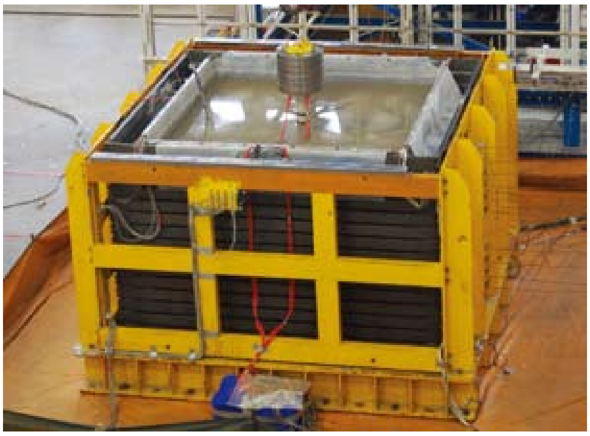

Fig. 3 The model pile with 6 steel disks on its top in saturated sand specimen on the shaking table.

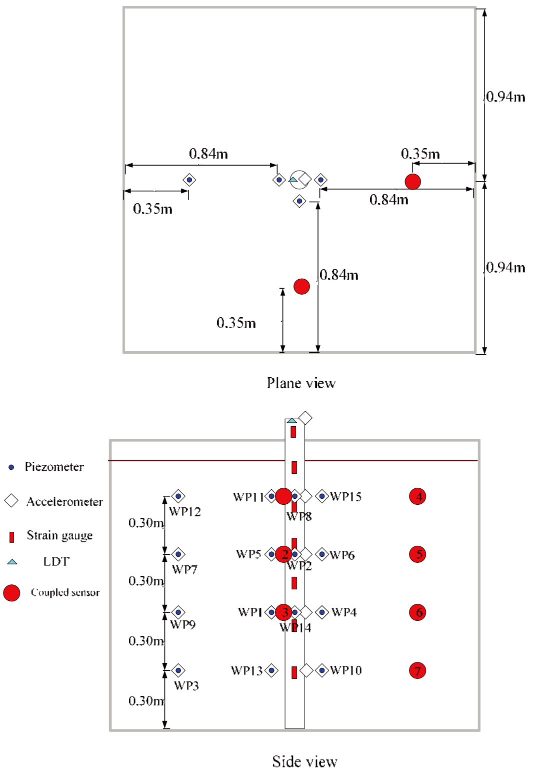

Fig. 4 Instrumentation on the pile and within the sand specimen.

Figure 4 is the layout of instrumentation on the model pile and in the sand specimen. During every test, pile top displacements, strains and accelerations at different depths on the pile, and pore water pressures and accelerations in the sand specimen (near field and far field) were measured. Besides, the frame movements at different depths of the laminar shear box were also recorded to evaluate the responses and liquefaction of the sand specimen using displacement transducers and accelerometers. Pore water pressures inside the sand specimen were measured continuously until sometime after the end of shaking to observe the dissipation of the water pressures. The height of the sand surface after each test was obtained for the settlement and density of the sand specimen. Soil samples were taken using short thin-walled cylinders at different depths after completion of the shaking tests to obtain the densities of the sand specimen.

Test Results

Lateral loading test

The test results in the static lateral loading tests shown in Fig. 5. indicated that the model pile exhibit linear elastic behavior without sand specimen. The curvatures of the pile were obtained from the measured strains on the pile at different depths.

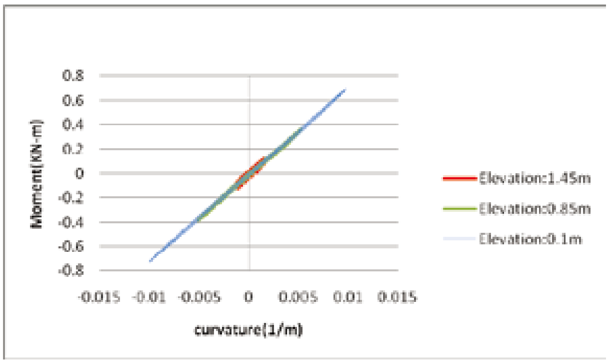

Fig. 5 Relationship of applied moment versus measured curvature at different depths of pile.

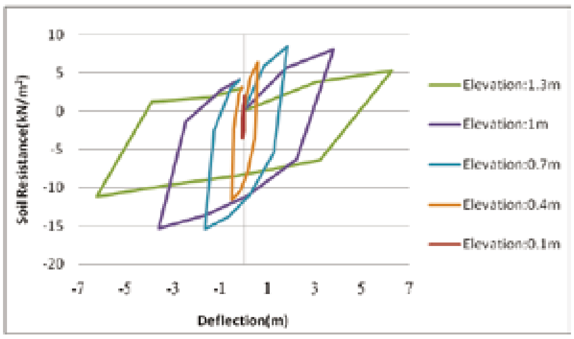

Fig. p-y curves at different depths in the static lateral loading test.

This study adopted nonlinear regression analysis to back-calculate the p-y curve of soil based on the test results. The bending moments along the length of the pile at discrete points calculated by the measurements of strain gauges were fitted using a fourth order polynomial function. The boundary conditions were satisfied by using Lagrange multiplier to solve the undetermined coefficients of the fourth order polynomial function. Then, soil reaction (p) was derived by double differentiation and pile deflection (y) was obtained by double integration of the moment function. Figure 6 shows the p-y curves at various depths in the static loading test.

Shaking table test

In order to investigate the inertial effect of the superstructure on the model pile under earthquake shaking, a series of shaking table tests were conducted with various mass mounted on the model pile. Based on the test results, there are some remarks in the following: (1) the kinematic force from the soil motion dominates the pile response because of the small inertia force from the superstructure; (2) for large inertia force (e.g. 6 disks of mass on the pile top), the response of pile was mainly governed by the inertia force from the superstructure; (3) for the inertia force between the previous two conditions, pile response was contributed by inertia effect from the superstructure and kinematic effect from soil motion. Therefore, these observations suggest that the mass and inertia force induced by the superstructure may play an important role on the soil-pile interaction.

According to the measurements of mini-piezometers in the sand specimen and accelerometers on the inner frames (Ueng et al., 2010), the sand specimen has fully liquefied under this one-dimensional sinusoidal shaking with frequency of 4 Hz and amplitude of 0.15 g. The amplification curve of the aluminum pile top with 6 steel disks during the post-liquefaction period is shown in Figure 7. The predominant frequency of the model pile within liquefied soil is identified at around 2 Hz. It is about the same as that of the model pile without soil (2.07 Hz). This clearly demonstrates the loss of soil constraint when liquefaction occurs. It appeared that the stiffness of the soil vanished when the specimen was fully liquefied.

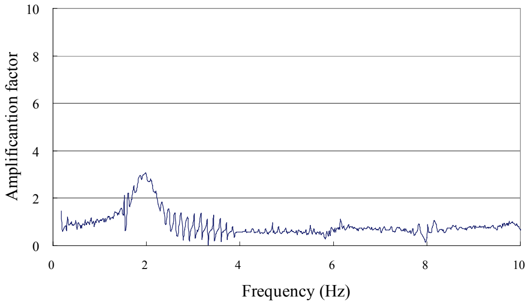

Fig. 7 Amplification factor vs. frequency for aluminum pile with 6 steel disks after initial liquefaction (Dr = 68.6 %).

Conclusions

Lateral load tests and shaking table tests were conducted on a model pile in the biaxial laminar shear box with and without saturated sand specimen. The displacements, strains and accelerations at different depths of the model pile were measured. The dynamic behavior of the model pile and the pile-soil system were evaluated based on the test results. Further tests and analyses of the test data will be performed to understand the soil-pile interaction, such as the relationship of ground reaction on the pile, and pore water pressure generation versus pile displacements (p-y curve) and their coupling. Based on these results, aseismic design criteria for pile foundations in liquefiable soils can be established for engineering practices.

References

Chen, C.H., Chiou, J.S. and Huang J.H. (1998),"Lateral loading test and analyses of CIP pile at Taipo, Chaiyi",The Chinese Journal of Mechanics, 14(2), 125-139. (in Chinese).

Rollins, K.M., Gerber, T.M., Lane, J.D. and Ashford, S.A. (2005), "Lateral resistance of a full-scale pile group in liquefied sand," J *J. Geotech. and Geoenviron. Eng.*, ASCE, 132(1), 115-125.

Ashford, S.A., Juirnarongrit T., Sugano T., and Hamada M. (2006). "Soil–pile response to blast-induced lateral spreading. I: field test," *J. Geotech. and Geoenviron. Eng.*, 132(2), 152-162.

Dobry, R.D. and Abdoun T. (2001). "Recent Studies on Seismic Centrifuge Modeling of Liquefaction and its Effect on Deep Foundations," State-of-the-Art Report (SOAP3), *Proc. 4th International Conference on Recent Advances in Geotechnical Earthquake Engineering and Soil Dynamics*, San Diego, CA, March 26-31, Vol. 2.

Abdoun, T., Dobry, R.D., O'Rourke, T., and Goh, S.H.(2003), "Pile Response to Lateral Spreads: Centrifuge Modeling," *J. Geotech. and Geoenviron. Eng*, ASCE, 869-889.

Tokimatsu, K., Suzuki, H., and Sato, M. (2005) "Effect of Inertial and Kinematic Interaction on Seismic Behavior of Pile with Embedded Foundations," Soil Dynamics and Earthquake Engineering, 25, 753-762.

Ueng, T.S., Wang, M.H., Chen, M.H., Chen, C.H. and Peng, L.H. (2006). "A large biaxial shear box for shaking table tests on saturated sand," *Geotechnical Testing Journal*, ASTM, Vol.29 (1): 1-8.

Ueng, T.S., Wu, C.W., Cheng , H.W. and Chen, C.H. (2010), "Settlements of saturated clean sand deposits in shaking table tests," Soil Dynamics and Earthquake Engineering, 30(1-2), 50-60.

Development of Damage Evaluation Techniques for Structural Foundation (I)

Yung-Yen Ko[1] Wei-Kuang Chang [2] Cheng-Hsing Chen[3]

柯永彥 [1]、張為光 [2]、陳正興 [3]

Abstract

Based on the measurement structural vibration, this study aimed to propose a data processing scheme and define a vulnerability index for the reasonable assessment of the damage state of structural foundation. A series of lateral loading tests on pier specimens were performed by NCREE for the study of the rocking response of a spread foundation. During these tests, the ambient vibration measurements were made on the fixed-base and flexible-base specimens in intact and damaged states, respectively, to investigate the influences of the base condition and the structural damage on the vibration response of the pier. In addition, the field vibration measurement was made at the Wensui Bridge of Provincial Highway No. 3. The modal analysis was also performed to examine the effect of pier foundation exposure due to scouring on the vibration behavior of the superstructures. Accordingly, the feasibility of the damage evaluation for structural foundation based on vibration measurement was verified.

Keywords: vibration measurement, damage evaluation, vulnerability index, foundation exposure

Introduction

In Taiwan, several major highway bridge failures have occurred in recent years, leading to considerable casualties and property losses. Most of them were related to the exposure of the pier foundation due to scouring, which reduced the bearing capacity of foundation. These disasters can be prevented if the damage or insufficient capacity of the foundation can be detected in advance, and the repair and retrofit works, or restraint of use is timely executed. However, the pier foundation exposure can not be directly observed visually if the water table is above the foundation level. Although it is possible to inspect the exposure by using instruments installed on the foundation, the flow-induced loading and the impact of the flow carryovers may destroy the instruments.

The structural vibration response of a soil-structure system shows the characteristics of the system itself, and reflects the boundary conditions as well. Hence, the measurement of structural vibration helps to inspect the damage of structural foundation. It is easy to perform and ensures the durability of sensors since they are not installed on the foundation. Moreover, the analysis methods are well-developed, and indices for damage evaluation were proposed and have been widely used. Therefore, the damage evaluation for the foundation using vibration measurement is worthy of development. Since the disaster mitigation of bridges has been an important issue, the focus of this study in the 1st year is on the bridge foundation.

Applications of Vibration Measurement on Structural Damage Evaluation

The vibration characteristics of a structure, such as the natural frequency, the damping, and the modal shape, are related to the mass, the stiffness, and the integrity of itself. If the structure is damaged, the natural frequency will be lowered due to the decrease of the stiffness, the damping will be increased because of the growth of the cracks, and the modal shape will be changed because of the redistribution of stiffness. Consequently, if the variations of the structural vibration characteristics are examined experimentally, the structural damage can be thus detected, quantified, and located. The vibration measurement tests often used for the characterization of the structure include:

[1] Associate Researcher, National Center for Research on Earthquake Engineering, yyko@ncree.org.tw
[2] Post-Doctoral Researcher, Department of Civil Engineering, National Taiwan University, d90521008@ntu.edu.tw
[3] Professor, Department of Civil Engineering, National Taiwan University, chchen2@ntu.edu.tw

1. Ambient Vibration Measurement: The ambient vibration is randomly generated by man-made or natural disturbances in the environment and has a wide frequency content. If the input ambient vibration and the excited structural response are measured simultaneously, the transfer function can be deduced for system identification. For the case that the input motion is unavailable, it is possible to characterize the structure merely by its excited response based on the assumption that the ambient vibration can be regarded as the white noise.
2. Forced Vibration Test: The artificial vibration sources such as moving vehicles, harmonic vibrator, and hammer are utilized to make the structure vibrate, helping to recognize the vibration characteristics of the structure under a larger strain level or for a specific vibration source.

Methods adopted for the interpretation of structural vibration in this study are described as follows:

1. Fast Fourier Transformation (FFT): Since it is not easy to recognize directly the frequency content of vibration in time domain, the vibration time history is usually transformed into frequency domain by spectrum analysis. The fast Fourier transformation (FFT) is an efficient algorithm to compute the discrete Fourier transform and is very common in practice. The Fourier spectrum obtained shows the frequency content of the vibration, and thus the structure can be characterized accordingly.

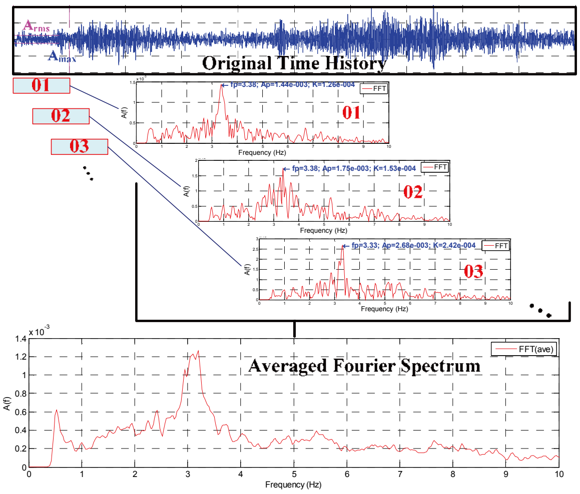

Fig. 1 Processing of averaged Fourier spectrum.

2. Averaged Fourier Spectrum: When the long-term field vibration measurement is made, the vibration characteristics at different moments show a certain variance since the environment and the vibration source are not constant. To eliminate the dispersion, Samizo et al. (2007) used a concept that sections with a fixed duration are extracted from the overall record, and each section is partially overlapped with the next. The Fourier spectrum is calculated in each section, and accordingly the structural natural frequency is indentified. All the natural frequencies are averaged to obtain a representative one. Based on this idea, here an averaged Fourier Spectrum is deduced instead, as shown in Fig. 1. Thus, the structural characteristics are better described, while the time-dependent variance can still be reduced.

When the vibration measurement is applied to the structural damage evaluation, characteristic system parameters are usually used to reveal the damage state. For the quantification of the structural damage, the variation of the natural frequency is often used. However, random errors might be produced in the measurement and influence the precision. The modal shape is usually adopted to locate the damage. If the natural frequency and the vibration amplitude are integrated into a concise index, it is not only easy to use, but also shows the damage state more effectively. Nakamura (1997) proposed the vulnerability indices based on microtremors for the ground, the viaduct, and the rigid block, which are positively correlated to the vibration amplitude and negatively correlated to the natural frequency. The one for the viaduct is more appropriate for the purpose of this study.

If the viaduct is excited by the ground motion (see Fig. 2) so that the deck experiences an acceleration α_{sg}, then the moment at the lower end of each column caused by the quasi-static inertia force applied on the deck, $M=m\alpha_{sg}h/2$. Considering the possible flexural failure at the lower column end, the vulnerability is related to the maximum strain at the column section:

$$\varepsilon = \frac{M}{EI}\cdot\frac{b}{2} = \frac{m\alpha_{sg}h}{2EI}\cdot\frac{b}{2} = m\alpha_{sg}\cdot\frac{h^3}{6EI}\cdot\frac{3b}{h^2} = \frac{m\alpha_{sg}}{k}\cdot\frac{3b}{h^2}$$

$$= \frac{1}{(2\pi)^2}\cdot\frac{3b}{h^2}\cdot\frac{\alpha_{sg}}{f_s^2} = \frac{1}{4\pi^2}\cdot\frac{3b}{h^2}\cdot\frac{A_s}{f_s^2}\alpha_g = K_{sg}\alpha_g \tag{1}$$

where $k=6EI/L^3$ is the lateral stiffness of the viaduct, $f_s=(1/2\pi)\sqrt{k/m}$ is the natural frequency in Hz of the viaduct, α_g is the ground surface acceleration, and A_s is the viaduct amplification factor at the frequency f_s. Then K_{sg} is the viaduct vulnerability index, revealing the potential or the status of the flexural failure at the lower column end. It can also be used to estimate the foundation exposure and the degradation of supporting soil since they lower the rocking stiffness of the pier.

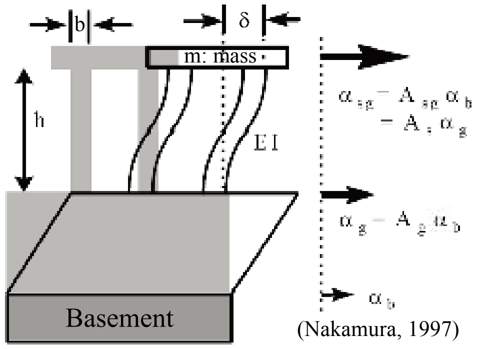

Fig. 2 Viaduct frame excited by ground motion

Ambient Vibration Measurement on RC Pier Specimens

A series of lateral loading tests on scaled RC pier specimens were performed by NCREE to investigate the reduction of the ductility demand of the pier due to the rocking response of the foundation. The specimen is composed of a square footing, a column and a cap beam, as shown in Fig. 3(a). Two base conditions were introduced to clarify the foundation rocking behavior. One was the fixed base condition, in which the footing was anchored into the strong floor to keep it from rocking. The other was the flexible base condition, in which the footing was rested on a neoprene pad, simulating the foundation on stiff soil. During the test, the lateral load was applied to the top of the pier to simulate the seismic loading, as shown in Fig. 3(a). Fig. 3(b) and Fig. 3(c) show the flexural failure state at the lower end of column for the fixed and flexible base conditions. The former was more severely damaged, which indicates that the rocking of the foundation decreases the plastic deformation of piers subjected to lateral loads.

During the tests, ambient vibration measurements were made on fixed-base and flexible-base specimens prior and posterior to the tests, that is, in an intact state and in a damaged state. The effects of the base condition as well as the structural damage of the pier on its vibration characteristics, such as the natural frequency and the corresponding amplification factor, were investigated. Velocity sensors were attached on the cap beam and on the strong floor, and the ambient vibrations were synchronously recorded for 20 mins. Since the flexural failure developed mainly along the load direction, only the vibration in the horizontal longitudinal (HL) direction is discussed here.

For a better characterization of the structure, the averaged transfer function of the vibration at the cap beam to that at the floor was deduced by the "averaging" processing scheme for each case, as shown in Fig. 4. For the fixed base condition, the natural frequency is 5.00 Hz with an amplification factor of 105.3 in the intact state; while in the damaged state, the natural frequency is 2.20 Hz, 56 % dropped because of the stiffness reduction caused by the damage, and the amplification factor is lowered to 81.2 probably due to the damping from the cracks. As for the flexible condition, the natural frequency is 3.58 Hz and the amplification factor is 28.7 in the intact state, both smaller than in the fixed base condition because of the stiffness reduction and the additional damping from the neoprene pad. In the damaged state, the natural frequency is 2.42 Hz, 32.5% dropped, and the amplification factor is lowered to 35.2.

It is noticed that the flexural failure of the column reduced the stiffness of the pier, thereby causing the drop of its natural frequency. When the damage is more severe, the drop is more significant. Therefore, the variation of the natural frequency reflects the damage level of the pier. As for the amplification factor, it was raised by the stiffness reduction due to damage yet was lowered by the damping from the cracks. Therefore, the amplification factor increased when the damage is minimal and decreased when the damage is severe. In addition, the system stiffness in the flexible base condition was lower than in the fixed base one, and thus the natural frequency was lowered, while the amplification factor was decreased due to the damping from the neoprene pad. These can be regarded as the possible influences on the vibration of the pier caused by the foundation stiffness reduction due to the exposure or the supporting soil degradation.

Since the pier size remained the same, Eq. (1) can be simplified into $K_{sg}= A_s / f_s^2$. Then, the vulnerability index was calculated for each case: for the fixed base and intact state, K_{sg}=4.21; for the fixed base and damaged state, K_{sg}=16.77; for the flexible base and intact state, K_{sg}=2.24; and, for the flexible base and damaged state, K_{sg}=6.02. The vulnerability indices in the damaged state were higher than in the intact state in both base conditions, and the increment was larger in the fixed base condition since the failure was more severe. Thus, the vulnerability index is verified to give a reasonable estimation of the structural damage level.

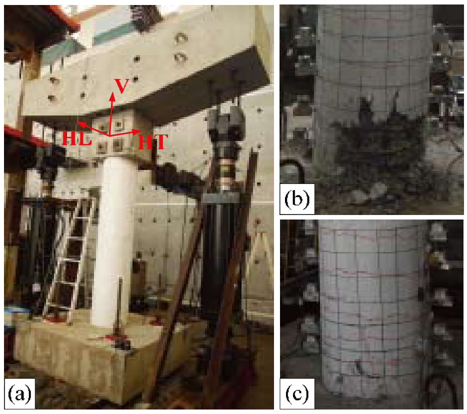

Fig.3 (a) Pier specimen and damage state for: (b) the fixed base and (c) the flexible base conditions.

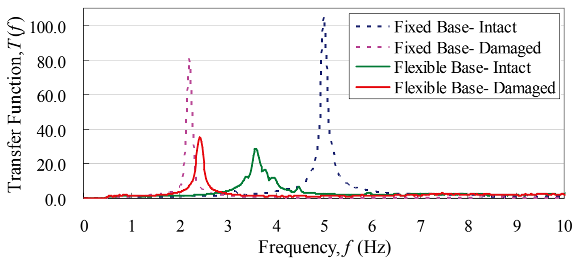

Fig.4 Transfer function of vibration for each case.

Field Vibration Measurement of Bridge

The Wensui Bridge of Provincial Highway No. 3 had suffered the exposure of the caisson foundations of the piers due to scouring, and the reconstruction of foundations using the pile group to replace the caisson was started in late 2008 and has been finished in late

2009. During the reconstruction, the riverbed level beside the pier P3 was lowered for the work space, making the caisson exposed for 5.5~7m (see Fig. 5). In order to investigate the vibration characteristics of the bridge superstructures at different levels of foundation exposure, vibration measurements were made at the pier P3 with severe foundation exposure and the neighboring pier P2 with slight foundation exposure, which had been reinforced by gabions. The sensors were deployed on the deck beside the expansion joint at P2 and P3 respectively, and the vibrations in the horizontal longitudinal (HL) direction and in the horizontal transverse (HT) direction at both piers induced by normal traffic flow were synchronously and continuously recorded for 20 mins.

Fig. 6 shows the average Fourier spectrum of the vibrations at P2 and P3. For the HL direction, the spectral curves of P2 and P3 are similar, with a main peak at the frequency of about 3.5 Hz. It might be the constraint in the HL direction provided by the deck and girders that makes the vibration characteristics of the two piers close to each other. Therefore, the vibration in HL direction is not able to reflect the exposure of foundation effectively. As for the HT direction, the averaged Fourier spectrum of P2 has two peaks, located at 1.7 Hz and 2.1 Hz, respectively; while only a major peak at 1.7 Hz shows for P3, with larger amplitude than the peak at 1.7 Hz for P2.

For a clearer interpretation of the peaks in these average Fourier spectra, the model of the unit P2-P3 of the Wensui Bridge was generated using the SAP 2000 software for the modal analysis. The soil was modeled by spring elements, and the foundation exposure was simulated by removing the soil springs. The modal shapes obtained are given in Fig. 7. The 1st mode is the in-phase coupled HT translation-rocking responses of P2 and P3 with a fundamental frequency of 1.72 Hz, in which the modal displacement of P3 is larger. The 2nd mode is the out-of-phase coupled HT translation-rocking responses of P2 and P3 with a fundamental frequency of 2.09 Hz, in which the modal displacement of P2 is larger. Thus, regarding the peaks in the average Fourier spectra, the one at 2.1 Hz in the spectrum of P2 characterizes the structural behavior P2, while the one at 1.7 Hz in both the spectra of P2 and P3 characterizes P3. Since the severe foundation exposure of P3 reduced its lateral stiffness, the lower predominant frequency and the larger amplitude of the vibration of P3 were exhibited, which even influenced the vibration behavior of P2.

Moreover, the vulnerability indices for P2 and P3 were calculated using Eq.(1). Since the measurements were synchronously performed at the two piers, the A_s in Eq.(1) was substituted with the peak amplitude of Fourier spectrum, and for P2 the peak at 2.1 Hz was adopted. The vulnerability index of P2 is 1.42×10^{-5}, and of P3 is 4.37×10^{-5}, apparently higher than P2. This vulnerability index is thus proved to reasonably reflect the exposure of pier foundation in practice.

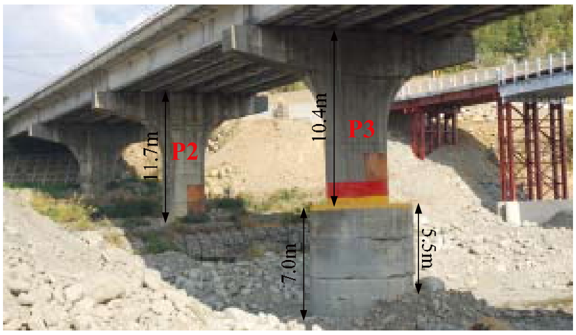

Fig. 5 The foundation exposure of Wensui Bridge.

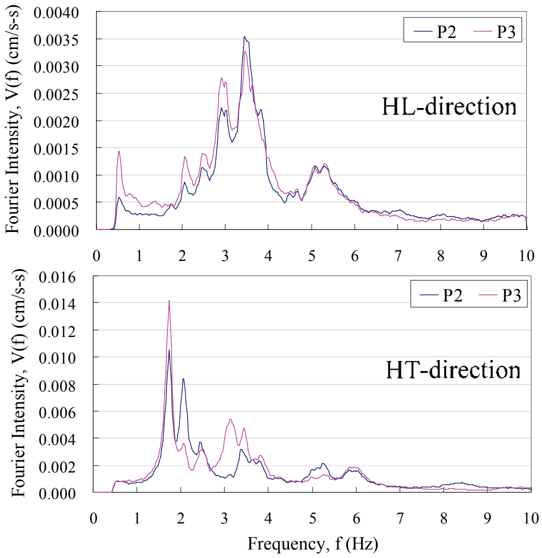

Fig. 6 Averaged Fourier spectrum of the vibrations at P2 and P3 of Wensui Bridge.

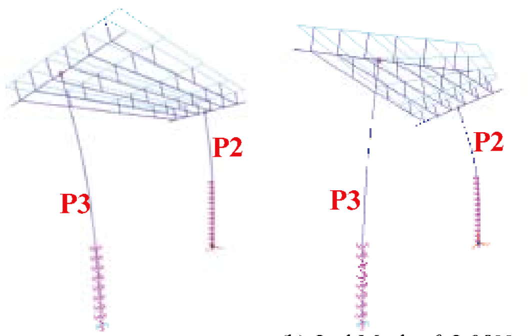

Fig. 7 Modal shapes of Wensui Bridge unit model.

References

Samizo M, Watanabe S, Fuchiwaki A and Sugiyama T. (2007), "Evaluation of the structural integrity of bridge pier foundations using microtremors in flood conditions", Quarterly Report of the Railway Technical Research Institute, 48(3), pp. 153-157.

Nakamura Y. (1997), "Seismic vulnerability indices for ground and structures using microtremor", Proceedings of World Congress on Railway Research, Florence, Italy.

Investigation of the Effective Damping Ratio Considering Soil-Structure Interaction (Ⅱ)

Shang-Yi Hsu [1] Cheng-Hsing Chen [2] Jiunn-Shyang Chiou [3]

許尚逸 [1] 陳正興 [2] 邱俊翔 [3]

Abstract

To incorporate the effects of soil-structure interaction (SSI) into the structural design, the most important issue is to quantify the effects of SSI for a soil-structure system. For design purpose, it is well recognized that the natural frequency and associated damping ratio are the key parameters for structural analysis. The natural frequency and associated damping ratio of the Equivalent Fixed-Base (EFB) model constructed can be calculated through explicit equations, and can represent the dynamic characteristics of the original soil-structure system. In this study, the EFB model of a multi-degree-of freedom (MDOF) structure considering the SSI effects is proposed with the concept of conventional modal analysis and used to evaluate the maximum seismic responses of MDOF structure and foundation system with response spectrum method.

Keywords: soil-structure interaction, foundation impedance, equivalent fixed-base model, seismic regulation

Introduction

To incorporate the effects of SSI into the structural design, the most important issue is to quantify the effects of SSI for a soil-structure system. For design purpose, it is well recognized that the predominant frequency and associated damping ratio are the key parameters for structural analysis. The former is used to locate where the maximum response will be, and the latter controls the magnitude of maximum response. Based on such understanding, this study aimed at quantifying the effects of SSI on a soil-structure system. Since the phenomenon of SSI is very complex for a general structure with large number of degree-of-freedom, this study used a simple structure founded on elastic half-space as the fundamental model to deduce how the predominant frequency and associated damping ratio were affected by the effects of SSI. Once these two parameters were quantified for a soil-structure system, an Equivalent Fixed-Base (EFB) model, which had taken the effects of SSI into account, can be constructed. This equivalent model is actually a rigid-base model that can be conveniently applied in a conventional structural analysis for engineering design.

SSI Analysis Model of an MODF Structure

The typical model usually used in describing the effects of soil-structure interaction is a lumped MDOF elastic structure with N storeys supported on elastic half-space. The structure is characterized by the mass m_i and mass moment of inertia J_i for the i^{th} floor, the mass m_0 and mass moment of inertia J_0 of the foundation, the lateral stiffness k_i, and the proportional damping coefficient c_i. The height of the i^{th} floor is denoted by h_i. For simple case, it is assumed that the foundation is rigid and perfectly bonded to the underlying soils. When the system is subjected to earthquake excitations, denoted by ground acceleration $\ddot{x}_g$, the response of the system can be depicted as shown in Fig. 1. This system is N+2 DOF's： one horizontal displacement (relative to the foundation) for each floor, $x_i(t)$, where $i = 1 \sim$ N；the horizontal translation of the foundation, $x_I(t)$ ；and the rotation of the system, $\theta(t)$. Therefore, the

[1] Associate Research Fellow, National Center for Research on Earthquake Engineering, syhsu@ncree.org
[2] Professor, Department of Civil Engineering, National Taiwan University, chchen2@ntu.edu.tw
[3] Research Fellow, National Center for Research on Earthquake Engineering, jschiou@ncree.org

displacement relative to the ground for each floor, $x_{f,i}(t)$, can be expressed as

$$x_{f,i}(t) = x_i(t) + x_I(t) + h_i\theta(t) \tag{1}$$

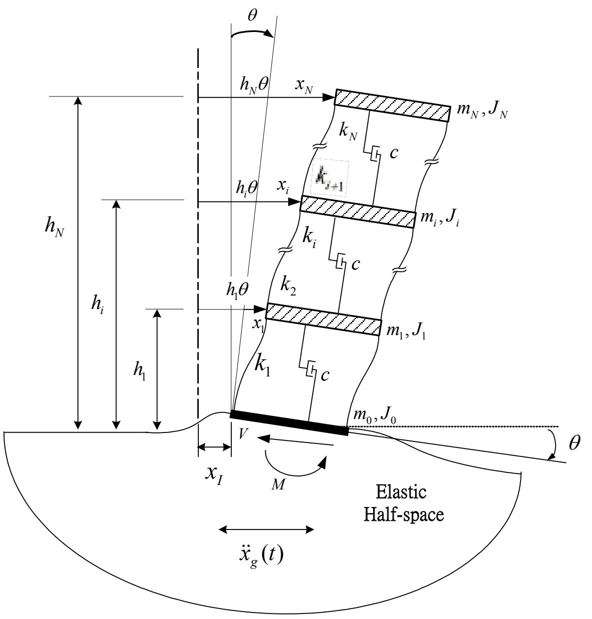

Fig. 1 Simplified model for SSI analysis with MDOF structure system

Considering the dynamic equilibrium of the structural inertia forces, the horizontal forces and the overturning moments for whole system, the motion equations of this system in frequency domain can be written as follows:

$$\mathbf{k}\ \ \mathbf{m}\ddot{\mathbf{X}} + \mathbf{c}\dot{\mathbf{X}} + \mathbf{k}\mathbf{X} + \mathbf{m1}\ddot{X}_I + \mathbf{mh}\ddot{\Theta} = \mathbf{-m1}\ddot{X}_g \tag{2a}$$

$$\mathbf{1}^T\mathbf{m}\ddot{\mathbf{X}} + m_T\ddot{X}_I + d_T\ddot{\Theta} + K_{VV}(i\omega)\cdot X_I = \mathbf{-}m_T\ddot{X}_g \tag{2b}$$

$$\mathbf{h}^T\mathbf{m}\ddot{\mathbf{X}} + d_T\ddot{X}_I + I_T\ddot{\Theta} + K_{MM}(i\omega)\cdot\Theta = \mathbf{-}d_T\ddot{X}_g \tag{2c}$$

where $\mathbf{X} = \{\mathrm{x}_i(i\omega)\}$ is the column vector of structural displacements relative to foundation, $\mathbf{h} = \{h_1 \ \ ...... \ \ h_N\}^{\mathbf{T}}$ is the column vector of foundation-to-storey heights, $\mathbf{m}$ is the mass matrix of structure, $\mathbf{c}$ is the viscous damping matrix of structure, $\mathbf{k}$ is the stiffness matrix of structure, $m_T = m_0 + \mathbf{1}^{\mathbf{T}}\mathbf{m1}$ is the total mass of structure and foundation, $J_T = \sum_{i=0}^{n} J_i$ is the sum of centroidal moments of inertia of structure and foundation, $d_T = \mathbf{h}^{\mathbf{T}}\mathbf{m1}$, and $I_T = J_T + \mathbf{h}^{\mathbf{T}}\mathbf{mh}$ is the total moment of inertia of structure and foundation with respect to the central axis of the foundation. $K_{VV}(i\omega)$ and $K_{MM}(i\omega)$ are the translational and the rocking impedances of foundation, respectively. The impedance functions depend on the configuration of foundation and the dynamic properties of the foundation soils. For some typical foundations, the published impedance functions can be applied directly. It must be noted that those foundation impedances are frequency-dependent and complex-valued due to the radiation damping of wave motions in the semi-infinite half-space.

To derive the overall displacement for each floor directly, the column vector of $\mathbf{X_f}(i\omega)$ can be substituted for the structural displacements vector, $\mathbf{X} = \{\mathrm{x}_i(i\omega)\}$. Herein, $\mathbf{X_f}(i\omega)$ is the Fourier transforms of the time function $\mathrm{x}_f = \{x_{f,i}(t)\}$. So, the original motion equations (2a) ~ (2c) can be rewritten in matrix formation:

$$\mathbf{A}\cdot\begin{Bmatrix}\mathbf{X_f}\\ X_I\\ \Theta\end{Bmatrix} = -\begin{Bmatrix}\mathbf{m1}\\ m_T\\ d_T\end{Bmatrix}\ddot{X}_g \tag{3a}$$

$$\mathbf{A} = \begin{bmatrix} \mathbf{-}\omega^2\mathbf{m}+\mathbf{k}^* & -\mathbf{k}^*\mathbf{1} & -\mathbf{k}^*\mathbf{h} \\ \mathbf{-}\omega^2\mathbf{1}^T\mathbf{m} & \mathbf{-}\omega^2 m_0 + K_{VV} & 0 \\ \mathbf{-}\omega^2\mathbf{h}^T\mathbf{m} & 0 & \mathbf{-}\omega^2 J_T + K_{MM} \end{bmatrix} \tag{3b}$$

Equation (3) above is the control function of an MDOF structure and soil interaction system, and the dimension of matrix A is $(N+2)\times(N+2)$. However, solving the $N+2$ coupled equations at each particular frequency requires intensive computation and may make this direct method infeasible for large-order models. In this study, an efficient methodology applying modal analysis is presented to uncouple the equations.

Based on the concept of classical modal analysis, the total displacement amplitude of each floor in the frequency domain, $\mathbf{X_f}$, can be expressed in the terms of the mode shapes as follows:

$$\mathbf{X_f} = \mathbf{\Phi Y} + \mathbf{1}X_I + \mathbf{h}\Theta = \mathbf{\Phi Y_f} \tag{4a}$$

$$\mathbf{Y_f} = \left[\mathbf{Y} + \mathbf{\Phi}^{-1}\mathbf{1}X_I + \mathbf{\Phi}^{-1}\mathbf{h}\Theta\right] \tag{4b}$$

where $\mathbf{\Phi}$ is the matrix consisting of mass normalized mode shapes of the fixed-base MDOF structure and satisfies the orthogonality for the mass matrix $\mathbf{m}$, the damping matrix $\mathbf{c}$, and the stiffness matrix $\mathbf{k}$ of MDOF structure. $\mathbf{Y_f} = \{\mathrm{Y}_{f,j}\}$ is the column vector of total displacement amplitude for each floor relative to the modes of MDOF structure and $\mathrm{Y}_{f,j}$ is the total displacement amplitude of j^{th} mode.

Diminishing the DOF's of equation (3) from $N+2$ to N by substituting equations (2b), (2c) into equation (3) and applying the orthogonality conditions, equation (3), when pre-multiplied by $\mathbf{\Phi}^{\mathrm{T}}$, becomes the simplified and decoupled formation of modal analysis method in structural dynamic analysis.

$$\ddot{\mathbf{Y}}_{\mathbf{f},j}+\left(F_{SSI}\right)_j\cdot\left(\omega_j^*\right)^2\mathbf{Y}_{\mathbf{f},j}=-\gamma_j\ddot{X}_g \tag{5a}$$

$$\left(F_{SSI}\right)_j=\frac{1+\dfrac{a_j\left(\beta_j\right)^2}{-a_j\left(\beta_j\right)^2+S_j}}{1+\dfrac{a_j+1}{-a_j\left(\beta_j\right)^2+S_j}+\dfrac{1}{-b_j\left(\beta_j\right)^2+R_j}} \tag{5b}$$

where $\left(\omega_j^*\right)^2=\omega_j^2\left(1+i2\xi_j\beta_j\right)$, ω_j is the j^{th} mode frequency of MDOF structure, ξ_j is the viscous damping ratio of j^{th} mode, $\beta_j=\omega/\omega_j$ is frequency ratio of j^{th} mode, $R_j=K_{MM}/\left(\omega_j^*\right)^2\Gamma_j^{\,2}$ is the normalized impedance coefficient of rocking, $S_j=K_{VV}/\left(\omega_j^*\right)^2\gamma_j^{\,2}$ is the normalized impedance coefficient of translation, $a_j=m_0/\gamma_j^{\,2}$, and $b_j=J_T/\Gamma_j^{\,2}$. γ_j and Γ_j are the participation factors of mass and moment of j^{th} mode, respectively.

Now, equation (5) has been transformed into the decoupled equation in terms of the relative displacement as a result of modal analysis for MDOF structure of fixed-base model, but with a modified complex-valued function, $\left(F_{SSI}\right)_j$. The formulation of $\left(F_{SSI}\right)_j$ for MDOF structure-and-soil system is similar to the F_{SSI} of simple model with SDOF structure in previous research. In this, the application of the analysis procedure combined with the concept of modal analysis for the SSI analysis of MDOF structure is elucidated.

MODF Equivalent Fixed-base Model

Like the EFB model of SDOF structure-and-soil system in previous research, the original SSI system can be replaced by a MDOF equivalent fixed-base model (MDOF EFB model) with the dynamic characteristics for each mode, such as the natural frequency, $\left(\tilde{\omega}_I\right)_j$, and the equivalent damping ratio, $\left(\tilde{\xi}_I\right)_j$, in which the equation (5) can be rewritten as

$$\ddot{Y}_{f,j}+\left(\tilde{\omega}_I^2\right)_j\cdot\left(1+i2\left(\tilde{\xi}_I\right)_j\cdot\left(\beta_I\right)_j\right)Y_{f,j}=-\gamma_j\ddot{X}_g \tag{6}$$

where $\left(\tilde{\omega}_I\right)_j$ is the predominant frequency of the MDOF EFB model of j^{th} mode, $\left(\beta_I\right)_j=\omega/\left(\tilde{\omega}_I\right)_j$ is the frequency ratio of j^{th} mode, and $\left(\tilde{\xi}_I\right)_j$ is the equivalent damping ratio of j^{th} mode.

From equations (5) and (6), the modification factor μ for j^{th} predominant frequency of the SSI system compared to the same structure founded on a fixed-base can be determined by

$$\mu_j^2=\left[\left(\tilde{\omega}_I\right)_j/\omega_j\right]=[\left(F_{SSI}\right)_j]_{RE} \tag{7}$$

where $[\left(F_{SSI}\right)_j]_{RE}$ represents the real part of $\left(F_{SSI}\right)_j$ and the structure damping is neglected. For dimensionless frequency $a_0=\omega r_0/C_s$ less than 1, the values of k_{VV} and k_{MM} can be regarded as frequency independent and be replaced by averaged values $\bar{k}_{VV}$ and $\bar{k}_{MM}$.

Under such circumstance, equation (7) can be simulated by a hyperbolic function of $\left(Gr_0/\omega_j^2M_j\right)$ and be represented by

$$\mu_j^2=\frac{Gr_0/\omega_j^2M_j}{Gr_0/\omega_j^2M_j+\left(\left(E_0\right)_j\right)^{-1}} \tag{8a}$$

$$\left(E_0\right)_j=\left[\frac{a_{1,j}}{\bar{k}_{VV}}+\frac{b_{1,j}}{\bar{k}_{MM}}\frac{H_j^2}{r_0^2}\right]^{-1} \tag{8b}$$

where $H_j^2=\Gamma_j^2/\gamma_j^2$, $(E_0)_j$ is the initial slope the hyperbola and a function of the configuration of the structure and the foundation.

Another important issue is to calculate the damping ratio of the equivalent fixed-base model. In the current study, it is suggested to choose the damping ratio corresponding to each predominant frequency $\left(\tilde{\omega}_I\right)_j$ and regarded as a frequency-independent damping ratio of the system. It will be called the equivalent damping ratio $\left(\tilde{\xi}_I\right)_j$ of MDOF EFB model.

$$\left(\tilde{\xi}_I\right)_j=\xi_j\mu_j+\frac{1}{2\mu_j^2}\cdot[\left(F_{SSI}\right)_j]_{IM} \tag{9}$$

Response Spectra Method for an SSI System

Based on the modal motion equation of MDOF EFB model above, the spectral acceleration value, $S_{aD}((\tilde{\omega}_I)_j,(\tilde{\xi}_I)_j)$, can be determined by the parameters of the predominant frequency and the equivalent damping ratio of SSI system for each mode. So, for j^{th} mode, the maximum roof displacement of MDOF structure considering SSI effects, $\left(\tilde{x}_f\right)_{j,\max}^i$, can be represented by

$$\left(x_f\right)_{j,\max}^i=\phi_{ij}\frac{\gamma_j}{M_j\left(\tilde{\omega}_I\right)_j^2}S_{aD}\left(\left(\tilde{\omega}_I\right)_j,\left(\tilde{\xi}_I\right)_j\right) \tag{10}$$

According to the balance of inertial forces from Eq (3a), the maximum elastic force of the ith floor of j^{th} mode, $\left(\tilde{x}_f\right)^i_{j,\max}$, can be determined from

$$\left(f_S\right)^i_{j,\max} = m_i \phi_{ij} \frac{\gamma_j}{M_j} S_{aD}\left(\left(\tilde{\omega}_I\right)_j, \left(\tilde{\xi}_I\right)_j\right) \qquad (11)$$

and the sum of elastic forces of each floor is the maximum base shear force of j^{th} mode, $V^j_{\max}$, and can be computed as follows:

$$V^j_{\max} = \frac{\gamma_j^2}{M_j} S_{aD}\left(\left(\tilde{\omega}_I\right)_j, \left(\tilde{\xi}_I\right)_j\right) \qquad (12)$$

where γ_j^2 / M_j is the effective modal mass of j^{th} mode. The sum of maximum over-turning moments for each floor up to the foundation is the maximum base moment of j^{th} mode, $\left(M_0\right)_{j,\max}$, can be determined as：

$$\left(M_0\right)_{j,\max} = \frac{\Gamma_j \gamma_j}{M_j} S_{aD}\left(\left(\tilde{\omega}_I\right)_j, \left(\tilde{\xi}_I\right)_j\right) \qquad (13)$$

Finally, for the seismic design, the maximum values of the inertial forces and displacements of structural members can be computed with the superposition of each modal response by SRSS (Square Root of the Sum of the Squares) method or CQC (Complete Quadratic Combination) method.

Case Study

In this study, a structural system with ten storeys shear-type building was used in the numerical case study to investigate the difference of analysis result between EFB model and conventional fixed-base model. This structure, as shown in Fig. 2, is a ten-storey shear-type building resting on a rigid, circular foundation at the surface of a homogeneous site located in Seismic Zone 1 of Taipei basin. The soil shear wave velocity of the site is 100 m/s. The impedance function for the surface-circular type foundation proposed by Velectsos and Wei (1971) was applied in this analysis. Based from the results of MDOF EFB analysis, the first predominant frequency of EFB system was 1.8 Hz lower than the first modal frequency of MDOF structure (2.225 Hz) and the equivalent damping ratio was 5.3 % slightly higher than the structural damping ratio; the second predominant frequency of EFB system was reduced from 6.626 Hz (the second modal frequency of this structure) to 6 Hz and the equivalent damping ratio was 7.8 %. These evidences suggest that the dynamic parameters of soil-foundation and structure system are different from the original structural properties of the MDOF structure and further indicate how the seismic responses be affected by SSI.

The spectra acceleration values corresponded to the first and second predominant frequency of EFB model, $S_{aD}((\tilde{\omega}_I)_j, (\tilde{\xi}_I)_j)$, had been computed from the design spectrum of Taipei basin Zone 1 (as shown in Fig. 3). Therefore, the maximum base shear force and base moment were determined by the superposition of the responses of first two modes by SRSS method. From the results, the maximum base shear force was 39969 kN; and the maximum base moment was 934597.5 kN-m for EFB model considering the SSI effects. Also, the maximum base shear force and base moment for conventional fixed base analysis without the contribution of SSI were 40810.7 kN and 953401.4 kN-m, respectively.

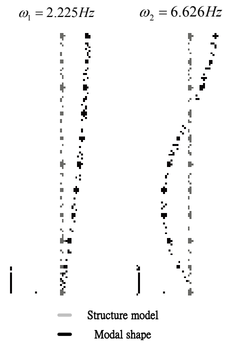

Structure	m_i	8×10^3	ton
	k_i	7×10^7	kN/m
	h_i	3.5 x i	m
	J_i	7×10^4	$ton\cdot m^2$
	ξ	0.05	—
Foundation	r_0	6	m
	m_0	1.6×10^4	ton
	j_0	1.4×10^5	$ton\cdot m^2$
Ground	ρ	1.9	ton/m^3
	ν	0.33	—
	Cs (G3)	100	$m/\sec$

Fig. 2 MDOF structure model and the dynamic parameters for analysis

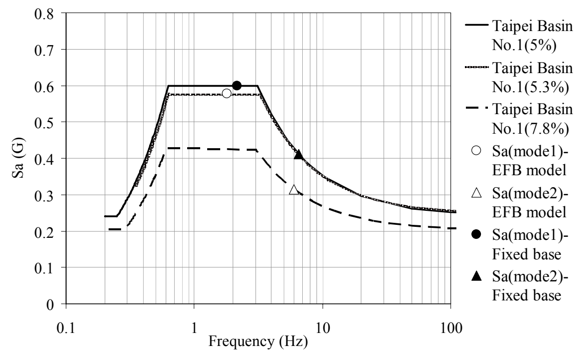

Fig. 3 The spectra acceleration values of the roof for EFB model and fixed base model.

Conclusion

The Equivalent Fixed-Base (EFB) model for the general MDOF structure and the SSI response spectra method proposed in this study were used to characterize completely the effects of soil-structure interaction. This equivalent model is actually a rigid-base model that can be applied conveniently in a conventional structural analysis for engineering applications and seismic design.

References

Chen, C.H., Hsu, S.Y., “Equivalent Fixed-Base Model for Soil-Structure Interaction Analysis,” Journal of Mechanics, Vol. 22, No. 3, 2007, pp. 167-180.

A Study of Two Full-Scale Three-Story Steel Concentrically Braced Steel Frames

Keh-Chyuan Tsai[1], Chih-Yu Wei[2], An-Chien Wu[3], Ching-Yi Tsai[4], Chih-Han Lin[5]

Ker-Chun Lin[6], Eric Lumpkin[7], Po-Chien Hsiao[8] and Charles Roeder[9]

蔡克銓 [1]、魏志毓 [2]、吳安傑 [3]、蔡青宜 [4]、林志翰 [5]、林克強 [6]
Eric Lumpkin [7]、Po-Chien Hsiao [8]、Charles Roeder [9]

Abstract

The "NEES-SR SG International Hybrid Simulation of Tomorrow's Braced Frames" is an international collaborative research among NCREE, University of Washington (UW), University of California, Berkeley (UCB) and University of Minnesota (UM). In this project, two large-scale braced frames have been constructed and tested at NCREE. In this paper, the test specimen is a single bay three-storey concentrically braced steel frame (CBF), where braces were arranged in a multi-story cross-brace configuration. A500 steel tubular braces were used for the first 3-story CBF specimen. After the first test, the specimen did not have any significant fracture except those at the six braces. Thus, six new gussets and A36 steel H-shape braces were installed to replace the damaged tubular braces. Large out-of-plane displacement and local buckling of braces were observed in both tests. There were no any severe fracture found on beams and columns of the frame. Further this paper introduces the specimen and elucidates preliminary test results.

Keywords: Concentrically braced frame, gusset plate, flexural buckling, local buckling.

Introduction

Special concentrically braced frame (SCBF) has been a rather common lateral force resisting system for buildings. SCBFs develop cyclic inelastic deformations through axial yielding and post buckling deformations of the brace. Braces are normally connected to the beams and columns in the braced frame through gusset plate connections. The SCBF gusset plate connections must resist the full tensile and compressive capacities of the brace during significant cyclic loading, and sustain large inelastic out-of-plane deformations when the brace buckles. To resist the expected yield capacity of the brace, current AISC seismic design provisions (AISC, 2005) for SCBFs require that the gusset plate should be stronger than the brace. Thus, the geometric limit of "2t" requirement (illustrated in Fig. 1a) is used to assure that gusset plate will permit plastic rotations for brace out-of-plane buckling. In order to improve the performance of the gusset plate connections, the research team at the University of Washington proposed another gusset plate clearance requirement (Lehman et al, 2008). The proposed clearance requirement uses an elliptical line to define the "8t" clearance instead of the "2t" linear clearance as shown in Fig. 1b. These two different gusset plate design methods were used in the previous 2-story SCBF specimens. Their performance were compared and presented in the reference paper (Lin et al., 2009). Only the elliptical 8t gusset plate requirement was used in this study.

[1] Professor, National Taiwan University, kctsai@ntu.edu.tw
[2] Assistant Research Fellow, National Center for Research on Earthquake Engineering, cywei@ncree.org.tw
[3] Assistant Research Fellow, National Center for Research on Earthquake Engineering, acwu@ncree.org.tw
[4] Graduate Student, National Taiwan University, d98521004@ntu.edu.tw
[5] Assistant Research Fellow, National Center for Research on Earthquake Engineering, hank@ncree.org.tw
[6] Research Fellow, National Center for Research on Earthquake Engineering, kclin@ncree.org.tw
[7] Graduate Student, University of Washington, lumpkin@u.washington.edu
[8] Graduate Student, University of Washington, pchsiao@u.washington.edu
[9] Professor, University of Washington, croeder@u.washington.edu

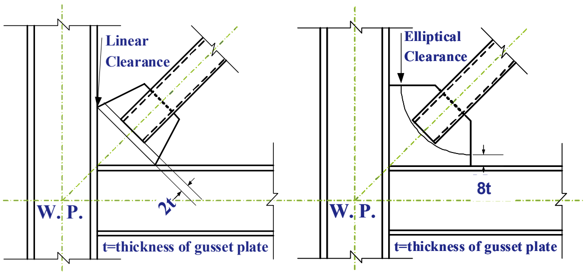

(a) (b)

Fig. 1 Clearance requirements of gusset plates
(a) Current AISC 2t requirements
(b) The UW proposed 8t requirements

Experimental Program

The test specimen is a single bay, three-story X-bracing concentrically braced frame (Fig. 2a). It consists three beams (Top: W24x94, Lowers: W21x68) and two columns (W12x106). The column center-to-center spacing is 6000 mm, the height of first story is 2,928 mm and the height of second and third stories is 3190mm. All beams and columns material are A992 steel. Six steel braces were installed on the specimen, arranged in a two-story X-shape and an inverted V configuration. A500 grade steel tubes (HSS125x125x9) were used as braces in the Phase I test, while A36 grade steel wide-flange braces (H175x175x7.5x11) were used in the Phase II test. The width of concrete slab is 2160 mm and thickness of 200mm (125mm thick concrete over 75mm deep metal deck) for each floor. The thickness of all gusset plates is 10mm. In order to minimize the out-of-plane displacement of the three-story frame, a three-dimensinoal lateral supporting frame was built around the specimen (Fig. 2b).

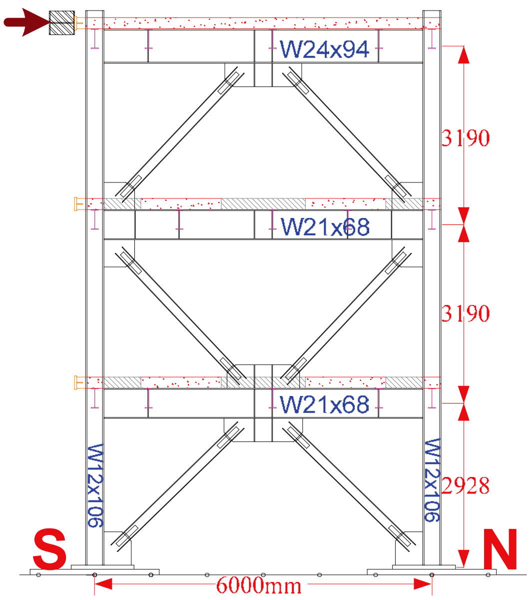

(a) Frame elevation

(b) Experimental setup

Fig. 2 Setup of Specimen WF

Only the in-plane displacements of the frame were imposed in the test. The lateral loads were applied specifically to the center of the roof floor slab. Four MTS 100-ton actuators were attached to a transfer beam, which was connected to two edge beams (H200x200x8x12) at the two longitudinal sides of the concrete slab. The actuators extending out which push the SCBF toward the north are positive displacements and forces. The loading protocol adopted was based on ATC-24 and SAC recommendations (Fig. 3).

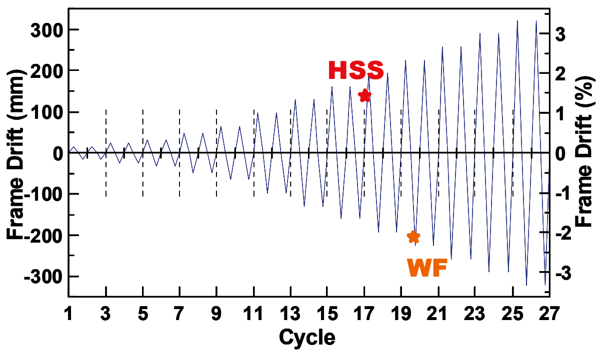

Fig. 3 Loading protocol and the instances of the first fracture occurred in these two tests

Instrumentation Plan

In order to observe and record the responses of the test specimen during the cyclic loading tests, two kinds of instrumentations were implemented as follows:

1) Strain gauges: The strain gauges were setup on beams, columns and braces, and some strain gauges were also located inside the concrete slabs. These concrete strain gauges should be installed before the concrete slabs were completed.

2) Displacement transducers (LVDTs, dial gauges,

string pots and Temposonics): There were about 90 displacement measuring devices used in the test. The braces were expected to have large out-of-plane displacement, thus, a great number of string pots were adopted in this test to measure the out-of-plane displacement of braces. Six temposonics were installed to measure each storey's displacement (two in each floor). The displacement value measured by temposonics in the top floor served as a basis in controlling the actuators. To monitor the responses of specimen and boundary elements, dial gauges and LVDTs were placed around the three-storey concentrically braced frame. Some photos of the instrumentation are in Figs. 4 to 7.

Fig. 4 Middle gusset instrumentation (string pots)

Fig. 5 Measuring out-of-plane displacement in lower gusset (LVDT)

Fig. 6a

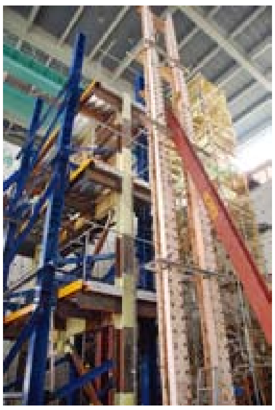

Fig.6b

Fig. 6a Measuring out-of-plane displacement in middle span of brace (string pot)

Fig. 6b Measuring story's displacement (temposonics)

Test Results

The tests exhibited the expected behavior of brace buckling and achieved a substantial total roof drift greater than +/-1.5% radians. Brace fractures were the primary mode of failure. Figure 3 pointed out the arrivals of the first fracture that occurred in the two tests. Figure 7 shows the comparison of the lateral force versus deformation relationships between the two tests. The HSS frame reached a roof drift capacity of -1.67% to 1.67% rad. (total range of 3.34% rad.) and peak 1st story drift of -1.94% to 1.86% rad. (range of 3.8% rad.), peak 2nd story drift of -2.14% to 2.06% rad. (range of 4.2% rad.), and peak 3rd story drift of -1.04% to 1.06% rad. (range of 2.1% rad.). The WF frame reached a roof drift capacity of -1.99% to 2.31% rad. (total range of 4.3% rad.) and peak 1st story drift of -2.14% to 2.31% rad. (range of 4.45% rad.), peak 2nd story drift of -2.51% to 3.03% rad. (range of 5.54% rad.) and peak 3rd story drift of -1.35% to 1.59% rad. (range of 2.94% rad.). The third story has the smallest peak story drift due to the heavy roof beam. In addition, the beam-column connections in the upper two floors were moment connections, but in the second floor were simple connections.

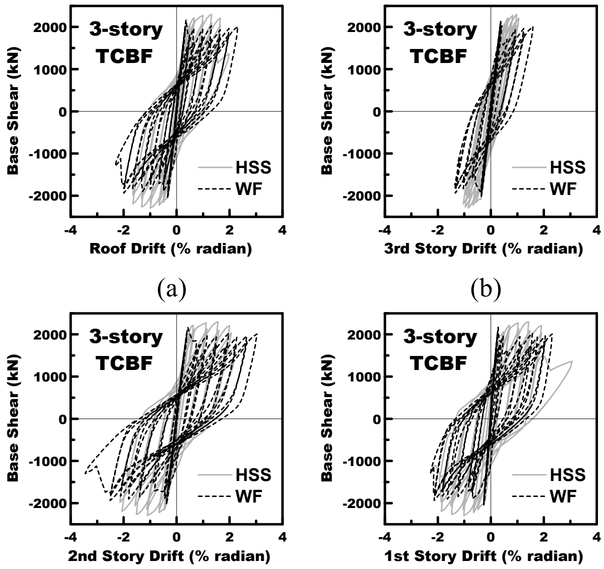

(a) (b) (c) (d)

Fig. 7 Base shear versus story drift relationships

Figure 8 compares each brace out-of-plane (OOP) displacement versus inter-story drift relationships for both tests. The maximum OOP displacement in HSS test is about 350 mm for the braces in 1st and 2nd story before it fractured. In WF test, the maximum OOP displacement is about 390 mm before it fractured. The maximum 3rd story brace OOP displacement is 250 mm for WF test and 225 mm for HSS test, respectively. Fig. 9a and 9b show the brace buckling shape before fracture occurred. Fig 10a and 10b are the typical local buckling shapes of the HSS and WF braces. The first tension brace fractures in two tests are shown in Figs. 10c and 10d.

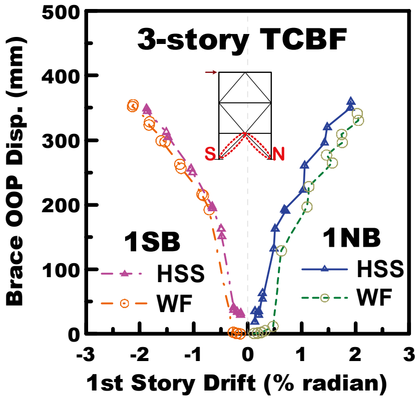

(a) First story

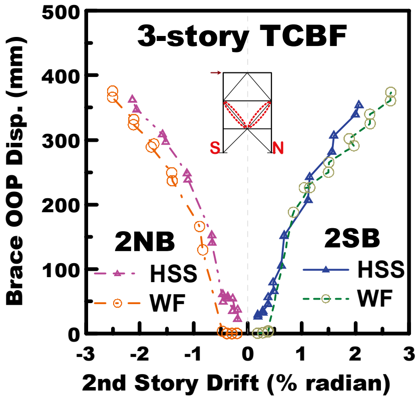

(b) Second story

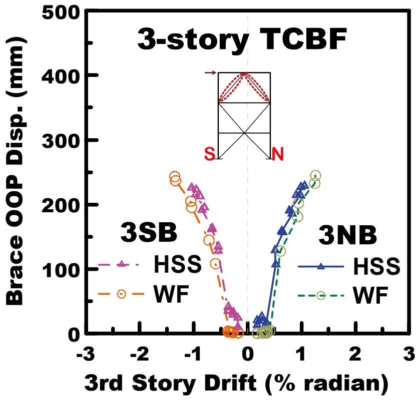

(c) Third story

Fig. 8 Brace out-of-plane displacement versus inter-story drift relationships

(a) HSS at 1.67%

(b) WF at 2.32%

Fig. 9 Out-of-plane displacement comparison:

(a) HSS at -1.67 %

(b)WF at +2.32%

(c) HSS at +1.67%

(d) WF at -2.32%

Fig. 10 Local buckling and fracture of the braces

Summary and Conclusions

Test results show that the energy-dissipation performance of the three SCBF specimens using the multi-story X-bracing configuration is satisfactory. No any significant strength or stiffness degradation was found before fracture occurred in the braces during the tests. The occurrence of the severe out-of–plane deformation of the braces and gussets did not reduce the strength performance of the SCBF systems using the X-brace configuration. This is because the tension braces developed its full strength in a timely manner. The total drift capacity for two tests is 3.34% (HSS) and 4.3% (WF), respectively. This suggests that the ductility of SCBF specimen using the wide-flange braces is better than specimen using tubular braces.

References

AISC 2005, Seismic Provisions for Steel Buildings, AISC/ANSI Standard 341-05, American Institute of Steel Construction, Chicago, IL.

Lehman, D. E., Roeder, C. W., Herman, D., Johnson, S. & Kotulka, B. 2008, Improved Seismic Performance of Gusset Plate Connections, ASCE, *Journal of Structural Engineering*, Vol.134, No. 6, pp.890-901, Reston, VA,.

Lin, C.H., Tsai, K.C., Wei, C.Y., Wang, K.J., Tsai, C.Y., Wu, A.C., Powell, J., Clark, K. & Roeder, C. 2009, Cyclic Tests of A Full-Scale 2-Story Steel Concentrically Braced Frame, 5th International Symposium on Steel Structures, Korea, March 12-13.

Earthquake Source Parameters and Micro-tremor Site Characteristics (Micro-Earthquake Monitoring)

Tao-Ming Chang[1], Hung-Hao Hsieh[2], Che-Min Lin[3], Chun-Hsiang Kuo[3] and Kuo-Liang Wen[4]

張道明[1]、謝宏灝[2]、林哲民[3]、郭俊翔[3]、溫國樑[4]

Abstract

An active fault micro-earthquake monitoring network for the three Science parks of Taiwan was set up using dense broadband seismometers. Micro-earthquakes and anomalous seismicity could be observed as well as active faults and source parameters, which are important materials for numerical simulations and analysis of earthquake potential that will to be established. In the latter half of 2008, the micro-earthquake monitoring network of the Central Taiwan Science Park (CTSP) was set up to integrate three networks into an integrated network. There were a total of 47 stations in this network in monitoring active faults from Hsinchu to Tainan County in the western Taiwan. The earthquake data processing and position were done using the programs developed by the authors. There was no seismicity under the Hsinchu Science Park (HSP) and Hsinchu City. Most earthquakes occurred in the Sanyi-Puli seismic zone and in the eastern or southeastern side of active faults at the Western Foothills. In the Southern Taiwan Science Park (STSP) area, the epicenters in this region are more dispersed. The earthquakes were observed in all regions between the Western Foothills and the coastal area. The central part of the network near the CTSP is relatively a quiet area of seismicity for the other area.

Keywords: Science Park, earthquake monitoring, active fault, earthquake location

Introduction

The focus of this project is on the three Science parks, which are the major economic resources of Taiwan. These Science parks are all located near the active faults of first category due to the tectonics of Taiwan. And the high seismicity of the area poses a great danger to the factories and equipments inside the parks. This project established a monitoring network for the active faults using dense broadband seismometers. Micro-earthquakes and anomalous seismicity could be observed as well as fault activities and source parameters, which are relevant materials in numerical simulations and analyses of earthquake potential that will to be established.

This project is part of a series of studies being guided by the National Center for Research on Earthquake Engineering (NCREE) regarding the highly-technological Science parks of Taiwan to determine active parameters of faults, numerical simulations of ground motions, site effect, earthquake early warning, etc. The results will be integrated to for the future review of seismic design, hazard analysis, and earthquake potential. The analysis of micro-tremor site characteristics, installations of two soil-gas earthquake monitoring stations for the Hsincheng and Hsinhua Fault, construction of the Geologic Surveyed Database of TSMIP stations, and the techniques of earthquake hazard and potential analysis were already established. For the micro-earthquake monitoring of the active faults, 15 broadband seismometers were installed throughout

1 Associate Research Fellow, National Center for Research on Earthquake Engineering, tmchang@ncree.org.tw

2 Assistant Research Fellow, National Center for Research on Earthquake Engineering, hhhsieh@ncree.org.tw

3 Associate Research Fellow, National Center for Research on Earthquake Engineering, cmlin@ncree.org.tw, chkuo@ncree.org.tw

4 Professor, Dep. of Earth Science, National Central University and Division Manager, National Center for Research on Earthquake Engineering, wenkl@s319m.gep.ncu.edu.tw

Hsinchu, Mouli and other vicinities for the Hsinchu Science Park (HSP) since 2005. And 11 broadband seismometers were further installed throughout Tainan, Chiayi, and Kaohsiung County for the Southern Taiwan Science Park (STSP) since 2006. In the latter half of 2008, the micro-earthquake monitoring network of the Central Taiwan Science Park (CTSP) was set up to integrate these three networks into an integrated active fault monitoring network of the Western Taiwan.

Micro-Earthquake Monitoring Network

Data quality of the observed micro-earthquakes depends on the location and installation of seismometers. The station should be installed in a secluded place to increase the signal-to-noise ratio. Therefore, the station locations were all chosen with caution, measured the background noise beforehand if necessary, and continues to take notice of the variation of background noise to ensure the data quality.

A standard operating procedure was created in installing a broadband station which depends on the tests and experiences in years. The quality of the incident seismic waves could increase by setting a cement foundation on the bottom of a bucket and several long nails to fix the bucket on the bottom of a hole. Otherwise, the lateral of the bucket, in which a seismometer is placed, should avoid touching the surrounding soils of the hole to decrease the surface noise. The moisture-proof and heat insulation are good help to keep a stable monitoring operation. High-sensitivity broadband seismometers were used in the project. The sampling rate is 100 points per second and the recording is continuously done to avoid losing any micro-earthquake. A set of solar energy equipment and a GPS antenna were installed at each station to supply the electricity and correct the internal clock of the seismometer.

The coding of the stations was done according to the seismometers types (the first letter, B indicates the broadband type), the districts (the second letter), the geology or topography (the third letter), and the location (the fourth letter). This kind of station coding is beneficial to identify, change or make extension of the network in the future.

In order to cover all active faults near the Science parks and integrate all networks, 21 broadband seismographs were installed to cover Taichung, Changhua, Nantou, Yunlin, and Chiayi County. Figure 1 shows the map of the whole micro-earthquake monitoring network. The purple circles are the new stations for the CTSP. There are total of 47 stations of the network in monitoring active faults from Hsinchu to Tainan in the western Taiwan.

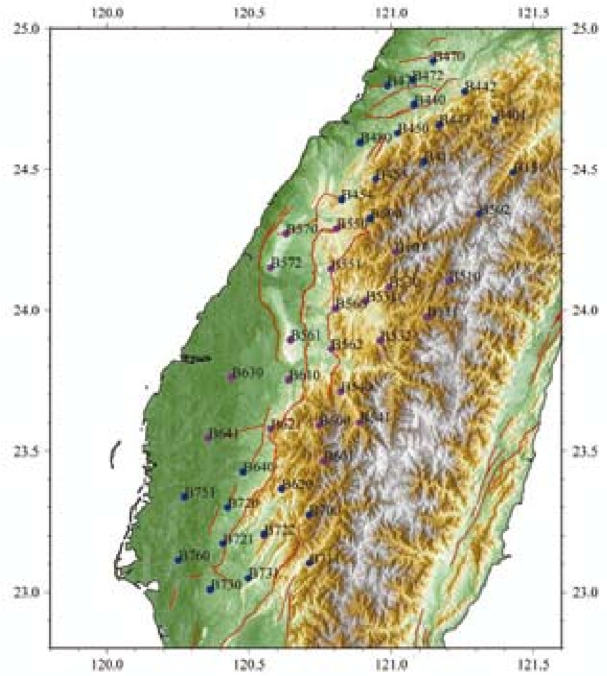

Fig. 1 The map of the micro-earthquake monitoring network

Earthquake Data Processes

The data size of the monitoring network is about 5 GB per day. The traditional earthquake auto-location methods are inadequate for the observed earthquakes due to small magnitudes, thus data processing program for the monitoring network was developed also in this project (Chang, 2009). In the processing, the daily recordings were converted to the SAC formation. Then the P- and S-wave arrival times were distinguished and marked by different quality symbols for every cutting event. The above two steps must be done manually. Consequently, the earthquakes could be located. This scheme was illustrated in Fig. 2. Because the seismometers are highly sensitive, the HHT (Hilbert-Huang Transform) of EMD (Empirical Mode Decomposition) were also combined in the program to remove the long-period background noise such as those brought by winds or tides (Fig. 3).

The program HYPO 71 (Lee and Lahr, 1972) was implemented to estimate the occurrence time, epicenter location, focal depth and magnitudes for each earthquake using the arrival times of P- and S-waves. The velocity model of earthquake location is the same as that of CWB (Central Weather Bureau). The M_L is inadequate for our micro-earthquake network due to the high-frequency waveform and small magnitude that the M_d was estimated based on the epicentral distance and duration time of each station.

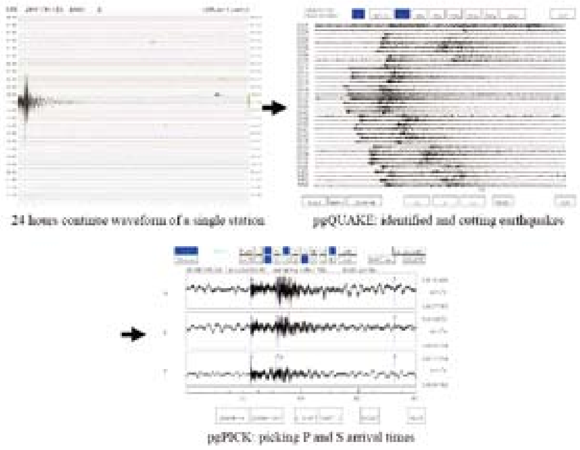

Fig. 2 Procedures of the earthquake data processing system developed

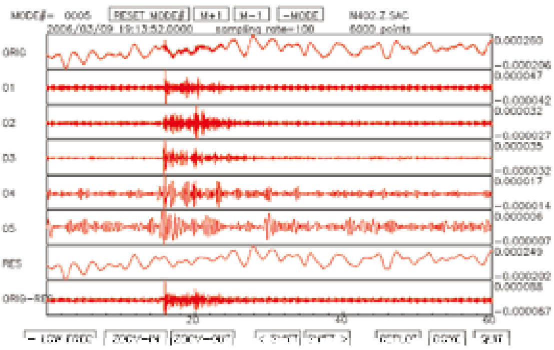

Fig. 3 The process of EMD for a waveform

Micro-earthquake Location

After the setup of the micro-earthquake monitoring network in CTSP on December 2008, the three networks of Science parks were integrated into one big network. The seismic data of the 47 stations were then analyzed together. Before the integration, the data of HSP and STSP networks were analyzed. The result of earthquake location for original HSP, old STSP and integrated networks are presented and discussed in this section.

A total of 6,288 earthquakes were located by the HSP network from 2006/1/22 to 2008/11/9. The magnitudes M_d were between 0 and 3. The distribution of epicenters is shown in Fig. 4. Earthquakes mostly occurred near the surface between the depth of 0 and 10 km. A small number of earthquakes occurred between the depth of 10 and 20 km. the depths of earthquakes did not show any relation to the faults. The earthquakes deeper than 20km are few in the range of HSP network, but they occurred in the east of the network, in Xueshan and in Central Mountain Range. Because these deeper earthquakes are outside the network, the reliability of the position is lower. There was no seismicity under the HSP and Hsinchu City. Most earthquakes occurred in the eastern or southeastern side of active faults in the Western Foothills. There are three groups, namely: the northern group, which includes two sub-groups in the south-southeastern side of the Tapingti Fault; the central group, which is located in the southeast side of the Shihtan and Shenchoshan Faults; and the southern group with the densest earthquakes and is located in the Sanyi-Puli seismic zone.

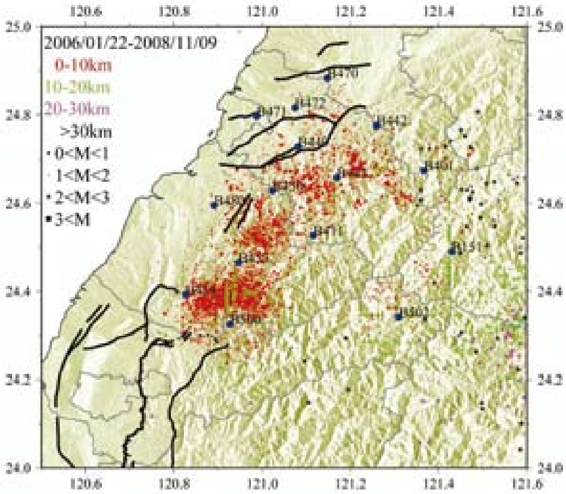

Fig. 4 The earthquakes located by the HSP network

A total of 3,649 earthquakes were located by the STSP network from 2006/12/13 to 2008/11/3. In the STSP area, the number of earthquakes with magnitude bigger than 2 is apparently more than that in the HSP area. The distribution of epicenters is shown in Fig. 5. Most of the earthquakes occurred between the depth of 0 and 20 km. Deeper earthquakes also occurred outside of the network. The epicenters in this region were more dispersed. The earthquakes were observed between the Western Foothills and the coastal area. The dense seismicity is along the Chukou, Muchiliao, and Liuchia Faults. And, there is also an earthquake group in the north end of the Chaochou Fault.

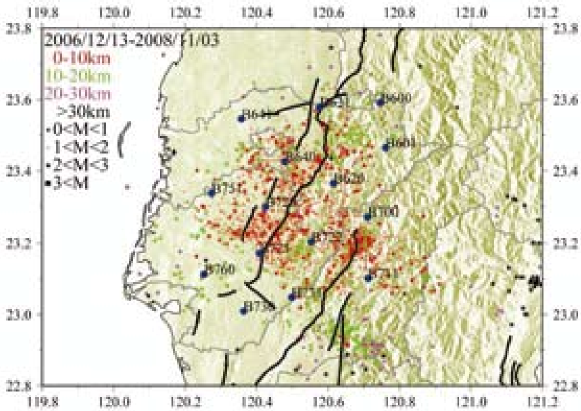

Fig. 5 The earthquakes located by the STSP network

A total of 1,517 earthquakes were located by the integrated network until April 2009. Because the operating period is still short, the number of observed earthquakes is less. The distribution of epicenters is shown in Fig. 6. The distribution in the northern and southern part of the network is approximately the same as that observed by original HSP and STSP networks. The seismic zones, like Sanyi-Puli seismic zone, identified by the integrated network were more complete because of the better coverage. Furthermore, the central part of the network near the position of the Chelungpu Fault is relatively a quiet area of seismicity for the other area. The quiet area has been observed also in the CWB historical catalog. The phenomenon may result in the occurrence of the 1999 Chi-Chi Earthquake.

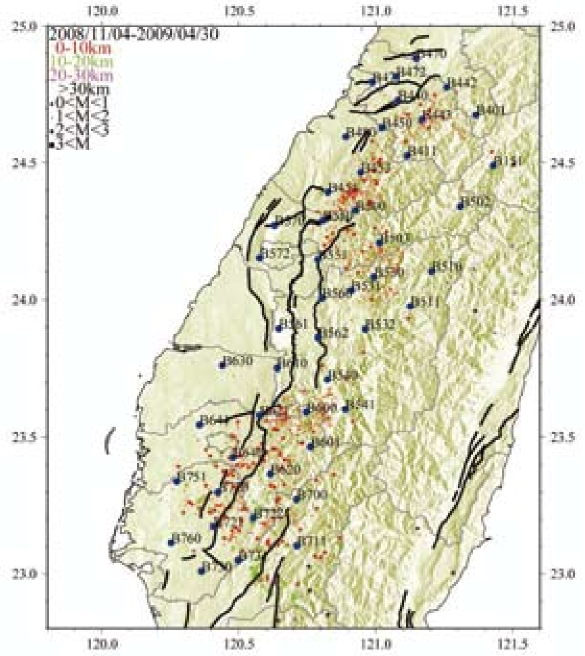

Fig. 6 The earthquakes located by the integrated Science park network

Aftershocks of the 2009/11/5 Mingjian Earthquake

On 5 November 2009 at exactly 17:32:57.7 (local time), a ML 6.2 earthquake took place at Mingjian, Nantou County located in the central part of Taiwan. According to the earthquake report of the Central Weather Bureau (CWB), the main shock epicenter was located at 23.79°N and 120.72°E. The focal depth was 24.1 km. The maximum ground shaking level was up to Intensity VII at Mingjian. Because the epicenter is close to that of the Chi-Chi Earthquake, people paid attention to the earthquake. Since the broadband seismometers utilized are very sensitive, the waveforms would saturate under the near-source strong ground motion. This kind of large earthquake like Mingjian Earthquake can not be located by the established micro-earthquake monitoring network. Fig. 7 shows the aftershocks observed four days after the event. The aftershocks are more than 300 and are concentrated on the southeast part of the mainshock. The depths of aftershocks are less than the mainshock ranging between the depth of 10 and 20km.

Fig. 7 The aftrershocks of the 2009/11/5 Mingjian Earthquake located by the science park network

Conclusions

The micro-earthquake monitoring network for the science parks of Taiwan has been set up by NCREE. This network is powerful for micro-earthquake monitoring and helpful in understanding the seismicity and active faults in the area. The accurate earthquake location of Hypo DD and the focal mechanism will be studied in the future to determine the important source parameters relevant in earthquake warning system.

References

Huang, N. E., Shen, Z., Long, S. R., Wu, M. C., Shin, H. H., Zhang, Q., Yen, N. C., Tung, C. C., and Liu, H. H. (1998), "The empirical mode decomposition and the Hilbert spectrum for nonlinear and non-stationary time series analysis", *Proc. R. Soc. Lond. A.*, 453, 903-995.

Lee, W.H.K. and Lahe, J. C. (1972), "Hypo71：A computer program for determining hypocenter, magnitude, and first motion pattern for local earthquakes", *USGS open file Rep.*, 100pp.

Chang, T. M. (2009), "Earthquake data processing system installation and using guide", NCREE Rep., NCREE-09-066. (In Chinese)

Earthquake Source Parameters and Micro-tremor Site Characteristics Study-Geochemical Monitoring

Vivek Walia [1], Shih-Jung Lin [2], Tsanyao Frank Yang [3] and Kuo-Liang Wen [4]

瓦里亞 [1]、林世榮 [2]、楊燦堯 [3]、溫國樑 [4]

Abstract

The study of active faults and earthquake precursory provides a basis for anticipating of future earthquakes and related phenomena such as surface faulting, and other geological/tectonic features. Taiwan is product of ongoing collision of Eurasian plate with Philippine Sea plate. The ongoing collision between the different plates makes Taiwan and highly active tectonically and intensively faulted. The present work is focused on Hsincheng fault in Hsinchu area and the Hsinhua fault in Tainan for earthquake monitoring using soil-gas method to determine the influence of such formations on enhanced concentrations of different gases in soil to monitor the tectonic activity in the region, along with some weekly monitoring results for the establishment of monitoring station at Jiaosi in Ilan area. To carry out the present investigation variation in temporal soil-gases compositions was measured at established continuous earthquake monitoring stations along the above said faults. Observations have shown potential precursory signals for some major earthquakes in the region.

Previous year's results have shown that Hsinhua and Hsincheng faults have different tectonic settings and a tectonic based physical model was proposed. Based on the anomalous signatures from monitoring stations we are in a state to identify the area for impending earthquakes and we have tested it for some major earthquakes which rocked the whole Taiwan in recent times.

Keywords: Soil-gas, Fault, Earthquake, Tectonic, Radon, CO_2

Introduction

The continuous monitoring of changes in the daily variation of soil-gas composition along some active faults are demonstrated as good investigating tool to monitor the tectonic activities in the region (Walia et. al, 2009a; Walia et al., 2005; Fu et al., 2005; Yang et al., 2006). Studies on diffuse degassing from sub-surface carried out have clearly shown that gases can escape towards the surface by diffusion and by advection and dispersion as they are transported by rising hot fluids and migrate along preferential pathways such as fractures and faults (Yang et al., 2003). To explain radon migration over large distances, several models have been elaborated and it has been established that radon is monitoring using soil gas method (Etiope and Martinelli, 2002).

The island of Taiwan is a product of the arc-continent collision between Philippine Sea plate and Eurasian plate which make it a region of high seismicity. In the southern area of island, the Eurasian plate is subducting under the Philippine Sea plate while in the northern area of the island, the Philippine Sea plate bounded by the Ryukyu trench is subducting beneath the Eurasian plate. Behind the Ryukyu trench, the spreading Okinawa trough has developed. The northern part of Taiwan Island is located at the western extrapolation of the Okinawa trough. The present work is focused on Hsincheng fault in Hsinchu area and Hsinhua fault in Tainan for

[1] Associate Research Fellow, National Center for Research on Earthquake Engineering, walia@ncree.org.tw
[2] Assistant Research Fellow, National Center for Research on Earthquake Engineering, sjlin@ncree.org.tw
[3] Professor, Department of Geosciences National Taiwan University, tyyang@ntu.edu.tw
[4] Deputy Director, National Center for Research on Earthquake Engineering, wenkl@ncree.org.tw

earthquake monitoring using soil gas method. It is well established that distribution of soil gas compositional variations can been employed as the precursors for earthquakes (Walia et al., 2005; Yang et al., 2006) and for mapping of fault zones (Walia et. al, 2009a; Fu et al., 2005).

Presently our work is focused on temporal geochemical variations of soil-gas composition at established geochemical observatories along the above said faults in Hsinchu, Tainan and Ilan areas of Taiwan, respectively and to determine the influence of enhanced concentrations of soil gases to monitor the tectonic activity in the region.

Methodology

To carry out the present investigation, temporal soil-gases compositions variation were measured regularly at continuous earthquake monitoring stations using RTM2100 (SARAD) for radon and thoron measurement (for details see previous reports).

Results from monitoring stations

Investigations during the observation period have shown potential precursory signals for some major earthquakes in the region. Both the above said faults are located on/near National Science Industrial Park (NSIP), the industrial hub of Taiwan, and can be a cause of concern for urban life making it necessary to check the activity to these faults. During the observation we have found that in some cases a number of earthquakes occur in short span of time i.e within 1-5 days. These earthquakes can be considered as aftershocks/foreshocks of big earthquakes or different earthquakes. In the present study we have considered these as one seismic event.

Hsincheng Fault

During the observation period (i.e Jan., 2006 until Dec., 2009) potential precursory signals have been recorded for some earthquakes that occurred in the region (see Fig. 1 and previous reports). About 55 seismic events were observed during the observation period at this monitoring station and 30 of these have shown precursory signals. Those which have shown no precursory signals are deep focus earthquakes or monitoring station may be effected by the heavy rainfall during that period. During the period of observation, about 45 anomalies were observed and out of these 30 anomalies can be correlated with the seismic events (Table 1). Most of the non-correlated events are either having no soil-gas data or are deep focused events. During heavy rains, water percolated down and affected the gas emanation thus prevented gas to migrate towards the surface. For the above mentioned period of observation, about 67% of anomalies can be correlated with seismic events in the region and the rest of anomalies may have occurred due to on going crustal deformation in the region and not enough to produce an earthquake. The confidence level of monitoring station along the Hsincheng fault is found be 2.03 and indicative the monitoring station is good for earthquake monitoring.

Hsinhua Fault

A continuous monitoring station was established at selected point at end of October, 2006 using radon detectors RTM 2100 along with carbon-di-oxide detector (see Fig. 2 and previous reports). In the observation period potential precursory signals were recorded for some earthquakes that occurred in the region.

Totally, about 63 seismic events and 57 anomalies were recorded at this monitoring station. From these, 46 can be correlated with seismic events. All of non-correlated events occurred during heavy rainy season and thus no anomalies can be detected for these events. This monitoring station has shown better confidence level (i.e. 4.3) than monitoring station along the Hsincheng fault, hence seems to be a better station (Table1). It has been found that during period of observation we have recorded more number of seismic events as well as number of precursory anomalies at Hsinhua as compare to Hsincheng fault which may indicate the this region may be seismically more active.

Ilan Area

In addition to continuous monitoring at established monitoring stations, we are trying to find appropriate site to build new monitoring stations on other active faults, for the purpose of having dense network of monitoring stations. In this phase of the project we did some field surveys in Ilan area using the soil-gas sampling procedure (reported in previous reports). About 150 samples were collected and analyzed for ^{222}Rn, ^{4}He, CO_2, CH_4, Ar, O_2 etc. (Fig. 3a). The occurrence of deeper gas emanation is investigated by the soil-gas surveys and is followed by weekly monitoring of two selected sites with respect to tectonic activity to check the sensitivity of the sites (Fig. 3b). One site is selected for long term monitoring and station was established on the basis of coexistence of high concentration of helium, radon and carrier gases and sensitivity towards the tectonic activity in the region.

Discussions

From the temporal variation of soil-gas during the observation at both the monitoring stations it has been found that both the faults have different characteristics which are indicated by the different anomaly pattern. Our observations show that at Hsinhua fault monitoring station the soil-gas shows diurnal and nocturnal variations in silent period. This variation was found to be disturbed before some seismic event and thus, considered to be a precursory anomaly. Whereas in the case of Hsincheng Fault soil-gas variation don't show diurnal and nocturnal variations and values above the threshold values can be denied as precursory anomaly. To filter out the effect of diurnal and nocturnal variations we prepared online database where we can find the average values of soil-gas ranging from 1 hour to 24 hours. For data analysis and identifying anomalies we use 24 hour average values of soil-gas for both the stations.

Long term geochemical monitoring at the established earthquake monitoring stations along the Hsincheng and the Hsinhua faults within the Hsinchu and Tainan areas, respectively, has been done continuously. Results have shown that Hsinhua and Hsincheng faults have different tectonic settings. It has been found that variations in soil-gas at Hsincheng fault were disturbed by the stress variation due to tectonic activities along Okinawa Trough and Rkukyu Trough which are located in north and central eastern part of Taiwan, respectively in addition to local earthquakes within a periphery of about 50km from the monitoring station (Walia et. al, 2009b). Whereas in the case of Hsinhua fault, soil-gas variations were observed to be due to tectonic activities along the Luzon Arc and other tectonic activities in southern part of Taiwan. So, Hsinhua monitoring station shows precursory signals for earthquakes occurring south or south eastern part of Taiwan, whereas, for Hsincheng faults, most of soil-gas variation precursory signals were recorded for the earthquakes that occurred along Okinawa Trough and Rkukyu Trough. These findings enabled us to propose a model dividing the whole Taiwan into various tectonic zones (Walia et al., 2009b). Based on the anomalous signatures from monitoring stations we are in a state to identify the area for impending earthquakes and we have tested it for some major earthquakes which rocked the whole Taiwan in recent times. Data is obtained from the monitoring stations run by NCREE and NTU in collaboration and fits well in proposed model (Fig. 4).The result from the present study shows that the soil-gas method may be useful for fault and earthquake monitoring studies along the Hsincheng fault, Hsinchu area of NW Taiwan. Long time continuous and comprehensive monitoring may be needed to find correlation of earthquakes with degassing along the established monitoring station at Jiaosi monitoring station in Ilan area to understand the characteristics of earthquakes in that region.

References

Etiope, G., Martinelli, G. (2002). "Migration of carrier and trace gases in the geosphere: an overview". *Phys. Earth Planet. Int.,* 129, 185-204.

Fu, C.C., Yang, T.F., Walia, V., Chen, C-H. (2005). "Reconnaissance of soil gas composition over the buried fault and fracture zone in southern Taiwan". *Geochemical Journal*, 39,427-439.

Walia, V., Yang, T.F., Lin, S-J., Hong, W-L., Fu, C-C., Wen, K-L.,Chen, C-H. (2009a). "Geochemical variation of soil-gas composition for fault and earthquake precursory studies along Hsincheng fault in NW Taiwan". *Appl. Radiat. Isotopes, 67, 1855- 1863.*

Walia, V., Yang, T.F., Lin, S-J., Hong, W-L., Fu, C-C., Wen, K-L.,Chen, C-H. (2009b). "Continuous temporal soil-gas composition variations for earthquake precursory studies along Hsincheng and Hsinhua faults in Taiwan". *Radiat. Meas.,* 44, 934-939.

Walia, V., Virk, H.S., Yang, T. F., Mahajan, S., Walia, M. and Bajwa, B.S. (2005). "Earthquake prediction studies using radon as a precursor in N-W Himalayas, India: a case study". *TAO*, 16(4), 775-804.

Yang, T.F., Chou, C.Y., Chen, C-H, Chyi, L.L., Jiang, J.H. (2003). "Exhalation of radon and its carrier gases in SW Taiwan". *Radiat. Meas.* 36, 425-429.

Yang, T.F., Fu, C.C., Walia, V., Chen, C-H., Chyi, L.L., Liu, T.K., Song, S.R., Lee, M., Lin, C.W., Lin, C.C., (2006). Seismo-geochemical variations in SW Taiwan: multi-parameter automatic gas monitoring results, *Pure Appl. Geophys.*, 163, 693-709.

Table.1: Statistical analysis of recorded data at both the monitoring stations.

Station Name	Total Anomalies (a)	Total seismic events (b)	Anomalies related with events (c)	Anomalies not related with seismic events (d)	Signal (%) (c/a)	Noise (%) (d/a)	Confidence level (Signal/Noise)
Hsinchu	45	55	30	15	67%	33%	2.03
Hsinhua	57	63	46	10	81%	19%	4.26

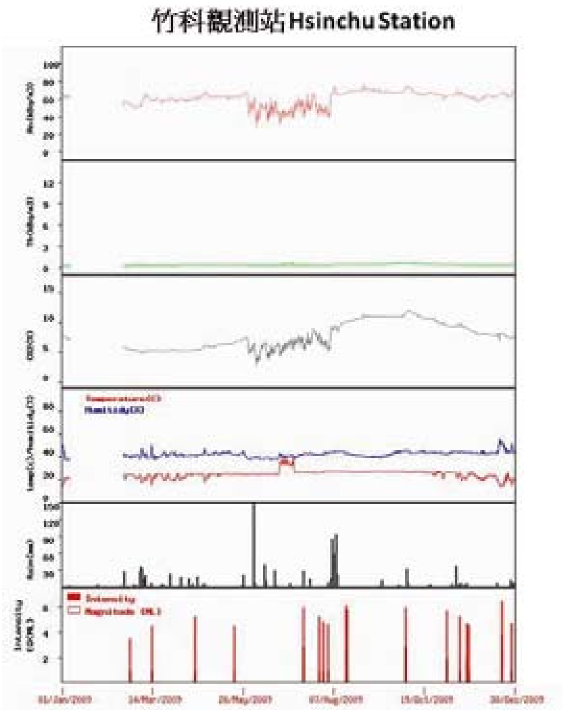

Fig.1. Variations of radon, thoron, carbon dioxide and rainfall at Hsinchu monitoring station and its correlation with earthquakes during 2009.

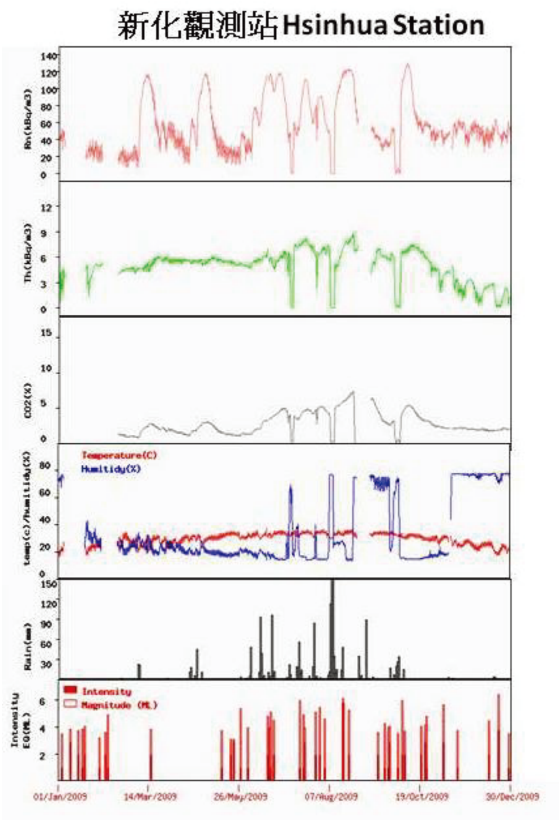

Fig.2. Variations of radon, thoron, carbon dioxide and rainfall at Hsinchu monitoring station and its correlation with earthquakes year 2009.

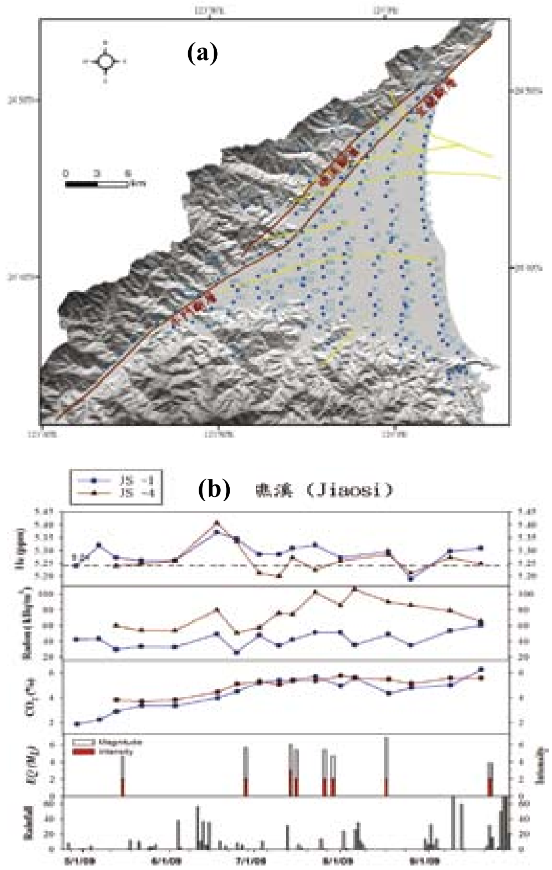

Fig.3. (a) Distribution of soil-gas survey in Ilan Plain (blue dot represent the sampling points) (b) weekly monitoring at the Jiaosi, Ilan area.

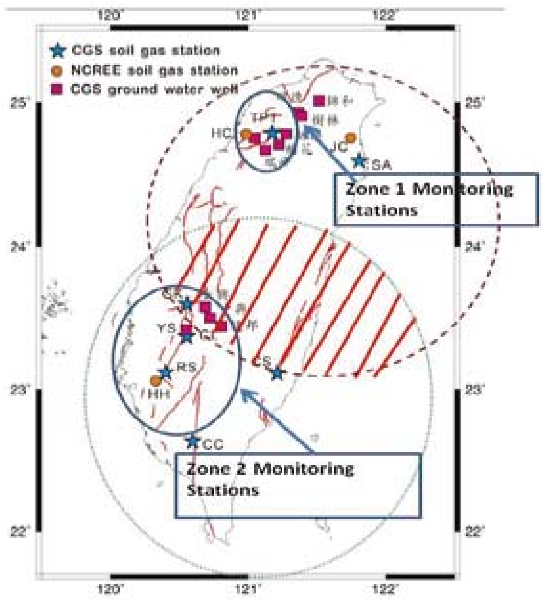

Fig.4. Tectonic based physical model of Taiwan dividing the island into two tectonic zones (red and green circles representing zone 1 and 2, respectively), whereas dashed area is the common tectonic zone for expected earthquakes.

Effects of Uncertainties to the Simulated Performance of Water System under Seismic Conditions

Gee-Yu Liu [1] and Hsiang-Yuan Hung [2]

劉季宇 [1]、洪祥瑗 [2]

Abstract

The ability to assess the serviceability of water systems after major earthquakes is very important to urban earthquake disaster preparedness and mitigation. In this study, the effects of uncertainties in ground motions and pipeline damages to the simulated performance were investigated and found of little or no influence. The characteristics of networking of a water system were found to have a predominant factor to its seismic performance.

Keywords: water systems, serviceability, seismic scenario simulation, uncertainties

Background

The ability to assess the serviceability of water systems after major earthquakes is very important to urban earthquake disaster preparedness and mitigation. In the previous year, such technique has been developed by Liu et al. (2009) using the software EPANET. The water system of Taipei metropolitan area was selected as a test bed for case study. EPANET is a computer program developed and maintained by the U.S. Environmental Protection Agency for the simulation of hydraulic and water quality behavior within a pressurized pipe network (Rossman, 2000). In this study, the hydraulics of water systems are introduced, the modeling of pipe breaks and leaks are explained, and the effects of uncertainties in ground motions and pipeline damages to the simulated serviceability of water system under seismic conditions will be further investigated.

Hydraulics of Water Network Systems

Figure 1 depicts the schematic diagram of a simplified water network. A water network system usually consists of tanks, reservoirs, pumps, valves and numerous pipes and nodes. The hydraulics of such a system can be assumed as pressurized pipe flows, and can be solved by using two sets of equations (Rossman, 2000). Let there be N nodes, NF fixed nodes (e.g. tanks and reservoirs) and K pipes in a water network, then the first set prescribe the difference of water head at the ends of each pipe and read:

$$H_i - H_j = h_{ij} = r \cdot Q_{ij}^n + m \cdot Q_{ij}^2$$

where H, h, Q, r, n and m are the nodal head, head loss, flow rate, resistance coefficient, flow exponent and minor loss coefficient, respectively. The most widely used empirical formulae to decide the value of r are the Darcy-Weisbach, Hazen-Williams or Chezy-Manning equation, all of which employ flow rate and various pipe parameters. The second set prescribes the balance of flow at each node and read:

$$\sum_j Q_{ij} - D_i = 0$$

where D_i is the demand at node i. By using these two sets of equations, the pipe flow can be solved in terms of the water heads H_i at N nodes and the pipe flow rate Q_{ij} (from node j to node i) in K pipes.

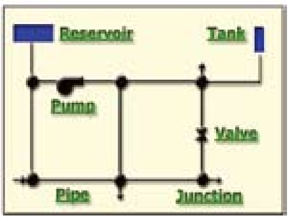

Fig. 1 The schematic diagram of a simplified water network system (Rossman, 2000)

---

[1] Associate Research Fellow, National Center for Research on Earthquake Engineering, karl@ncree.org.tw

[2] Assistant Research Fellow, National Center for Research on Earthquake Engineering, hyhung@ncree.org.tw

Pipe Damages and Their Hydraulic Models

Pipe damages can be classified into two types: pipe breaks and pipe leaks. A pipe break and its hydraulic model can be depicted as the left schematic diagram in Fig. 2. At each of the broken ends, a reservoir and a short pipe with a check valve are needed being added to mimic the mechanism of water flowing into the atmosphere. To take into account the effect of a pipe break in simulation, several steps to modify the hydraulic model of the broken water system should be taken. They are (Liu et al., 2009): (1) Decide the location and elevation of pipe break point, (2) Remove the original link (pipe segment), (3) Add two new nodes A and B at the location of pipe break point, (4) Add two new links connecting the original pipe segment ends to A and B, respectively, (5) Add two new nodes A' and B' with the elevation of pipe break point and designate them as reservoirs, and finally (6) Add two new links connecting A-A' and B-B' and specify them with one-way check valves

On the other hand, a pipe leak and its hydraulic model could be depicted as the right schematic diagram in Fig. 2. A pipe leak is hydraulically equivalent to a sprinkler with a specific discharge coefficient and an orifice size. This sprinkler is further proven to be equivalent to a fictitious pipe linking the original pipe and an added reservoir (Shi et al., 2006). A check valve is designated to the fictitious pipe ensuring that water flows from the leaking pipe to the reservoir. The steps to modify the hydraulic model of the leaking water system could be summarized as follows (Liu et al., 2009): (1) Decide the location and elevation of pipe leak point, (2) Remove the original link (pipe segment), (3) Add a new node A at the location of pipe leak point, (4) Add two new links connecting the original pipe segment ends to A, (5) Add a new node A' with the elevation of pipe leak point and designate it as a reservoir, and finally (6) Add a new link connecting A and A' and specify it as a fictitious pipe with a diameter of corresponding pipe leak model, and also specify it with a one-way check valve.

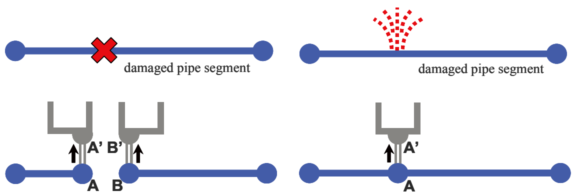

Fig. 2 A pipe break (left), a pipe leak (right) and the their hydraulic models (Shi et al., 2006)

Strong Motion and Uncertainty

The earthquake-induced ground motion intensity, e.g. peak ground acceleration (PGA), can be simulated by using appropriate attenuation laws. For the case of Taiwan region, a formulae has been proposed (Jean et al. 2002), expressed as follows:

$$\mathrm{PGA} = 0.003694 \cdot e^{1.7538 \cdot M} \cdot [R + 0.1222 \cdot e^{0.7832 \cdot M}]^{-2.0564}$$

where M and R are the earthquake magnitude and the distance (in Km) from the site to the seismic source, respectively. This formula is of Campbell form and the coefficients were determined from the ground motions of 15 past earthquakes in Taiwan. In addition, a standard deviation of 0.68-0.75 (in natural logarithmic scale) of the ground motion data with respect to the formula was reported. Figure 3 depicts the attenuation curves of this formula at selected earthquake magnitudes.

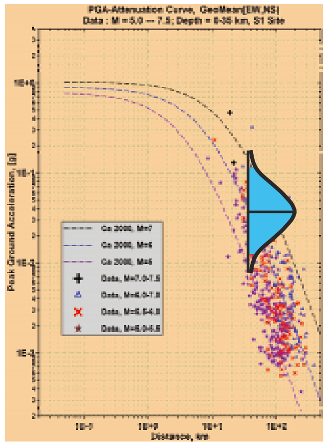

Fig. 3 The attenuation curves for Taiwan region at selected earthquake magnitudes (Jean et al. 2002)

Pipe Repair Rate and Uncertainty

Repair rate (RR) is defined as the number of repairs (or damages) per unit pipe length (km unit in this paper). It is widely employed to indicate pipe fragility. Numerous investigations have been made to formulate the relationship between pipe repair rate and earthquake-induced strong motions and ground failures. The pipe materials and diameter affect the pipe repair rate, too. Particularly, an approach has been proposed to achieve the repair rates caused by ground shaking and by ground deformation separately (Yeh et al., 2006). Following this approach, a regression model for the effect of ground shaking (PGA in gal) solely can be expressed as follows:

$$RR = 1.028 \times 10^{-3} \cdot \mathrm{PGA}^{0.9735} \quad (\mathrm{R}^2 = 0.9388)$$

Here, the six empirical data points were attained from the ground deformation-free areas in Taiwan in the 1999 Chi-Chi earthquake. Pipes with a diameter equal to or greater than 200mm were selected for use, which consist of 596.13km of pipe length and 158 repairs, yielding an average of 0.265 repairs per km (cf. 0.439 repairs per km to pipe mains in the 1995 Kobe earthquake reported by ALA, 2001, probably combined with the effect of ground deformation). In addition, these data points give a standard deviation of 0.0739 (in $\log_{10}$ scale) or 0.1701 (in natural logarithmic scale) with respect to the regressed curve.

The empirical evidence has strongly indicated that large pipes over 12” (300mm) diameter have lower repair rates than do common diameter distribution pipes of 4” to 12” diameter (ALA 2001). As a result, judgment has been made here to revise the above equation for the implementation to large pipes. The following equation was tentatively proposed in this study to simulate pipe damages.

$$RR = \begin{cases} 1.2\times10^{-3}\cdot PGA^{0.9735} & \phi \le 300\text{mm} \\ 0.8\times10^{-3}\cdot PGA^{0.9735} & 300\text{mm} < \phi \le 500\text{mm} \\ 0.4\times10^{-3}\cdot PGA^{0.9735} & 500\text{mm} < \phi \end{cases}$$

where $\alpha = 0.9735$. Various curves of pipe repair rate have been illustrated in Figure 4.

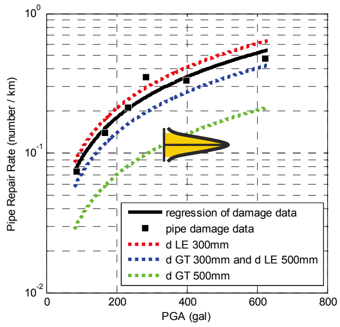

Fig. 4 Various curves of pipe repair rate

Case Study

The water system of the Taipei metropolitan area operated by the Taipei Water Department (TWD) has been selected as a test bed for the case study. It provides service to the Taipei City as well as four other cities of the Taipei County. TWD has a service region of 434 square kilometer, and serves water to 1.51 million customers or 3.85 million people. The daily water supply is around 2.5 million tons. The entire water system is hydraulically separated into 10 service areas. The scenario of an M7.5 earthquake associated with the Hsincheng fault has been considered. The assessment procedure followed the Monte Carlo method and employed 100 simulations for the network of each service area. The simulated distributions of serviceability index for the TWD water system are depicted in Figure 5. Here, the serviceability index (SI), the ratio of flow at demand nodes before and after the earthquake, was used to quantify the water network seismic performance in each service area. The attained SI values vary between 0.44 and 0.92. Figure 6 depicts the SI value of each of the 100 simulations for the 10 TWD service areas following the assumed M7.5 earthquake. Significant difference can be observed from the deviation of SI values of each service area from simulation to simulation. For example, Service Areas 01 (Shih-lin Bei-tou) and 07 (Chang-hsin Nan-gang) show a very limited deviation, while Service Area 04 (Ming-sun) shows a very large deviation. It seems that the network characteristics rather than other factors have a predominant effect on the water system’s seismic performance.

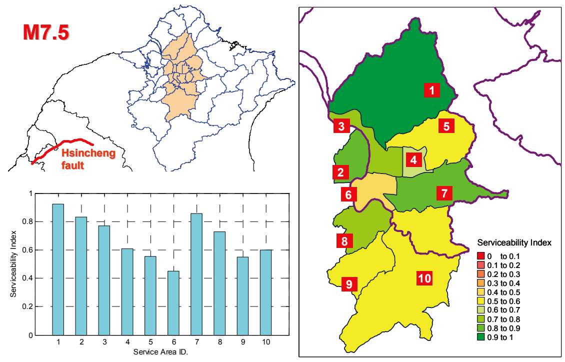

Fig. 5 The Hsincheng earthquake scenario and the distribution of simulated serviceability index of each service area in Taipei region

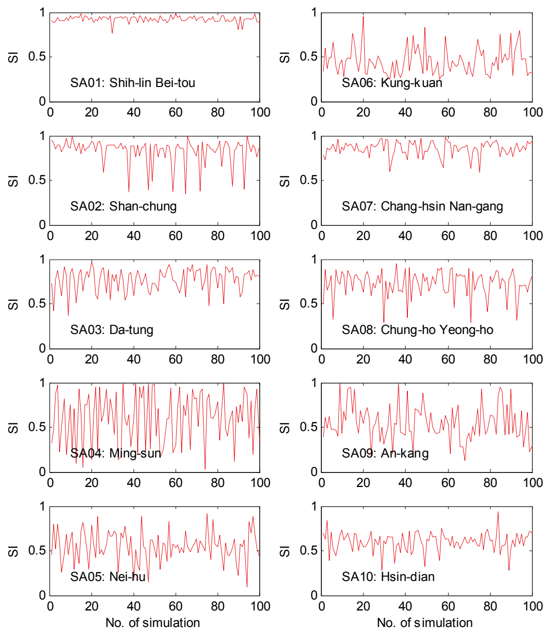

Fig. 6 The SI value of each of the 100 simulations in the Monte Carlo method for the 10 TWD service areas following the considered M7.5 earthquake

In order to investigate the effects of uncertainties to the assessment results, two groups of assessment were further conducted. The first was to adopt the attenuation law together with a standard deviation of 0.68. During the generation of a random multiplier to adjust the simulated PGA value, a truncation of beyond ±1.0 standard deviation was enforced. The second was to adopt the pipe repair rate model together with a standard deviation of 0.1701. Again, a truncation of beyond ±1.0 standard deviation was enforced. Figure 7 depicts the convergence of the simulated SI value for each service area following the M7.5 earthquake scenario. The red solid line, blue dotted line and green dash-dotted line refer to the results without adopting any uncertainty, with deviation in ground shaking model, and with deviation in pipe repair rate model, respectively. The depicted convergence curves show the average of the simulated SI values of the first 1 to 100 simulations. The symbol denoted on each curve refers to where the simulated SI value begins to converge within a tolerance of 0.02 with respect to the average of 100 simulations. It is to indicate the speed of the simulated SI value to converge. An overview of Figure 7 indicates that uncertainties in both the strong motion attenuation and pipeline repair rate have little or no significant effect on the final SI value. Also, there is no clear tendency that these uncertainties will affect the speed of convergence.

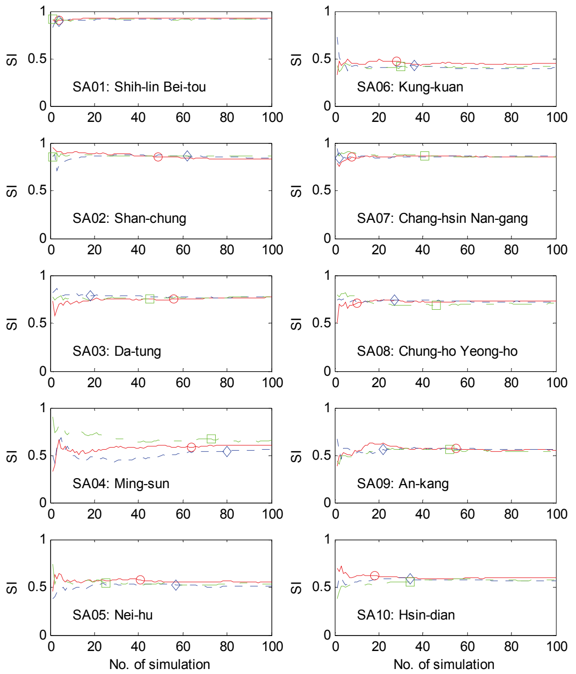

Fig. 7 Convergence curves of the simulated SI values for TWD service areas in the M7.5 earthquake scenario (red: no uncertainty considered, blue: with uncertainty in ground shaking model, green: with uncertainty in pipe repair rate)

Conclusions

In this study, the hydraulics of water network systems have been introduced, the modeling of pipe breaks and leaks has been explained in detail, and the effects of uncertainties in ground motions and pipeline damages to the simulated performance of water system under seismic conditions have been investigated and found of little or almost no influence. The characteristics of networking of a water system seem to provide the predominant factor to its seismic performance.

Acknowledgement

This research work was funded by the National Science Council, Taiwan under Grant No. NSC-96-2625-Z-492-007, and was carried out using the network data of the Taipei Water Department for hydraulic analysis. Both are gratefully acknowledged.

References

ALA (American Lifelines Alliance) (2001). Seismic Fragility Formulations for Water Systems, http://www.Americanlife linesalliance.org.

Hwang, H., Chiu, Y.-H., Chen, W. and Shih, B.-J., (2004). "Analysis of Damage to Steel Gas Pipelines by Ground Shaking Effects during the Chi-Chi, Taiwan Earthquake," Earthquake Spectra, 20(4), pp.1095-1110.

Jean, W.-Y. 2002. Private communications.

Liu, G.-Y. and Hung, H.-Y., (2009) "Hydraulic Performance Analysis of Water Systems under Major Earthquakes," Proc. 6th Taiwan-US-Japan Workshop on Water System Seismic Practices, Taipei, Taiwan.

Rossman, L. A. (2000). EPANET 2 User's Manual, EPA, Cincinnati, OH.

Shi, P., O'Rourke, T. D. and Wang, Y. (2006). "Simulation of Earthquake Water Supply Performance", Proc. 8th U.S. Nat. Confer. Earthquake Eng., Paper No. 1295, San Francisco, CA.

Yeh, C. H., Shih, B.-J., Chang, C.-H., Chen, W.-Y. Walter, Liu, G.-Y. and Hung, H.-Y., (2006). "Seismic Damage Assessment of Potable Water Pipelines," Proc. 4-th Int. Confer. Earthquake Eng., Taipei, Taiwan.

Developing Information System for Earthquake Emergency Response and Disaster Prevention

Chih-Hsin Chen[1], Wei-Chang Chen[2], Chin-Hsun Yeh[3]

Abstract

Along with the development and updating of Taiwan Earthquake Loss Estimation System (TELES), the databases and seismic disaster assessment models have been fully developed at the National Center for Research on Earthquake Engineering (NCREE). However, those valuable data and research results could not be shared to the public due to the expensive cost of GIS software and protection of intellectual property right. From the information sharing point of view, NCREE planned to build an information system through the web geographic information system (Web-GIS) technology. Started in 2009, the information system for earthquake emergency response and disaster prevention was set up which integrated the result of early assessment of seismic disaster and the function of seismic scenario simulation and has provided information to search and rescue organizations

Keywords: Taiwan Earthquake Loss Estimation System (TELES), Web-Geographic Information System (Web-GIS), Seismic Disaster Simulation, Early Assessment of Seismic Disaster.

Introduction

The main objective of this study is to establish a seismic response and disaster prevention information system on internet so that the damage estimates of general building stocks, various kinds of facilities and lifeline systems can be used more effectively; and also to offer valuable information to all search and rescue organizations or emergency decision-making units at the shortest period of time after earthquake occurs.

The software and technologies we used to establish the information system for earthquake emergency response and disaster prevention were MapInfo's MapXtreme and Microsoft VS.NET, AJAX, HTML, and XML. The tasks of setup this system include the following: (1) seismic disaster information management system, (2) seismic early assessment and seismic disaster simulation system, (3) seismic scenario simulation system, and (4) bridge investigation system.

Seismic Disaster Information Management System

In order to provide seismic disaster evaluation and analysis to search and rescue organizations, and to coordinate and annual earthquake prevention training to be hosted by the National Disaster Prevention and Protection Commission, the Seismic Disaster Simulation Division at the National Center for Research on Earthquake Engineering established a seismic disaster information upload and management system. When strong earthquake occurs, NCREE will notify and send a group of well trained members to the worst affected area. There will be disaster evaluation, collection, and investigation teams and administrative support group. For the disaster investigation team, they will be responsible in investigating the actual disaster in the site, and in providing the accurate disaster information back to NCREE. Then, the disaster collection team will be collecting all the information and be the ones uploading the data to the established “Seismic Disaster Information Upload and Management System”; The said system can also provide features in arranging disaster information and pictures issued through electronic media (Fig.1).

As can be noticed, the purpose of the “Seismic Disaster Information Upload and Management System” is to record the earthquake disaster in details. It offers seven types of loose survey form such as on building, road and bridge, non-structural building, harbor and airport, geology, living system, and historic monument. The multimedia and picture files can also be stored in the database. The “Disaster Information Upload and Management System”

[1] Assistant Technician, National Center for Research on Earthquake Engineering
[2] Assistant Research Fellow, National Center for Research on Earthquake Engineering
[3] Research Fellow, National Center for Research on Earthquake Engineering

integrates MapXtreme Web Map, AJAX, and Microsoft Silverlight technologies to provide asynchronous data update, precise disaster loss point positioning, reviewing and verifying disaster report, and seismic information exhibits. Once the new seismic disaster information is added to the database, the contents of the information or report will be evaluated and reviewed carefully; then will be released to the public as an official seismic disaster report. Further to exhibit and evaluate the seismic disaster information, it also builds a Web Service interface for external releasing; whereas it shares data and integrates them with other Web-GIS systems.

This system has been used and had undergone modifications during the “Wen-Chuan earthquake, China 2008”. And, to prevent abuse by general users, its login system combined with “NCREE Friends’”; makes sure that the only the logged in user can access or upload disaster-related information with his or her permissions.

Fig. 1 The interface of seismic disaster information and management system

Display of Earthquake Disaster Information

People are always expecting to understand the distribution of earthquake disasters after the shock. The feedback data in our management system can be shared to the public via the internet. Therefore, in this study, we took the 921 earthquake has been chosen as our study case to establish an earthquake disaster display system. The system is based on Web-GIS technology, and in this system, detailed investigation reports and pictures of damaged building and bridges can be seen shown on the browser (Figs.2 & 3).

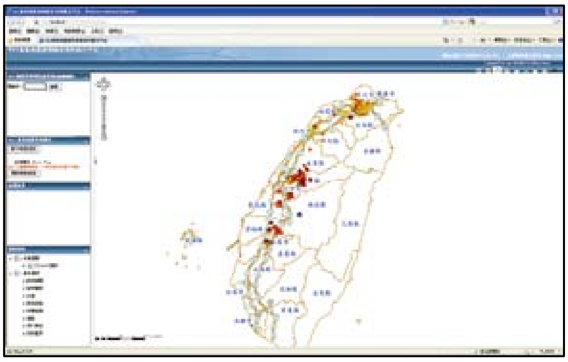

Fig. 2 Distribution map of damaged buildings

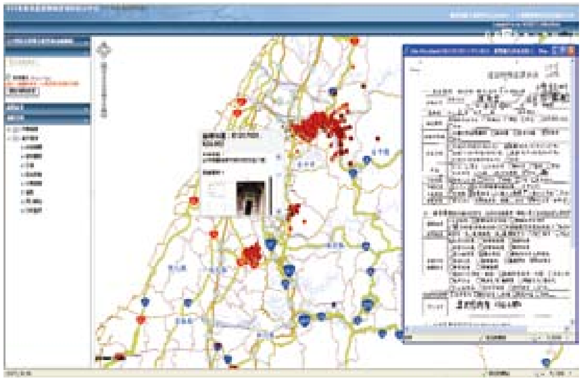

Fig. 3 The interface of browsing investigation reports and pictures

Display of Seismic Early Assessment and Disaster Simulation

“Taiwan Earthquake of Loss Estimates System” or TELES is an earthquake disaster simulation system. For effective and accurate simulation of the disaster caused by an earthquake, it must have a complete database and analysis models. Although NCREE offers TELES application for free, it currently does not provide database to general users. In order to offer variety of seismic evaluation results to public and disaster prevention units, a so-called "Seismic Early Assessment and the Seismic Disaster Simulation System” has been established using Web-GIS technology.

Results of Seismic Early Assessment

The TELES starts simulating a seismic disaster after receiving the earthquake message from the Central Weather Bureau through email. Based on the seismic parameters form the e-mail, TELES evaluates the building damages, casualties and economic loss. The result of assessment can be viewed or accessed on the website immediately (Figs.4 & 5). Through the website, the disaster rescuers on site can view clearly the thematic map of earthquake events, the location of earthquake epicenter, faults direction and disaster loss distribution. Furthermore, the researchers can download related data for follow-up study.

The seismic disaster reports, which come from "The Disaster Information Upload and Management System", can be accessed also on the established system. The user can view the detail of the seismic disaster report, e.q. location of disaster losses, information of latitude and longitude and hyperlink of complete report. All the results of seismic early assessment and disaster report can be seen on the same map; it really assists disaster assessment and provides more precise information to the personnel of the rescue team.

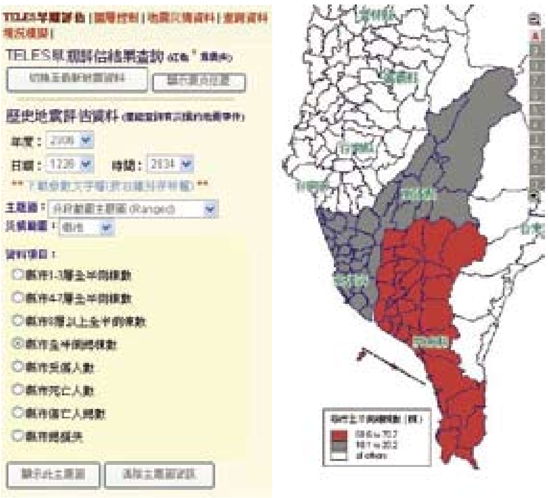

Fig. 4 Query results and thematic map of seismic early assessment

Fig. 5 Exhibition of seismic disaster report

Results of Seismic Disaster Simulation

Using TELES earthquake simulation technology can build a seismic loss simulation database, which contains potential seismic hazards analysis, general building damage assessment, casualties and economic losses. In this study, an online seismic disaster simulation distribution and inquiry system has been constructed to combine the pre-built seismic loss database, and to provide a variety of seismic disaster simulation results on the Web-GIS (Fig.6).

Users can set earthquake scale (5.1~7.3 scale), focal depth (10~90 km.), epicenter location (latitude 21.1~25.9, longitudes 119.1~122.9), and faults (0~135 degree) to simulate an earthquake disaster. The result is not only shown on the map, but also exhibited by different types of thematic map such as range, dot density, individual values, pie chart, or bar chart, spatial units (counties or towns), and the simulation subjects (building damage, casualties, fire, shelter, debris). Also, the feature is very useful for general seismic disaster education and training.

Fig. 6 Assessment results and thematic map of seismic disaster simulation

Applications for Bridges Investigation

Bridges damaged under strong earthquake impact, could reduce the efficiency of post-earthquake rescue efforts and may cause huge casualties and property losses. In order to estimate the damage distribution of bridges after earthquake, Directorate General of Highways (DGH) launched a project to establish an early seismic loss estimation module for highway bridges. NCREE have participated into this project since 2008 and have devoted building to build and integrating said module into TELES. However, the data acquired from were still insufficient for loss assessment.

An extensive investigation of bridge seismic capacity was performed in this joint project to complete the database. Software engineers developed bridges investigation software which is able to be executed via PDA and stand alone machines. The software was developed on Microsoft.NET framework. Wild field investigators are capable of inserting or importing data in PDA (Fig.7) and stand alone hardware (Fig.8), however, advanced functions of search, sorting and image browsing are available in stand alone machines only.

Fig. 7 PDA application of bridges investigation

Fig. 8 Bridges investigation application executed in a stand-alone environment

Conclusion

In this study, through the Web-GIS technology, the TELES has been well-known to public. It provides general education to users and the information of early assessment of seismic disaster to rescue decision-makers. In order to prevent serious disaster and thus accelerate seismic aftermath rescue, the TELES Web-GIS system will be improved further on its performance of display data and will be added with the satellite photographs layer to its base map as part of future studies.

The Engineering Geological Database for Strong Motion Stations in Taiwan

Kuo-Liang Wen[1,2] and Hung-Hao Hsieh[3]

溫國樑[1,2]、謝宏灝[3]

Abstract

More than 680 seismic stations all over Taiwan have been established by the Central Weather Bureau (CWB) to record ground motion data. In order to obtain the geological conditions and soil profiles at these strong motion stations, a site investigation project was developed by the National Center for Research on Earthquake Engineering (NCREE) and CWB in 2000. The site investigation mainly consists of three parts: the basic description of a site, the on-site boring, and the Suspension P-S Logger technique which is used to determine the P and S wave velocities of the stratum at various depths. The Suspension P-S Logger technique, using a single down-hole probe with one source and two receivers, allows continuous measurements of wave velocities with high resolution. There were 47 seismic stations investigated in 2009. With reference to Kyoshin Net in Japan and ROSRINE in USA, a preliminary engineering geological database for 401 seismic stations investigated during 2000 to 2008 has been constructed on NCREE's website for researchers' convenient access to their needed data.

Keywords: Geological Database, Wave Velocity, Seismic Station, P-S Logger, Suspension P-S Velocity Logging System

Introduction

Taiwan is located in the Circum-Pacific seismic belt --- the most active seismic region in the world. Preventing severe losses of lives and properties caused by large earthquake is a major concern for the people in this region. The Taiwan Strong Motion Instrumentation Program (TSMIP) was initiated by CWB in 1991 to monitor ground motions at over 680 free-field stations around Taiwan. Once a major earthquake happens, the records of ground motions from TSMIP provide useful information for the operation of hazard mitigation. The ground responses monitored by seismographs reveal the characteristics of ground motions in different geological conditions, and these data can be used to improve the design spectrum and the current building codes.

More than 1,000 seismic stations have been installed in Japan to monitor ground responses during an earthquake. Researchers can download the data on ground responses via a web site called "Kyoshin Net". The basic information of a station site, physical properties of soils, and wave velocity of the stratum measured by the down-hole velocity logging technique are also available on the site. After 1994 Northridge earthquake, a project called "Resolution of Site Response Issues from the Northridge Earthquake", ROSRINE, was conducted to study the site responses in the USA. Related information can be accessed in the said web site to download the geological information and the wave velocity profile of a specified station.

The distribution of seismic stations in Taiwan is the densest in the world, although the amount of seismic stations installed by CWB is less than that in Japan and USA. However, the application of earthquake data is being restricted by having an incomplete geological database. Therefore, in 2000, NCREE and CWB collaborated to perform site investigation in obtaining basic soil properties and wave velocity of the stratum. There are 47 seismic

[1] Professor, Dep. of Earth Science & Inst. of Geophysics, National Central University.
[2] Division Head, National Center for Research on Earthquake Engineering.
[3] Assistant Research Fellow, National Center for Research on Earthquake Engineering.

stations which were investigated in 2009 and are shown in Figure 1. The code of the stations is listed in Table 1. There are 448 seismic stations investigated during the period of 2000 to 2009 and are shown in Figure 2. With reference to Kyoshin Net in Japan and to ROSRINE in USA, a preliminary engineering geological database for the 401 seismic stations investigated during the year 2000 to 2008 has been constructed on NCREE's website for convenient information access. This is named, "Geological Surveyed Database of CWB Strong Motion Station" and its website address is at http://geo.ncree.org.tw (as shown in Figure 3).

Figure 1. The 47 seismic stations investigated in 2009.

Table 1. The seismic stations investigated in 2009.

Sta. Code	Sta. Code	Sta. Code
HWA001	HWA039	TTN011
HWA006	HWA041	TTN016
HWA008	HWA043	TTN018
HWA010	HWA044	TTN022
HWA011	HWA045	TTN028
HWA013	HWA047	TTN031
HWA016	HWA049	TTN032
HWA019	HWA053	TTN033
HWA020	HWA054	TTN034
HWA023	HWA057	TTN035
HWA025	HWA060	TTN036
HWA030	HWA062	TTN038
HWA031	ILA051	TTN043
HWA035	TTN001	TTN045
HWA036	TTN002	TTN046
HWA037	TTN003	

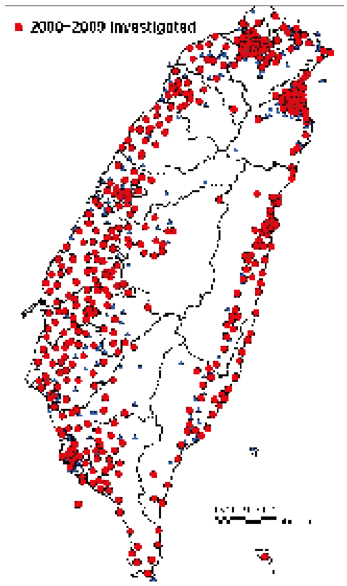

Figure 2. The 448 seismic stations investigated during 2000~2009.

Figure 3. "Geological Surveyed Database of CWB Strong Motion Station" Website

The local site conditions play an important role in determining ground responses during an earthquake. Different site conditions could induce amplification or de-amplification at different period ranges in the response spectra. This factor is called the "site effect". Besides, in a seismic hazard analysis, the motion at a site's bed rock is predicted by the attenuation low from the earthquake source. According to the 2000 Uniform Building Code (UBC), 1997 National Earthquake Hazards Reduction Program (NEHRP) provisions in the USA, and the revised Earthquake-resistant Code in Taiwan, the ground motion at free field is evaluated by the response at bed rock times the coefficient of site effect. The coefficient of site effect is related to the magnitude of earthquake and the local site conditions. Thus, a complete geological database is essential to the evaluation of site effect for earthquake engineering.

Suspension P-S Logging Technique

The Suspension P-S Logging Technique developed by the OYO Corporation in Japan was used in this project to measure the primary wave velocity (Vp) and the shear wave velocity (Vs) of the stratum. The source and the receiver of this measuring system were integrated into a single probe within a short distance. Therefore, the wave velocities of the stratum can be measured continuously and precisely.

A borehole was first drilled at the chosen site and then filled with water. If the surrounding soil on a borehole is not stable and is easily eroded, the borehole may be lined with a plastic tube. The probe was then put into the borehole at a specified depth. A primary wave or a shear wave may be generated by the source in the probe. The primary wave was propagated through the surrounding soil in the direction perpendicular to the borehole axis (horizontal direction). Also, the shear wave was propagated through the soil along the vertical direction. Each receiver consists of a hydrophone and a geophone in receiving the primary wave and the shear wave, respectively. A normal pulse and a reverse pulse were triggered by the source in order to check the received signals. The time histories of those received signals should then be in the same shape but with 180 degrees phase difference, since the two shear waves were propagated through the same soil media.

Typical measured signals of the primary waves and the shear waves from the logging computer are shown in Figure 4, where H1 and /H1 represent the signals received by the upper receiver in normal and reverse directions, H2 and /H2 represent the signals received by the lower receiver in normal and reverse directions, V1 and /V2 represent the signals received by the upper and lower receivers, respectively. From the time histories of H1 and H2, the first arrival time for the upper receiver and the lower receiver was picked as ts1 and ts2. Since the distance between the two receivers is 1 m, the shear wave velocity can be determined as:

$$v_s \text{ (m/sec)} = \frac{1}{t_{s1} - t_{s2}} \tag{1}$$

Similarly, the primary wave velocity is:

$$v_p \text{ (m/sec)} = \frac{1}{t_{p1} - t_{p2}} \tag{2}$$

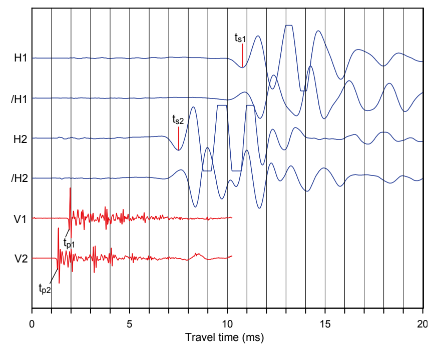

Figure 4. Typical measurements from the Suspension P-S Logging System.

Engineering Geological Database

There are three major items in the Engineering Geological Database in Taiwan. The first item is the general information of the station site that includes latitude and longitude of the station, ground water level, geographical/topographical conditions, and surrounding structures. The second item refers to the physical properties of soils. The SPT-N value, water content, unit weight, soil classification, and grain size distribution are obtained by on-site boring, sampling, and laboratory testing. After the borehole was drilled, the Suspension P-S Logging Technique was utilized to measure the wave velocity of the stratum at every 0.5m. The wave velocity of the stratum is an important index for site classification, so it is selected as the third item in the database. If the geological condition of the station site is classified as a rock outcrop, only the general environmental investigation was performed to collect the basic information of the station.

This project has been conducted for nine years. At present, site investigations at 408 station sites were completed with the following distribution: 37 stations in 2000, 65 stations in 2001, 49 stations in 2002, 54 stations in 2003, 40 stations in 2004, 26 stations in 2005, 50 stations in 2006, 49 stations in 2007, 31 stations in 2008 and 47 stations in 2009. These stations are located on the alluvial deposit, gravel, or even rock sites. The results were summarized on NCREE's website. For example, as shown in Figure 5, the general information for station TTN023 (the photo of the seismograph, the plan section and the cross section of the surrounding environment), the soil profile, the SPT-N value, the shear wave velocity, and the primary wave velocity of the stratum are all available on NCREE's website.

Most studies of site effect for earthquake ground motion are based on soil properties of the upper 30-m layer. In the 1997 UBC and 1997 NEHRP provisions in the USA, the average of the shear wave velocity for the top 30-m layer of soils is used as an index for the site classification. In the site classification of Taiwan free-field strong-motion stations, the site conditions were classified as class B (rock), class C (soft rock or very dense soil), class D (stiff soil), and class E (soft soil) according to the geological age, rock type, and the average SPT-N values for the upper 30-m layer of the stratum. With detailed subsurface soil profile and quantitative soil properties (SPT-N values and wave velocities) on a station site, the site effect of ground motions can be analyzed easily for a certain class of site conditions. Engineers may evaluate appropriate peak ground acceleration for the earthquake-resistant design of structures. According to the Classification Code of average shear wave velocity on the top 30-m soil layer (Table 2), the 37 seismic stations investigated in 2009, can then be classified. The classification is shown in Table 3.

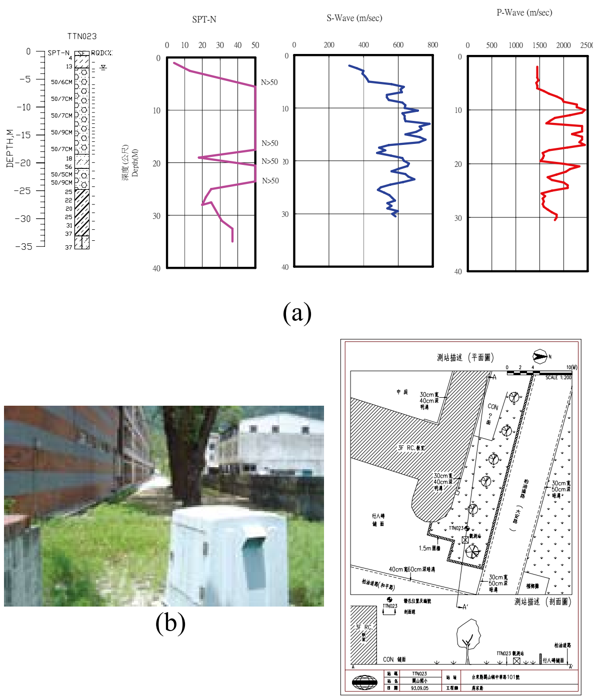

Figure 5. The information for station TTN023 in the database shown on NCREE's website.
(a) The soil profile, SPT-N value, and wave velocity profile.
(b) The photo of the seismic station in the field.
(c) The description of the plan section and the cross-section in the field.

Table 2. The shear wave velocity for the top 30m classification code (1997 UBC and NEHRP provisions).

Classification	The average of the shear wave velocity for the top 30m (V_{30})
A	$V_{30} \geq$ 1500m/sec
B	760m/sec $\leq V_{30} <$ 1500 m/sec
C	360m/sec $\leq V_{30} <$ 760m/sec
D	180m/sec $\leq V_{30} <$ 360m/sec
E	$V_{30} <$ 180m/sec

Table 3. The classification of 30 seismic stations which were investigated in 2009.

Sta. Code	Classification	Sta. Code	Classification
HWA001	C	HWA047	C
HWA006	C	HWA049	C
HWA008	D	HWA053	B
HWA010	D	HWA062	C
HWA011	C	ILA051	C
HWA013	D	TTN001	C
HWA016	C	TTN002	C
HWA019	C	TTN003	C
HWA020	C	TTN011	C
HWA025	C	TTN016	B
HWA030	C	TTN028	C
HWA031	C	TTN031	C
HWA035	C	TTN032	B
HWA036	C	TTN033	C
HWA037	C	TTN034	C
HWA041	C	TTN043	C
HWA043	C	TTN045	C
HWA044	C	TTN046	C
HWA045	C		

Conclusions

The site investigation at 448 TSMIP stations was completed by NCREE in cooperation with Taiwan's CWB. By sampling of soils in the borehole and using the Suspension P-S Logger Technique, specific geological and geotechnical data were obtained including soil profile, physical properties of soils, and wave velocities of the stratum. All the results of investigation were organized systematically in the database and made available in a preliminary web site. This project will be performed continuously in the following years. Combining with GIS techniques, the engineering geological database for strong motion stations in Taiwan will be more convenient for web usage. If an engineering project site is close to the strong-motion station, engineers may retrieve the geological and geotechnical properties of soils from the database to evaluate the site's ground response. Thus, this database is helpful for site effect analysis and earthquake-resistant design.

References

Kuo, C. H., D. S. Cheng, H. H. Hsieh, T. M. Chang, H. J. Chiang, C. M. Lin, and K. L. Wen (2009). "Comparison of three different methods in investigating shallow shear wave velocity structures in Ilan, Taiwan", Soil Dynamics and Earthquake Engineering. 29(1), 133-143.

Kuo, C. H., Wen, K. L., Hsieh, H. H., "Evaluating Vs30 assessors via borehole data in Taipei" Proceedings of the 2008 Taiwan-Japan Symposium on the Advancement of Urban Earthquake Hazard Mitigation Technology, pp.89-92, Taiwan, 2008.

http://geo.ncree.org.tw

Development and Application of Nonlinear Structural Analysis Platform

Yi-Jer Yu [1] , Ming-Chieh Chuang [2] and Keh-Chyuan Tsai [3]

游宜哲 [1]、莊明介 [2]、蔡克銓 [3]

Abstract

The development and applications of nonlinear structural analysis program PISA3D in this year include the following: (1) Analytical simulations of seismic steel jacketing RC bridge columns, (2) Participation in the 2009 E-Defense blind analysis contest, (3) Analytical studies of a full-scale steel building shaken to collapse, and (4) Development of the PISA4SB for applications in Taiwan school building seismic retrofit program.

Keywords: PISA3D, nonlinear analysis, PISA4SB

Analytical Simulations of RC columns

Fig. 1 Test setup for column specimens

Fig. 2. Specimen BMRL100 after test

Lin and Tsai (2009) investigated the use of external steel jacketing for seismic retrofit of non-ductile reinforced concrete (RC) bridge columns to prevent lap splice failure (Tsai and Lin, 2002). Three 1/2.5-scale specimens (Fig. 1) including a non-retrofitted specimen BMRL100 (Fig. 2) and two retrofitted columns were tested under cyclic loads. The two lap splice deficient columns, SRL1 and SRL2 were retrofitted by a 6mm thick octagonal and a 3mm thick elliptical steel jackets, respectively. The effectiveness of these two types of steel jackets in improving the ductility and strength of specimens using inadequate transverse reinforcing and lap splice details were examined. Tests confirmed that the proposed octagonal steel jacketing scheme can be successfully applied to enhance the seismic flexural performance of bridge columns with insufficient transverse steel.

The Platform of Inelastic Structural Analysis for 3-D Systems (PISA3D) (Lin *et al.*, 2009) was used in the numerical simulations. The flexibility-based fibered beam-column element (Spacone *et al.*, 2009) in PISA3D was adopted to represent the RC column member. Five integration points along the fibered beam-column element were chosen to integrate the element responses. The column section consists of 32 steel fibers (one for each No. 6 reinforcing bar) and 117 concrete fibers. This column model was subjected to a constant axial load of 1,400 kN and cyclic increasing lateral displacements. In the analytical models of the two jacketed-columns, the material of all the concrete fibers is considered as confined concrete with a compressive strength of 33.35 MPa computed from Mander's rule. For the steel fibers, a bilinear material property was adopted. The post-yielding to initial stiffness ratio of 0.01 was used. Figures 3a and 3b show the comparisons between the analytical and experimental cyclic responses of SRL1 and SRL2, respectively. As shown in these two figures, the cyclic stiffness and strength can be simulated reasonably well before the 4% radians lateral drift angle is reached in each specimen. The fibered

[1] Assistant Researcher, National Center for Research on Earthquake Engineering, yjyu@ncree.org.tw.
[2] Assistant Researcher, National Center for Research on Earthquake Engineering, mcchuang@ncree.org.tw
[3] Professor, National Taiwan University, Department of Civil Engineering, kctsai@ntu.edu.tw

beam-column element in PISA3D does not consider the pinching of concrete fibers and the low cycle fatigue of the longitudinal reinforcing bars. Thus, the cyclic pinching in the 0.01 to 0.04 radians peak drift cycles and the strength degradations resulting from the low cycle fatigue fractures of the longitudinal reinforcement after 5% lateral drift angle cycle cannot be captured in these analytical models. For the analytical model of Specimen BMRL100, the material of the cover concrete fibers and inside the confined core concrete fibers were considered as unconfined and confined concrete, respectively. The compressive strength computed following Mander's suggestions is 17.46 and 21.68 MPa for unconfined and confined concrete, respectively. The strength degradation of the BMRL100 column resulted from the bond slip was simulated by adopting the "fracture material" given in Fig. 4 in PISA3D to represent the steel fiber material of the longitudinal reinforcement. The maximum stress of the steel fiber, $f_s = f_l \mu p l_s / A_b$ can be calculated. The confining stress f_l can be obtained from the static equilibrium by cutting a free-body diagram at the centerline of the cross-section and assuming the stirrups are fully yielded. However, a 60% strength reduction factor has been adopted as it is believed that the double U-shaped stirrups could not develop full yielding due to the lack of anchorage. Figure 5 shows that the fibered column model can reasonably simulate well the cyclic degrading responses of Specimen

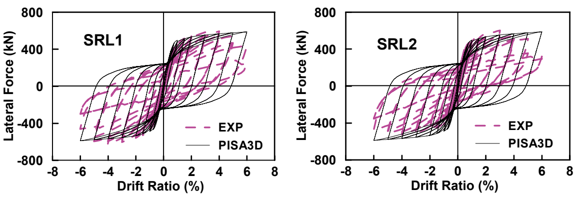

(a) (b)

Fig. 3 Comparing experimental and analytical cyclic responses: (a) Specimen SRL1, and (b) Specimen SRL2

BMRL100.

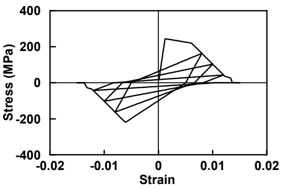

Fig. 4 Cyclic degrading stress versus strain relationships for steel fibers of BMRL100

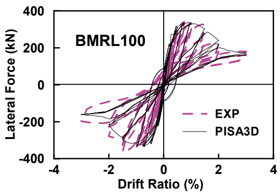

Fig. 5 Comparison between analytical and experimental cyclic responses.

Participation in E-Defense Blind Analysis Contest

Various full-scale frames were tested in Japan by the E-Defense research team using the world's largest 3-directional earthquake simulation table. In 2009, this shaking table was utilized for experimental tests of a full-scale five-story steel building with various kinds of dampers. Before the tests were executed, a blind prediction contest was held. The building used steel dampers in the first test (Fig. 6a), and viscous dampers in the second test (Fig. 6b). Tests using Japanese oil dampers, viscoelastic dampers, and no dampers, were also tested afterwards, but were not considered for the contest. One team from NCREE using the nonlinear structural analysis program OpenSEES and PISA3D was awarded the 2nd place in the 3D steel damper category, 3rd place in the 3D viscous damper category, and 3rd place in the 2D steel damper category. The analytical models of NCREE adopted a fiber beam-column element to represent the beams and columns. The frame beam member was considered as the steel and concrete composite beam. The nonlinear properties of the steel and the viscous dampers were modeled using the sub-assembly test results provided by the organizers. For further details about the blind analysis contest, please visit the website http://www.blind-analysis.jp/index_e.html.

(a) (b)

Fig. 6 Five-story steel building with (a) steel and (b) viscous dampers

Analytical Studies of a Full-Scale Steel Building Shaken to Collapse

In September 2007, the E-Defense shaking table was utilized for experimental tests of a full-scale four-story steel building shaken to collapse. Before the tests were executed, a blind prediction contest was held. Three groups of researchers from Taiwan's National Center for Research on Earthquake Engineering (NCREE) participated in the blind contest. One team used PISA3D, and submitted the 3-D and 2-D predictions. This PISA3D/NCREE team was awarded second place in the 2-D analysis research category. After the test, this four-story building was used as a case study to investigate modeling techniques for nonlinear structural responses and collapse analysis. The models for the simulation of steel hollow structural column buckling were discussed. A basic model incorporating non-degrading column elements was constructed first. Then the refinements were carried out by replacing the 1st story columns in the basic model with the degrading column elements. Two types of degrading column were considered including the fiber and hinge models, with and without the effects of axial-flexural interaction, respectively.

The Buckle material in PISA3D adopted the cyclic response rules proposed by Maison and Popov (1980) as shown in Fig. 7. Users could specify the values of control points and control slopes to adjust the hysteresis responses. The "FBC" column model adopted fibered beam-column element with a cross-section consisting of 44 fibers using the Buckle material model given in Fig. 7. Five integration points were used. In this study, the degradation characteristics in the cyclic responses obtained from the ABAQUS FE column analysis (Fig. 8) was used to calibrate the parameters of the FBC column model. Two levels of column axial loads (257 and 515 kN for corner column and center column, respectively) were chosen. At both axial force levels, the FBC column model can satisfactorily simulate the cyclic degrading responses of the ABAQUS FE model. It can be found that under the 515 kN constant axial load, the cyclic degradation of the ABAQUS FE model is more severe than in the case of 257 kN axial load. This phenomenon has been captured well by using the same set of degrading parameters in the two FBC models. Based on this finding, a refined model was constructed.

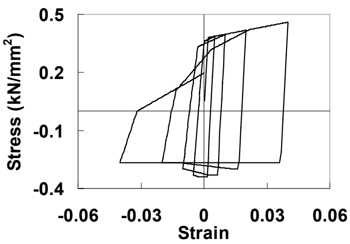

Fig. 7 The stress versus strain relationship of each fiber in the FBC model

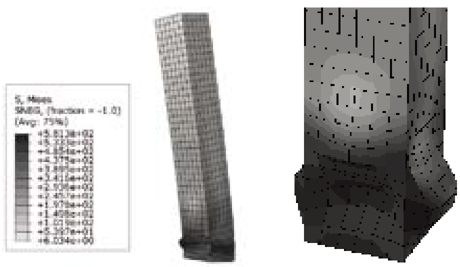
Fig. 8 Local buckling of the ABAQUS column model

The refined "FBC" frame model was constructed by replacing the 1st story columns of the basic model with the FBC model columns. Figure 9 compares the X and Y directions' 1st story drift time histories of Model FBC and test results (Tada *et al.*, 2008) under the collapse-level excitations. In both directions, the analytical results show good correspondence with the test responses. In addition, the time instant at which the inter-story drift of the analytical model reached 0.13 radian appears very close to that measured from the test (Figure 9b). It is illustrated that the refined FBC analytical model made in this study can simulate satisfactorily the collapse of the specimen.

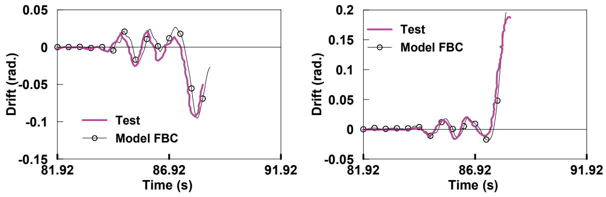

(a) X-direction (b) Y-direction

Fig. 9 First-story drift time histories

Based on the analytical and experimental studies, summaries and conclusions can be made as follows:

1. The basic frame model using bilinear hinge-model column elements have failed to predict the frame collapse time. The key reason is that the column strength degradation due to the local buckling has not been considered.
2. The ABAQUS column local buckling responses can be represented using the PISA3D fiber-model column with Buckle Material. The proposed FBC column model can conveniently incorporates the combined cyclic strength degrading effects among the varying axial loads and bi-axial bending moments. The collapse of the test frame is strongly governed by the severe local buckling of the columns in the first story. The collapse time of the test building can be simulated in the FBC frame model using this column model element. This suggests that the analytical force versus deformation relationships of the first story columns strongly affects the collapse prediction of the frame. Proper column's analytical model with reasonable degrading rules is important for the collapse simulation.

Development of the PISA4SB for Applications in Taiwan School Building Seismic Retrofit Program

According to the observations made after several major earthquakes occurred in Taiwan, school building has been found lacking of seismic resistance. The school building collapses were usually along the corridors and often caused by the short column effects, lack of lateral reinforcement and the embedded pipelines. Because school buildings could be required to serve as the emergency shelter after a strong earthquake, seismic evaluation and retrofit of school building are extremely urgent. Therefore, the National Center for Research on Earthquake Engineering (NCREE) has implemented the static pushover procedures (Chung *et al.*, 2009) for the detailed seismic evaluation of school buildings. In the static pushover procedures proposed by NCREE, the hinge properties of columns, beams, brick walls and RC walls are carefully calibrated based on the full scale experiments conducted in NCREE in the past ten years. Furthermore, in order to enhance the user friendliness, auxiliary modules in calculating the hinge properties have been developed by NCREE researchers. This could allow engineers to more accurately apply commercially available softwares. However, when the auxiliary modules are applied on commercial software, user must first define before assigning the sections to the corresponding columns, beams, brick and RC walls in the text-based files. Without the graphic user interface, errors have been found common in the cross-platform operations. In order to resolve these issues regarding the applicability to commercial software, based on PISA3D, NCREE has customized the nonlinear structural analysis program, PISA4SB (Platform of Inelastic Structural Analysis for School Buildings) specifically for the school building structures. The structural model templates (Fig. 10) are provided in the PISA4SB to allow the user to conveniently construct the analytical models (Fig. 11) for typical low-rise school buildings. After the gravity load analysis is conducted, PISA4SB automatically incorporates the column axial loads in calculating the parameters for the multi-linear degrading material properties of any plastic hinge. PISA4SB evaluates the capacity curve and computes the seismic performance point based (Fig. 12) on the given design response spectrum provided by the user for the school building's site. Any engineer can conveniently apply the PISA4SB to complete the seismic evaluation of a school building without cross-platform operations. Several applications of PISA4SB show that PISA4SB is a simple and complete solution for the static pushover procedures proposed by NCREE.

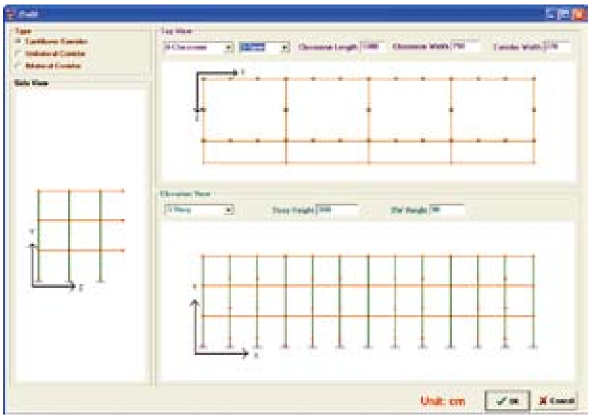

Fig. 10 The structural model templates for typical low-rise school buildings.

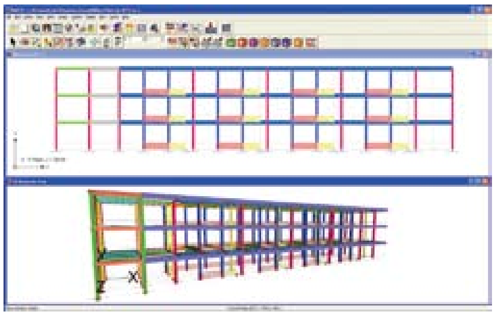

Fig. 11 The analytical model of PISA4SB

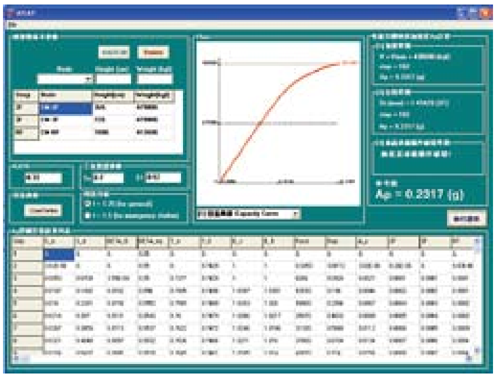

Fig. 12 PISA4SB provide the module to compute the performance point

References

Tsai, K. C., and Lin, M.L. (2002), "Steel Jacket Retrofitting of Rectangular RC Bridge Columns to Prevent Lap Splice and Shear Failures," *Report No. NCREE 02-15*, National Center for Research on Earthquake Engineering.

Lin, B. Z., Chuang, M. C. and Tsai, K. C. (2009), "Object-oriented development and application of a nonlinear structural analysis framework," *Advances in Engineering Software*, 40, pp. 66-82.

Spacone, E., Filippou, F. C., and Taucer, F. F. (1996), "Fibre beam-column model for non-linear analysis of R/C frames: part 1. formulation," *Earthquake engineering and structural dynamics*, Vol. 25. 711-725.

Maison, B. F., and Popov, E. P. (1980), "Cyclic response prediction for braced steel frames," *Journal of the Structural Division*, Vol. 106, No. 7, p.1401–p.1416.

Tada, M., Tamai, H., Ohgami, K., Kuwahara, S., and Horimoto, A. (2008), "Analytical simulation utilizing collaborative structural analysis system," *Proceeding of 14th World Conference on Earthquake Engineering*, Beijing, China.

Chung, L. L. *et al.* (2009), "Technology Handbook for Seismic Evaluation and Retrofit of School Buildings," *Report No. NCREE 09-23*, National Center for Research on Earthquake Engineering.

Preliminary Implementation and Numerical Tests of Online Updating Hybrid Simulation Method

Yuan-Sen Yang (楊元森)[1], Keh-Chyuan Tsai (蔡克銓)[2]

Abstract

This report briefly presents the progress of implementing the framework of a new method to run a hybrid simulation termed as online updating hybrid simulation. The online updating hybrid simulation is aimed to solve a problem of inconsistency when simulating dynamics of a structure with repetitive substructures, while only one of the substructures can be simulated by a physical specimen. This work is a collaborative work between the National Center for Research on Earthquake Engineering (NCREE) and the Mid-America Earthquake (MAE) Center. NCREE is planning on developing algorithms for the updating of material models used in the finite element analysis according to instantly measured data. Further details of the upcoming work will be described in the near future.

Keywords: Hybrid simulation, online updating, numerical model, optimization, neural network

Introduction

Experimental and numerical earthquake simulations are two important approaches in observing the behaviors of structures subjected to extreme earthquake loads. In addition to numerical simulation and experimental simulation, which are commonly employed approaches in earthquake engineering simulation, hybrid simulation approach is widely used as well. To simulate the dynamic response of a structure, a part of the structure (or a substructure) can be simulated by one or more physical specimens in laboratories, while the remaining part of the structure can be simulated by numerical simulation. Commonly, the numerical parts of the structure are the parts where researchers have reasonable numerical models to simulate, while the experimental parts of the structure are more unknown. As shown in Fig. 1, a hypothesis bridge structure with two short piers and two long piers was tested using hybrid simulation. Assuming the short piers would encounter more violent deformation and would go into more severe damages than the long ones while subjected to earthquakes, the behaviors of the short piers are not well known and are more difficult to simulate numerically. The two short piers were then simulated by two physical substructure specimens, while the longer piers and other components of the bridge were numerically simulated in the hypothetical hybrid simulation.

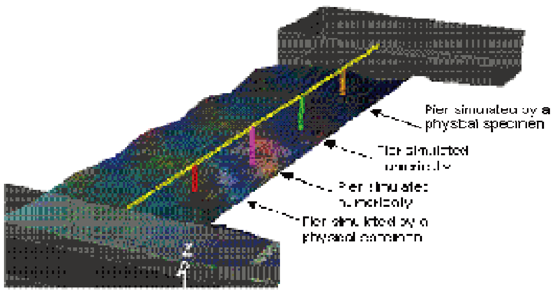

Fig. 1 A hybrid simulation with two physical substructure specimens (plotted using GISA3D [1])

In some cases, however, repetitive substructures may have inconsistent structural behaviors if identical substructures have different structural behaviors. It is not practical to construct specimens for all of these parts because of high experimental cost of multiple substructure hybrid simulation. Only one or a few substructures can be simulated experimentally in a laboratory, while the rest of them need to be numerically simulated. The difference of structural behaviors results in inconsistent responses among substructures and may lead to unconvincing structural system responses. An idea of online updating of numerical models during a hybrid simulation has been proposed by Elnashai [2] to improve the consistency among substructures in a hybrid simulation, as shown in Fig. 2. Conceptually, researchers learn more about

1 Assistant Professor, National Taipei University of Technology, ysyang@ntut.org.tw
2 Professor, National Taiwan University; Consultant of NCREE, kctsai@ntu.org.tw

the structural behaviors of the experimental substructures during the progress of the test, and have more information to tune the presumed parameters of the numerical models.

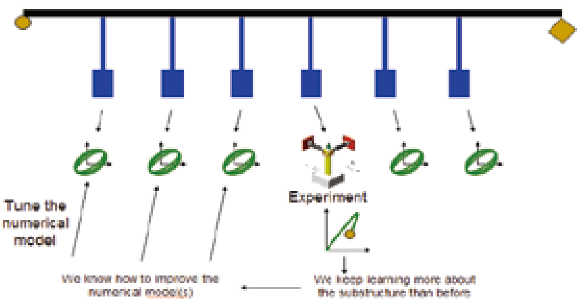

Fig. 2 An online updating hybrid simulation with one physical substructure and many roughly identical online updating numerical substructures.

Online Updating Hybrid Simulation Framework

To distinguish from an online updating hybrid simulation, a hybrid simulation [3,4] without online hybrid simulation is called conventional hybrid simulation in this paper. The flowchart of a conventional hybrid simulation is shown in Fig. 3. The time sequence of a conventional hybrid simulation in each time step is shown in Fig. 4.

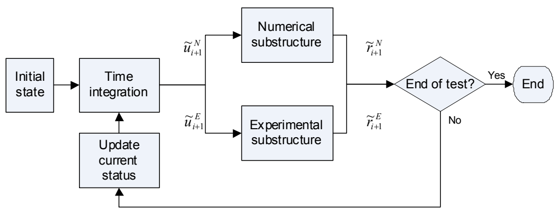

Fig. 3 Flowchart of a conventional hybrid simulation

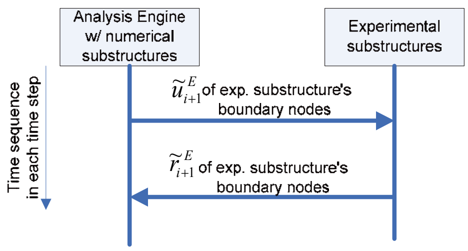

Fig. 4 Time sequence diagram of a conventional hybrid simulation in each time step

The procedure of an online updating hybrid simulation [5] is basically based on a conventional one, except that there is an additional parameter analysis module, and the original numerical substructure module is modified so that it allows updates of some of its numerical parameters (as shown in Fig. 5). Figure 6 presents the time sequence diagram of online-updating hybrid simulation in each time step.

The parameter analysis module calculates a set of parameters for the numerical model based on the experimental data. The par^N_{i+1} is a set of calculated parameters for the numerical model at time step i+1. The modified numerical substructure module updates the numerical model according to par^N_{i+1} and calculates its resisting force $\tilde{r}^N_{i+1}$ regarding the displacement $\tilde{u}^N_{i+1}$. Online updating hybrid simulation is based on the following assumptions:

(1) Assumption of similarity of numerical models: It is assumed that we have a numerical model for the experimental substructure, and the numerical model is similar to that of the numerical substructure. For detailed description and formulations, please refer to [5].

(2) Assumption of small change of resisting force history: It is assumed that the change or updating of the numerical model does not lead to a significant change on their past history. For detailed description, formulations, and figures, refer to [5].

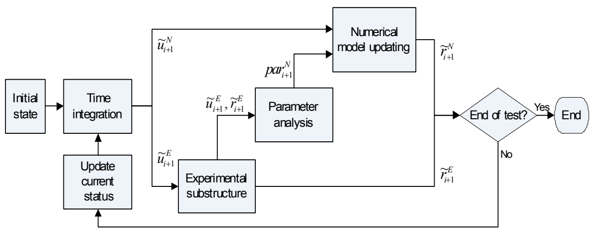

Fig. 5 Online updating hybrid simulation flowchart [1]

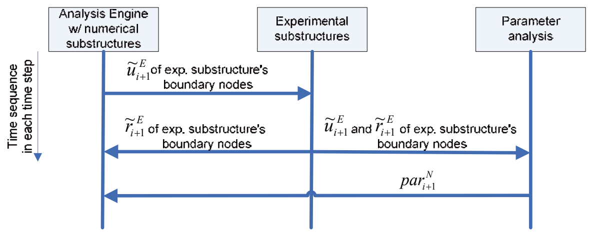

Fig. 6 Online updating hybrid simulation flowchart [1]

Preliminary Numerical Test

In this work, a bridge structure with two double-skinned concrete-filled tubular (DSCFT) piers was test using the proposed online updating hybrid simulation method. The structural design of the bridge was modified from the bridge structure used in the Taiwan-Canada transnational hybrid simulation project carried out in 2006 [6]. Both piers have height of 22.5 meters in the preliminary numerical test. Each span of deck was 40 meters, except that the left span was 45 meters, resulting in asymmetry of the structure along the x-axis. The bridge tested in this work as shown in Fig. 7 (plotted using OpenSees Navigator [7]), was subjected to the ground motion of Chi-Chi earthquake recorded at station CHY024. The ISEEdb system [8,9] with OpenSees numerical simulation tool [10] was employed in the tests. Forty-two seconds of trilateral ground motion (including north-south, east-west and vertical directions) was inputted. The time increment was set to 0.02. There were 2,100 time steps in each simulation. Classical Rayleigh's damping ratio was set to 3% based on a preliminary modal analysis showing the first two natural periods which were 1.7s and 1s, respectively.

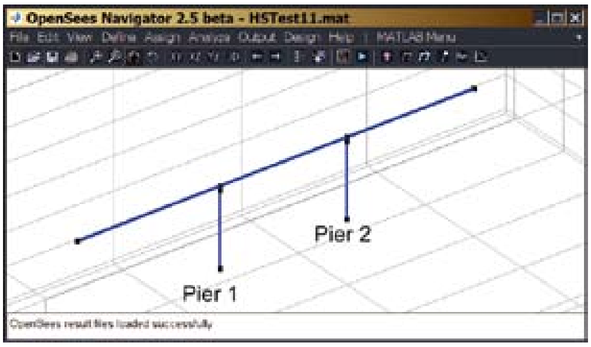

Fig. 7 Bridge structure tested in this work

In this work, no physical tests were done. To test the proposed online updating hybrid simulation method, all hybrid simulations were simulated numerically. The structure and sub-structure piers were simulated numerically, including the sub-structure referring to a physical experimental pier. The physical experimental substructure was simulated by a sophisticated numerical model, a fiber-sectioned beam-column element. The numerical substructure was simulated by a bilinear model composed of a linear beam-column element with bilinear rotational bilateral rotational springs.

The numerical test includes the following analysis cases:

(1) Case A: This case of analysis simulated the conventional hybrid simulation. The Pier 1 was simulated by a sophisticated numerical model, representing its physical behavior. The Pier 2 was simulated by a bilinear model, representing a numerical model, which is mostly simpler than its physical behavior, in a conventional hybrid simulation. It should be noted that, the sophisticated model was used to represent the physical model only because the physical behavior of a substructure is often more complicated than a numerical model. It is not consequent though that the sophisticated model is a more accurate model to simulate the substructure.

(2) Case B: The analysis Case B simulated an online updating hybrid simulation. Same as the Case A, Pier 1, representing the physical substructure, was simulated by a sophisticated model. Pier 2 was simulated by a bilinear model which bilinear parameters may be updated by the proposed method. This analysis case represents the usage of the proposed online updating hybrid simulation method.

(3) Case C: This case simulated the actual dynamic response of the bridge system subjected to the aforementioned ground motion. Both piers in this case were simulated by a sophisticated model.

The material properties of the fiber-section model were based on the concrete and steel material tests done in the aforementioned transnational experiment. The bilinear model of the DSCFT pier was based on the mechanical behaviors introduced in [11]. The optimization method adopted in the preliminary test was a Simplex method [12] implemented in MATLAB [13].

Figure 8 shows the first 9 seconds of the displacement responses along x-axis (***Ux***) at the top of the Pier 1. The ***Ux*** on both tops of the piers were about the same due to the high axial stiffness of the deck. It can be seen that, the Case B, which employed the proposed online updating hybrid simulation method, is closer to the Case C. It is because the initial stiffness of the bilinear model of the Pier 2 was updated according to the Pier 1's responses in the first few seconds of the simulation. The drift ratio of the ***Ux*** peak around the 9th second was about 1.8% toward (-x)-direction, which is the maximum peak of the displacement histories over the simulation.

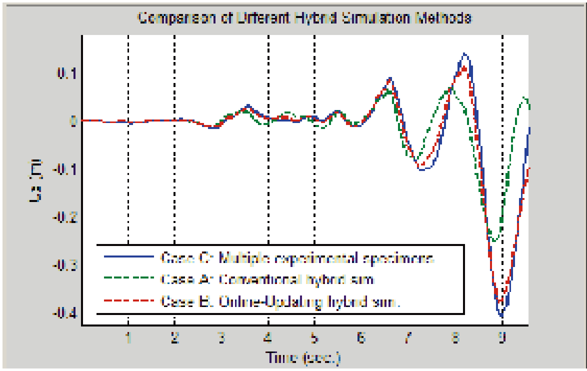

Fig. 8 The ***Ux*** responses before the maximum peak

The online updating hybrid simulation, however, did not perfectly match the Case C result. After the maximum peak at the 9th second, as shown in Fig. 9, the case B result did not catch well the response of the Case C, yet it is still generally better than the Case A (conventional hybrid simulation method). It should be noted that Case B and Case C used different numerical models for the Pier 2. Certain differences of the responses can be expected if different numerical models were used.

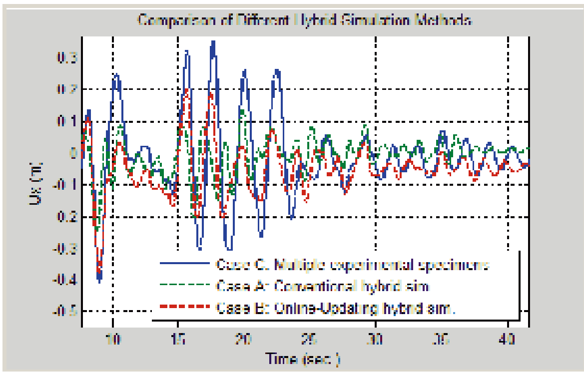

Fig. 9 The ***Ux*** responses after the maximal peak

The differences between the Cases B and C can be seen by comparing their hysteresis loops. Figures 10 and 11 show the ***Ux-Fx*** hysteresis loops of the Pier 2 in the Cases B and C, respectively. It can be seen that the bilinear model dissipated much energy in the case B than the fiber-section model did in the Case C, even if the initial stiffness of the bilinear model was updated at the very beginning of the simulation of the Case B. This may be the reason that the response in the Case B decayed significantly after the ***Ux*** peak.

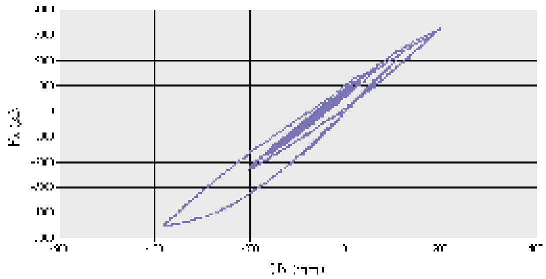

Fig. 10 Hysteresis loop of the fiber-section model

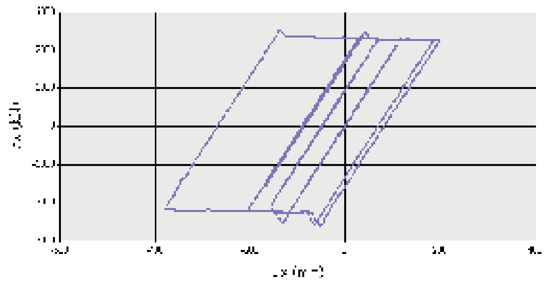

Fig. 11 Hysteresis loop of the bilinear model

Summary

This work introduced the initial implementation of the proposed online updating hybrid simulation method and carried a set of numerical tests. Three simulation cases were carried out. The Case A represented a hybrid simulation using a conventional method; the Case B represented the usage of the proposed online updating hybrid simulation, while the Case C represents a complete experimental result. It is shown that the online updating method performed better than the conventional hybrid simulation in the conducted tests.

Moreover, this paper presents the progress of the research work on online updating hybrid simulation method. At present, this method is not yet mature and reliable enough to be employed to any real hybrid simulation. More examples are needed in the near future to verify the accuracy and reliability of the online updating method. In addition, there are still many technical issues to discuss, such as discussion on the changes of kinematic energy and strain energy after material parameters are updated, and the rationality of the changes of the material parameters during the hybrid simulation.

References

1. Lin, B. Z., Chuang, M. C., Tsai, K. C. 2009. “Object-oriented Development and Application of a Nonlinear Structural Analysis Framework,” Advances on Engineering Software, Vol. 40, No. 1, pp. 68-82.
2. Elanshai, A. S. 2008. Personal communication.
3. Takanashi, K., Nakashima, M. 1987. “Japanese activities on on-line testing,” Journal of Engineering Mechanics, ASCE, 113(7), 1014-1032.
4. Mahin, S.A., Shing, P.B., Thewalt, C.R., Hanson, R.D. 1989. “Pseudodynamic test method - Current status and future direction,” Journal of Structural Engineering, ASCE, 115(8), 2113-2128.
5. Yang, Y.S., Tsai, K.C., Elnashai, A.S., Kwon, O.S., Lin, S.L. (2009). “Preliminary Study on Online Updating Hybrid Simulation,” NCREE Report 09-001. National Center for Research on Earthquake Engineering, Taipei, Taiwan.
6. Tsai, K. C., Yang, Y. S., Wang, K. J., Wang, S. J., Lin, M. L., Weng, Y. T., Chen, P. C., Cheng, W. C., Chuang, M. C., Lin, B. Z., Lau, D. T. and Chang, Y. Y. 2007. "Network Platform for Structural Experiment and Analysis (II): Taiwan-Canada Collaborative Pseudo-Dynamic Experiment” Technical report NCREE 07-018, National Center for Research on Earthquake Engineering, Taipei, Taiwan.
7. Schellenberg, A., Yang, T. (2007). “OpenSees Navigator,” available at http://peer.berkeley.edu/OpenSeesNavigator/.
8. Yang, Y.S., Hsieh, S.H., Tsai, K.C., Wang, S.J., Wang, K.J., Cheng, W.C., Hsu, C.W. 2007. “ISEE: Internet-based simulation for earthquake engineering Part I: database approach,” Earthquake Engineering and Structural Dynamics, 36(12), 2291-2306.
9. Wang, K.J., Tsai, K.C., Wang, S.J., Cheng, W.C., Yang, Y.S. 2007. “ISEE: Internet-based simulation for earthquake engineering Part II: the application protocol approach,” Earthquake Engineering and Structural Dynamics, 36(12), 2307-2323.
10. Pacific Earthquake Engineering Research Center, “Open System for Earthquake Engineering,” OpenSees Web Page, available: http://opensees.berkeley.edu/
11. Lin, M. L., Tsai, K. C. 2003. “Mechanical Behavior of Double-skinned Composite Steel Tubular Columns,” Proceedings of the Joint NCREE-JRC Conference, National Center for Research on Earthquake Engineering, Taipei, Taiwan.
12. Lagarias, J. C., Reeds, J. A., Wright, M. H., Wright, P. E. 1998. "Convergence Properties of the Nelder-Mead Simplex Method in Low Dimensions," SIAM Journal of Optimization, Vol. 9 Number 1, pp. 112-147.
13. Mathworks, Inc. “MATLAB and Simulink for Technical Computing,” a web page available at http://www.mathworks.com/

A Strain Field Measurement Method for Surfaces with Out-of-plane Deformations

Yuan-Sen Yang [1] , Chang-Wei Huang [2] , Bei-Ting Chen[3] , Chiun-lin Wu[4]

楊元森 [1]、黃仲偉 [2]、陳北亭 [3]、吳俊霖 [4]

Abstract

This paper presents the progress of a follow-up development of the ImPro Strain, an image-based surface strain field measurement system. The ImPro Strain assumes that the measurement regions are planes. In this work, an alternative surface deformation measurement method is prototyped so that it is also suitable to measure out-of-plane deformation. The photography hardware is based on commodity digital cameras and their accessories. The software prototyped in this work is based on open source toolkits. Image template matching is performed on image pairs taken by a dual-camera facility. Four-node finite element shape functions are adopted for image reconstruction during sub-image template matching to decrease the geometric distortion induced by the viewing angle differences between two cameras.

To evaluate the accuracy of this system, a set of zero-strain tests are carried, and the photos of an RC-wall experiment performed and a steel braced frame are used in this work. The results show that this system is capable to capture out-of-plane deformation and its strain fields.

Keywords: Digital image-based measurement, dual-camera system, image reconstruction

Introduction

Deformation measurement is an important work in most of the structural experiments. A strain gauge provides a straightforward and accuracy approach to measure single point strain, and has been widely employed in earthquake engineering experiments. In addition to strain gauges, remote measurement technologies, such as image-based measurement, have also been commonly employed by a wide range of experiments in automobile industry, military industry, and medical discipline, *etc*. By using high quality industrial digital cameras or similar optical sensors with accessorial software, measurement systems acquire images and calculate movements and/or deformations of objects. Several commercial products have been available in the market. However, commercial systems are expensive that may hinder wide practical applications in civil engineering industry. In addition, most of the systems are encapsulated and do not provide their software modules or software development toolkits, so that it is not easy for researchers to modify their functionalities or customize them to meet different requirements for various experiments. In addition to purchase encapsulated facilities, it is important as well to employ the image-based measurement techniques, software toolkits, and relative knowledge for wider applications on not only earthquake engineering experiments but also on future widely deployed, low-cost and reliable structural health monitoring.

This center has been employing state-of-the-art image-based measurement technology since the first large-scale dynamic RC collapse experiments in 2005. A MATLAB-based software, named ImPro, was developed to measure 2-D dynamic displacement histories of specimens being tested on a shake table. A system named ImPro Strain [1], extended from the ImPro aforementioned, was then developed to

[1] Assistant Professor, National Taipei University of Technology, ysyang@ntut.edu.tw
[2] Assistant Professor, Chung-Yuan University
[3] PhD Student, Chung-Yuan University
[4] Associate Research Fellow, National Center for Research on Earthquake Engineering

measure 2-D displacements and strain fields of specimen plane regions in static tests.

Prototyped Method and System

This work prototyped an alternative method to measure surface strain fields through image-based measurement. Similar to the ImPro Strain, this system uses dual-camera calibration and stereo triangulation for 3-D positioning. With random spray patterns painted on the measurement regions, displacements of any arbitrary point P in the regions can be traced by image template matching. The image template matching is to maximize the following formulation:

$$C(\mathbf{D}) = \frac{\sum_{s\in S, s'\in S'} [G_0(s)G_d(s')]}{[\sum_{s\in S} G_0^2(s) \sum_{s'\in S'} G_d^2(s')]^{1/2}} \quad (1)$$

where the $G_0(s)$ and $G_d(s')$ are the color intensity fields around point P before and after it is moved. The s' in $G_d(s')$ which leads to a maximal C(**D**) is regarded as the point P after it is moved.

Image template matching operation may lead to inaccuracy or unexpected error when we are trying to match sub-images of photos taken by different cameras with different view angles. As shown in Fig. 1, for example, a rectangle measurement region is geometrically distorted in different ways in two cameras. Matching images or sub-images from one photo to another without considering the distortion condition lead to inaccuracy or unexpected mismatch.

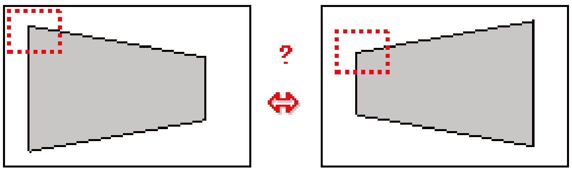

Fig. 1: Distortions from different view angles

To solve this problem, image reconstruction is performed in this work. Based on the camera calibration results, both images can be reconstructed so that they are equivalent as if they were taken from the same view angle. In the image reconstruction, four-node linear finite element iso-parametric formulations [2], as shown in Fig. 2, are employed in this work.

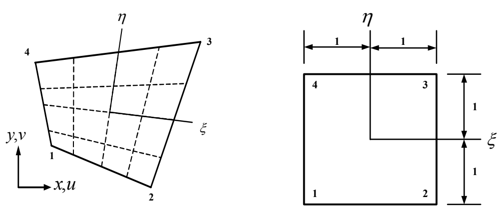

(a) x-y coord. system (b) ξ-η coord. system

Fig. 2: Four-node iso-parametric element represented in different coordinate systems

Similar to the ImPro Strain, the system prototyped in this work is written using MATLAB environment, and is based on an open source C/C++ written computer vision toolkit named OpenCV developed by Intel, Inc. [3] and a MATLAB written tool named Camera Calibration Toolbox [4]. In this work, the OpenCV is used for image template matching, while the Camera Calibration Toolbox is used for camera calibration, image reconstruction, and stereo triangulation.

System Verifications

The prototyped system is verified by using photos taken in several zero-strain tests and large-scale experiments. Due to a page limit of this paper, only the application of this system to a zero-strain test, a steel braced frame experiment, and an RC-wall experiment, are shown in this paper.

Zero-strain Test

A zero-strain test is to measure the strain fields of a rigid plate with zero stress and strain. Photos of the plate with different rigid-body movement are taken. Since the plate were placed at different locations, the photos (or optical signals) taken are much different. However, it is supposed that the measured strain fields, which are calculated through a series of processes of image reconstruction, template matching and stereo triangulation, should be zero theoretically. The actual calculated strain fields in a zero-strain test are an important index of image-based measurement accuracy. Figure 3 shows the rigid plate used in the zero-strain presented in this paper. The plate was moved horizontally by 0.02mm, 0.32mm, 1.28mm, 2.56mm and 5.12mm in order, then moved vertically in the same way. Table 1 lists the measured displacements using the prototyped system. Table 2 presents the average value of measured strain fields.

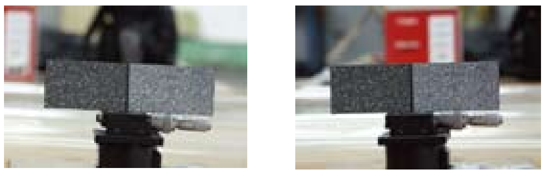

(a) Photos taken by left-hand-side camera (b) photos taken by right-hand-side camera

Fig. 3: Rigid plate in the zero-strain test

According to the zero-strain tests, it is estimated that, with 12-million-pixel Canon 450D digital cameras, the displacement measurement accuracy are 0.014mm and 0.064mm along horizontal and vertical axes, respectively. The actual physical size a pixel represents differs from locations in image, but roughly it is 0.05mm in this test. The accuracy is around 0.3 to 1 pixel. Compared to the ImPro Strain, which achieving 0.03 to 0.06 pixels, the accuracy of the prototyped approach is not very competitive. It is probably because stereo triangulation the major error source, which is diluted over the measurement region because ImPro Strain only applies triangulation at boundaries. In addition, it should be mentioned that the feature of the prototyped method in this work is its capability on out-of-plane deformation measurement, not plane strain field accuracy.

Table 1: Measured displacements

	Measurement horizontal displacements (mm) (rigid plate moved horizontally)				
Disp. (mm)	Max	Min	Average	Absolute error	Relative error
0.02	0.0214	0.0161	0.0199	0.0001	0.50%
0.32	0.3248	0.3120	0.3188	0.0012	0.38%
1.28	1.2790	1.2600	1.2691	0.0109	0.85%
2.56	2.5544	2.5367	2.5463	0.0137	0.54%
5.12	5.1259	5.1001	5.1133	0.0067	0.13%
	Measurement vertical displacements (mm) (rigid plate moved vertically)				
Disp. (mm)	Max	Min	Average	Absolute error	Relative error
0.02	0.0296	0.0177	0.0233	0.0033	16.55%
0.32	0.3278	0.3069	0.3187	0.0013	0.40%
1.28	1.2854	1.2650	1.2741	0.0059	0.46%
2.56	2.5766	2.5522	2.5623	0.0023	0.09%
5.12	5.1994	5.1700	5.1838	0.0638	1.25%

Table 2: Measured strain fields

	Measurement horizontal displacements (mm) (rigid plate moved horizontally)	
Disp. (mm)	Average strain (exx)	Average strain (eyy)
0.02	-6.1937×10^{-6}	-2.4930×10^{-5}
0.32	9.5504×10^{-6}	2.6242×10^{-5}
1.28	3.4454×10^{-5}	5.3549×10^{-5}
2.56	5.3986×10^{-5}	6.9756×10^{-5}
5.12	1.0914×10^{-4}	1.0061×10^{-4}
	Measurement vertical displacements (mm) (rigid plate moved vertically)	
Disp. (mm)	Average strain (exx)	Average strain (eyy)
0.02	-1.4186×10^{-5}	-1.6549×10^{-5}
0.32	-5.1797×10^{-5}	-3.6087×10^{-5}
1.28	-5.0911×10^{-5}	-2.2190×10^{-5}
2.56	-1.2157×10^{-5}	-5.1413×10^{-5}
5.12	-5.1600×10^{-5}	-1.2380×10^{-4}

RC-wall Experiment

The RC-wall experiment (Fig. 4(a)) was carried out at NCREE [5] and the photos taken were analyzed by ImPro Strain [1,7]. These photos are re-used in this work. Two measurement regions at two corners were selected as shown in Fig. 4(b). Figs. 5 and 6 demonstrate the measured strain fields at different stages of the experiment. The measured strain fields are close to those measured using the ImPro Strain. Because of the page limit, only a few demonstration figures are shown here. Complete image-based measurement strain fields of this experiment can be found in [6] and [7].

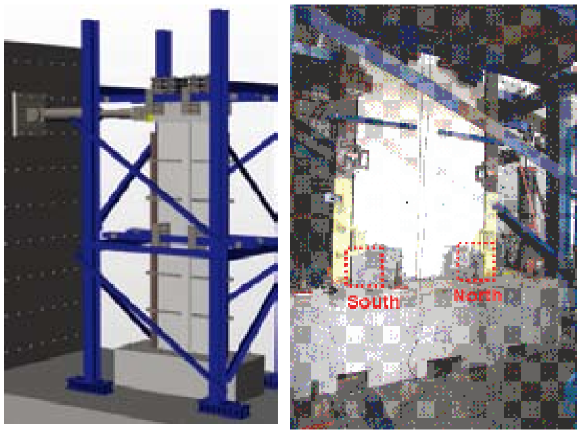

(a) RC-wall configuration [5] (b) Measurement regions [1]

Fig. 4: RC-wall experiment

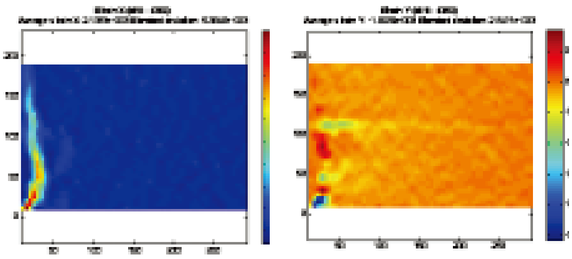

(a) Strain field exx (b) Strain field eyy

Fig. 5: Left-corner strain fields (Top Ux=91mm)

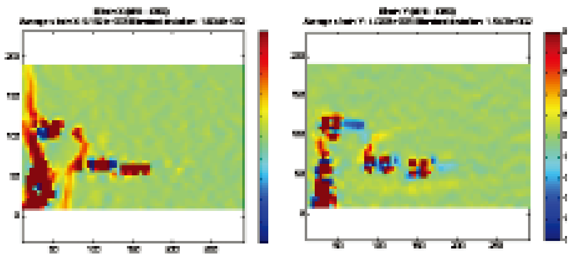

(a) Strain field exx (b) Strain field eyy

Fig. 6: Left-corner strain fields (Top Ux=183 mm)

Steel Braced Frame

A concentrically braced frame was carried at NCREE [8]. A plate connecting a brace and a gusset plate was observed by a dual-camera system as shown in Fig. 7. Out-of-plane deformation occurred to the observed plate during the experiment. Therefore, the ImPro Strain is not suitable for the measurement job. In this work the photos are used evaluate the prototyped system. The red grid in the Fig. 8 is post-processed, representing the measurement region.

Fig. 7: Steel braced frame test and camera setup

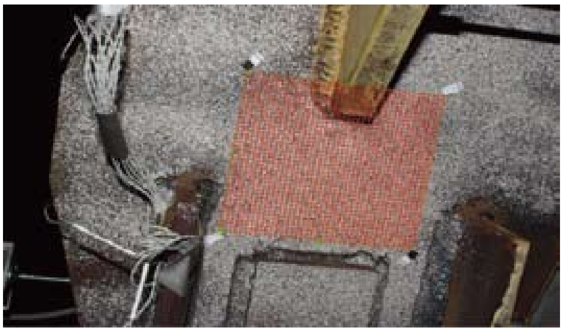

Fig. 8: A photo taken in the steel braced frame test

(Red grid is post-processed, showing measurement region)

Figures 9(a) and 9(b) show an example of the shape of the plate before and after it is deformed. Each rectangle cell in the measurement region grid is positioned through image template matching and stereo triangulation. The thorny signals at the lower-right part of the grid should be ignored as it is not what researchers are interested. These signals are thorny because the two cameras take different faces of the protruding connector, and the image pairs can not be matched. The out-of-plane deformation is observed using the prototyped method in this work. Further information of the measured data of the plate can be found in [6].

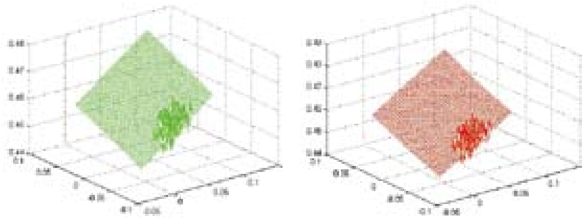

(a) Initial shape (b) Deformed shape

Fig. 9: Deformation/movement measurement plots

Summary

In this work, a surface deformation measurement method was prototyped to measure out-of-plane deformation, while the original ImPro Strain was only applicable on plane surfaces. Four-node finite element shape functions were adopted for image reconstruction during sub-image template matching to decrease the geometric distortion induced by the viewing angle differences between two cameras.

A set of zero-strain tests were carried to estimate the accuracy of the prototyped method. Although the accuracy of measurement of plane strain fields using the prototyped method is not as high as that ImPro Strain does, this method captures out-of-plane deformation which ImPro Strain can not. The photos of an RC-wall experiment performed and a steel braced frame were used in this work. The results demonstrate that this system is capable to capture both in-plane and out-of-plane deformation and their strain fields.

References

1. Yang, Y. S., Huang, C. W., Chen, B. T., & Wu, C. L. (2008). “Image-based Surface Strain Field Measurement of a Post-Tensioned RC-Wall Cyclic Test,” *Eleventh East Asia-Pacific Conference on Structural Engineering & Construction* (EASEC-11), Taipei, Taiwan, November, 2008.
2. Zienkiewicz, O. C. & Taylor, R. L. (2005). *The Finite Element Method for Solid and Structural Mechanics 6 Ed.*, Elsevier, UK.
3. Intel Corp. "Open source computer vision library,” Web page: http://www.intel.com/research/mrl/research/opencv
4. Bouguet, J. Y. (2007). "Camera calibration toolbox for MATLAB,” Web page: http://www.vision.caltech.edu/bouguetj/calib_doc/index.html
5. Chen, P. C. (2008). “International Collaborative Test on Post-tensioned RC Shear Wall,” NCREE Newsletter, 3(1), pp.6-9, 2008.
6. Chen, B. T. (2009). "Application of Digital Image Measurements in Structural Experiments," Master thesis, Chung-Yuan University, Taiwan. (in Chinese)
7. Yang, Y. S., Huang, C. W., Chen, B. T. & Wu, C. L. (2009). "Image-based Surface Strain Field Measurement of an RC-Wall Cyclic Test," NCREE Technical Report NCREE-09-002, National Center for Research on Earthquake Engineering, Taiwan.
8. Tsai, K. C., Lin, K. C., Wei, C. Y. & Lin, C. H. (2009). "Performance and Analysis of Full Scale Special Concentrically Braced Frames," NCREE Technical Report NCREE-09-010, National Center for Research on Earthquake Engineering, Taiwan. (in Chinese)

Nonlinear Analysis of Reinforced Concrete Structures by VFIFE Method

Chung-Yue Wang [1] Ren-Zuo Wang [2] and Ling-Yuan Chang [3]

王仲宇 王仁佐 張鈴菀

Abstract

A novel motion analysis method, the so-called vector form intrinsic finite element (VFIFE) method, was used to simulate the nonlinear behavior of reinforced concrete structures. Two-dimensional solid finite elements were used to model the concrete, and truss elements were adopted to model the steel reinforcements. An equivalent uniaxial strain model that can characterize the nonlinear monotonic loading behavior of concrete material by Darwin and Pecknold was adopted. The investigation first considered the development of a consistent material model that matches the analytical model made by Darwin and Pecknold. In the second part, the results of VFIFE method were compared with experimental results for the behavior of concrete under monotonic, uniaxial and biaxial loadings. Numerical examples demonstrated that the nonlinear responses of RC structures can be analyzed effectively by the proposed equivalent uniaxial strain model of concrete in two-dimensional solid finite elements and truss elements.

Keywords：vector form intrinsic finite element, reinforced concrete structure, equivalent uniaxial strain model

Introduction

Reinforced concrete is one of the most widely used modern building materials. To improve the mechanical properties of high-strength concrete, reactive powder are commonly used to satisfy criteria of safety, durability, and serviceability. In order to ensure the serviceability requirement, it is necessary to predict the deflections of RC structures under service loads.

A novel motion analysis method, the so-called vector form intrinsic finite element (VFIFE) method is utilized in this study. Two-dimensional solid finite elements were adapted to model concrete. The truss elements were adopted to model the steel reinforcements. Both models were used to simulate the nonlinear responses of reinforced concrete structures.

Fundamentals of the V-5 method of 2D solid element

Basic assumptions

Basic assumptions in the VFIFE method are:

1. In a path element, deformation of the structural element is small. The internal nodal force shall have small deformation and large displacement.
2. In a path element, geometrical change of the internal nodal force can be neglected.

In the spatial point, basic assumptions in the VFIFE method are:

1. The deformation of the structural element to approximate uniform deformation.
2. The displacement interpolation functions in element are adopted.
3. The element mesh is continuum.

Motion analysis of the basic steps

The position and the geometry of the structure member are described by a set of mass particles. At a time t ($t_a \le t \le t_b$), the equation of motion for a mass particle can be established by using of Newton's 2nd law of motion,

$$m\ddot{\mathbf{d}} = \mathbf{P} + \sum_{i=1}^{n}\mathbf{p}_i - \sum_{i=1}^{n}\mathbf{f}_i,\ t_a \le t \le t_b \qquad (1)$$

The displacement vector d is mathematically expressed as,

$$\mathbf{d} = \mathbf{x}(t) - \mathbf{x}_a = \begin{Bmatrix} x(t)-x(t_a) \\ y(t)-y(t_a) \end{Bmatrix} \qquad (2)$$

---

[1] Professor, National Central University, Department of Civil Engineering, cywang@ncu.edu.tw.

[2] Associate Research Fellow, National Center for Research on Earthquake Engineering, rzwang@ncree.org.tw.

[3] Master, National Central University, Department of Civil Engineering, clw721130@pchome.com.tw.

$\mathbf{x}_a$ is the displacement vector of mass particle at time t_a .

In this project, a 3-node plane element was adopted. $\mathbf{x}_\alpha(t)$ $\alpha = 1,2,3$ are the node displacement vectors of the element. The nodal deformation can be calculated as follows:

Step 1: Estimate the rigid body displacement and rotation.

Step 2: Let the element have a reversed rigid body motion from time t to t_a. Comparing the geometry at time t and the geometry at time t_a, the element of the deformation can be calculated.

Then, the deformation coordinates $(\hat{x}, \hat{y})$ is defined. The deformation of 2D solid elements in an arbitrary point is:

$$\hat{u} = N_2\hat{u}_2 + N_3\hat{u}_3 \quad (3)$$

$$\hat{v} = N_3\hat{v}_3 \quad (4)$$

$$N_i = \frac{1}{\alpha_1}(\beta_i\hat{x} + \gamma_i\hat{y}), \quad i = 2,3 \quad (5)$$

Where N_i is a shape deformation function in the deformation coordinates. The strain-stress relation of deformation solid is:

$$\hat{\boldsymbol{\varepsilon}} = \mathbf{D}_f\hat{\mathbf{u}} = \mathbf{B}\hat{\mathbf{u}}_n^* \quad (6)$$

$$\hat{\boldsymbol{\sigma}} = \mathbf{E}_a\mathbf{B}\hat{\mathbf{u}}_n^* \quad (7)$$

From the notion that external virtual work is equal to internal virtual work, we can compute the internal forces:

$$\hat{\mathbf{f}}_a^* = d_a\int_{A_a}\mathbf{B}^T\hat{\boldsymbol{\sigma}}_a dA_a \quad (8)$$

Equation (8) gives three nodal forces corresponding to the relative motion of the element. The other force components corresponding to the total element motion can be found from the force equilibrium conditions of the element.

The Constitutive Model of Concrete and Steel

In this study, the stress-strain relationship of concrete was adopted incrementally for the orthotropic material in VFIFE Method. This relationship was built in the principal direction. In addition, the principal stress direction is equal to the principal strain direction. Then, the constitutive model of concrete can be computed from the following expressions:

$$\Delta\boldsymbol{\sigma} = \mathbf{D}\Delta\boldsymbol{\varepsilon}$$

$$= \frac{1}{1-\nu^2}\begin{bmatrix} E_1 & \nu\sqrt{E_1E_2} & 0 \\ \nu\sqrt{E_1E_2} & E_2 & 0 \\ 0 & 0 & (1-\nu^2)G \end{bmatrix}\begin{Bmatrix} d\varepsilon_1 \\ d\varepsilon_2 \\ d\gamma_{12} \end{Bmatrix} \quad (9)$$

Where E_1 、E_2 and ν are stress-dependent material properties, where material axes 1 and 2 coincide with the current principal stress axes, and G is the shear modulus of the material.

The shear modulus G can be established by the following equation based on an assumption that there is no particular direction,

$$(1-\nu^2)G = \frac{1}{4}(E_1 + E_2 - 2\nu\sqrt{E_1E_2}) \quad (10)$$

Basic assumption of equivalent uniaxial strain

The concept of "equivalent uniaxial strain" was developed in order to keep track of the degradation of stiffness and strength of plain concrete and allow actual biaxial stress-strain curve to be duplicated from "uniaxial" curves.

$$\begin{Bmatrix} d\sigma_1 \\ d\sigma_2 \\ d\tau_{12} \end{Bmatrix} = \begin{bmatrix} E_1 & 0 & 0 \\ 0 & E_2 & 0 \\ 0 & 0 & G \end{bmatrix}\begin{Bmatrix} d\varepsilon_{1u} \\ d\varepsilon_{2u} \\ d\gamma_{12} \end{Bmatrix} \quad (11)$$

In which,

$$d\varepsilon_{1u} = \frac{1}{1-\nu^2}(d\varepsilon_1 + \nu\sqrt{E_2/E_1}d\varepsilon_2) \quad (12)$$

$$d\varepsilon_{2u} = \frac{1}{1-\nu^2}(\nu\sqrt{E_1/E_2}d\varepsilon_1 + d\varepsilon_2) \quad (13)$$

The curves selected for compressive loading were based on an equation suggested by Saenz (see Fig. 1)

$$\sigma_i = \frac{E_0\varepsilon_{iu}}{1 + \left(\frac{E_0}{E_s} - 2\right)\left(\frac{\varepsilon_{iu}}{\varepsilon_{ic}}\right) + \left(\frac{\varepsilon_{iu}}{\varepsilon_{ic}}\right)^2} \quad (14)$$

In which,

$$E_i = \frac{d\sigma_i}{d\varepsilon_{iu}} \quad (15)$$

where E_0 is the tangent modulus of the initial part of the ascending branch; E_s is the secant modulus which corresponds to the maximum compression stress σ_{ic} and the equivalent uniaxial strain ε_{ic} at the peak unaxial stress.

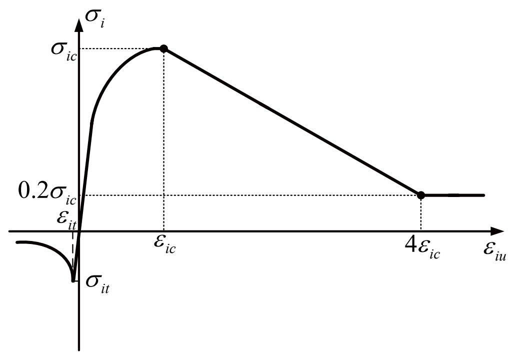

Fig 1. Equivalent uniaxial strain stress-strain curve

The equivalent uniaxial strain stress-strain curve can be computed from the following three steps:

Step 1. Determination of σ_{ic} and σ_{it}

The classification of constitutive relationships must be guided by an interactive failure criterion for concrete. Various proposals have been made to describe the failure strength characteristics of concrete. Among these proposals, the most popular is Kupfer's failure surface (Kupfer and Gerstle, 1973) which provides the biaxial strength of concrete under compression-compression, tension-compression and tension-tension as follows:

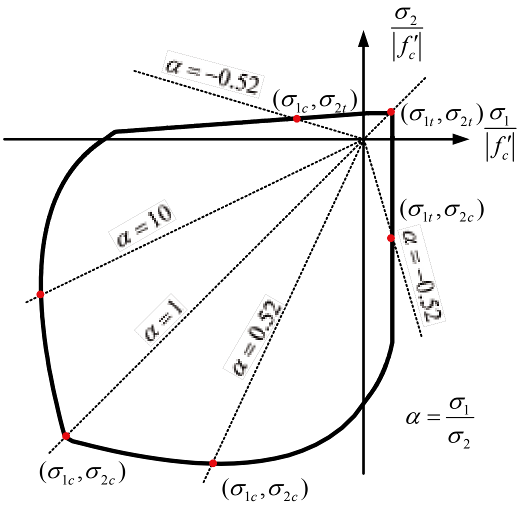

Fig 2. Biaxial strength envelope

(1) In the compression – compression stress space:

$$\sigma_{2c} = \frac{(1+3.65\alpha)}{(1+\alpha)^2} f_c', \quad \sigma_{1c} = \alpha\sigma_{2c} \tag{16}$$

(2) In the tension-compression stress space:

$$\sigma_{1t} = (1-0.8\frac{\sigma_2}{f_c'}) f_t', \sigma_{2c} = \frac{(1+3.28\alpha)}{(1+\alpha)^2} f_c' \tag{17}$$

(3) In the tension–tension stress space:

$$\sigma_{1t} = f_t', \sigma_{2t} = f_t' \tag{18}$$

Wherein f_c' is the compressive strength of cylinder specimen; α is the ratio of principal stresses; σ_{ic} is the maximum compressive stress; σ_{it} is the maximum tensile stress; $1c$, $2c$ and $f'c$ are negative for compression.

Step 2. Determination of ε_{ic}

When $|\sigma_{ic}| \geq |f_c'|$

$$\varepsilon_{ic} = \varepsilon_p \left[3\left(\frac{\sigma_{ic}}{f_c'}\right) - 2 \right] \tag{19}$$

When $|\sigma_{ic}| < |f_c'|$

$$\varepsilon_{ic} = \varepsilon_{cu}\left(-1.6\left(\frac{\sigma_{ic}}{f_c'}\right)^3\right) + \varepsilon_{cu}\left(2.25\left(\frac{\sigma_{ic}}{f_c'}\right)^2\right) + \varepsilon_{cu}\left(0.35\left(\frac{\sigma_{ic}}{f_c'}\right)\right) \tag{20}$$

Where ε_{cu} is the strain at peak stress for the real uniaxial curve.

Step 3. Determination of Poisson's Ratio ν

$$\nu = 0.2 \tag{21}$$

Equation (21) is adopted in compressive-compressive and tension-tension conditions.

$$\nu = 0.2 + 0.6(\frac{\sigma_2}{f_c'})^4 + 0.4(\frac{\sigma_1}{\sigma_{1t}})^4 \tag{22}$$

$$\nu \leq 0.99$$

Equation (22) is adopted in uniaxial compressive and tension- compressive conditions.

Due to the steel reinforcing bars, RC structures can carry tension and compression forces. In structural analysis, the truss element is the simplest form of structural elements. It is used to model the steel reinforcements in RC structures. In this study, the concrete and reinforcing bars were represented by different material model. These models are combined together with a model for the interaction between reinforcing bar and concrete through perfect bond in describing the behavior of the composite reinforced concrete material.

To account for the bond-slip effect between concrete and reinforcement, an elastic-plastic model of reinforcement is proposed for the numerical simulation (see Fig. 3).

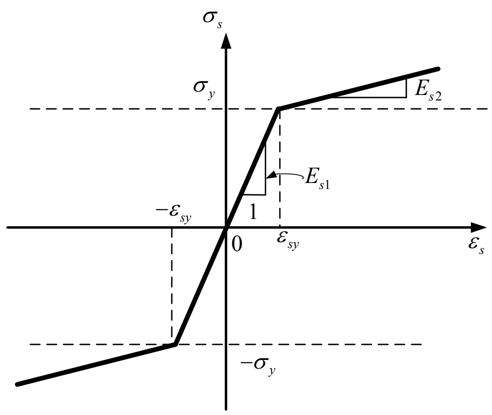

Fig 3. Steel stress-strain relation

If the reinforcing steel is subjected to tension stress behavior:

when $\varepsilon_s \leq \varepsilon_{sy}$, adopt $E_s = E_{s1} = E_{s0}$

when $\varepsilon_s > \varepsilon_{sy}$, adopt $E_s = E_{s2} = 0.01E_{s0}$

where E_{s0} is the initial modulus of a steel reinforcement; and ε_{sy} is yielding strain of a steel reinforcement, $\varepsilon_{sy} = \sigma_y / E_{s0}$.

If the reinforcing steel is subjected to compression stress behavior:

when $\varepsilon_s \geq -\varepsilon_{sy}$, adopt $E_s = E_{s1} = E_{s0}$

when $\varepsilon_s < -\varepsilon_{sy}$, adopt $E_s = E_{s2} = 0.01E_{s0}$

Numerical Examples

In this study, two numerical examples are presented to demonstrate both the capability and the accuracy of the VFIFE method in a nonlinear dynamic analysis of RC structures. The first example correlates the experiment result (Burns), analysis result (Barzegar) and result of the numerical simulations by VFIFE method (see Fig. 4).

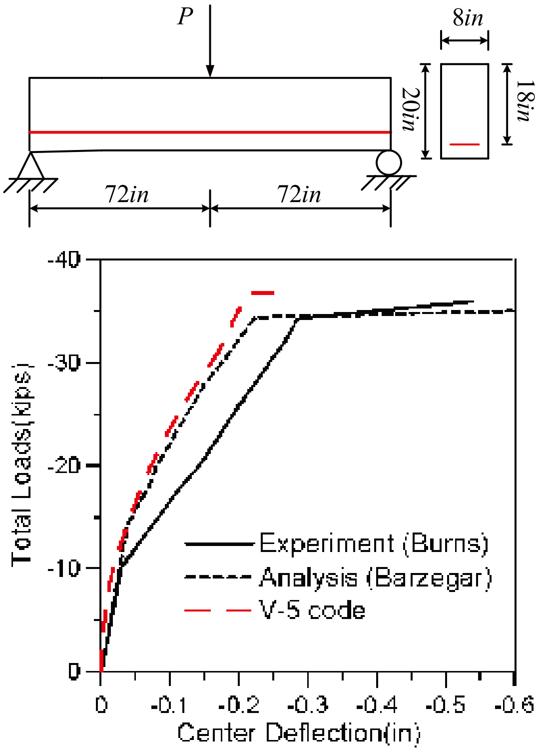

Fig 4. Comparing the results of the numerical simulations and experimental response on force displacement curve.

Compressive strength of concrete cylinder specimen $f'_c = -4.82 ksi$

Strain at peak stress for the real uniaxial curve $\varepsilon_{cu} = -0.0022 in/in$

Uniaxial tensile strength of concrete $f'_t = 0.482 ksi$

Elasticity modulus of concrete $E_c = 3800 ksi$

Poisson's Ratio $\upsilon = 0.2$

Mass density $\rho = 150 \,{}^{lb}\!/\!{}_{ft^3}$

Ratio of the stresses $\rho = 0.99\%$

Elasticity modulus of steel reinforcement $E_s = 29500 ksi$

Yield strength of steel reinforcement $f_y = 44.9 ksi$

The second example compares experiment result (Bresler), analysis result (Kwak) and result of the numerical simulations by VFIFE method (see Fig. 5).

Conclusions

In this project, an extension of the VFIFE approach for the nonlinear analysis of RC structure is introduced. Two examples were used to demonstrate the effectiveness of the VFIFE method in nonlinear response of RC structures by the proposed equivalent uniaxial strain model of concrete.

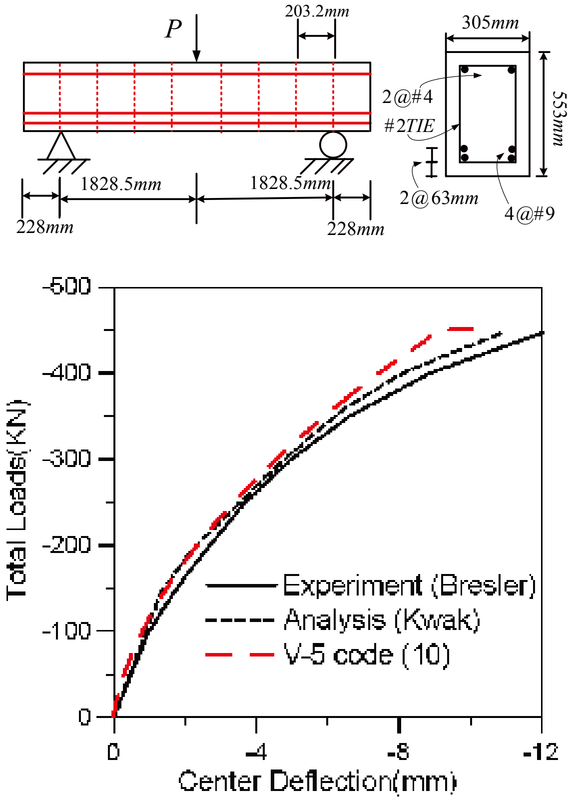

Fig 5. Comparing the results of the numerical simulations and experimental response on force displacement curve.

Compressive strength of concrete cylinder specimen $f'_c = -3.49 ksi$

Strain at peak stress for the real uniaxial curve $\varepsilon_{cu} = -0.0022 in/in.$

Uniaxial tensile strength of concrete $f'_t = 0.349 ksi$

Elasticity modulus of concrete $E_c = 3367 ksi$

Poisson's Ratio $\upsilon = 0.2$

Mass density $\rho = 150 \,{}^{lb}\!/\!{}_{ft^3}$

Ratio of the stresses $\rho = 1.53\%$

#9: $\begin{cases} \text{Elasticity modulus of steel reinforcement } E_s = 31600 ksi \\ \text{yielding strain of a steel reimforcement } f_y = 80.5 ksi \end{cases}$

#4: $\begin{cases} \text{Elasticity modulus of steel reinforcement } E_s = 29200 ksi \\ \text{yielding strain of a steel reimforcement } f_y = 50.1 ksi \end{cases}$

#2: $\begin{cases} \text{Elasticity modulus of steel reinforcement } E_s = 27500 ksi \\ \text{yielding strain of a steel reimforcement } f_y = 47.2 ksi \end{cases}$

Construction and Application of NCREE Information and Knowledge Services (II)

Kuang-Wu Chou [1], Wen-Hsiang Tu[2], Chun-Yu Lin[3], Shang-Hsien Hsieh[4], and Hsien-Tang Lin[5]

周光武 [1]、涂文祥[2]、林峻毅[3]、謝尚賢[4]、林顯堂[5]

Abstract

In order to manage and disseminate the accumulated research accomplishments of NCREE, this work developed knowledge management tools and information management systems, and improved the existing information systems to meet new requirements. An earthquake engineering knowledge retrieval system, based on this work last year (2008), was developed for dissemination of the NCREE research accomplishments. In addition, an experiment information management system integrates all the existing experiment management tools that had already developed, and offers complete services from the application of an experiment to its finish. Finally, a cooperation platform was established to help NCREE colleagues co-manage important documents and at the same time implement the information security policy of NCREE.

Keywords: information retrieval system, ontology, experiment data and flow management, experiment online application, cooperation platform

Introduction

The National Center for Research on Earthquake Engineering (NCREE) has delivered valuable research and accumulated extensive knowledge in areas such as large-scale experiments; innovative experimental technologies; seismic design, evaluation, and retrofit of structures; and seismic hazard simulation. If the knowledge gets managed, disseminated, and demonstrated effectively, it may form a strong basis of further research and may be used to solve more problems in the field of earthquake engineering. Therefore, how to manage the NCREE knowledge and promote its applications is one of the focuses of this work. Extending out the effort done in the past years, an earthquake engineering knowledge retrieval system was developed as a tool of knowledge management. Besides, this work considers that the data exploited or produced by experiments can be reused as a valuable asset of NCREE. The experiment online-application system and NCREE Data Center was thus created to manage experiment input and output data as well as the related information (Chou et al., 2008). Then the experiment flow management system (Chou et al., 2009) was developed to offer more information management services for experiments. In 2009, those experimental systems were further integrated into an experiment information management system that provides complete services during the whole life time of an experiment, from its application to finish. Finally, this work considers that raising the NCREE colleagues' working efficiency may promote both the quantity and quality of the NCREE researches. A cooperation platform was therefore established to help NCREE colleagues co-manage important documents and at the same time implement the information security policy of NCREE.

[1] Associate Technologist, National Center for Research on Earthquake Engineering, kwchou@ncree.org.tw
[2] Associate Technologist, National Center for Research on Earthquake Engineering, whtu@ncree.org.tw
[3] Assistant Technologist, National Center for Research on Earthquake Engineering, cylin@ncree.org.tw
[4] Professor, Department of Civil Engineering, National Taiwan University; Division Head, National Center for Research on Earthquake Engineering, shhsieh@ntu.edu.tw
[5] Doctor of Philosophy, Department of Civil Engineering, National Taiwan University, d93521003@ncree.org.tw

Development of Earthquake Engineering Knowledge Retrieval System

This work and Department of Civil Engineering of National Taiwan University cooperate to develop an earthquake engineering knowledge retrieval system, OntoPassage. OntoPassage is based on the earthquake engineering ontology created in 2008 and provides users with domain-specific information retrieval services differing from what are provided by general-purpose search engines like Google. As shown in Fig. 1, OntoPassage can be used in two modes: the traditional retrieval mode and the conceptual retrieval mode. The method of conceptual retrieval is the focus of this work here. It appears capable of giving more precise search result than traditional information retrieval methods (Lin, 2009).

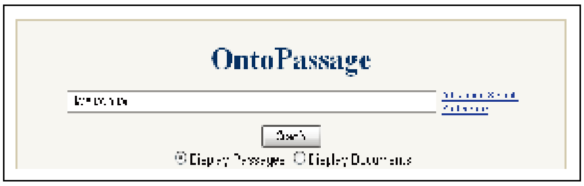

Fig. 1 Entry to the OntoPassage system

In the following, an example is given on how OntoPassage handles a query with the phrase Base Isolation under either the traditional or conceptual mode. Under selection of the traditional retrieval mode (i.e. selection of the Display Document radio button), the system found 84 related papers. The first page of the retrieved result shows top 5 papers that appear agreeing with the query (see Fig. 2). The user may choose the first paper and then review its full text as shown in Fig. 3. But users need to find the paragraph themselves in which they are interested.

With the same query and the selection of the conceptual retrieval mode (i.e. selection of the Display Passage radio button), the system found 83 related papers. Here what the system targets is not a document but partitions of this document. For convenience, we name a partition “passage”. Before the system performs information retrieval, document passages have been determined according to the query and the query-related concepts from the earthquake engineering ontology we already developed (Chou et al., 2009). Thus we say this system found 940 passages that appear agreeing with the Base Isolation query.

The same as in the traditional mode, the page 1 of the retrieved result in the conceptual mode lists top 5 agreeing documents. Top 3 agreeing passages, beneath each listed document, are also listed and each assigned an identifier followed by their similarity ranks (See Fig. 4). The right side of each result page shows how the topics of a document distribute over a concept tree or concept network. Besides, when the user chooses a document for review, the system will mark the agreeing passage in a full-text review (see Fig. 5). The left-top of this review page shows a concept tree or network that constitutes the chosen document. Such a concept view could help users rapidly figure out what the document describes. In addition, the second row in the left column of the document review page lists all the topics and positions of their corresponding passages. The user can switch among those topics, and the passage marked in the full-text view also change correspondingly. The third row lists the passages of other documents also containing the chosen topic. This function helps users study a concept across different documents.

Fig. 2 Page 1 of the retrieved result in the traditional retrieval mode

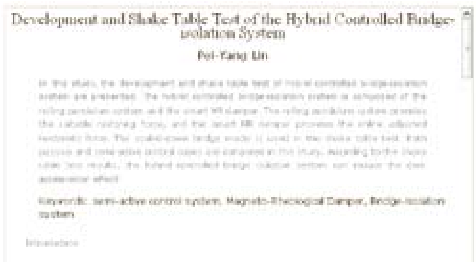

Fig. 3 Paper full-text review in the traditional retrieval mode

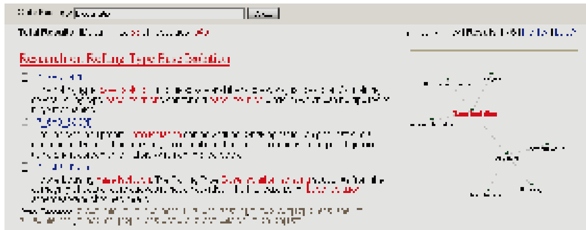

Fig. 4 Page 1 of the retrieved result in the conceptual mode

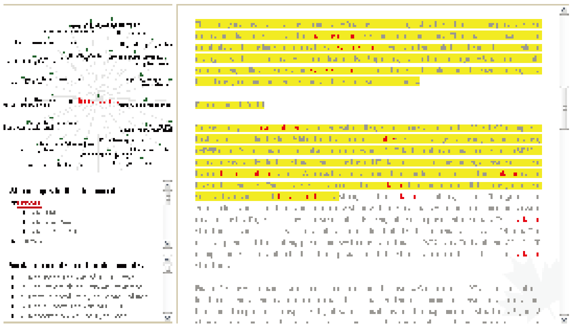

Fig. 5 Paper full-text review in the conceptual retrieval mode

Experiment Information Management

The development of experiment information management systems has been conducted for two years since 2007. First, a management system named NCREE Data Center was released in 2007. It provides a user interface and a central repository for users to store and manage their experimental data. In 2008, this work extended its focus from experimental data to all experiment-related information. Thus the experiment online-application system and experiment flow management system were developed and provides more convenient services to help researchers follow through some required experimental processes.

In 2009, NCREE began implementing a concept of integrated experiment information management in order to further carry out the experiment information management, and to reduce resource consumption and researcher effort on managing experiment information. It was expected that the integration of management systems could help users understand and then work more efficiently with the experiment information management. A concept of experiment life cycle was then conducted into the experiment information management. This concept describes what should be done during the life cycle of an experiment, which comprises five stages: application, review, plan, execution, and finish. The objective in application and review is to e-enable experiment preparation information and the objective in the last three stages focuses on experimental data collection.

Fig. 6 shows the integrated management system proposed in this work. This system implements the five stages of experiment life cycle by integrating the experiment online-application system, the experiment flow management system, and NCREE Data Center. As the front end of the whole system, the experiment online-application system is responsible for the application and review stages. The experiment flow management system, as the back end system, takes charge of the plan, execution, and finish stages. On the other hand, NCREE Data Center collects data generated from those five stages and makes the data compliant with the NCREE Data Model. That is, as long as users operate the online-application system and the flow management system, any experiment-related data or information will be concurrently saved into NCREE Data Center.

Although development of the online application and flow management systems can refer to the existing experiments in NCREE, it is still a challenge how to identify system requirements and how to design the user interface. In addition to satisfying the existing experiment operation flow, the system design should consider problems that may arise when the experiment information management intervenes any ongoing experiment. For now, two problems hinder the implementation of this system. First, the existing experiment operation flow has no distinction among the plan, execution, and finish stages. Second, there is no regulation on experimental data exchange between researchers and technicians. The solution on the two problems is what we currently investigate as new system requirements.

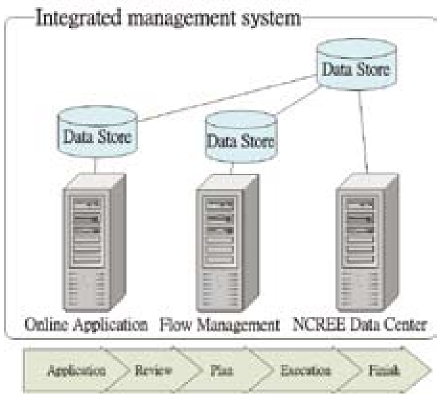

Fig. 6 Integrated management system

The prototype of the integrated management system was released for users to test in mid 2009. This work will base new system requirements on users' feedback to improve the management system. Besides, in order to ensure the system’s availability, a plan to recover the management system was developed. This disaster recovery plan covers backup and recovery mechanisms for management subsystems, databases, and file structures.

NCREE Web Information Service

Document management is crucial for an organization to maintain and secure its important information. Management tools are also required to facilitate document manipulation that is repetitive and complicated.

Table 1 shows some typical document operations and their corresponding problems which document managers usually encounter. To prevent document management from becoming a burden, we began thinking about what are the requirements on document management (see Table 2), what properties an ideal document management should have (see Table 3), and how to implement such document management system in minimum time.

In this work, a cooperation platform was developed to carry out document management. Based on the network infrastructure of NCREE, this platform provides management services along with an interface that controls flow of all the required operations and makes it smooth and reasonable. Its management interface (the back end) and user interface (the front end) are well designed, so users can efficiently obtain their solutions of document management. As shown in Fig. 7, a document library named the document center (文件中心) is created on this platform. Through this center, we can perform document management operations supported by this platform.

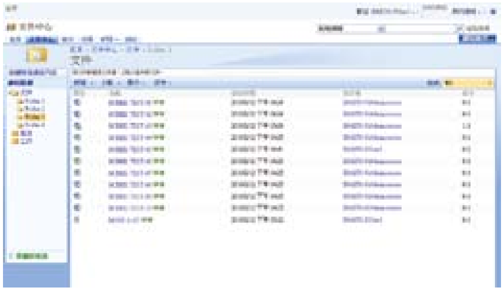

Fig. 7 Document center

With the help of this document management system, colleagues responsible for the information security of NCREE can manage their documents the way following the security policy they are required to implement. If any document modification is made by any colleague, it can be easily traced and the management system will notify the colleague of that modification. Besides, the system protects documents from being modified concurrently by more than one colleague.

To facilitate colleague cooperation, this management system provides a version control of documents. Prior to being published, a document is usually modified into several versions by different users. The versions allowed for publication will be determined by colleagues who this system authorizes to review documents. Here this system manages not only the repository of all versions but also all operations within the whole course of document revision. Without the help of this system, reviewing colleagues are often required to signoff for validating major versions. Colleagues participating in the course of revision thus need paper to print out for this signoff. Under document version control, however, such paper consumption that is not environmentally-friendly can be avoided.

Table 1 Typical document operations and problems

Operations	**Problems**
Create a file	Where to store this file? What file name can make this file transparent?
Update a file	How to find the file needing update? How to save a new version of a file and keep the older versions alive? How to co-manage a updating file?
Open a file	How to ensure this file is the latest version or the version the user requires? How to contact the most recent author if necessary?
Delete a file	How to recover a deleted file? How to ensure this file is actually deleted and no copies of it can be found?

Table 2 Requirements for document management

1	Methods to organize, sort and search files.
2	A file repository structure (e.g. trees) easy to maintain.
3	Methods to describe a file other than using the filename.
4	Automatic file naming.
5	A document revision record that keeps track of each modification made to a file.
6	Capable of monitoring files and notifying users of what happens on these files.
7	Capable of locking an updating file.

Table 3 Features of an ideal document management system

1	Storage of diverse document types
2	Built-in document version tracking.
3	Built-in file locking.
4	Automatic notification of file update..
5	Customized file management policy
6	Built-in file recovery mechanism.
7	Well-designed file security mechanism.
8	Customized view of files.

Conclusions

The earthquake engineering knowledge retrieval system OntoPassage has been developed on a basis of the earthquake engineering ontology this work created in 2008. OntoPassage offers a conceptual retrieval method that yields more precise result than traditional methods. This system is expected to boost the dissemination of NCREE's research achievements. In addition to improving this system's functions, this work will keep enriching the content of the earthquake engineering ontology and enriching system database with more knowledge documents. To implement the management of experiment life cycle, the integrated experiment information management system has successfully integrated the experiment online-application system, experiment flow management system, and the experimental data management system. This work will keep improving the functions of the integrated system so that it may fit into the whole course of the NCREE experiments. Finally, the cooperation platform has helped the colleagues responsible for the NCREE information security co-manage the documents all of them may access. Its e-enable document management flow, from modification, review signoff, to publication, can prevent users from printing out documents. This advantage could make NCREE colleagues work not only more efficiently but also more environmentally-friendly while avoiding unnecessary paper consumption.

References

Chou, K.-W., Tu, W.-H., Lin, C.-Y., Hsieh, S.-H. and Lin, H.-T. (2008), "Development and Application of NCREE Information Tools", *2007 NCREE Research Programs and Accomplishments*, *National Center for Research on Earthquake Engineering*, 113-116.

Chou, K.-W., Tu, W.-H., Lin, C.-Y., Hsieh, S.-H. and Lin, H.-T. (2009), "Development and Application of NCREE Information Tools", *2008 NCREE Research Programs and Accomplishments*, *National Center for Research on Earthquake Engineering*, 153-156.

Lin, H.-T. (2009), "An Ontology-based Passage Retrieval Method and Application for Domain-Specific Documents", Doctoral Dissertation, *Department of Civil Engineering*, *National Taiwan University*, 113-115(In Chinese).

Development of the On-Site Earthquake Early Warning Systems Using Neural Networks

Chu-Chieh J. Lin [1] and Zhe-Ping Shen [2]

林主潔、林哲平

Abstract

As part of the total solution of seismic hazard mitigation, the on-site earthquake early warning system (EEWS) is under development to provide a series of time-related parameters such as the magnitude of the earthquake, the time until strong shaking begins, and the seismic intensity of the shaking (peak ground acceleration). Interaction of different types of earthquake ground motion and variations in the elastic property of geological media throughout the propagation path resulted to a high nonlinear function. The neural networks were used to model these nonlinearities and the learning techniques were developed for the analysis of earthquake seismic signal. This warning system was designed to analyze the first-arrival from the three components of the earthquake signals in as early as 3 seconds after the ground motion is felt by the sensors. Then, the EEWS instantaneously provide a profile consists of parameters including the time until peak ground acceleration (PGA) and maximum seismic intensity. The neural network based system was trained using seismogram data from more than 1000 earthquakes recorded in Taiwan. The proposed EEWS can be integrated with distributed networks for site-specific applications. By producing accurate and informative warnings, the system has the potential to significantly minimize the hazard caused by earthquake ground motion.

Keywords: earthquake early warning system, neural networks, P-wave

Introduction

As one of the catastrophic natural disasters, earthquake usually caused tremendous damages to human beings. These irreversible damages include loss of human lives, public and private properties, as well as huge adverse economic impacts. Taiwan has suffered from the threatening of moderate earthquakes for a long time since Taiwan is located between Euro-Asian and Philippines tectonic plates on the Pacific Earthquake Rim. It is very difficult to avoid the damages caused by earthquake due to its high frequency of occurrence. If people can only receive the warning of the coming earthquake even by only few seconds, the damages can be reduced due to possible appropriate reaction.

The earthquake early warning system (EEWS) makes it possible to issue warning alarm before arrival of severe shaking (S-wave) and to provide sufficient time for quick response to prevent or reduce damages. The development of the EEWS is remarkable due to the solid background of the current development of the information technology and the earthquake observation technology. Based on the principle that the electronic signal is faster than the earthquake wave, the idea of EEWS was originated by Cooper in the U.S. since 1868. With the collaboration of California Institute of Technology and United States Geological Survey (USGS), Kanamori leaded the CUBE project in 1990. In Japan, Hakuno showed the idea of the earthquake early warning at an earlier stage. Also, the UrEDAS developed by JR is famous for their practical system. Recently, the Real-time Earthquake Disaster Prevention System and some other systems were developed and have been used in Japan. The Real-time Earthquake Information by JMA is based on the source information as a point source and therefore the accuracy of the predicted ground motion is limited especially for a large scale earthquake. In some engineering applications with higher demands,

[1] Associate Research Fellow, National Center for Research on Earthquake Engineering, jaylin@ncree.org.tw.

[2] Research Assistant, National Center for Research on Earthquake Engineering, zpshen@ncree.org.tw

the ground motion prediction shall not be limited to seismic intensity but shall be extended to more precise information such as further waveform information as well as peak ground acceleration (PGA).

The Neural Network has been applied to the ground motion prediction and generation since 1997 (Lin, 1999; Kuyuk and Motosaka, 2008 and 2009). Previous researches showed that the neural networks make it possible to provide more accurate, reliable and immediate earthquake information for society by combining the national EEWS and applying it to advanced engineering application as well as planning of hazard mitigation. This paper presents a state-of-the-art methodology using neural networks for forward forecasting of ground motion parameters (magnitude, PGA and estimated arrival time for strong motion) before S-wave arrival using initial part of P-waveform measured on-site. The estimated ground motion information can be used as warning alarm for earthquake damage reduction. The validity and applicability of the method have been verified using the CWB observation data sets of 2,505 earthquakes occurred in Taiwan.

On-Site Earthquake Early Warning System

The EEWS were expected to work efficiently at the sites with certain distance from the epicenter of the earthquake and also from the observation point where the earthquake motion (P-wave) is first observed. However, the EEWS was classified into 'on-site warning' and 'regional warning'. The regional warning EEWS was proposed and developed using the difference of the velocity for the beginning P-wave and destructive S-wave of the earthquake. Since 2007, Japan Meteorological Agency (JMA) began the general operation of the real-time earthquake information, which is composed of earthquake occurrence time and hypocenter information (the magnitude and the earthquake location) and is expected to provide warning and to substantially reduce casualties and physical damages of earthquakes. The EEWS by JMA could be called as 'national warning' due to the use of JMA-NIED system (nationwide earthquake observation system). One of the technical limits is its applicability to the near-source earthquakes. Although the propagation velocity of the waves depends on density and elasticity of the medium penetrated, the typical speed for the P-wave is around 5 km/sec and the speed for the S-wave is around 3 km/sec. If the area is far from the epicenter, say 100 km, then we will have at most 15 seconds reaction time before the S-wave arrives if the sensor at the observation station was able to pick up the earthquake signal (P-wave) and locate the epicenter within 18 seconds. However, if the location is less than 50 km from the epicenter of the earthquake, then the regional warning EEWS is almost useless since reaction time is less than one second. Therefore, the on-site EEWS has become increasingly important for areas located within the 50 km radius from the epicenter.

The EEWS developed in Taiwan by Central Weather Bureau (CWB) is similar to the one by JMA with so-called 'regional warning' or 'national warning'. While working with the sensor array from Taiwan Strong Motion Instrumentation Program (TSMIP), the EEWS has undergone various tests by cooperative research institutes since 2006, but the warning is only useful for the area located outside the 50 km radius of the earthquake epicenter. Therefore the on-site warning is much needed for a near-source earthquake. In addition, the effort to integrate the regional warning with on-site warning to become a more robust EEWS is noticed, and the on-site warning became increasingly significant for areas within the 50 km radius of the earthquake epicenter.

The on-site EEWS, as part of the total solution of seismic hazard mitigation, has been developed to provide a series of time-related parameters such as the magnitude of the earthquake, the time until strong shaking begins, and the seismic intensity of the shaking (peak ground acceleration). Interaction of different types of earthquake ground motion and variations in the elastic property of geological media throughout the propagation path resulted to high nonlinear function. Neural networks were used to model these nonlinearities and develop learning techniques for the analysis of earthquake seismic signal. This warning system was designed to analyze the first-arrival from the three components of the earthquake signals in as early as 3 seconds after the first ground motion is felt by the sensors at a rate of 50 samples per second. Then, the EEWS will instantaneously provide a profile consists of the estimates of hazard parameters, such as magnitude, arrival time of S-wave, and maximum seismic intensity (peak ground acceleration, PGA). The neural network based system is trained using seismogram data from more than 1,000 earthquakes recorded in Taiwan. The proposed EEWS can be integrated with distributed networks for site-specific applications. By producing accurate and informative warnings, the system has the potential to significantly minimize the hazards of a devastating ground motion.

Neural Network

Neural networks that possess a massively parallel structure are well-known as biologically-inspired soft computing tool. Their learning capabilities are provided by the unique structure of neural networks which allows the development of neural network based methods for certain mathematically intractable problems. Neural networks are formed by many interconnecting artificial neurons. Signals propagate along the connections and the strength of the transmitted signal depends on the numerical weights that are assigned to the connections. Each neuron receives signals from the incoming connections, calculates the weighted sum of the incoming signals, computes its activation function, and then sends signals along its outgoing connections. Therefore, the knowledge learned by a neural network is stored in its connection weights. To solve difficult engineering problems, it is necessary to design a task-specific neural network. Therefore, the neural network program developed by Lin using FORTRAN was used in this study. A combination of the Quick-Prop algorithm and the local adaptive learning rate algorithm were applied to the multiple-layer feed-forward (MLFF) neural networks to speed up the convergence rate of the networks. In addition, a mechanism to avoid over-training the neural networks for certain patterns was designed to monitor and equalize the influence of each pattern on the connection weights in the training case during each period. The average root-mean-square output error of the networks became lower while maintaining the generalization ability of the neural networks when using the adaptive process (Lin, 1999).

Furthermore, a new concept of grouping neural networks called Expert Group Neural Network (EGNN) (Lin et al., 2009) is also used in this study. The EGNN behaved like a group of experts, who grew up from different backgrounds with individual expertise and were able to provide the appropriate comment when working together as a committee. The optimal solution among the comments will be chosen with easiness and efficiency while solving this kind of inverse problem. Eight feed forward back-propagation neural networks trained by different inputs constituted the EGNN as a committee of experts to provide the time related information from earthquake accelerograms. The architecture of each neural network among EGNN is set to be different. It consisted of one input layer with 450 to 1500 neurons, two hidden layers and one output layer with 8 neurons. Each of the EGNN were used to analyze reversely the relationship between the initial few seconds of earthquake accelerogram and the magnitude as well as the waveform information (seismic intensity, peak ground acceleration, and arrival time of S-wave) of a specific earthquake.

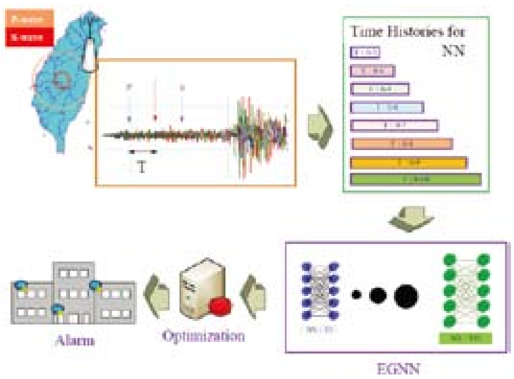

Figure 1 The framework of the on-site EEWS

Proposed Methodology and Case Study

The authors have proposed the new ground motion estimation method using neural networks and have verified its validity and applicability. The EGNN were trained with the data from first 3 seconds to 10 seconds of the earthquake accelerograms separately, as shown in Figure 1. The earthquake magnitude, PGA (seismic intensity) and arrival time of S-wave were predicted using the waveform data from in situ sensors. In this case, when the real-time information measured from the in situ sensors is verified as earthquake using 1 second of time history after the arrival of P-wave at the site, the initial 3 seconds part of the earthquake accelerogram (P-waveform) was used as the input for the neural network (NN:T-3) to estimate the magnitude of the earthquake, the PGA (seismic intensity) in three directions of the earthquake, and the arrival time of the S-wave. At the same time, the sensors are recording and the initial 4 to 10 seconds part of P-waveform were used as the input for the neural networks (NN:T-4, NN:T-5, .., NN:T-10) to estimate the parameters for EEWS. The best prediction was then chosen from these eight results through certain optimization algorithm or time factor. The emergency response actions can be activated right after receiving the warning due to the seismic intensity of the earthquake as well as the remaining time before the strong S-wave occur.

The training and testing (validation) data were prepared using the earthquake accelerograms recorded in Taiwan from 1992 through 2006, the magnitude of these earthquake were from Ritcher Scale 4.0 to 8.0. There are around 60,000 recorded accelerograms from 2,505 earthquakes. Among them, the training data were randomly chosen using around 50,000 earthquake records (almost 80% of the total) from 2,371 recorded earthquakes, while the testing data were prepared using the rest 10,000 earthquake records (almost 20% of the total) from 1,012 recorded earthquakes.

Figure 2-3 shows the comparison of the results in prediction of seismic intensity and arrival time for S-wave of NN model T-3. In Fig. 2, R^2=0.6977 for PGA and the accuracy of the exact seismic intensity prediction is around 51% while the accuracy for the ± one degree seismic intensity is around 90%. Figure 3 shows that R^2=0.6051 for the accuracy of the estimated arrival time for S-wave. If a tolerance of ±20% is considered feasible for warning people on the arrival time of S-Wave, then the accuracy is around 60%.

As for the comparison of results in prediction of seismic intensity and arrival time of S-wave from NN model T-10, the R^2=0.7714 for PGA and the accuracy for the exact seismic intensity prediction is around 50% while the accuracy for the ± one degree seismic intensity is around 95%. For the estimated arrival time of S-wave within ±20% tolerance, the accuracy is around 60%.

It has been found that the accuracy of the predicted peak ground motion is drastically improved compared the results of NN:T-10 to NN:T-3 since more earthquake information (10 seconds of earthquake accelerogram) is provided for neural network to be considered, however, the disadvantage for NN:T-10 is the time loss of 7 seconds.

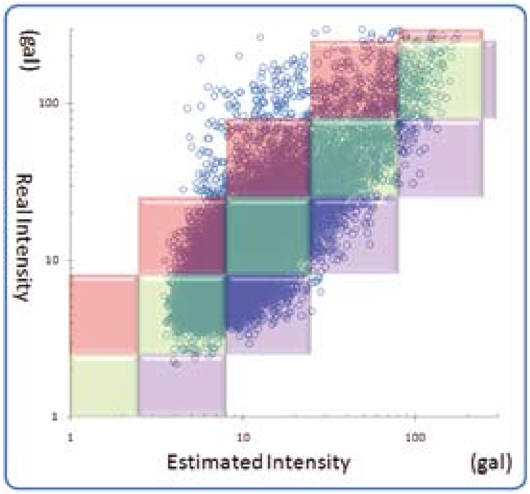

Figure 2 Comparison of the real and estimated seismic intensity (T-3)

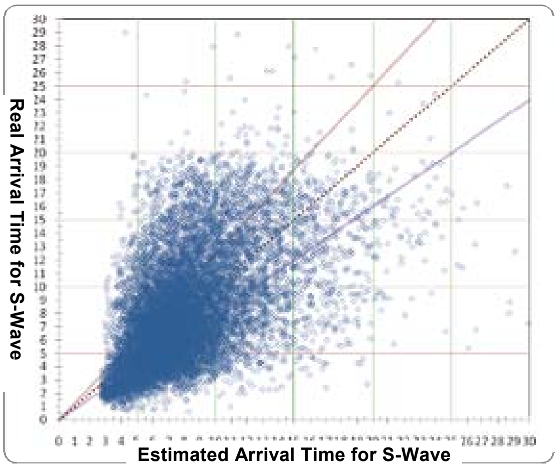

Figure 3 Comparison of the real and estimated arrival time for S-wave (T-3)

Conclusions

In this report, the authors presented the early stage development of the on-site EEWS using neural networks as the recent research achievement of the project. It is always better to be well prepared in times of severe earthquakes and since the obstacles could be expected beforehand. The methodology using EGNN were described and its results show great potential in the application. During a large earthquake, time factor is the key countermeasure, thus a good optimization algorithm to determine immediately when and what information must be provided. Besides, the development of the data analysis method as well as the verification of the reliability of the communication lines and system would be needed in handling the online utilization of the EEWS with more robustness. The immediate, accuracy and reliability of the earthquake information are needed and should be integrated with the EEWS. Therefore, the EEWS is able to consequently bring huge benefits on the earthquake hazard mitigation. With further research on the use of the observed earthquake record and enhancing the accuracy and immediate response of the real-time ground motion prediction, the possibility of the on-site EEWS is within reach.

References

Cooper, J.D., (1868), San Francisco Daily Evening Bulletin, November 3

Horiuchi, S., H. Negishi, K. Abe, A. Kamimura, and Y. Fujinawa (2005). An Automatic Processing System for Broadcasting Earthquake Alarm, *Bull. Seism. Soc. Am.* **95**, 708-718.

Kuyuk H.S., and Motosaka, M., 2008, "Spectral Forecasting of Earthquake Ground Motion using Regional and National EEWS for Advanced Engineering Application against Approaching Miyagi-ken Oki Earthquakes," *14th World Conference on Earthquake Engineering*, Beijing, China: CD-ROM: No. S05-03-013

Kuyuk, H.S., and Motosaka, M., 2009, "Forward spectral forecasting of ground motion with the information of earthquake of earthquake early warning systems for structural control," *Journal of Japan Association for Earthquake Engineering*, Vol.9, No.3.

Lin, C-C.J., 1999, "A Neural Network Based Methodology for Generating Spectrum Compatible Earthquake Accelerograms" *Ph.D. thesis, Dept. of Civil Engrg.,* UIUC, Urbana, IL

Lin, C.-C. J. and Sung, Y.C. "Expert Group Neural Networks for Structural Health Diagnosis of Mau-Lo Creek Cable-stayed Bridge" *Innovative Computing, Information and Control Express Letters – An International Journal of Research and Survey (ICIC-EL)*, Vol.3, No.1, 47-52 (2009).

Nakamura, Y. (1988). On the Urgent Earthquake Detection and Alarm System (UrEDAS), *Proc. 9th World Conference on Earthquake Engineering*, 673-678.

Wu, Y.-M., and H. Kanamori (2005). Experiment on an onsite early warning method for the Taiwan early warning system, *Bull. Seism. Soc. Am.* **95**, 347-353.

Feasibility Study of Structural Response Prediction by Scenario-based Technique

Ping-Yun Wu [1] and Tzu-Kang Lin [2]

吳炳昀 [1]、林子剛 [2]

Abstract

Earthquake occurs frequently in Taiwan, thus may caused serious damages to structures. To avoid the collapse of building during an earthquake similar to the 921 Chi-Chi earthquake, a real-time earthquake early warning system (EEWS), which can predict the structural response efficiently and accurately during an earthquake, has been developed in this study. The scenario-based technique were developed herein based on the strong-motion seismograph network records from the Central Weather Bureau (CWB) while the verification of the regression modules was also conducted to check the feasibility of the scenario-based technique by comparing the predicted amplitude coefficients with the amplitude coefficients from real structural responses.

Keywords: Earthquake early warning system, scenario, regression

Introduction

It is known that when earthquake happens, the farther the distance between the structure and earthquake's epicenter, the longer the time that it will take to propagate the energy to the structure. Meanwhile, due to the different wave speeds between pressure (P) wave and shear (S) wave, there will always be difference on their reaching time. Recently, the concept of real-time earthquake early warning system (EEWS) is proposed based on the time delay characteristic. Meanwhile, estimation of the peak structural response is also an important issue. It is expected that the peak structural response can also be roughly predicted with the early warning system. By inputting earthquake characteristic such as the magnitude of the earthquake, the peak ground acceleration (PGA), and the distance between the structure and epicenter into the real-time EEWS system with scenario simulation technique, the amplification coefficient for each floor of the structure respective to the ground response can be obtained easily.

Scenario -based Technique

The supporting theory on the scenario-based technique is derived from the branch of informatics, the Support Vector Machine (SVM) method. To integrate the scenario-based technique into the real-time EEWS System, the first thing is to decide the proper SVM module in estimating the structural response. In this study, the two most correlated earthquake parameters obtain from the preliminary analysis right after the earthquake, which are the distance to the epicenter and the magnitude of the earthquake, were chosen as the basic classification condition for the SVM modules. The corresponding scenario-based modules were then built up by taking other parameters into consideration, such as the structure damping ratio, the soil type, etc. As the EEWS concept mentioned above, the response amplitude of a structure will be obtained by inputting the parameters obtained from the strong ground motion stations of the CWB to the SVM modules of the real-time EEWS System. The flowchart of the system is shown in Fig. 1.

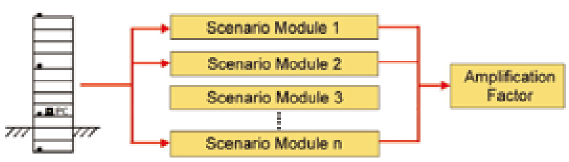

Fig. 1 Flowchart of the proposed system

[1] Undergraduate student, National Taiwan University Civil Engineering, ckwuda@gmail.com

[2] Associate Research Fellow, National Center for Research on Earthquake Engineering, tklin@ncree.org.tw

Regression Analysis

Regression analysis is commonly referred to as a statistical method for analyzing data. The main purpose of using regression analysis is to find the specific relationship between data, or the correlation between two or multiple parameters. Furthermore, a mathematical model can be built to predict specific interested variables through investigating these parameters. In this study, the regression analysis method will be conducted accompanied with the scenario-based techniques to predict the roof amplification factor of a structure under an earthquake. Since the regression model developed here is based on the earthquake data collected before, the method can be expected to be reliable with high precision for response estimation.

To discuss the relationship between the independent earthquake characteristic variables and the structural response variables, the Response Surface Methodology (RSM) is conducted in this study. The RSM is an extended application of the combination between mathematics and statistics, and it is usually found in the design of experiments where they are used to optimize the design variables.

First, an unknown objective function should be assumed where

Y is the structural response; $X_1, X_2, \cdots, X_n$ are the independent variables, and ε is the error. The optimized design variable values and the regression model can be established by using a large amount of records from the database.

Generally, two common RMSs were used for design purpose. One is the approximation of lower order polynomial, which is called the first-order model defined as follows:

$$Y = \alpha_0 + \sum_{i=1}^{N} \alpha_i x_i \tag{1}$$

Another one is the polynomial with higher order, which is the second-order model defined by the following:

$$Y = \alpha_0 + \sum_{i=1}^{N} \alpha_i x_i + \sum_{i=1}^{N} \alpha_{ii} x_i^2 + \sum_{i<j}\sum \alpha_{ij} x_i x_j \tag{2}$$

The interaction model and pure quadratic model are the other two options for regression analysis.

The form of interaction model can be expressed as follows:

$$Y = \alpha_0 + \sum_{i=1}^{N} \alpha_i x_i + \sum_{i<j}\sum \alpha_{ij} x_i x_j \tag{3}$$

The form of pure quadratic model is shown below:

$$Y = \alpha_0 + \sum_{i=1}^{N} \alpha_i x_i + \sum_{i=1}^{N} \alpha_{ii} x_i^2 \tag{4}$$

The model includes a constant (α_0), first order terms (α_i), interaction terms (α_{ij}), and second order terms (α_{ii}). Both interaction and pure quadratic models are parts of second order regression models. There is no second order term in intersection models and no intersection term in pure quadratic models. A comparison of four regression models mentioned above was conducted in this study in order to determine the most effective regression model.

The Construction and Analysis of Scenario-based System

In this study, the Tai Power Building was taken as the study sample. A total of 26 sensors were distributed at the B3, 1F, 9F, 19F, and RF floors of the major structure and B2, 5F, and RF of the secondary structure. All these sensors were arranged on the floor surface. By utilizing these sensors, the peal acceleration values of each floor will be collected whenever an earthquake happened, and in the mean time, the time history analysis for the finite element method (FEM) model of the Tai Power Building will be conducted by using different time history records in the Taipei basin. The regression of Scenario-based modules was based on the analysis result of 500 earthquake records.

Fig. 2 The Tai Power Building

When earthquake happened, due to the difference of the magnitude, distance to epicenter, and intensity, the structure responses usually behave in different ways. In the analysis of the Tai Power Building, the magnitude of earthquakes, distance to epicenter, ground accelerations, the frequencies of the earthquake, and the time differences between P wave and S wave were taken as five independent variables. The relationship between the roof floor amplitude and the five variables will be discussed, and the regression formula for predicting the responses of the roof floor of the structure can be obtained. By comparing the correlation coefficients between the 5 variables and the amplification factor of the roof floor, it can be found that the magnitude of earthquake and the distance to epicenter are the two governing variables with the highest correlation to the amplification factor of the roof floor in both the X and Y directions. From the result, these two variables will be used in the classification standard of the scenario-based modules.

After determining the variables with the highest correlation, the data were classified into two groups based on the value of the earthquake magnitude. The standard is to divide the database into two groups with approximately equal records. In this analysis, the earthquake magnitude 6 is the first standard which separates the data into two groups. The first group includes data with earthquake magnitude larger than 6 and the other is data smaller than 6. For each group, the distance to the epicenter is used as another classification criterion. For the group in which the magnitude of the earthquake is smaller than 6, the criterion is that the distance to epicenter equals to 60km. For another group, the criterion is that the distance to epicenter equals to 130km. The four groups of Scenario-based modules are shown in Fig. 3.

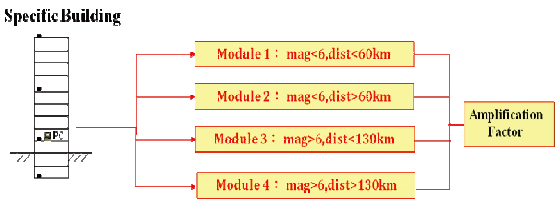

Fig. 3 The Scenario-based modules

As shown in Figure 3, each group of data will be fitted into a regression model, and there will be one regression formula for each scenario-based module. The comparison of the scenario-based regression module having magnitude smaller than six and distance smaller than 60km with the real magnitude is shown in Figure 4. By the method developed in this study, when an earthquake happened, the amplification factor of the roof floor of the structure can be rapidly estimated and the possible responses of the structure can be calculated.

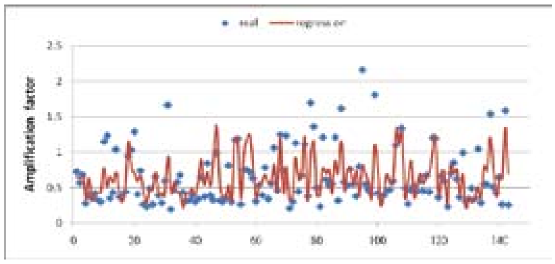

Fig. 4 The module of mag<6 and dist<60kmin

The Test of the Scenario-based System

In this section, some randomly selected data were used to test the reliability of the regression formula generated from the previous regression analysis. To test the amplification factor predicted by the regression formula, the earthquake data of the Tai Power Building from the CWB database, which were not being used in establishing the regression module, were selected. The data were classified and fitted into its corresponding scenario-based module. The five earthquake parameters, namely: the earthquake magnitude, the distance to epicenter, the frequencies of earthquakes, and the time differences between P wave and S wave, are then inputted to the regression formula of the module. The amplification factor of the roof floor has then finally compared with the practical value.

The comparison between the regression amplitudes and error is shown in Table 1. Two groups of modules, mag<6, dist<60km and mag>6, dist<130km were taken as examples here. As shown in Table 1, there are errors between the amplification factor based on the regression formula and practical amplification factor. The errors are greater in the module of mag<6, dist<60km in contrast with mag>6, dist<130km.

Tale1 1. Comparison of amplification factor in x-direction

Time	Amp X	Regression Amp X	Error
mag<6, dist<60km			
2005/10/05 16:16:35	0.64	0.45	-25.85%
2000/11/20 00:07:09	0.75	0.45	-40.23%
mag>6, dist<130km			
1996/07/29 20:20:53	0.64	0.73	13.86%
2002/03/31 06:52:49	2.84	2.92	2.78%

Table 2. Comparison of intensity in x-direction

Time	Practical intensity	Intensity estimated
mag<6, dist<60km		
2005/10/05 16:16:35	2	2
2000/11/20 00:07:09	2	2
mag>6, dist<130km		
1996/07/29 20:20:53	3	3
2002/03/31 06:52:49	6	6

Conclusions

From the results discussed above, the feasibility of predicting the structure response by scenario-based regression formula has been verified. According to the comparison between the estimated amplification factor and practical ones, accuracy improvement of the system is still required. Improvement of the accuracy will be a big challenge for future studies. In the present study, same problems happened in every scenario-based module. When an extremely large value appeared, it may not be included into the regression trend line. As a result, larger error occurs. To avoid such situations and to increase the accuracy of regression analysis, different scenario-based estimation method can be tried in order to figure out the best regression result, and then the predicted amplification factor may be closer to the practical ones. In addition, other regression models, such as nonlinear regression models, can also be introduced in the future study and compared with the present regression method in order to find out the best way for regression analysis.

Furthermore, the Tai Power Building was used in the present study, but due to the different characteristics of different structures, such as structure's damping ratio, the arrangement of a structure, etc. the roof floor amplification factor would definitely be different. The characteristic of structure should be considered when building another real-time EEWS by scenario-based technique. Moreover, the EEWS system is expected to be implemented in a customized way.

References

[1] MATLAB. *User's Guide.* The MathWorks, Inc.: Natic, MA, 1992

Editing of Popular Science Handbook on Earthquake Engineering

Zheng-Kuan Lee[1], Shyh-Bin Chiou[2], Hui-Lin Chang[3] and Keh-Chyuan Tsai[4]

李政寬 [1]、邱世彬 [2]、張惠玲 [3]、蔡克銓 [4]

Abstract

The September 21, 1999 Jiji earthquake shook all of Taiwan and caused massive damage, and many other catastrophic have occurred around the world during the past decade. Members of the public must make sure that their homes will be safe in the event of an earthquake, and should know how to buy an earthquake-resistant home. In order to respond to the public's need for knowledge and enhance disaster prevention awareness, the National Center for Research on Earthquake Engineering (NCREE) recently compiled a popular science handbook on earthquake engineering entitled "Building a Safe Homeland—Introduction to Earthquake Engineering." This book has won widespread praise since it was first published in September 2009. This work results report provides an introduction to the handbook's key content items.

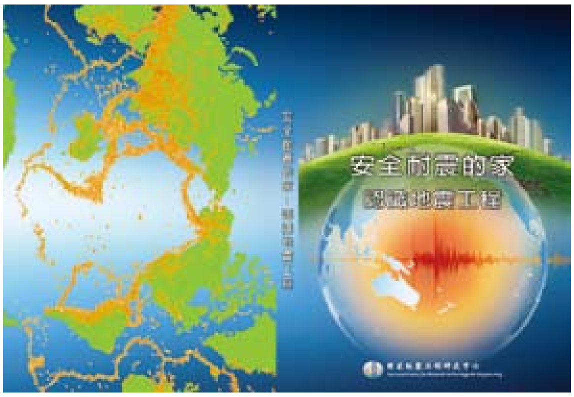

Cover of Popular Science Handbook on Earthquake Engineering

Foreword

Taiwan—"a beautiful island in a magnificent ocean"—has been shaped by geological activity and climatic changes. Everyone living here must adapt to and prepare for the eventuality of earthquakes and typhoons. Due to the advance of technology, typhoon forecasts are accurate enough that everyone can prepare and protect themselves. In contrast, scientists still have no way of accurately forecasting when and where earthquakes will strike, nor can they predict how strong earthquakes will be. Earthquakes will always be a threat to society, and will always be hard to defend against.

Earthquakes are simply the shaking of the earth. When the epicenter of an earthquake is in a sparsely-populated, undeveloped area, the earthquake will not cause many deaths and injuries. But if the epicenter of a strong earthquake is near a city or heavily postponed area, the quake may cause severe loss of life due to collapsing buildings. A major earthquake occurring near an urban area will test every building: Buildings with strong earthquake resistance will survive, but buildings with poor resistance will be damaged or collapse. Whether a building is able to withstand shaking in an earthquake is literally a matter of life and death.

Since Taiwan has experienced many earthquakes during the last three decades, citizens have become increasingly concerned about the safety of their homes and other buildings. The National Center for Research on Earthquake Engineering has compiled this handbook in order to introduce

[1] Associate researcher, National Center for Research on Earthquake Engineering
[2] Assistant researcher, National Center for Research on Earthquake Engineering
[3] Project assistant researcher, National Center for Research on Earthquake Engineering
[4] Former NCREE manager and professor, Department of Civil Engineering, National Taiwan University

earthquake-resistant construction from an "engineer's point of view," and also interest young students in earthquake engineering research and practice. This book uses clear and simple text, illustrations, and simulated experiments to explain earthquakes, the ways that they cause damage, and things to look for when buying a house.

The 10th anniversary of the great 1999 Jiji earthquake has recently passed. Children who were in elementary school children at that time have now grown up and are in high school or university. Perhaps many have not vivid memories of the earthquake. Although our recollections and impressions may fade and disappear, we can preserve and use our experiences and lessons learned. If we can employ these lessons to prevent future disasters, then the suffering of the victims of the Jiji earthquake will not have been in vain. NCREE hope that this handbook can pass on valuable experience and lessons about earthquakes.

Introduction

The field of earthquake engineering spans a wide range of disciplines. All technologies that can alleviate damage from earthquakes and quickly restore the normal functions of society are included within earthquake engineering. One way of looking at earthquake engineering is to divide it into an upstream area of seismology, a mid-stream area of engineering technology, and a downstream area of risk management. Each of these areas is highly specialized and complex.

While most people may not be very familiar with earthquake engineering, they are certainly very concerned about the safety of their homes. This book is therefore positioned as an instructional popular science textbook, and is entitled "Building a Safe Homeland—Introduction to Earthquake Engineering." The book's goal is to increase public awareness of the need to prevent earthquake damage, and increase curiosity and interest in earthquake engineering. We avoid the use of mathematical equations in his book, and instead rely on photographs, illustrations, and easy-to-understand text to explain scientific and engineering concepts. We hope that the comic book-like format will give readers a clearer picture of seismic activity, earthquake damage, the principles of earthquake-resistant construction methods, how to find an earthquake-resistant home, how to protect yourself from earthquakes at home, and guidelines for building inspection after an earthquake. We also hope that this book will make high school students interested in civil engineering, environmental engineering, and new earthquake-resistance technologies.

Some of the materials used in this handbook were obtained from government agencies and university professors, and we are very grateful for their permission to use these items. Some materials were provided by personnel at the National Center for Research on Earthquake Engineering (NCREE), and some materials were arranged and produced by the editorial committee before receiving visitors at NCREE. The editorial committee acknowledges that there may be errors or omissions in the contents of this book, and asks readers to provide their comments and corrections in order to help us continue to make improvements

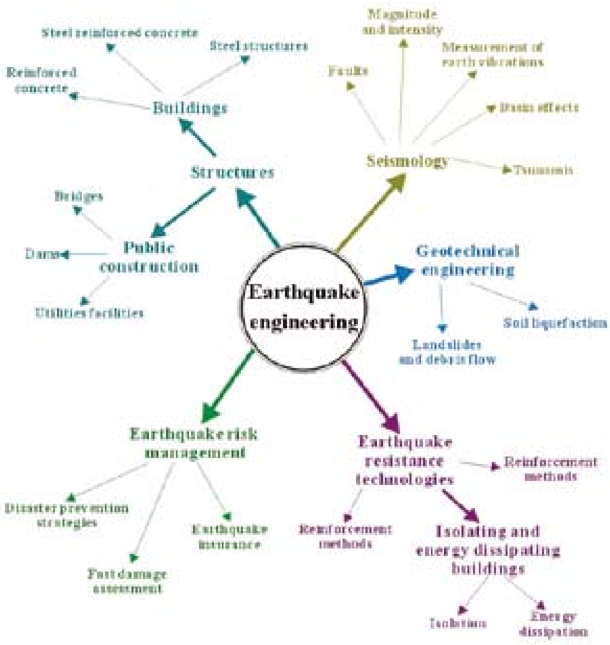

Overview of Earthquake Engineering

Key Current Areas of Work

After completing the Chinese version of a popular science handbook on earthquake engineering, the working group will publish an English translation, and hopes to establish an "earthquake engineering science education web site" within the next one or two years. This web site will contain even more videos and interpretive information, and will be a step toward the goal of establishing an "earthquake engineering online museum." When that time comes, domestic and foreign students, teachers, and ordinary people will be able to learn about the practical aspects of earthquake engineering and the importance of preparedness and preventive measures.

Contents

Relevant Online Information

■ **Earthquake-related information**

- **Central Weather Bureau**
  http://www.cwb.gov.tw
  Weather forecasts, weather observations, earthquake forecasts, typhoon information, "One Hundred Questions about Earthquake" introducing basic earthquake knowledge
- **Seismic Monitoring System, Incorporated Research Institutions for Seismology**
  http://www.iris.edu/seismon
  Global real-time earthquake monitoring information
- **Earthquake Hazards Program, US Geological Survey**
  http://earthquake.usgs.gov
  Global earthquake information and research
- **Central Geological Survey, MOEA**
  http://www.moeacgs.gov.tw
  National geology, minerals, fault surveys, and research
- **Taiwan Geoscience Portal, Central Geological Survey, MOEA**
  http://twgeoref.moeacgs.gov.tw
  Geoscience information, survey documents, and shared library/archive materials concerning Taiwan and nearby marine areas
- **921 Online Museum**
  http://921.gov.tw
  Literature, photographs, videos, stories, activity awareness, educational resources, and earthquake historic sites connected with the 921 earthquake
- **Fukuwa Laboratory, Environmental Research Department, Nagoya University, Japan**
  http://www.sharaku.nuac.nagoya-u.ac.jp/laboFT/bururu_english/index.htm
  Interesting popular science experiments concerning earthquake engineering
- **National Center for Research on Earthquake Engineering**
  http://www.ncree.org
  Earthquake resistance technology research, fast assessment of earthquake damage, building structural experiments
- **921 Online Museum**
  http://921.gov.tw
  Literature, photographs, videos, stories, activity awareness, educational resources, and earthquake historic sites connected with the 921 earthquake
- **Fukuwa Laboratory, Environmental Research Department, Nagoya University, Japan**
  http://www.sharaku.nuac.nagoya-u.ac.jp/laboFT/bururu_english/index.htm
  Interesting popular science experiments concerning earthquake engineering

■ Disaster rescue and relief units	
●	**Fire safety video news channel, National Fire Agency, Ministry of the Interior** *http://www.nfa.gov.tw* Fire safety legal queries, fire prevention knowledge, fire safety information, disaster relief and emergency rescue information *http://enews.nfa.gov.tw/V4index-enews.asp* Fire safety tips, fire safety classroom, disaster relief documentaries
●	**National Construction & Planning Administration, MOI** *http://www.cpami.gov.tw* Earthquake-resistant building design standards and explanation
●	**Executive Yuan National Disasters Prevention and Protection Commission** *http://www.ndppc.nat.gov.tw* Disaster prevention projects, inter-agency disaster prevention coordination and integration
●	**Debris flow prevention information web site, Soil and Water Conservation Bureau, Council of Agriculture** *http://246.swcb.gov.tw* Debris flow warning and prevention information, online family learning, major debris flow incident reports
●	**Atomic Energy Council** *http://www.aec.gov.tw* Radiation contaminated home queries, environmental radiation detection

■ Professional engineering associations	
●	**Taipei Professional Civil Engineers Association** *http://www.tpce.org.tw* Structural safety assessment, water and soil conservation facility assessment
●	**Taipei Structure Engineering Association** *http://www.tsea.com.tw* Structural safety appraisal, structural reinforcing appraisal, earthquake resistance assessment
●	**Taipei/Taiwan Professional Geotechnical Engineers Association** *http://www.pga.org.tw* Site foundation surveys, soil and rock core assessment, earth retaining structure and supports, foundation improvement and grouting, side slope stabilization
●	**Taiwan Professional Civil Engineers Association** *http://www.twce.org.tw* Assessment of structural safety, assessment of water and soil conservation facilities

發行：財團法人國家實驗研究院國家地震工程研究中心
出版：財團法人國家實驗研究院國家地震工程研究中心
地址：台北市辛亥路三段200號
電話：(02)6630-0888
傳真：(02)6630-0858
http：//www.ncree.org.tw
ISBN：978-986-85281-3-0
99年5月出版